Design of Luminescent Polypyridyl-Imidazole Based Ruthenium Complexes and Implication of Machine Learning and Artificial Intelligent Tools to Analyse Their Stimuli-Responsive Behaviours

A Thesis

Submitted for the Degree of

Doctor of Philosophy (Science)

of

Jadavpur University

by

Anik Sahoo

DEPARTMENT OF CHEMISTRY

JADAVPUR UNIVERSITY

JADAVPUR, KOLKATA 700032

INDIA

2024

যাদবপুর বিশ্ববিদ্যালয়
কলকাতা-৭০০০৩২, ভারত

*JADAVPUR UNIVERSITY
KOLKATA-700 032, INDIA

FACULTY OF SCIENCE: DEPARTMENT OF CHEMISTRY : INORGANIC CHEMISTRY SECTION

CERTIFICATE FROM THE SUPERVISOR

This is to certify that **Mr. Anik Sahoo** who got his name registered on 22.08.2019 and having index No. 35/19/Chem./26, has submitted his thesis entitled "Design of Luminescent Polypyridyl-Imidazole Based Ruthenium Complexes and Implication of Machine Learning and Artificial Intelligent Tools to Analyse Their Stimuli-Responsive Behaviours" on 11/07/2024 for the award of Ph.D. (Science) degree of Jadavpur University. The work embodied in the thesis is absolutely based upon his own work under my supervision and that neither this thesis nor any part of it has been submitted for any degree/diploma or any other academic award anywhere before.

Sujoy Baitalik 11/07/2024

(SUJOY BAITALIK)

Signature of the Supervisor
& Date with official seal

Professor Sujoy Baitalik
Department of Chemistry
Jadavpur University
Kolkata- 700 032, India

দূরভাষ: ২৪১৪-৬৬৬৬/৬১৯৪/৬৬৪৩/৬৪৯৫/৬৪৪৩ প্রসারণ: ২৪৬৯ Website:www.jadavpur.edu Phone:2414-6666/6194/6643/6495/6443 Extn.2469
দূরবার্তা: (৯১)-০৩৩-২৪১৪-৬৪১৪/৬২১০/২৪১৩-৭১২১ E-mail : hod@chemistry.jdvu.ac.in Fax: (91)-033-2414-6414/6210/2413-7121

Dedicated
To
My Family

Nothing in life is to be feared, it is only to be understood. Now is the time to understand more, so that we may fear less.

…….Marie Curie

PREFACE

The research documented in the thesis titled "Design of Luminescent Polypyridyl-Imidazole Based Ruthenium Complexes and Implication of Machine Learning and Artificial Intelligent Tools to Analyse Their Stimuli-Responsive Behaviours" was conducted at the Department of Chemistry of Jadavpur University from 2018 to 2024. The thesis comprises seven chapters.

Chapter 1 provides an insightful overview of the photophysical and electrochemical characteristics of Ru(II) complexes derived from polypyridine ligands. The narrative delves into a concise review of Ru(II) complexes incorporating diverse polyheterocyclic ligands, placing special emphasis on their thoughtful design and photophysical attributes. The discussion extends to the modulation of photophysical properties in the presence of various external stimuli. Additionally, a thorough exploration unfolds, shedding light on the intricate Boolean logic operations and artificial intelligence-based tools demonstrated by these complexes. The review encapsulates their optical and electrochemical responses in the presence of a broad spectrum of activating inputs. Finally, the chapter concludes with a thoughtful reflection on the objectives and scope of this dissertation.

Chapter 2 details the synthesis and thorough characterization of a polypyridyl-imidazole-based bridging ligand (phen-H_2PhImz-bpy) with three bidentate coordinating sites and its monometallic, bimetallic, as well as trimetallic Ru(II) complexes. The investigation focuses on the systematic modulation of MLCT absorption, emission, and redox behavior with the gradual incorporation of Ru^{2+} units. The study establishes structure-property relationships, revealing that the complexes are promising building blocks for various light-harvesting applications.

Chapter 3 presents thorough investigations on the anion- and acid-responsive behaviors of the three Ru(II) complexes as reported in Chapter 2. Thereafter, the adaptive neuro-fuzzy inference system (ANFIS) encompassing five membership functions, viz., triangular (trimf), trapezoidal (trapmf), generalized bell-shaped (gbellmf), Gaussian (gaussmf), and pi-shaped (pimf), has been employed for accurate prediction of the

experimental data as well as for appropriate modeling of the sensing characteristics of the complexes.

Chapter 4 explores the anion- and pH-sensing behaviors of an imidazole-dicarboxylate-based Ru(II)-bipyridine complex employed for the creation of multiple Boolean and fuzzy logic systems. The absorption, emission, and electrochemical behaviors of the metalloreceptor were significantly modulated upon the influence of basic anions (such as F^-, AcO^-, and $H_2PO_4^-$) as well as by altering the pH of the solution. The metalloreceptor demonstrates several advanced Boolean functions, namely, three-input OR gate, set–reset flip-flop logic, and traffic signal, by employing its electrochemical responses through proper use of different inputs. Several soft computing tools, viz., artificial neural networks (ANN), fuzzy logic systems (FLS), and adaptive neuro-fuzzy inference system (ANFIS), are also employed to foresee the experimental sensing data and to appropriately model the protonation-deprotonation behaviors of the metalloreceptor.

Chapter 5 discusses the anion-responsive behaviors of two heteroleptic bis-tridentate Ru(II) complexes comprising of 2,6-bis(benzimidazole-2-yl)pyridine (H_2pbbzim) as well as 2-naphthyl (tpy-Naph) and 9-anthryl (tpy-Anth) substituted terpyridine ligands. Remarkable changes in their absorption, emission, as well as electrochemical and spectroelectrochemical responses, occur in the presence of selected anions. Restoration of their initial states is made possible by acid, and the process is reversible. The spectral, electrochemical, and spectroelectrochemical responses of the complexes upon the influence of anions and acid were employed to mimic the operations of YES-NOT and set-reset flip-flop logic gates. Finally, machine learning tools such as artificial neural networks (ANNs), adaptive neuro-fuzzy inference system (ANFIS), and decision tree (DT) regression are employed to analyze and forecast the experimental data. The outcomes of the ANN, ANFIS, and DT methods are also tallied with the experimental results.

Chapter 6 examines the cation- and anion-responsive behaviors of a terpyridyl-imidazole-based bifunctional receptor (tpy-HImzPh_3NMe_2). The compound serves as a multi-channel sensor for both anions (F^-, CN^-) as well as cation (Fe^{2+}). Experimental and

computational analyses, including DFT and TD-DFT calculations, provide insights into the electronic structure of the receptor as well as the mode of interaction with incoming ions. The receptor demonstrates several Boolean logic functions. Additionally, ANNs, ANFIS, and decision tree regression analysis are executed to thoroughly analyze and also predict the ion-sensing behavior of the receptor.

Chapter 7 addresses the modulation of spectral properties of a terpyridyl-imidazole-based bifunctional receptor (tpy-HImzPh_3). Significant alteration in its absorption and emission spectral profiles takes place in the presence of selected cations and anions. The spectral responses are utilized for mimicking several Boolean logic functions. Fuzzy logic is also implemented to establish an infinite-valued setup, while ANN and ANFIS are employed for accurate prediction of the experimental data.

ACKNOWLEDGEMENTS

This dissertation would not have been possible without the help of so many people in different way throughout my research carrier. I want to acknowledge those people who played a role directly or indirectly for the successful completion of my thesis.

First and foremost, I would like to express my sincere gratitude to my supervisor Professor Sujoy Baitalik for his enthusiasm and immense knowledge. His continuous encouragement and guidance helped me to solve every problem in my research work. I am greatly benefitted by his resourceful insight on my analysis and numerous revisions. He has always taught me with patience and perfection. Not only is he a good PhD guide, but also a good advisor who helped me to take right decision in every aspect of life. This journey was impossible to complete successfully without his constant guidance and motivation. His hard work and positive energy has always been an inspiration for me. I am both grateful and delighted for my time working with Prof. Sujoy Baitalik.

It is my pleasant duty to express special thanks to the Department of Chemistry, Jadavpur University for providing me the opportunity to accomplish my research work. I wish to express my sincere gratitude to the present Dean, Faculty Council of Science, Prof. Ashis Kumar Sarkar, the Head of the department, Prof. Kajal Krishna Rajak and the Section-in-charge, Prof. Partha Roy for providing the departmental and laboratory facilities. I also extend my heartfelt gratitude to all the faculty members and non-teaching staffs of this department for their help and supportive cooperation. I would specially like to acknowledge Prof. Samaresh Bhattacharya, Prof. Nitin Chattopadhyay, Prof. Chittaranjan Sinha, Prof. Subrata Mukhopadhayay, Prof. Jnan Prakash Naskar, Prof. Kalyan Kumar Mukherjee, Prof. Mahammad Ali, Dr. Tapan Kumar Mondal, Prof. Saurabh Das, Dr. Bibhuti Bhusan Shaw, and Dr. Partha Mahata for their kind cooperation and constant encouragement throughout my journey of research.

I am thankful to CSIR-HRDG for awarding me JRF and SRF fellowship for the last five years to carry out my research work smoothly.

I would like to acknowledge DST for providing single crystal X-ray diffractometer in FIST and Time-Resolved Nanosecond Spectrofluorimeter in PURSE programme to the Department of Chemistry, Jadavpur University.

I am greatly appreciate the invaluable assistance and suggestions of my former lab-mates Dr. Dinesh Maity, Dr. Srikanta Karmakar, Dr. Sourav Mardanya, Dr. Debiprasad Mondal, Dr. Manoranjan Bar, Dr. Poulami Pal, Dr. Animesh Paul, Dr. Shruti Mukherjee and Dr. Sourav Deb who have already completed their doctoral degree from our lab. I am also fortunate to have wonderful junior lab-mates Tanusree Ganguly, Toushique Ahmed, Soumi Das, Sohini Bhattacharya, Raju Biswas, Tuhin Abedin and Sucheta Gorain who always stood by and supported me whenever I needed them. All the fun we had in the last five years became a good memory for my entire life. I am blessed to get an opportunity to work with such helpful and friendly research group.

It was really impossible to complete this journey without the unconditional love, support and encouragement from my family members, especially from my parents Srikanta Sahoo and Amita Sahoo. I want to express a heartfelt gratitude to my family members who always kept me in their prayers.

A heartfelt love and gratitude to my elder brother, Sumanta Sahoo, my sister-in-law, Puja Dutta Sahoo and my niece Spriha Sahoo for their unfailing support, continuous encouragement and blessing that has made this journey a successful one.

It is a genuine pleasure to express my appreciation to my close friends for their support and encouragement during the last five years. I am indebted to my friends Arijit and Subhamoy for helping me with data analysis of my research work. I wish to express my sincere thanks to my roommates Subhamoy for his co-operation and understanding

during this period. Last but not the least, I extend my special thanks to my very close friends Arijit, Subhamoy, Rajesh, Debabrata, Puspendu, Gopal and Laxmikanta for providing me the company and support through every step of this journey.

Again, I would like to thank each and every person, whom I have failed to mention personally, for encouraging me in every possible way during the course of this study.

Finally I would like to thank the almighty for his blessing to journey of completion of my thesis.

(Anik Sahoo)
Department of Chemistry,
Inorganic Chemistry Section,
Jadavpur University,
Kolkata-700032, India

CONTENTS

1.1. General Introduction

Ru(II) complexes with polypyridine ligands play promising role in diverse field of research such as artificial photosynthesis, dye-sensitized solar cells, photocatalysis, molecular electronic devices and chemosensors. Ru(II)-polypyridine complexes possess excellent photophysical and redox characteristics which in turn make them suitable candidates for the aforementioned applications.[1-10] The significant progress in this area began with the inclusion of the $[Ru(bpy)_3]^{2+}$ complex by virtue of its unique combination of photophysical and electrochemical properties[11-21] and also because of its excellent photosensitizing characteristics.[22-28] Later on, a variety of polypyridine ligands were designed, incorporating either bidentate chelating sites of the 2,2'-bipyridine (bpy) type or tridentate chelating sites of the 2,2':6',2''-terpyridine (tpy) type, in order to control the topology as well as photo-redox characteristics of the resulting complexes. Ru(II) complexes with ligands of bpy types display strong and long-lived luminescence at room temperature (RT), while the complexes possessing terpyridine-type ligands show no emission, accompanied with an extremely short-lived excited state {lifetime (τ) =250 ps}.[25-28] The octahedral complexes from bpy-type ligands lead to diastereomeric mixtures that are frequently challenging to separate. Conversely, the $[Ru(tpy)_2]^{2+}$-type complexes produce achiral rod-like structures.[22-24]

Modulation of photo-redox properties of this sort of complexes is essential criteria for their utility in various applications.[11-21] Fine tuning of the said properties could be feasible upon incorporation of suitable chromophoric units as well as different types of receptor moieties that can interact with various external stimuli, such as anions, cations, pH, temperature and light. The major goal of this dissertation is to design luminescent Ru(II) complexes bearing both bipyridine- as well as terpyridine-type ligands and utilized the complexes to mimic various sophisticated functions such as those of sensors and switches. To achieve our goal, we have judiciously incorporated several heterocyclic motifs such as azole (imidazole and thiazole) moieties as well as stilbene units in the complex architectures. The azole protons under the coordinating influence of Ru(II) units became acidic which upon interaction with selective anionic guests could induce substantial modulation in the photo-redox properties in the resulting complexes. Taking advantage of one or more stilbene motif (s), reversible trans-cis isomerization

accompanied with remarkable alteration of their physico-chemical properties could be feasible. Temperature is also expected to play a vital role on the emission characteristics of the Ru(II) complexes, in particular with the terpyridine-type ligands, through adjustment of their ^{3}MLCT-^{3}MC energy barrier. Hence, temperature induced alteration of emission characteristics is also a distinct possibility in this sort of Ru(II)-polypyridine complexes. In conjunction with experimental demonstrations, theoretical investigations employing density functional theory (DFT) as well as time-dependent (TD)-DFT will be thoroughly investigated to understand the electronic nature of the complexes as well as for appropriate assignments of their spectral bands.

One of the major objectives of the present dissertation is to utilize the spectral and electrochemical responses of the complexes in presence of different stimuli to mimic the operations of multiple Boolean Logic (BL) as well as Fuzzy Logic (FL). Within Boolean Logic (BL), the output signal fluctuates between the two extremes of "0" or "1".[29-48] However, practical systems frequently encompass an immense array of intermediate states. To effectively handle these in-between states, Fuzzy Logic (FL) proves to be a suitable option.[49-55] Hence, we employed Fuzzy Logic (FL) to devise an algorithm based on infinite-valued logic, utilizing the spectral output of the complexes in the presence of various stimuli for better understanding the stimuli-responsive behaviors of the complexes.[56-68] Executing comprehensive sensing experiments that involve varying the analyte concentration across a broad range can be extremely laborious, time-intensive, and financially demanding. In order to overcome this lacuna, we employed several advanced artificial intelligence based soft computing techniques, including Artificial Neural Network (ANNs), Fuzzy Logic (FL), Adaptive Neuro-Fuzzy Inference System (ANFIS) and supervised learning based decision tree regression (DTR)[69-74] to analyze and predict the experimental stimuli-responsive behaviors of the complexes.

1.2. Overview of the Photophysical Behaviors of Ru(II) Complexes Based on Polypyridine Ligands

We have already discussed in the previous section that Ru(II) complexes of polypyridyl ligands are potential building blocks for light harvesting applications due to their unique combination of photophysical, photochemical, and electrochemical properties.[23-27] The

complexes strongly absorb in the visible (between 420 and 500 nm), display strong room temperature (RT) luminescence in the red and decay to the ground state via primarily ^{3}MLCT state with lifetimes that vary between a few nanoseconds to a few microseconds.[23-27,75-77] Photophysical properties of parent $[Ru(bpy)_3]^{2+}$ and $[Ru(tpy)_2]^{2+}$ are depicted in Table 1.1 and Figure 1.1. The absorption spectral profile of complexes is characterized by metal-to-ligand charge transfer (MLCT), metal-centered (MC), and ligand-centered (LC) bands. The positioning of these bands is contingent upon the electronic nature of the ligand environment (Figure 1.1.). A review of the literature indicates that complexes of the $[Ru(bpy)_3]^{2+}$ type demonstrate superior luminescent properties when compared to their $[Ru(tpy)_2]^{2+}$ analogs.[23-29,76-81] While both categories of complexes exhibit prominent absorption bands in the visible region resulting from MLCT transitions, they also feature highly intense bands in the UV region attributable to ligand-centered transitions. [23-29,78-86]

Table 1.1. Photophysical Components of the Parent Ru(II) Complexes in Deaerated CH_3CN at RT.

Complex	λ_{max}^{abs} (MLCT), nm	λ_{max}^{em}, nm	τ_{exst}, 298 K, ns	Ref.
$Ru(bpy)_3^{2+}$	454	620	800	23,28
$Ru(tpy)_2^{2+}$	475	628	< 5	23,28

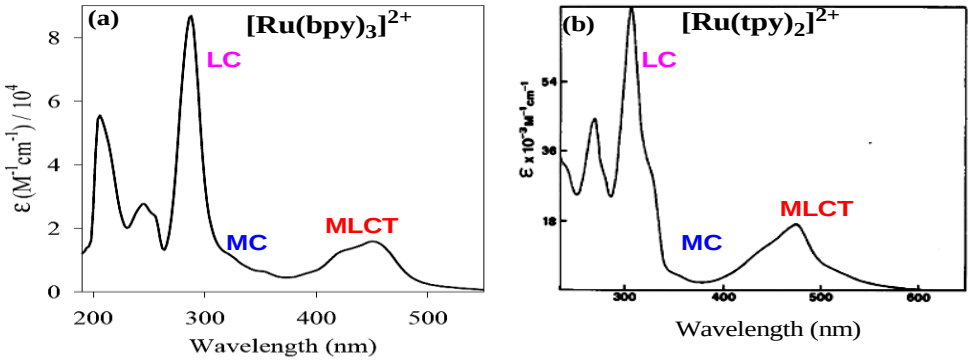

Figure 1.1. UV-vis absorption spectral profiles of $[Ru(bpy)_3]^{2+}$ (a) and $[Ru(tpy)_2]^{2+}$ (b) in MeCN.

Upon light irradiation, the complexes first go the ^{1}MLCT excited state, followed by very rapid intersystem crossing to either ^{3}MC or ^{3}MLCT states, or both. Subsequently, they

deactivated to the ground state through either radiative or non-radiative pathway.[23-29] The deactivation process primarily relies on the energetic relationships among the ^{3}MLCT, ^{3}MC, and ^{3}LC states. In complexes containing the $[Ru(bpy)_3]^{2+}$ moiety, the lowest-energy excited state is primarily ^{3}MLCT, and it experiences radiative deactivation with a relatively prolonged lifetime. In contrast, complexes containing the $[Ru(tpy)_2]^{2+}$ motif typically exhibit non-emissive or very weakly emissive behavior due to the close proximity of their emitting ^{3}MLCT and non-emitting ^{3}MC states at room temperature (Figure 1.2).

1.3. Electrochemical Behaviors of Ru(II) Complexes Based on Polypyridine Ligands

The electrochemical characteristics of polypyridine Ru(II) complexes are intriguing due to their reversible nature. The highest occupied molecular orbital (HOMO) is primarily located on the metal site, indicating that oxidation converts Ru(II) to Ru(III). Conversely, the lowest unoccupied molecular orbital (LUMO) is localized over the pyridine rings, and during reduction, electrons accumulate on the LUMO of the polypyridine ligands.[72-75] It is noted that mono-metallic complexes typically exhibit a single reversible oxidation in the positive potential window and multiple reduction peaks in the negative potential window.

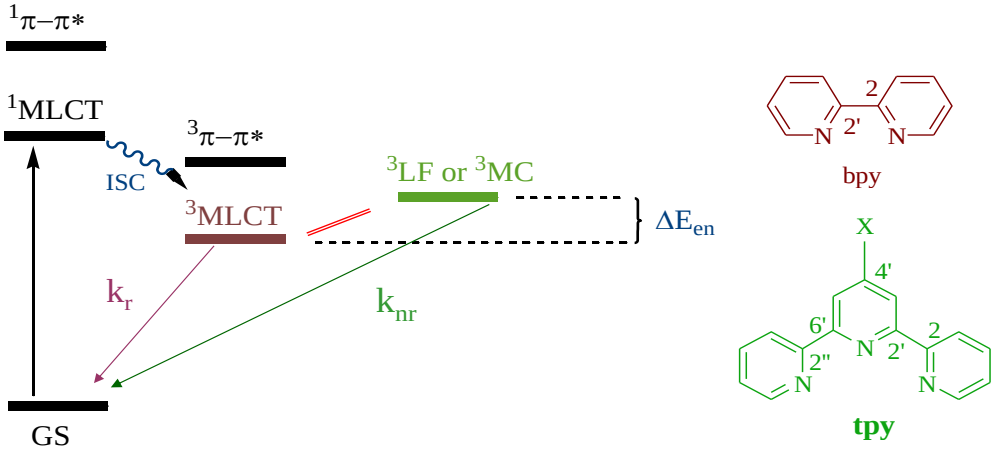

Figure 1.2. Simplfied energy profile diagram.

1.4. Implementation of Logic Functions

Electronic devices play a crucial role in our everyday lives, reshaping the world by facilitating communication, sharing information, and managing the storage and processing of data. The operational principles of these digital electronic devices are rooted in the logical foundations of Boolean algebra. In practical terms, Boolean algebra involves manipulating two binary codes, namely "On-state (1)" and "Off-State (0)." Data processing relies on logical operations with single or multiple logic inputs, resulting in a single output in each case. Typically, eight fundamental logic operations, viz. OR, AND, XOR, NOR, NAND, XNOR, INHIBIT (INH), and IMPLICATION (IMP) are employed for this purpose. Beyond these, more complex combinational logic operations can be derived from the fundamental logic systems. The fundamental circuits undergo arithmetic and other intricate operations, leading to the creation of various complex circuits such as half-adder/subtractor, [87-91] keypad-lock, [90-92] set-reset-flip-flop, [92-95] memory-device, [94-96] multiplexer/demultiplexer/exciplex, [97-99] and encoder/decoder, [34] among others.

Silicon-based technology is highly efficient for modern integrated circuits, but its primary limitation lies in size constraints. Molecular computation surpasses silicon-based devices by operating with information at the nanometer scale. Consequently, molecular mimicry of logic gates, proposed by de Silva in 1993, [30-31] is considered to be a promising alternative. Therefore, the design of stimuli-responsive molecules becomes crucial to achieve computation at the molecular-level. The output signals of these molecules, triggered by various external stimuli such as temperature, anions, cations, pH, light, etc., are frequently employed to construct diverse binary logic functions.

1.5. A Concise Examination of Ru(II) Complexes Formed by Poly-Pyridine Ligands: A Brief Overview

Research groups worldwide have published numerous noteworthy reviews and papers highlighting the photophysical, photochemical, and electrochemical characteristics of Ru(II) complexes encompassing both bipyridine and terpyridine type ligands,.[23-29,75-81] The optoelectronic properties of the complexes can be adjusted by modifying the electronic distribution in the ligand backbone or through interaction with different external guests, including anions, cations, temperature, pH, solvent, and light. This

dissertation will examine pertinent literature that aligns with the subject matter of our current study.

Das and colleagues synthesized a set of ruthenium(II) diimine complexes (**1-3**) and explored the ligand-localized charge transfer states (ILCT and LLCT) through optical absorption and emission studies (Scheme 1.1).[100]

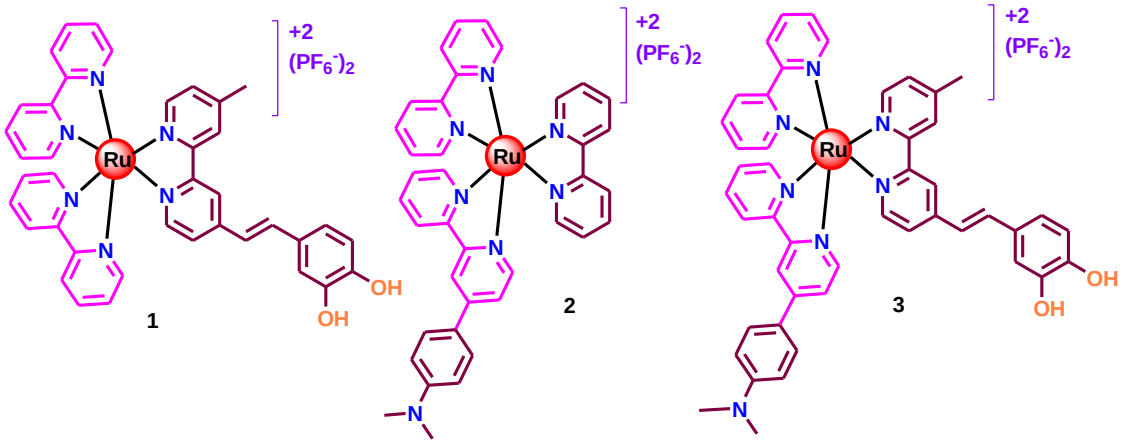

Scheme 1.1

Maiya *et al* have synthesised a photo-redox switch by employing $[Ru(phen)_3]^{2+}$ motif as the active unit and quinone/hydroquinone as control unit (Scheme 1.2). The quinone form is non-luminescent at room temperature while the electrochemically generated hydroquinone form is luminescent with quantum yield of 0.02 (λ_{max}= 601 nm).[101]

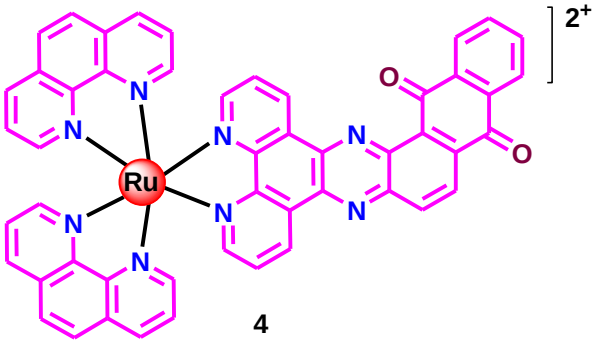

Scheme 1.2

Meyer and his colleagues have detailed the synthesis and analysis of an amide-bridged dinuclear architecture of the type, $[Ru(bpy)_2(bpy\text{-}ph\text{-}NH\text{-}CO\text{-}trpy)Ru(bpy)(OH_2)]^{4+}$ (where bpy=2,2′-bipyridine; bpy-ph-NH-CO-trpy=4-(2,2′:6′,2″-terpyridin-4′-

yl)-N-[(4′-methyl-2,2′-bipyridin-4-yl)methyl]benzamide).[102] This assembly is noteworthy for incorporating both a light-harvesting chromophore and a water oxidation catalyst. The inclusion of a saturated methylene linker preserves the individual characteristics of the chromophore and the catalyst, maintaining the properties of the water oxidation catalysis together with a deliberate slow energy transfer from the excited state of the chromophore to the catalyst (Scheme 1.3).

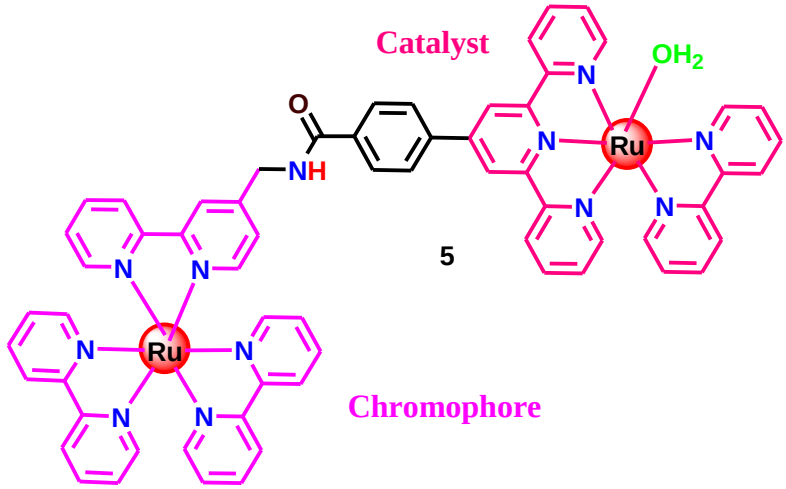

Scheme 1.3

Rau and his collaborators designed mixed-metal complex composed of ruthenium(II) and gold(III) metals, by employing tetrapyridophenazine (tpphz) bridging ligand (Scheme 1.4).[103] This complex exhibits an isostructural and isoelectronic nature similar to widely recognized photocatalysts containing palladium(II) or platinum(II). Concentration-dependent ^{1}H-NMR spectroscopy and XRD studies conducted by the researchers reveal that electrostatic repulsion among the gold(III) moieties surpasses the attractive π-stacking interaction. Additionally, theoretical calculations, based on the newly acquired structural data, confirm an increased positive charge on the bridging ligand and significantly altered orbital symmetry compared to the previously studied palladium(II) complex. Notably, this marks the first instance of a tpphz ruthenium(II) complex where π-stacking is entirely inhibited.

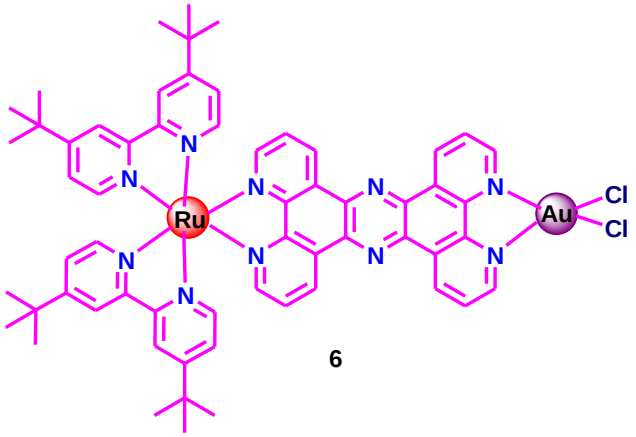

6

Scheme 1.4

Campagna and colleagues have adeptly produced two ligands with N_{amine} substitutions on guanidine-pyridine/pyrimidine frameworks, demonstrating their proficiency in coordinating to a Ru^{II} center and resulting in the creation of a six-membered chelate ring. Additionally, assessment of the $Ru^{III/II}$ potentials for these newly synthesized complexes (**7** and **8**) indicates that both ligands showcase robust donating capabilities, surpassing those of the commonly employed polypyridyls, viz. bipyridine or phenanthroline (Scheme 1.5).[104]

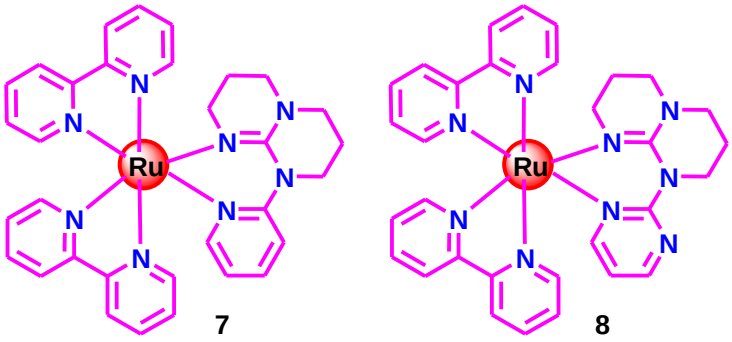

7 8

Scheme 1.5

Shatruk and colleagues proposed a pathway to enhance the electron-injection yield of Ru-dipyrrinate dyes and improve the power conversion efficiency of DSSCs incorporating these dyes. They synthesized three Ru(II)-dipyrrinate complexes $Ru(bpy)_2$(3-TDP) (**9**), [$Ru(H_2dcbpy)$(Hdcbpy)(3-TDP)] (**10**), and [$Ru(H_2dcbpy)$(Hdcbpy)(TPADP)] (**11**), where bpy=2,2′-bipyridine, dcbpy=4,4′-dicarboxylato-2,2′-bipyridine, 3-TDP=3-thienyldipyrrinate, and TPADP=triphenylamino-dipyrrinate. These complexes

were characterized using electrochemical and photophysical methods, along with theoretical electronic structure calculations at the DFT level (Scheme 1.6).[105]

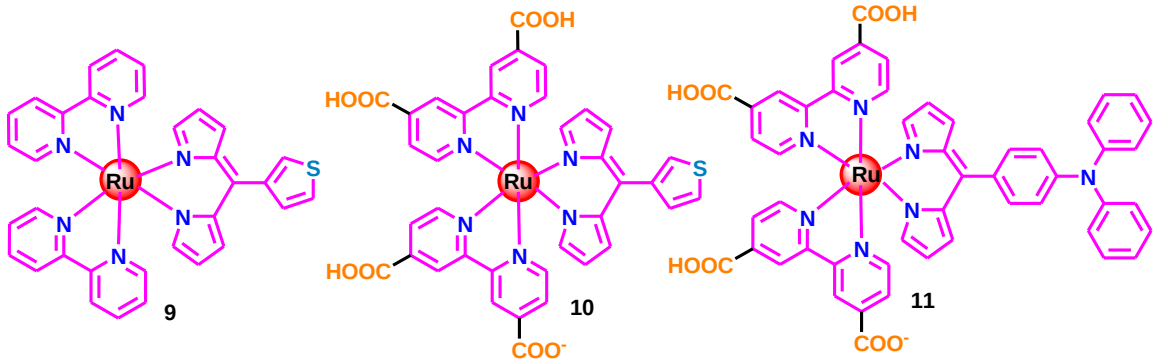

Scheme 1.6

Baley and colleagues discovered that incorporating diverse heterocyclic rings, such as furyl, pyrrolyl, thienyl, and bithienyl groups, into the terpyridine moiety effectively enhances the properties of excited-state emission (Scheme 1.7).[106] These heterocyclic rings contribute to increased delocalization, leading to the stabilization of the ^{3}MLCT state. Consequently, the triplet MC-MLCT energy gap expands, resulting in an observable enhancement in the luminescence properties. The emission quantum yield is notably high compared to the parent $[Ru(tpy)_2]^{2+}$, with the bithienyl-substituted complex exhibiting a remarkable 100-fold increase in emission quantum yield. The electron-donating effect of the heterocyclic unit induces a destabilization of the metal-centered HOMO, manifesting as a bathochromic shift in the absorption and emission profiles of the complexes.

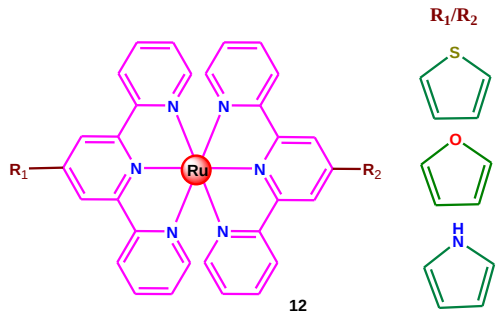

Scheme 1.7

Vos's research team presented a series of Ru(II)-terpyridine complexes (**13-18**) linked with triazole/tetrazole motifs (Scheme 1.8).[107,108] These complexes exhibit a pronounced absorption band around 480 nm and an emission band near 700 nm at room

temperature (RT), with lifetimes ranging from 20 to 80 ns. The ligands' σ-donor characteristics increased upon deprotonation, amplifying the energy of the ^{3}MC state. Consequently, deprotonation of the triazole/tetrazole moiety results in a nearly doubled enhancement of the lifetime compared to the parent $Ru(tpy)_2$ complex. In contrast, protonation leads to a quenching of the emission intensity.

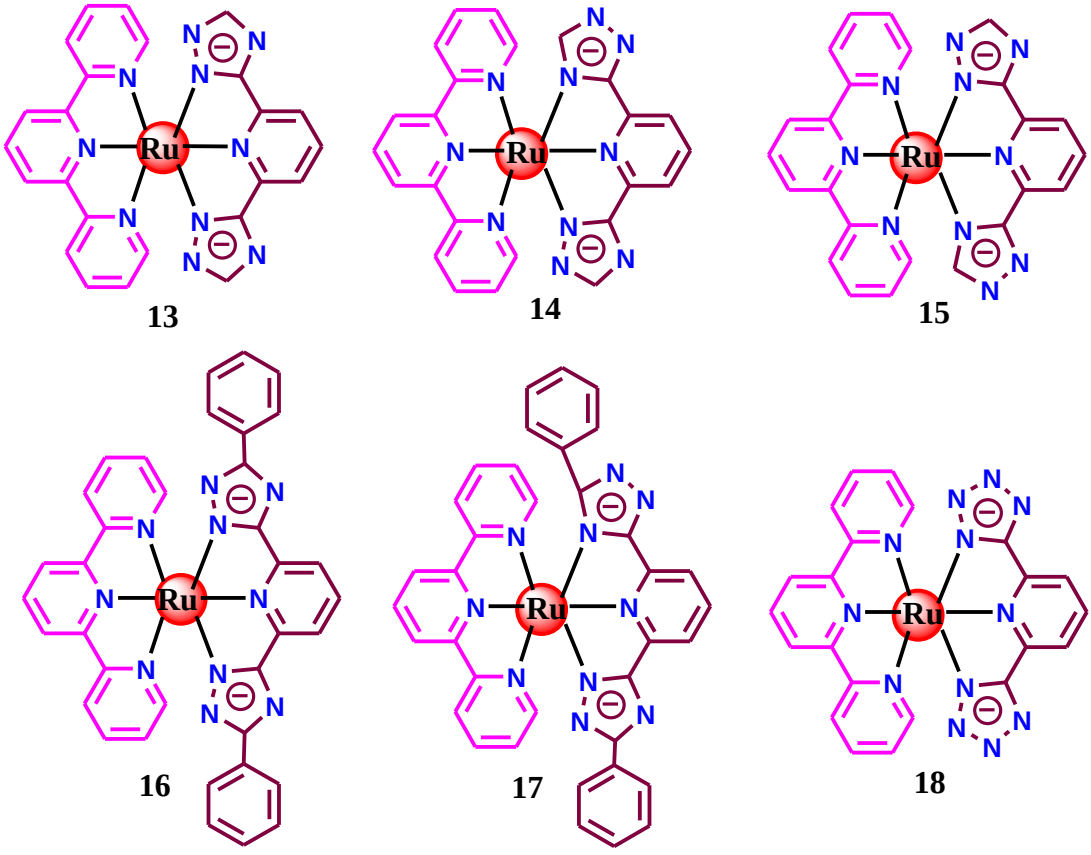

Scheme 1.8

1.6. Switching of Photophysical and Electrochemical Properties of Ruthenium (II) Complexes Derived From Polypyridine Ligands

In the preceding section, we explored various approaches aimed at enhancing the photo-redox properties of Ru(II)-bipyridine/terpyridine type complexes. Researchers worldwide are keenly interested in systematic tuning of photo-redox behaviors of complexes under the influence of diverse external stimuli. This endeavor aims to position these complexes as versatile building blocks with a broad range of applications. In the following section, we will provide a concise overview on the modulation of

photophysical and electrochemical behaviors exhibited by Ru(II)-polypyridine complexes in response to different external stimuli.

Sessler and colleagues conducted studies on the anion-sensing capabilities of Ru(II)-polypyridyl complexes, specifically focusing on dipyrrolylquinoxaline (DPQ) phenanthroline derivatives (Scheme 1.9).[109] Upon coordination with Ru^{2+}, the NH protons of the pyrrole moiety exhibited increased acidity compared to the free ligand. Notably, the complex demonstrated a strong interaction with F^- in DMSO, with a binding constant of 1.2×10^4 M^{-1}, surpassing the free ligand by nearly 30 times. Additionally, the research group presented another Ru(II) complex (**20**) with a similar framework and investigated the changes in its emission characteristics in the presence of $H_2PO_4^-$. The emission intensity at 630 nm decreased upon incremental addition of $H_2PO_4^-$, revealing a binding constant of 1.0×10^5 M^{-1}. Jobs-plot analysis indicated the formation of a 1:1 complex with $H_2PO_4^-$.

Subsequently, Anzenbacher and collaborators explored a luminescence-lifetime based sensor involving a related Ru(II)-complex (**21**) (Scheme 1.9).[110] Both the emission intensity and the excited-state lifetime experienced substantial reduction upon addition of F^- and CN^- in a MeCN medium. The binding constants of receptor-anion interaction were estimated and found to lie within the range of 4.3×10^5 $M^-$to 6.4×10^5 M^{-1}.

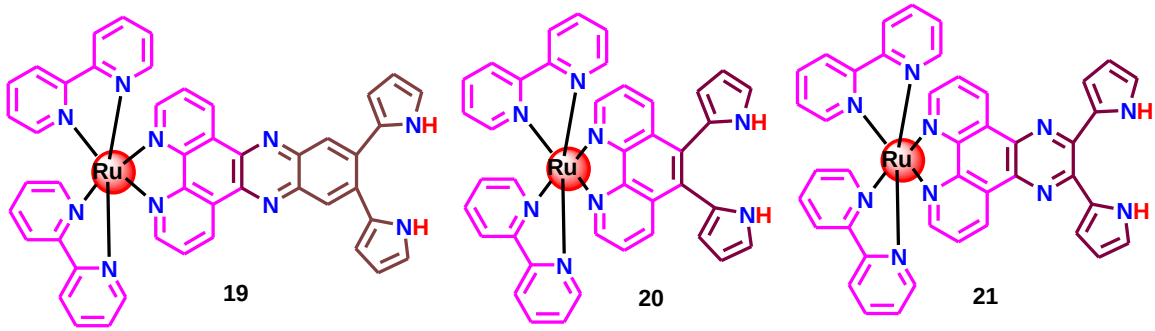

Scheme 1.9

Molina and colleagues devised a Ru-complex (**22**) utilizing a phenanthroline-imidazole based ligand appended with ferrocene motif (Scheme 1.10).[111] The complex exhibits notable selectivity for Cl^- sensing. Upon incremental addition of Cl^-, a substantial enhancement in luminescence intensity is noted, reaching almost 30 times relative to its initial level. Furthermore, a cathodic shift in the Fe(II)/Fe(III) couple is observed, while the Ru(II)/Ru(III) potential remains unaltered.

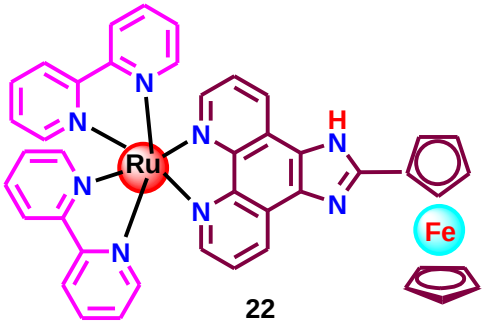

22

Scheme 1.10

Das and colleagues developed a series of Ru(II)-bpy monomers incorporating the dipyridylamine ligand motif (Scheme 1.11).[112] The anion sensing characteristics of the complexes were extensively examined through absorption, emission, and cyclic voltammetric analyses. The findings reveal that these complexes have the ability to function as potential sensors for specific anions, including F^- and CN^-, as evidenced by the noticeable visual color changes they undergo.

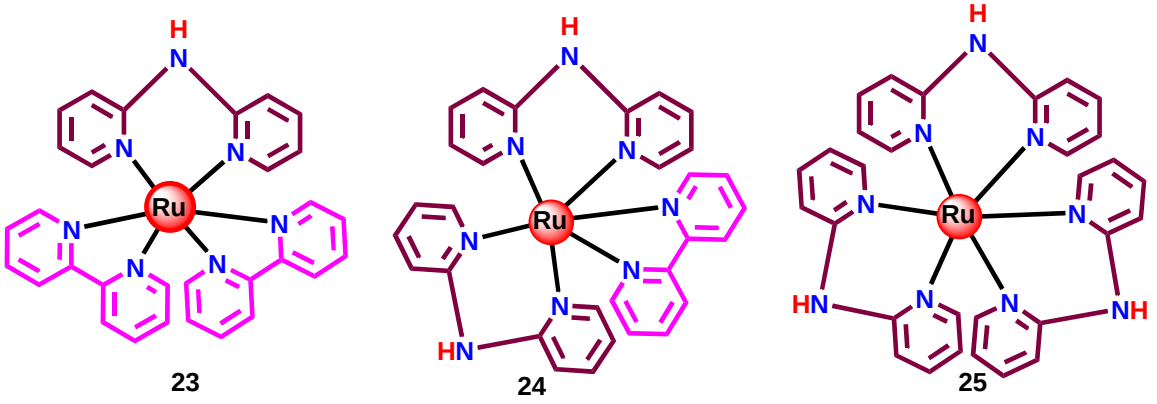

Scheme 1.11

Schmittel and colleagues designed two heteroleptic Ru(II)-complexes (**26-27**) incorporating bpyridine and phenanthroline units along with two formyl (-CHO) groups in the one of the phenanthroline ring (Scheme 1.12).[113] These complexes exhibit pronounced selectivity for CN^- through the formation of cyanohydrins intermediates. Notably, the emission intensity of the complexes increases with a blue shift of approximately ~100 nm upon the gradual addition of CN^-. Additionally, a visible color from red to orange is observed.

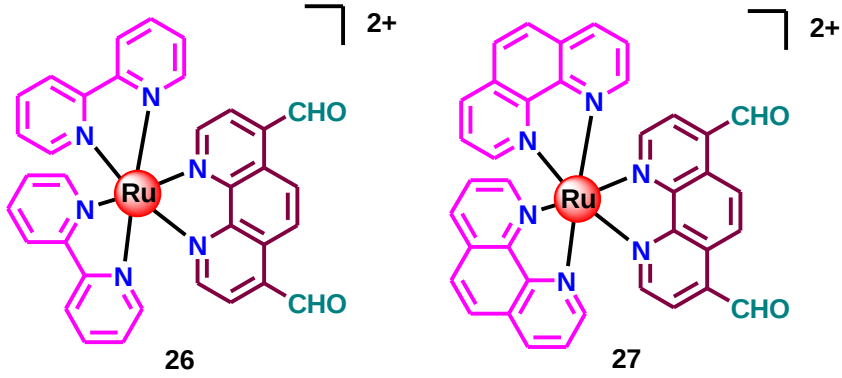

Scheme 1.12

Ye and colleagues synthesized a wide range of Ru(II)-complexes, specifically based on bis-imidazole derivatives (**28-31**), and conducted investigation on the anion-induced modulation of their photophysical and electrochemical properties (Scheme 1.13).[114-117] These complexes feature two NH-protons within their secondary coordination sphere. The interaction between imidazole NH protons and anions is influenced by the basicity of the anion and the acidity of the NH protons, resulting in three types of interactions: anion-NH hydrogen bonding, mono-deprotonation, and double-deprotonation. Notably, Cl^-, Br^-, I^-, NO_3^-, HSO_4^-, $H_2PO_4^-$, and OAc^- anions form hydrogen-bonding adducts with complex **28**. The excess addition of OAc^- induces the formation of the mono-deprotonated complex, visually evidenced by a color change from yellow to orange. However, in the presence of F^-, double-deprotonation occurs in two consecutive steps, ultimately leading to a violet colored solution.

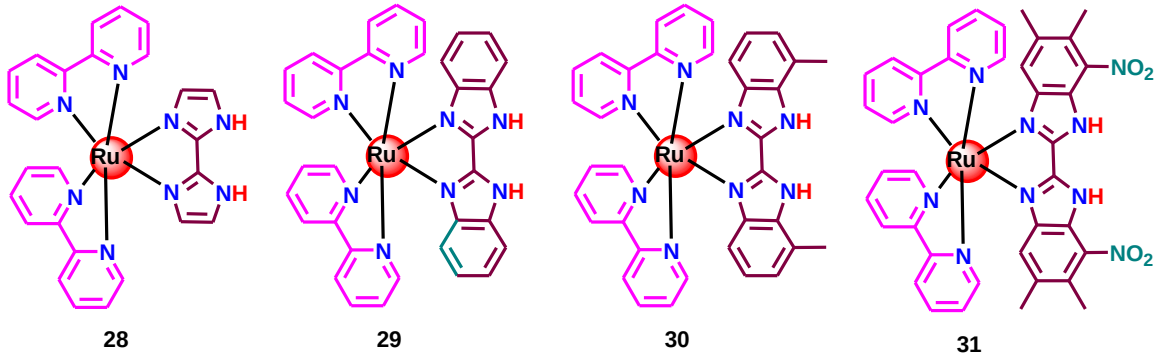

Scheme 1.13

Baitalik et al synthesized and thoroughly characterized Ru(II) and Os(II)-bpy complexes (**32** and **33**), encompassing a pyrenylimidazole-10-pyridin-2-yl-9H-9,11-diazacyclopenta[e]pyrene (HImzPPy) ligand.[118] The investigation delved into DNA and

anion binding phenomena of the complexes using absorption, steady-state and time-resolved emission, along with circular dichroism spectroscopy. In the presence of excess F^- and OAc^- ions, the deprotonation of the imidazole NH proton occurs, resulting in a significant reduction in emission intensity and leads to the "Off-state" of the system. Conversely, $H_2PO_4^-$ induces substantial upsurge of emission intensity in presence of $H_2PO_4^-$, probably because of the formation of hydrogen-bonded adduct, and corresponds to the "On-state." The binding constants for these systems were determined to be on the order of 10^6, with a detection limit in the range of 10^{-9} M (Scheme 1.14).

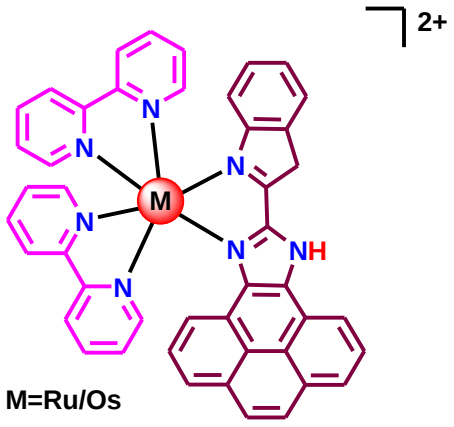

32/33

Scheme 1.14

Baitalik and colleagues additionally crafted a monometallic Ru(II) complex using a heteroditopic bpy-tpy type ligand with the composition, $[(bpy)_2Ru(tpy\text{-}Hbzim\text{-}dipy)](ClO4)_2$ (**34**) (Scheme 1.15).[119] This complex manifests an absorption peak around 470 nm, attributed to the MLCT transition. Moreover, the complex displays a solvent-dependent emission spectrum, with its maximum spanning from 628 to 649 nm and having its excited state lifetime ranging from 116 to 257 ns. The complex's ability to sense both anions and cations was explored through various optical channels. It was observed that in the presence of $H_2PO_4^-$ and HSO_4^-, the emission intensity increased, indicating the "On-state," while the presence of more basic anions (F^- and AcO^-) led to a reduction in emission intensity, representing the "Off-state." The cation-sensing aspect of the complex was also investigated by leveraging its free terpyridine motif. Among the bivalent 3d cations, only Fe^{2+} exhibited a noticeable color change from yellow to violet, making it a suitable colorimetric sensor for Fe^{2+} (Scheme 1.15).

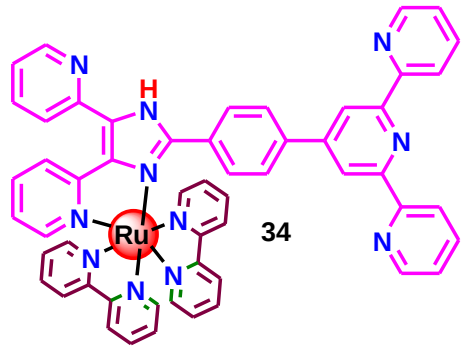

Scheme 1.15

Subsequently, the same research group developed a series of Ru(II)-terpyridine complexes (**35-37**) incorporating an anthraquinone unit in their structural motifs (Scheme 1.16).[120] These complexes exhibit remarkable luminescence properties at room temperature (RT), with lifetimes ranging from 1.5 to 52.8 ns, dependent on the solvent as well as ligand architecture. The inclusion of an electron-withdrawing anthraquinone unit enhanced the acidity of NH protons. Leveraging this feature, anion-induced alterations of the photophysical properties of the complexes were conducted in both organic and aqueous solutions. Notably, the complexes demonstrated remarkable selectivity for CN^- in aqueous solution with limit of detection lying in the order of 10^{-8} M.

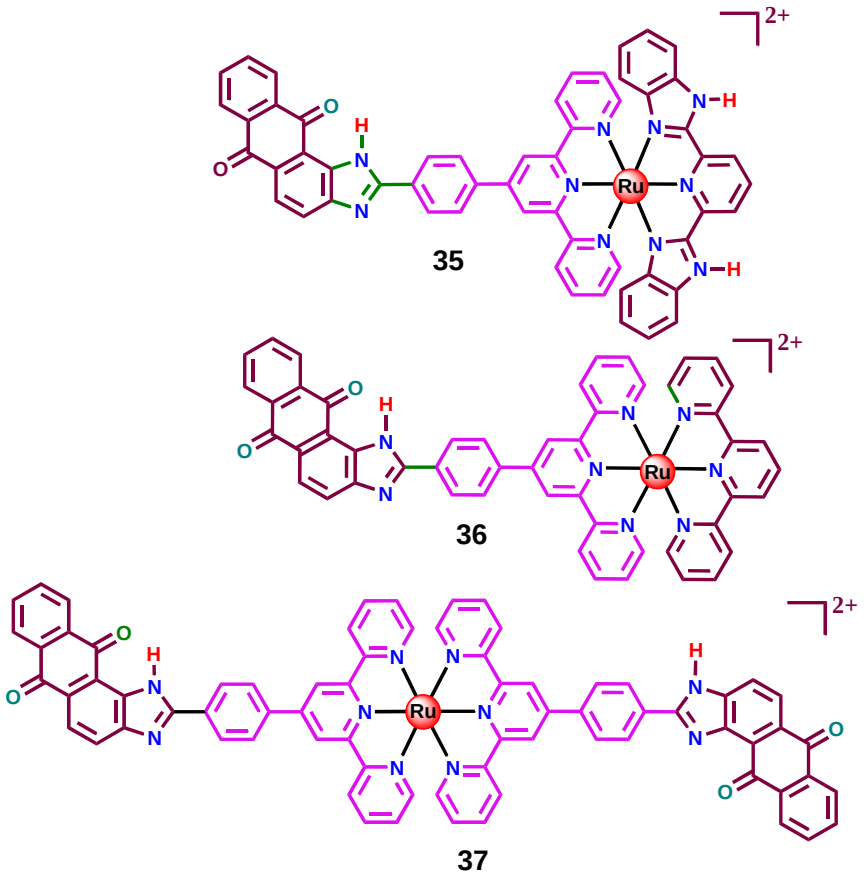

Scheme 1.16

1.7. A Brief Review on Boolean Logic Gates

Over the past few decades, computers have become an indispensable tool, playing a pivotal role in high-level calculations, data processing, communication, and information sharing.[29-48] The concept of processing information and performing computations at the molecular level was initially recognized by De Silva in 1993. This initiative aimed to create exceptionally compact yet powerful computers, which couldn't be achieved using traditional silicon-based technology. Logic gates are fundamental components used for executing binary arithmetic and logical operations, forming the foundation of contemporary computers. For molecular-level computation, molecular logic gates are essential. They can incorporate basic logic gates into combinational circuits, thus enabling computation on a nanoscale is feasible which is beyond the reach of silicon-based devices. The entire process involves encrypted data represented in binary digits. Binary operates on two extremes: 0 (false) or 1(true). Different fundamental logic gates

based on two inputs together with their outputs are represented in Table 1.2. A brief literature survey on selected molecular logic gates are discussed below.

Table 1.2. Truth Table of Different Two Input-One Output Binary Logic Gates.

Name		OR	NOR	AND	NAND	XOR	XNOR	IMPLICATION	INHIBIT
Symbol									
Truth Table									
Inputs		Outputs							
0	0	0	1	0	1	0	1	1	0
0	1	1	0	0	1	1	0	1	1
1	0	1	0	0	1	1	0	0	0
1	1	1	0	1	0	0	1	1	0

De Silva and co-worker constructed an AND logic operation by employing a tertiary amine appended benzo-15-crown-5 ether receptor. H^+ and Na^+ are used as the inputs, while the fluorescent signal of the receptor acts the output (Scheme 1.17).[121] The AND logic truth table is satisfied only when both chemical inputs are present in a sufficiently high concentration. It is to be noted that the tertiary amine receptor was employed for H^+ abstraction, while the benzo-15-crown-5 ether moiety was incorporated for Na^+ binding. The binding of these ions to their respective receptor units obstruct the PET channel to the anthracene fluorophore. However, blocking one of the PET channels alone is insufficient to induce fluorescence emission, which is why the presence of both inputs is necessary to activate anthracene fluorescence.

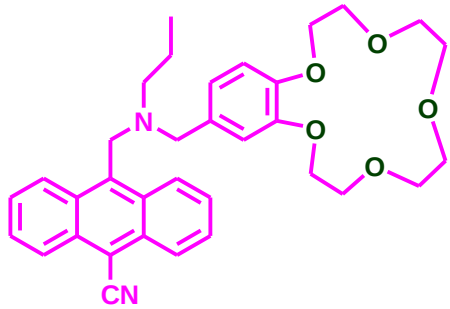

Sl. No.	Input 1 (H^+)	Input 2 (Na^+)	Emission Output
1	0	0	0
2	0	1	0
3	1	0	0
4	1	1	1

Scheme 1.17. AND logical operation in presence of H^+ and Na^+ ion.

Redmond and co-worker constructed NOR logical behavior of a Ru(II) complex (Scheme 1.18) by utilizing two inputs.[122] They selected the applied electric field as input 1 and Cu^{2+} ions as input 2. In the presence of either input, the luminescence intensity at 668 nm diminishes; indicating the 'Off-state' and the 'On-state' is achievable only when no input is applied. Consequently, the system effectively emulates the function of a NOR gate.

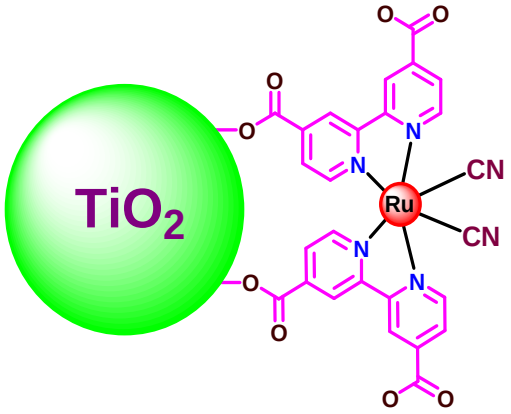

Sl. No.	Input 1 (V_{app})	Input 2 (Cu^{2+})	Output Emission at 668 nm)
1	0	0	1
2	0	1	0
3	1	0	0
4	1	1	0

Scheme 1.18. NOR logical operation in presence of electric field and Cu^{2+} ion.

Li and co-worker constructed an Ir(III)-based chemosensor which can mimic the function of AND and INHIBIT logic gates in presence of Hg^{2+} and histidine (Scheme 1.19).[123] It is observed that the free form of the complex is non-luminescent but in presence of histidine, the emission intensity increases slightly whereas a huge increase is observed in presence of both histidine and Hg^{2+}. Thus, the Ir(III)-based receptor illustrates the function of two input-two output AND and INHIBIT combinational logic gate as shown in Scheme 1.19.

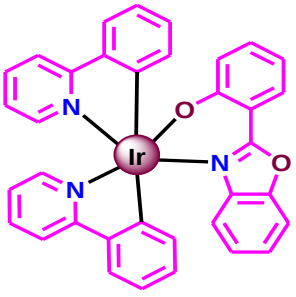

Inputs		Outputs	
Hg^{2+}	His	I_{545nm}	I_{460nm}/I_{545nm}
I_1	I_2	O_1	O_2
0	0	0	0 (<1)
0	1	0	0 (<1)
1	0	0	1 (~60)
1	1	1	0 (<1)

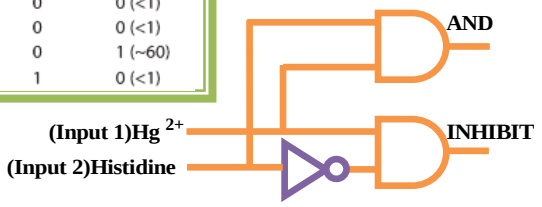

Scheme 1.19. AND and INHIBIT logic gate in presence of histidine and Hg^{2+}.

Das et al. showcased the functionality of the keypad lock utilizing a naphthyl-based receptor. In this experiment, Cu^{2+} and F^- were employed as the inputs, while the emission signal served as the output (Scheme 1.20).[124] To simplify the input sequence for the keypad lock password, the inputs Cu^{2+} and F^- were denoted as "A" and "D," respectively. In the initial input sequence, the order of "D" followed by "A" resulted in a pronounced emission signal at 422 nm (ON state), generating the concealed code "DAS" (where S signifies the ON state). Conversely, reversing the input sequence, with the first input as "A" and the second as "D," led to a reduced fluorescence at 422 nm, indicating the OFF state of the system. This sequence, identified as "ADO" (where O signifies the OFF state), failed to unlock the keypad due to an incorrect entry. This experiment underscores the effectiveness of using "DAS" as a secure code to open the fluorescent lock at 422 nm in the compound. In contrast, a two-digit numerical password allows for 90 different combinations (using digits 0-9), but opting for individual letters (A-Z) as PIN numbers, each representing a specific ionic input, expands the possibilities to 650 different combinations (Scheme 1.20).

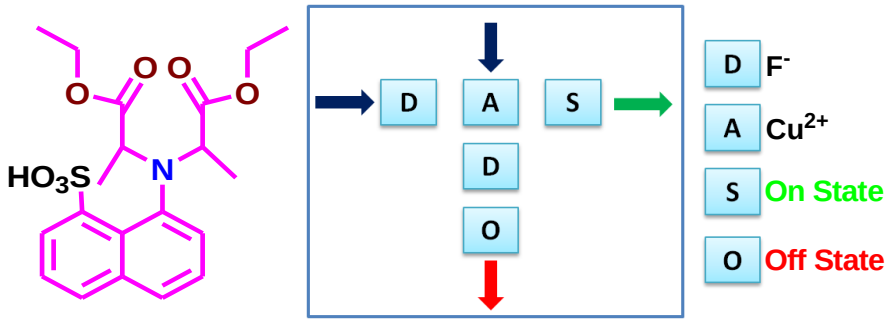

Scheme 1.20. Keypad locks in presence of F^- and Cu^{2+}.

Yan and colleagues engineered a receptor with oxygen and sulfur donor atoms that effectively emulates the function of multiple logic gates (Scheme 1.21).[125] In the creation of a NAND gate, they employed the emission intensity at 473 nm as the output signal with Fe^{2+} and $NOBF_4$ serving as the inputs. The introduction of either input individually has no impact on the emission spectral behavior of the receptor. However, the simultaneous addition of both inputs resulted in the quenching of emission intensity, effectively replicating the behavior of a NAND gate.

Secondly, the modification of emission intensity at 473 nm, induced by [$(NH_4)_2$ $Ce(NO_3)_6$] and CF_3COOH, was employed to establish an AND gate. In the presence of either input (Ce^{4+}/H^+), the emission intensity stays below the threshold level. However, when both inputs are present, the emission signal surpasses the threshold level, effectively replicating the behavior of an AND gate (Scheme 1.21).

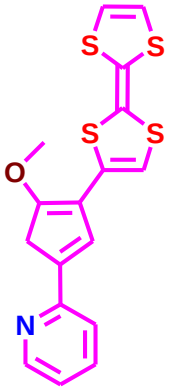

Input 1 (Fe^{2+})	Input 2 ($NOBF_4$)	Emission at 473 nm
0	0	1
0	1	1
1	0	1
1	1	0

Input 1 (Ce^{4+})	Input 2 (H^+)	Emission at 473 nm
0	0	0
0	1	0
1	0	0
1	1	1

Scheme 1.21. The molecular system emulates the operations of both NAND and AND logic gates.

Zhong and co-workers reported a diruthenium complex containing a redox-active amine bridge which can mimic the function of a flip-flop logic operation in presence of two electrochemical inputs (0.35 V and 0.75 V). Two NIR optical outputs, each displaying two level of signal intensity, are employed for the purpose (Scheme 1.22).[126] When the applied potential is 0.75 V (In 2), the absorption intensity at 1170 nm became high (the input and output strings were 01 and 10, respectively). On the contrary, when the applied voltage was 0.35 V (In 1), the absorption intensity at 1680 nm became high. When no inputs were applied, the output depends on the previous state as presented in the truth table. Consequently, the system emulates the function of a flip-flop logic gate (Scheme 1.22).

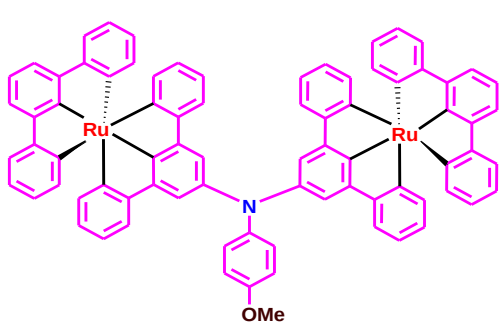

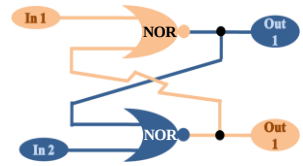

Sl. No.	Input 1 (E=0.35V)	Input 2 (E=0.75V)	Output 1 Absorption at 1170 nm	Output 2 Absorption at 1680 nm
1	0	0	Previous State	
2	0	1	1	0
3	1	0	0	1

Scheme 1.22. Flip-flop logic operation in presence of two electrochemical inputs and two NIR optical outputs.

Baitalik et al recently devised a molecular-level keypad lock utilizing a ruthenium-terpyridine complex (Scheme 1.23).[127] This system employs F^- and H^+ as the input, while the absorbance at 543 nm as the output signal. In this setup, H^+ is denoted as "C," while F^- is labeled as "A." The states of "ON" and "OFF" are represented by "N" and "E," respectively. When both H^+ and F^- are absent, the absorbance remains below the threshold, indicating the "OFF" state. The introduction of "C" followed by "A" signifies the "ON-state," creating the password "CAN." Conversely, altering the sequence to "A" followed by "C" results in the "OFF" state, generating the incorrect password, "ACE." This design ensures that only authorized users can access the protected information (Scheme 1.23).

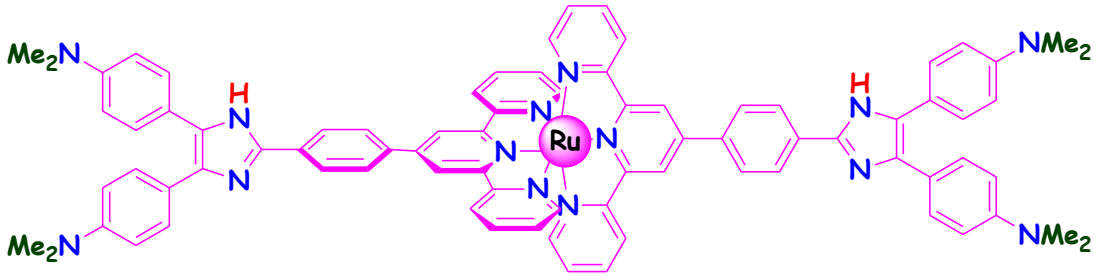

Sl.No	Input 1 (H^+)	Input 2 (F^-)	Absorption Output at 543 nm	Absorption Intensity at 543 nm
1	0	0	0 (low)	0.08
2	0	1	1(high)	0.37
3	1	0	0(low)	0.13
4	1(2nd)	1(1st)	0(low)	0.11
5	1(1st)	1(2nd)	1(high)	0.39

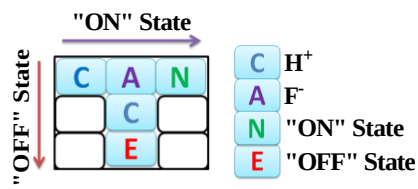

Scheme 1.23. Keypad-lock upon monitoring the absorbance at 543 nm in presence of two ionic inputs (F^- and H^+).

1.8. A Brief Review on Artificial Intelligence in Chemical System

Artificial Intelligence (AI) has fundamentally reshaped the landscape of chemical systems by revolutionizing predictive modeling, reaction optimization, and materials discovery. Through advanced machine learning techniques, AI enables precise property predictions and accelerates drug development and material design. Reaction planning benefits from AI's ability to suggest efficient pathways, while automation and robotics integrated with AI enhance experimentation and process control. Despite challenges like model interpretability, AI's capacity to analyze vast datasets and uncover complex insights has revolutionized chemical research, offering transformative solutions and expanding our understanding of the chemical phenomena. This review examines the impact of AI techniques such as fuzzy logic, artificial neural networks (ANNs), adaptive neuro-fuzzy inference systems (ANFIS), and supervised learning-based decision tree regression in the realm of chemical research.

Fuzzy logic, a specialized mathematical framework tailored for managing uncertainty, has evolved into an invaluable asset within chemical systems, demonstrating its efficacy in a multitude of applications. Its proficiency in modeling imprecise and ambiguous data stands out as a cornerstone, bringing about tangible improvements in process control, optimization, and pattern recognition within chemical processes. Through the incorporation of linguistic variables, fuzzy logic introduces a human-centric dimension to the analysis of intricate chemical systems, thereby elevating decision-making processes and augmenting the adaptability of the overall system. The impact of fuzzy logic is particularly evident in the field of chemical research, where it finds noteworthy application in process control and optimization. In the realm of process control, fuzzy logic's ability to handle imprecision and accommodate fluctuations in variables is harnessed to regulate conditions such as temperature, pressure, and flow rates in chemical reactors, ensuring enhanced stability and efficiency. Moreover, fuzzy logic plays a pivotal role in optimizing chemical processes by addressing uncertainties inherent in reaction conditions, leading to more robust and adaptive optimization strategies. The practical manifestation of fuzzy logic's utility is vividly illustrated through its successful implementation in real-world scenarios, where traditional control methods may falter. By offering a nuanced and adaptive approach to handling uncertainty, fuzzy logic continues to contribute significantly to the advancement of chemical research methodologies,

establishing itself as an indispensable tool in the pursuit of efficient and adaptive chemical systems.

Artificial Neural Networks (ANNs) have proven to be formidable tools in modeling complex relationships inherent in chemical datasets, showcasing capabilities that set them apart. Inspired by the intricate architecture of the human brain, ANNs show it's excellence in predicting modeling, classification, and pattern recognition. ANNs also possess remarkable ability to decipher nonlinear trends within data positions. The flexibility inherent in ANNs has empowered chemists by providing a versatile platform for predicting various chemical properties. ANNs also play a pivotal role in optimizing reaction conditions for complicated processes. The adaptability of ANNs in diverse datasets and their capacity to handle intricate relationships have made them indispensable tools in the hands of chemists, driving innovation and efficiency in various facets of chemical research.

Adaptive Neuro-Fuzzy Inference Systems (ANFIS) represent a potent synergy of two influential paradigms, blending the strengths of fuzzy logic and neural networks to construct highly effective hybrid models. This unique integration allows ANFIS to harness the interpretability of fuzzy logic and the learning capabilities of neural networks. By incorporating fuzzy rules directly into the learning process of Artificial Neural Networks (ANNs), ANFIS achieves a remarkable level of system adaptability, enhancing its capacity to handle uncertainties inherent in complex systems. The incorporation of fuzzy rules enriches the learning process of the ANFIS, enabling them to capture and model intricate relationships within chemical datasets. This hybrid approach has exhibited significant promise across diverse chemical applications, ranging from predictive modeling of complex reactions to real-time optimization of reaction conditions. ANFIS's success in predictive modeling underscores its ability to discern non-linear patterns and complex interactions within chemical data, providing valuable insights for researchers. Moreover, its real-time optimization capabilities contribute to the efficiency of chemical processes, ensuring adaptive adjustments to reaction conditions as they evolve. In essence, ANFIS stands as a testament to the potential unlocked through the fusion of fuzzy logic and neural networks, offering a versatile and powerful tool for advancing various facets of chemical research and applications.

Supervised learning-based decision tree regression has also emerged as a dependable and valuable tool for the analysis of chemical data. Decision trees provide an intuitive and visually accessible means to interpret complex relationships within datasets, making them particularly advantageous in the intricate domain of chemical research. The tree-like structure employed in decision tree regression facilitates sequential decision-making, aiding chemists in regression tasks where the goal is to predict continuous variables. Through this approach, chemists can gain insights into the key factors that significantly influence chemical outcomes, enhancing their understanding of the underlying processes. The simplicity of decision trees in representing complex relationships ensures ease of interpretation, allowing researchers to identify patterns and trends within chemical datasets efficiently. Decision tree regression excels in elucidating the hierarchical nature of influential variables, enabling chemists to prioritize factors based on their impact. This methodology is especially powerful in scenarios where non-linear relationships exist, providing a flexible framework for capturing intricate patterns in chemical data. Moreover, decision tree regression's ability to handle both qualitative and quantitative variables makes it a versatile tool in chemical data analysis. The transparency in the decision-making process allows chemists to validate and refine models, contributing to the robustness of predictions. In the dynamic field of chemical research, where understanding the nuances of influential factors is crucial, supervised learning-based decision tree regression stands out as an effective and accessible approach, supporting informed decision-making and advancing our comprehension of chemical processes.

The above-discussed AI-based methodologies prompted researchers with powerful tools to model intricate processes, predict outcomes, optimize conditions, and make informed decisions in the realm of chemical research. In this review, we delve into the transformative influence of cutting-edge AI techniques, such as enchanting the realms of fuzzy logic, intricate networks of artificial neural networks (ANNs), harmonious fusion in adaptive neuro-fuzzy inference systems (ANFIS), and illuminating paths paved by supervised learning-based decision tree regression, all within the captivating domain of chemical research. As AI continues to advance, its role in shaping the future of chemical systems is poised to expand even further. A brief literature survey on the implication of artificial intelligence based tools in chemical systems is discussed below.

However, implication of artificial intelligence based tools in predicting the stimuli-responsive behaviors of polypyridine-based complexes of Ru(II) are relatively sparse in the literature. A short discussion on the selected systems is provided below.

Gentili and coworkers designed an interesting compound, 1,3-Dihydro-1,3,3-trimethyl-80-nitro-spiro[2H-indole-2,30-[3H]naphth[2,1-b][1,4]oxazine], designated as SpO, comprising of photochromic, acidichromic, and metallochromic units within its molecular framework (Scheme 1.24).[128] They investigated detailed chromogenic behavior of SpO in MeCN and utilized the same for processing of both Boolean and Fuzzy logic. They employed $HClO_4$, $AlCl_3$, and $Cu(ClO_4)_2$ as the chemical inputs, coupled with UV radiation as the power source for this purpose. The optical output was quantified through the measurement of absorbance at specific wavelengths within the visible spectrum. SpO demonstrated a sophisticated five-state molecular switch, thereby providing a foundation for the execution of intricate Boolean logic circuits. Upon subjecting the chemical inputs to analog variations, the SpO solution exhibited a kaleidoscope of colors with infinite possibilities. This inherent property was further exploited through the utilization of RGB color coordinates as optical outputs, thus facilitating the realization of the fundamental operators associated with 'infinite-valued' Fuzzy logic (Scheme 1.24).

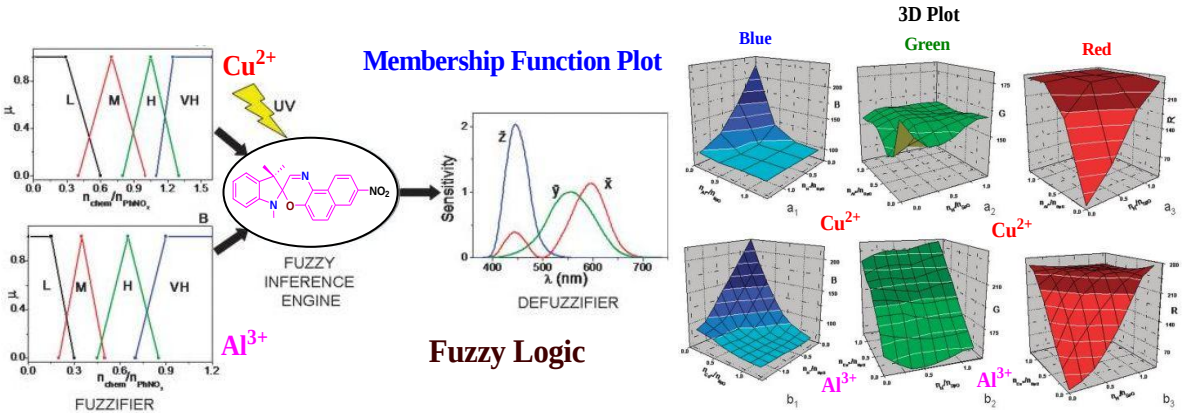

Scheme 1.24. Schematic representation of fuzzy logic based membership function plot and Blue (B), Green (G) and Red (R) coordinates as a function of the molar ratio of the ionic inputs.

Krishnamoorthy and co-worker constructed a biologically active interesting molecule, 2-(4'-N,Ndimethylaminophenyl)imidazo[4,5-b]pyridine (DMAPIP-b) as shown in Scheme 1.25.[129] Exploiting the multiple binding sites of the fluorophore, a diverse set of molecular logic gates was created by leveraging its fluorescence intensities across various wavelengths. The molecule's robust emission is significantly diminished in the presence of Fe^{3+}, and restoration occurs upon the addition of an equivalent amount of F^-. Additionally, a ternary system was established, considering three distinct fluorescence intensities at specific wavelengths. The gradual variation in emission intensities in response to analyte concentration was also harnessed to construct an infinite-valued fuzzy logic system. This fuzzy logic system was then integrated with a neuro-adaptation method to enhance the accuracy of predicting the dependency of molecular intensity on external inputs (Scheme 1.25).

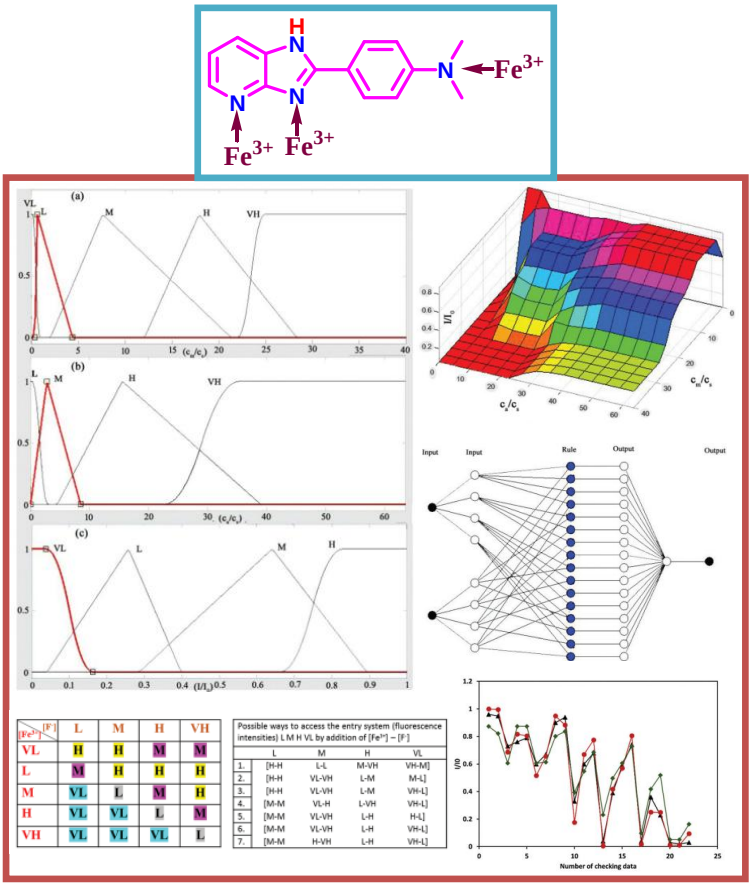

Scheme 1.25. Fuzzy and ANFIS models for predicting the dependency of molecular intensity in presence of external inputs.

Baitalik and collaborators conducted an extensive exploration onto the anion-sensing properties of a monometallic Ru(II)-bipyridine complex incorporating a pyrazole -3,5-bis(benzimidazole) moiety (Scheme 1.26).[130] They employed various optical spectral as well as square wave voltammetrric responses to thoroughly investigate the complex's anion-responsive behavior. In order to conduct in-depth analyses across a wide range of anion concentrations, the authors also applied multiple soft computing methodologies. They utilized neural network-based deep learning techniques including Artificial Neural Networks (ANNs) and the Adaptive Neuro-Fuzzy Inference System (ANFIS) to comprehensively analyze as well as to accurately interpret the multi-channel anion-sensing behavior exhibited by the complex.

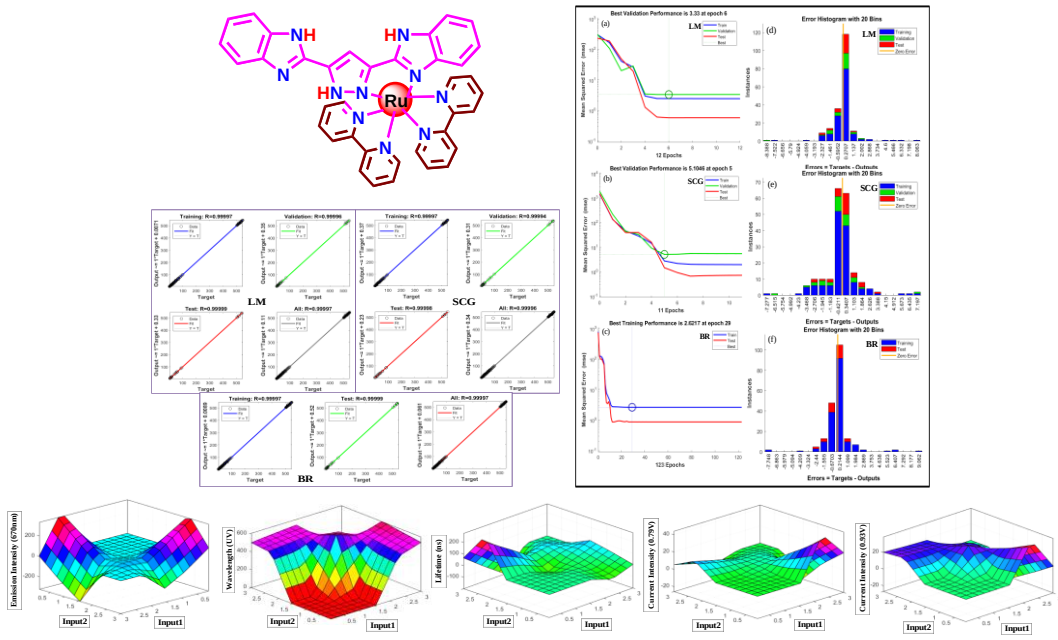

Scheme 1.26. Deep learning based neural network and neuro-fuzzy models.

1.9. Objectives and Scope of the Present Work

Upon a cursory examination of the literature, it becomes evident that coordination complexes of ruthenium(II) based on polypyridine-type ligands play pivotal roles in the development of photochemical molecular devices, by virtue of their exceptional photophysical and electrochemical properties. Among these polypyridines, the commonly utilized bipyridine (bpy) or terpyridine (tpy) type chelating units are intricately linked

with various aromatic and heteroaromatic units, as well as by electron-attracting or electron-releasing groups. Tpy-type ligands consistently yield achiral and rod-like architectures in resultant octahedral complexes, whereas their bpy-type counterparts produce complexes with intricate isomeric mixtures, the separation of which is exceptionally laborious. However, the primary shortcomings of Ru(II)-tpy type complexes lie in their suboptimal luminescence properties at room temperature and short excited-state lifetime in comparison to their bpy-type analogs. In this dissertation, we will employ both bidentate {bipyridine (bpy) or phenanthroline (phen-)} as well as terpyridine (tpy-) type chelating motifs for the construction of different types of Ru(II) complexes possessing improved room temperature luminescence characteristics which in turn could be utilized as potential building blocks for the construction of light harvesting materials.

In order to achieve our objective, we have synthesized several polypyridyl-imidazole based ligands that are capable for the formation of monometallic, bimetallic as well as trimetallic complexes upon treatment with appropriate Ru(II) precursors. To this end, a multi-dentate bridging ligand (**phen-H_2PhImz-bpy**) is designed wherein a 1,10-phenanthroline moiety is covalently coupled with 2-(4-(pyridine-2-yl)-1*H*-imidazole-5-yl)pyridine unit via phenyl-imidazole spacer. The bridge can offer a maximum of three bidentate coordinating units situated in stereochemically distinct positions. The bridging ligand is employed here to synthesize mono-, bi-, as well as trimetallic complexes of Ru(II) in combination with terminal bipyridine units as shown in Chart 1. The scope of the formation of the ligand as well as different types of Ru(II) complexes are summarized in Scheme 1.27 and Scheme 1.28.

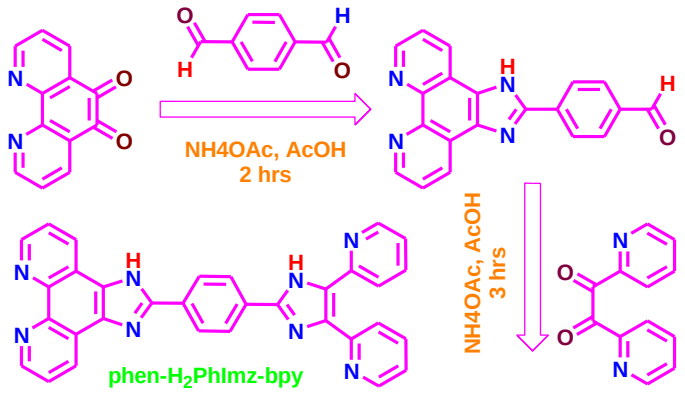

Scheme 1.27

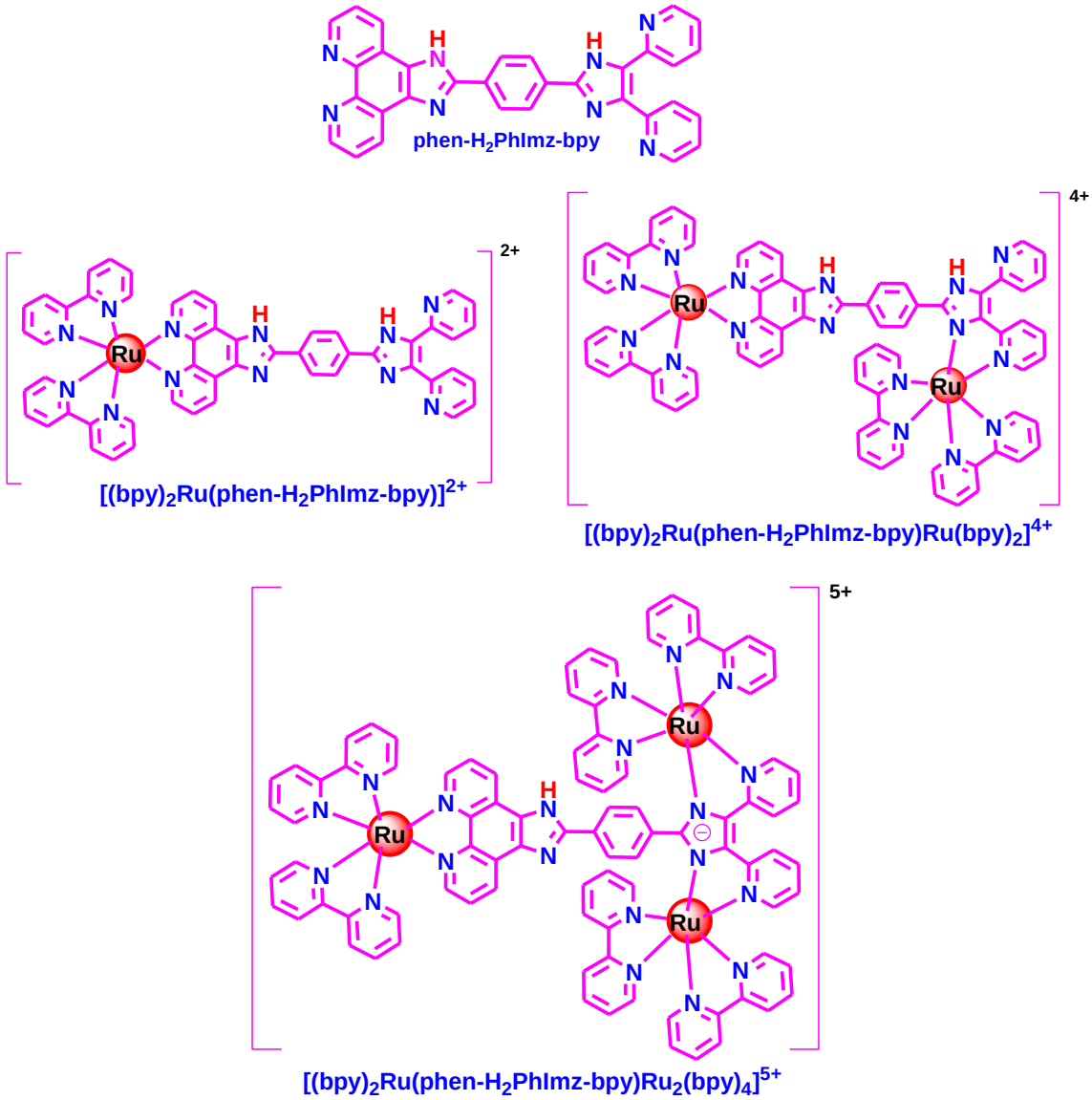

Scheme 1.28

In order to modulate the electronic structure in the complexes upon variation of coordinating atoms, we have synthesized an imidazole-4,5-dicarboxylic acid (H_3Imdc) ligand possessing an imidazole moiety connected by two carboxylic acids. The scope of formation of different types of monometallic Ru(II) complexes in combination with bpy ligands upon successive deprotonation of imidazole NH and carboxylic acid protons are outlined in Scheme 1.29.

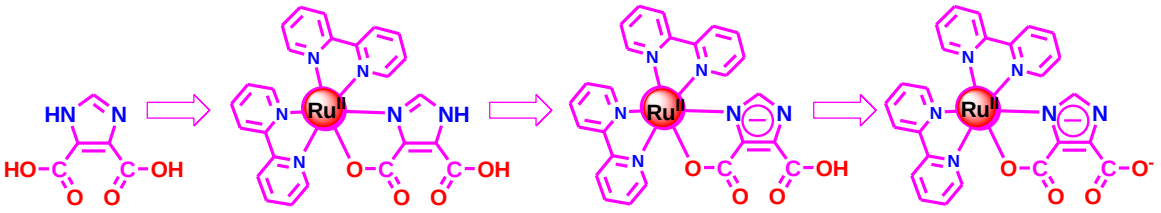

Scheme 1.29

Literature survey in previous section indicates that terpyridine-type complexes of Ru(II) are usually non-luminescent at room temperature because of presence of low-lying non-emissive triplet metal-centered (^{3}MC) state in the close vicinity to that of the emissive triplet metal-to-ligand charge transfer (^{3}MLCT) state. Through judicious choice of ligands, electron delocalization could be modulated in such a way that it would be possible to generate an excited state of the complex that can circumvent metal-centered thermal radiationless deactivation. Thus, there remain scopes for the synthesis of the terpyridine complexes of Ru(II) with enhanced triplet excited lifetimes which in turn could be utilized for light harvesting materials. To this end, we have synthesized two 4'-aryl substituted terpyridine derivatives (tpy-Ar), viz. 4′-(2-naphthyl)-2,2′:6′,2″-terpyridine (tpy-Naph) and 4′-(9-anthryl)-2,2′:6′,2″-terpyridine (tpy-An), wherein a potentially luminescent polyaromatic moiety is directly linked to the 4′-position of a terpyridine unit via a C-C single bond (Scheme 1.30). The scope of formation of different homo- and heteroleptic complexes of Ru(II) is outlined in Scheme 1.31. It is expected that the incorporation of the polyaromatic moiety, appropriately modulate the energy of the relevant excited states so that the resulting Ru(II) complexes could emissive at RT with elevated lifetimes.

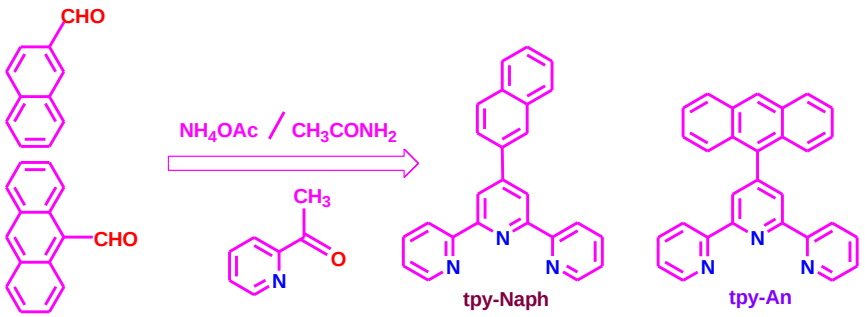

Scheme 1.30

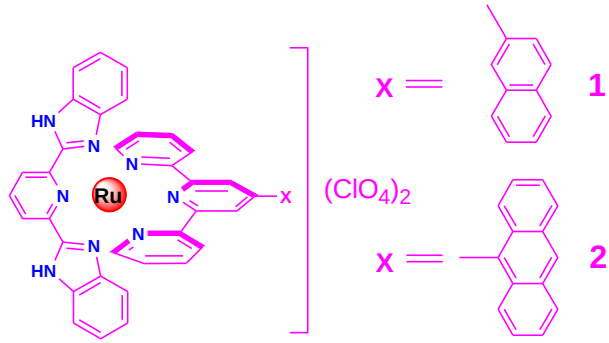

Scheme 1.31

Finally, two terpyridyl-imidazole based ligands (tpy-HImzPh$_3$ and tpy-HImzPh$_3$NMe$_2$) will also be synthesized for the design of different types of luminescent bis-tridentate Ru(II) complexes whose emission characteristic could be further modulated by suitable external stimuli, viz. temperature, anions, and cations as well as by pH. The scope of formation of ligands as well as their Ru(II) complexes are outlined in Scheme 1.32.

Following the synthesis of the ligands and their Ru(II) complexes, thorough characterization will be conducted using standard analytical tools and spectroscopic techniques, including elemental analysis, electrospray ionization (ESI) mass spectra, and NMR spectroscopic methods. Emphasis will also be given to ascertain the X-ray crystal structures of some representative complexes. Thorough investigations on the absorption and emission spectral properties of the synthesized metal complexes together with ligands will be conducted. Additionally, time-correlated single photon counting experiments will be employed to measure the excited state lifetime of the compounds. Electrochemical properties of the compounds will be scrutinized using cyclic and square wave voltammetry. Alongside experimental measurements, theoretical calculations utilizing density functional theory (DFT) and time-dependent (TD)-DFT methods will

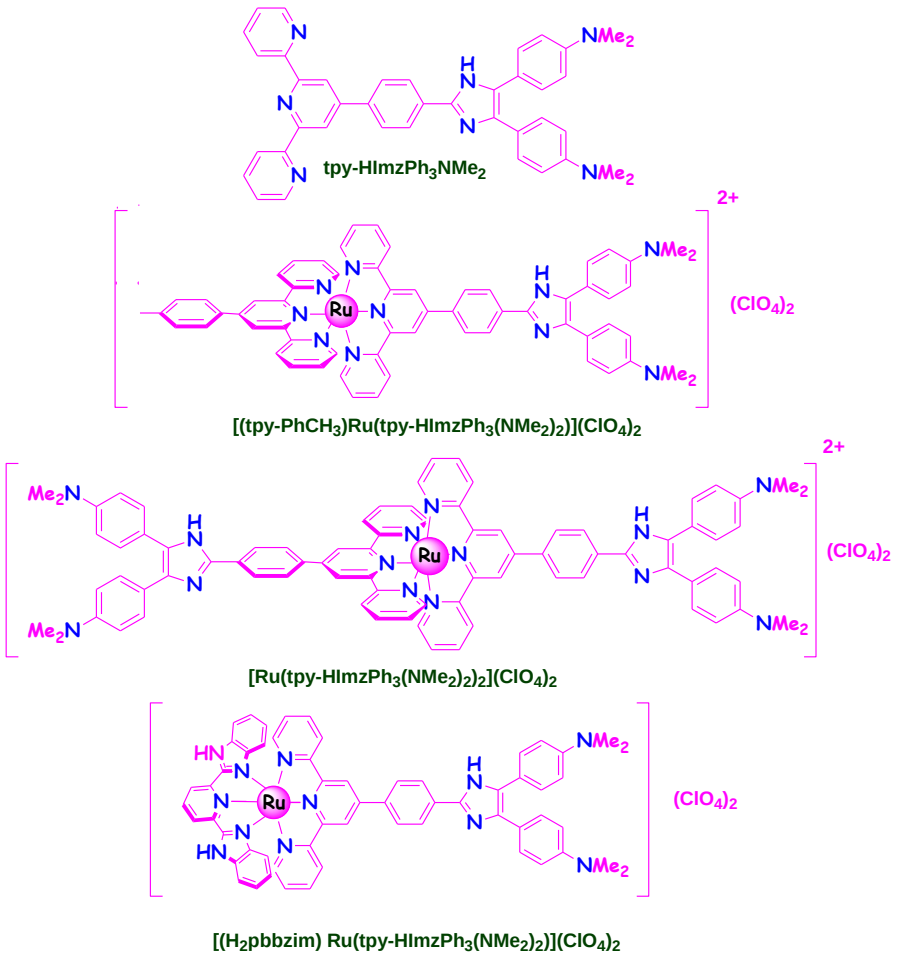

Scheme 1.32

also be performed. This aims to acquire insights into the electronic structures of the compounds and appropriately attribute the origin of the absorption and emission spectral bands that are observed experimentally.

One of the major objectives of the dissertation is to modulate the photo-redox properties of the compounds by leveraging their secondary coordination sphere. This manipulation will be achieved through various external stimuli (anion, cation, acid, base, temperature, to name a few) aiming to develop potential molecular sensors and switches.

Most of the metal complexes in this dissertation possess acidic imidazole NH proton(s) in their second coordination sphere. Upon exploiting the NH motif(s), anion-induced modulation of the photophysical and electrochemical properties could be achieved which can visualized through various optical channels (absorption, emission, and lifetime), as well as cyclic voltammetry (CV) and square wave voltammetry (SWV) (Scheme 1.33-1.34). The interaction between the complexes and anions will be assessed

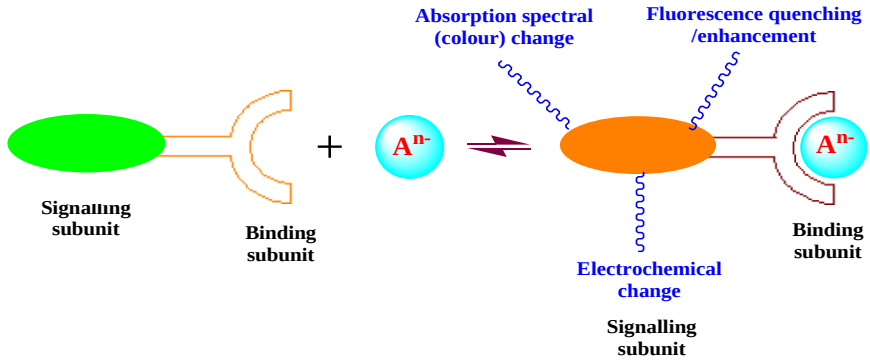

Scheme 1.33

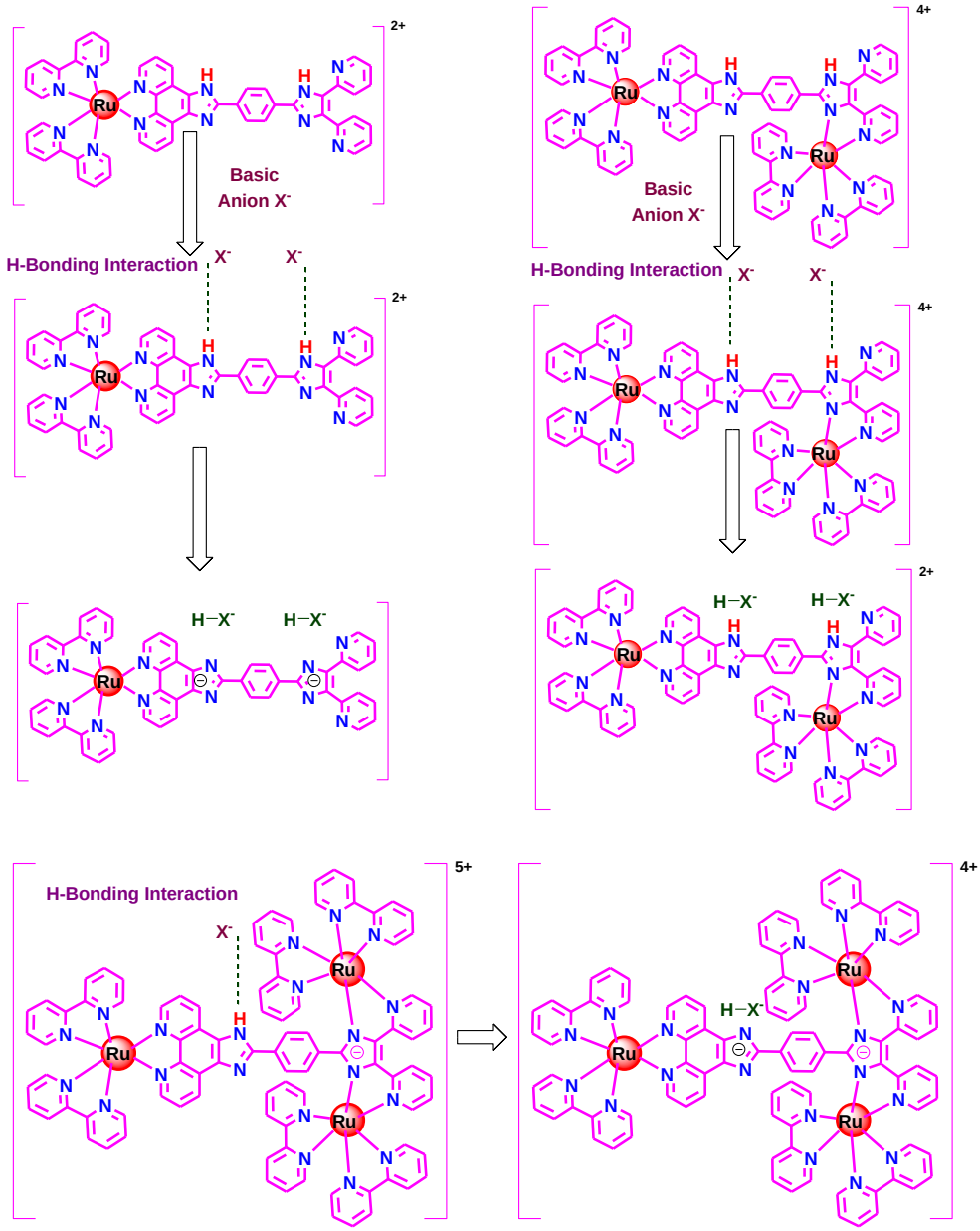

Scheme 1.34

through absorption and emission titration experiments. Additionally, we will explore the variation of the excited state lifetime of the complexes in the presence of anions to assess their potential as lifetime-based anion sensors.

The anticipated modifications in the photo-redox behaviors of the complexes, subject to various external stimuli (including anion interaction, exposure to acids, changes in pH, and alterations in temperature) form the foundation on further exploration. The spectral outputs, intricately tied to these stimuli, are meticulously harnessed in a sequential manner to unlock the potential of mimicking advanced Boolean logic operations. This systematic approach allows us to unravel the complex interplay between external factors and the photo-redox properties of the compounds. To delve even deeper into the intricacies of these phenomena, we venture into the realm of artificial intelligence (AI) and deploy an array of sophisticated soft computing tools. Fuzzy logic, with its ability to handle imprecise and uncertain data, is utilized to unravel nuanced patterns in the sensing behaviors of the complexes. Artificial Neural Networks (ANNs) then come into play, leveraging their capacity to model intricate relationships within datasets, offering a more profound understanding of the underlying complexities. The adaptive capabilities of the Adapted Neuro Fuzzy Inference System (ANFIS) will also be harnessed which could provide a hybrid model that blends the strengths of fuzzy logic and neural networks to enhance the system's adaptability in comprehending the multifaceted sensing behaviors of the receptors (Scheme 1.35). Our investigations also aim to assess the influence of diverse membership functions on the performance and outcomes of the Adaptive Neuro-Fuzzy Inference System (ANFIS). By analyzing this dependency, we seek to enhance our understanding of how specific membership functions affect the ANFIS model (Scheme 1.36).

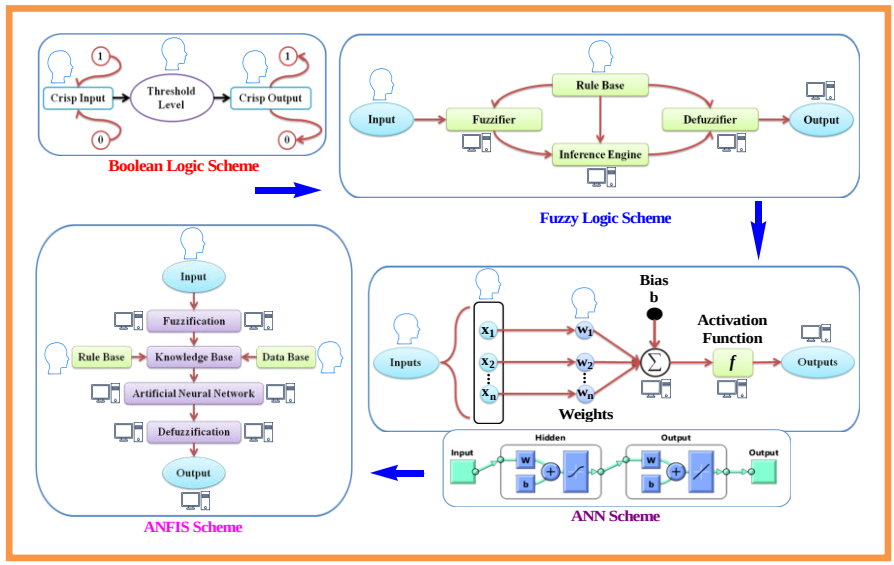

Scheme 1.35. Operational flowchart of binary logic, fuzzy inference system, artificial neural network and adaptive neuro-fuzzy inference systems.

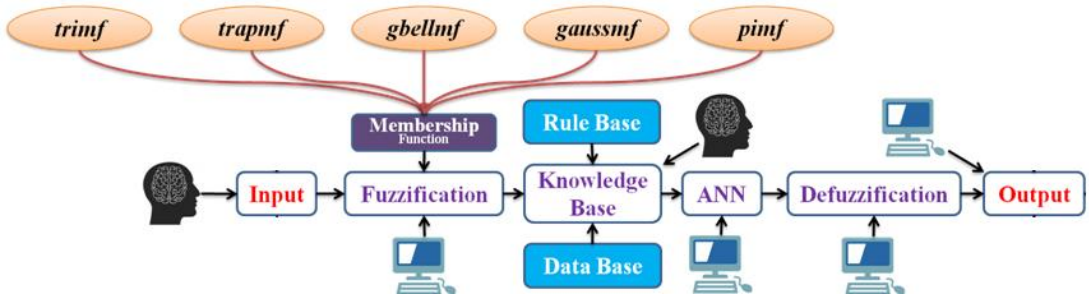

Scheme 1.36. Layers of ANFIS models with five different membership functions.

Furthermore, the precision of Supervised Learning-Based Decision Tree Regression is also been endorsed as a formidable tool, allowing us to analyze and predict with meticulous detail on the sensing behaviors of these complexes under the influence of diverse stimuli (Scheme 1.37). As we traverse the intricate landscape of molecular responses to external cues, the integration of advanced machine learning tools such as fuzzy logic, ANNs, ANFIS, and decision tree regression becomes indispensable, propelling us towards a comprehensive understanding of the complex interactions within this fascinating domain of chemical research (Scheme 1.38).

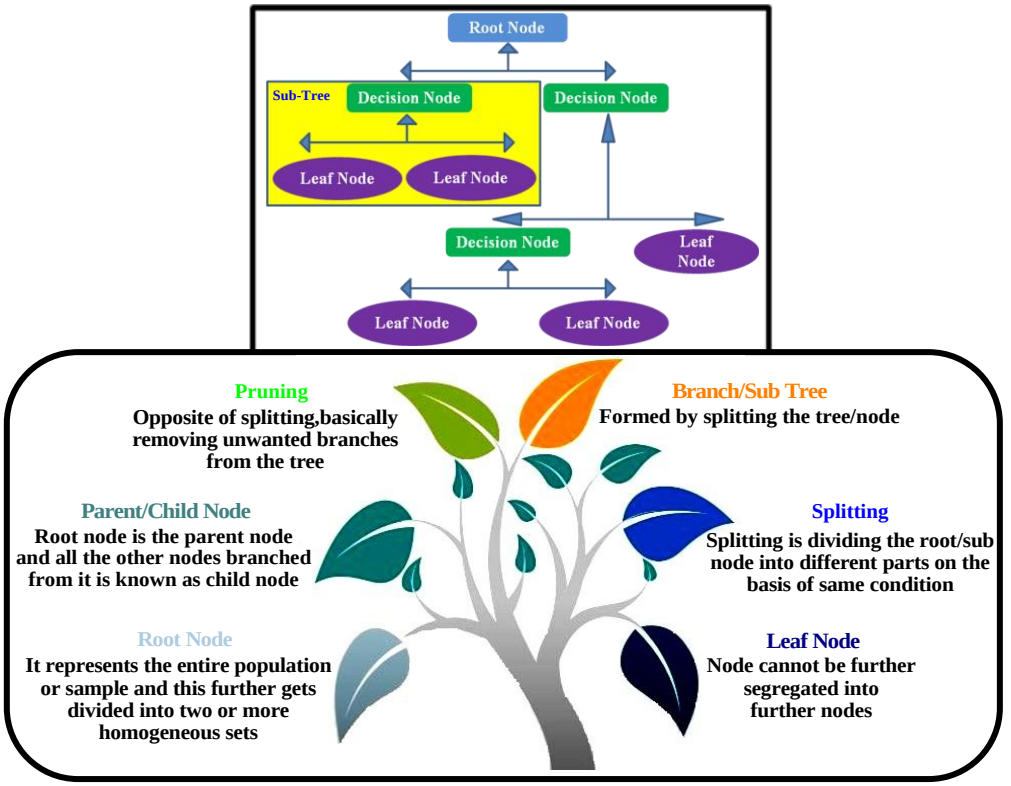

Scheme 1.37. Schematic presentation of a decision tree together with the description of each part.

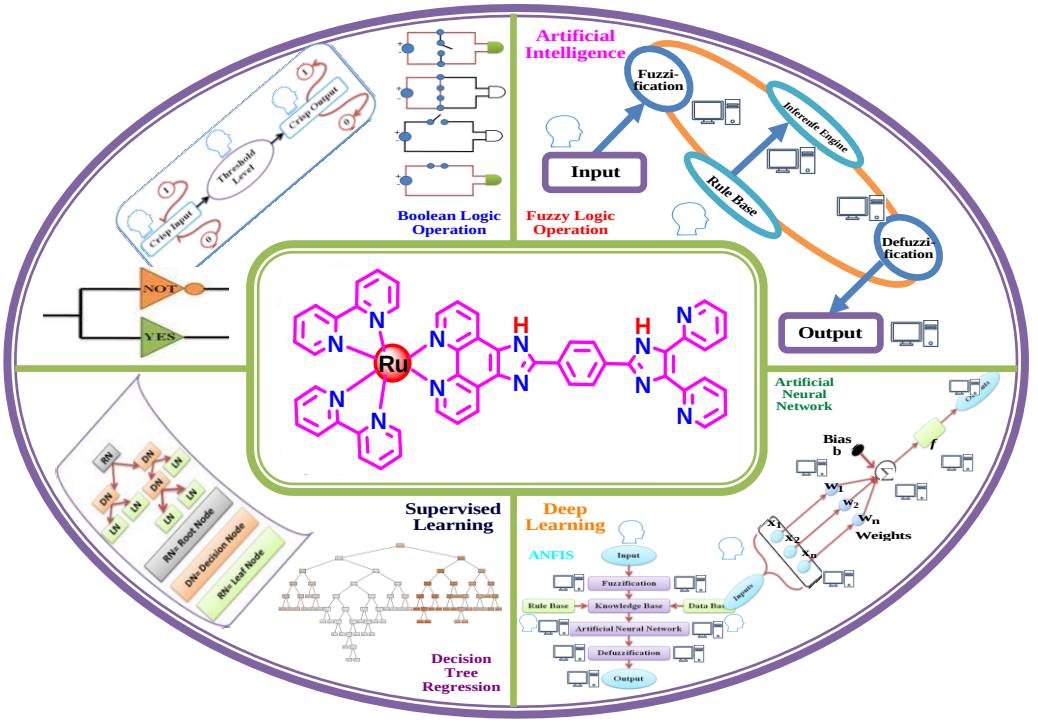

Scheme 1.38

Chapters 2-7 will present the implementation of our objectives and various scopes together with pertinent investigations.

Chapter 2 details with synthesis and thorough characterization of a polypyridyl-imidazole-based bridging ligand (phen-H_2PhImz-bpy) with three bidentate coordinating sites and its monometallic, bimetallic, as well as trimetallic Ru(II) complexes. The investigation focuses on the systematic modulation of MLCT absorption, emission, and redox behavior with the gradual incorporation of Ru^{2+} units. The study establishes structure-property relationships, revealing that the complexes are promising building blocks for various light harvesting applications based on thorough analysis of electronic absorption, emission spectral, and electrochemical characteristics.

Chapter 3 deals with thorough investigations on the anion- and acid-responsive behaviors of the three Ru(II) complexes as outlined in Chapter 2. Thereafter, adaptive neuro-fuzzy inference system (ANFIS) encompassing five membership functions viz. triangular (*trimf*), trapezoidal (*trapmf*), generalised bell shaped (*gbellmf*), gaussian (*gaussmf*), and pi-shaped (*pimf*) have been employed for accurate prediction of the experimental data as well as for appropriate modeling of the sensing characteristics of the complexes.

In chapter 4, anion- and pH-sensing behaviors of an imidazole-dicarboxylate-based Ru(II)-bipyridine complex are employed for the creation of multiple Boolean and fuzzy logic systems. The absorption, emission, and electrochemical behaviors of the metalloreceptor were significantly modulated upon the influence of basic anions (such as F^-, AcO^-, and $H_2PO_4^-$) as well as by altering the pH of the solution. The metalloreceptor demonstrates several advanced Boolean functions, namely, three-input OR gate, set-reset flip-flop logic, and traffic signal, by employing its electrochemical responses through proper use of different inputs. Several soft computing tools, viz. artificial neural networks (ANN), fuzzy logic systems (FLS), and adaptive neuro–fuzzy inference system (ANFIS) are also employed to foresee the experimental sensing data and to appropriately model the protonation-deprotonation behaviors of the metalloreceptor.

Anion-responsive behaviours of two heteroleptic bis-tridentate Ru(II) complexes comprising of 2,6-bis(benzimidazole-2-yl)pyridine (H_2pbbzim) as well as 2-naphthyl (tpy-Naph) and 9-anthryl (tpy-Anth) substituted terpyridine ligands have been presented

in chapter 5. Remarkable change in their absorption, emission as well as electrochemical and spectroelectrochemical responses occur in the presence of selected anions. Restoration of their initial states is made possible by acid and the process is reversible. The spectral, electrochemical and spectroelectrochemical responses of the complexes upon the influence of anions and acid were employed to mimic the operations of YES-NOT and set-reset flip-flop logic gates. Finally, machine learning tools such as artificial neural networks (ANNs), adaptive neuro-fuzzy inference system (ANFIS) and decision tree (DT) regression to analyse and forecast the experimental data. The outcomes of the ANN, ANFIS and DT methods were also tallied with the experimental results.

Cation- and anion-responsive behaviours of a terpyridyl-imidazole-based bifunctional receptor (tpy-HImzPh$_3$NMe$_2$) are presented in chapter 6. The compound serves as multi-channel sensor for both anions (F^-, CN^-) as well as cation (Fe^{2+}). Experimental and computational analyses, including DFT and TD-DFT calculations, provide insights into the electronic structure of the receptor as well as mode of interaction with incoming ions. The receptor demonstrates several Boolean logic functions. Additionally, ANNs, ANFIS, and decision tree regression analysis were executed to thoroughly analyze and also predict ion-sensing behavior of the receptor.

Chapter 7 deals with modulation of spectral properties of a terpyridyl-imidazole based bifunctional receptor (tpy-HImzPh$_3$). Significant alteration in its absorption and emission spectral profiles takes place in presence of selected cations and anions. The spectral responses are utilized for mimicking several Boolean logic functions. Fuzzy logic also implemented to establish an infinite-valued setup, while ANN and ANFIS are employed for accurate prediction of the experimental data.

1.10. References

1. Beaujuge, P.; Fréchet, J. Molecular Design and Ordering Effects in π-Functional Materials for Transistor and Solar Cell Applications. *J. Am. Chem. Soc*. **2011**, *133*, 20009-20029.
2. Ray, D.; Liang, C. K.; McClenaghan, N.; Bassani, D. Organic and Supramolecular Materials for LED and Photovoltaic Applications. *Curr. Phys. Chem*. **2011**, *1*, 169-180.
3. Song, W.; Chen, Z.; Brennaman, M.; Concepcion, J.; Patrocinio, A.; Murakami Iha, N.; Meyer, T. Making Solar Fuels by Artificial Photosynthesis. *Pure Appl. Chem*. **2011**, *83*, 749-768.
4. Swierk, J. R.; Mallouk, T. E. Design and Development of Photoanodes for Water-Splitting Dye-Sensitized Photoelectrochemical Cells. *Chem. Soc. Rev.* **2013**, *42*, 2357-2387.
5. Wasielewski, M. R. Self-Assembly Strategies for Integrating Light Harvesting and Charge Separation in Artificial Photosynthetic Systems. *Acc. Chem. Res.* **2009**, *42* , 1910-1921.
6. Nocera, D. G. Chemistry of Personalized Solar Energy. *Inorg. Chem.* **2009**, *48*, 10001-10017.
7. Gust, D.; Moore, T. A.; Moore, A. L. Realizing Artificial Photosynthesis. *Acc. Chem. Res.* **2009**, *42*, 1890 -1898.
8. Sumida, K.; Rogow, D. L.; Mason, J. A.; McDonald, T. M.; Bloch, E. D.; Herm, Z. R.; Bae, T. H.; Long, J. R. Carbon Dioxide Capture in Metal-Organic Frameworks. *Chem. Rev*. **2012**, *112*, 724-781.
9. Frischmann, P. D.; Mahata, K.; Würthner, F. Powering the Future of Molecular Artificial Photosynthesis with Light-Harvesting Metallosupramolecular Dye Assemblies. *Chem. Soc. Rev.* **2013**, *42*, 1847-1870.
10. Beaujuge, P.; Fréchet, J. Molecular Design and Ordering Effects in π-Functional Materials for Transistor and Solar Cell Applications. *J. Am. Chem. Soc*. **2011**, *133*, 20009-20029.
11. McConnell, A. J.; Wood, C. S.; Neelakandan, P. P.; Nitschke, J. R. Stimuli-Responsive Metal-Ligand Assemblies. *Chem. Rev*. **2015**, *115*, 7729-7793.

12. Intelligent Stimuli-Responsive Materials; Li, Q., Ed.; John Wiley & Sons, Inc.: Hoboken, Nj, **2013**.
13. Manez, R. M.; Sancenon, F. Fluorogenic and Chromogenic Chemosensors and Reagents for Anions. *Chem. Rev.* **2003,** *103*, 4419-4476.
14. De Silva, A. P.; Gunaratne, H. Q. N.; Gunnlaugsson, T.; Huxley, A. J. M.; McCoy, C. P.; Rademacher, J. T.; Rice, T. E. Signaling Recognition Events with Fluorescent Sensors and Switches. *Chem. Rev.* **1997**, *97*, 1515-1566.
15. Ko, C. C.; Yam, V. W. W. Coordination Compounds with Photochromic Ligands: Ready Tunability and Visible Light-Sensitized Photochromism. *Acc. Chem. Res*. **2018**, *51*, 149-159.
16. Kurihara, M.; Nishihara, H. Azo- and Quinone-Conjugated Redox Complexes-Photo- and Proton-Coupled Intramolecular Reactions Based on d-π Interaction. *Coord. Chem. Rev.* **2002**, *226*,125-135.
17. Cui, B-B.; Zhong, Y-W.; Yao, J. Three-State Near-Infrared Electrochromism at the Molecular Scale. *J. Am. Chem. Soc*. **2015**, *137*, 4058-4061.
18. Jia, C.; Wang, J.; Yao, C.; Cao, Y.; Zhong, Y.; Liu, Z.; Liu, Z.; Guo, X. Conductance Switching and Mechanisms in Single-Molecule Junctions. *Angew. Chem. Int. Ed*. **2013**, *52*, 8666 -8670.
19. Haga, M.; Ali, M. M.; Maegawa, H. Nozaki, K. Yoshimura, A.; Ohno, T. Photoexcited States of Dinuclear Ru Complexes Bridged by Proton-Dissociable Benzimidazole Derivatives. *Coord. Chem. Rev*. **1994**, *132*, 99-104.
20. Motoyama, D.; Yoshikawa, K.; Ozawa, H.; Tadokoro, M.; Haga, M. Energy-Storage Applications for a pH Gradient between Two Benzimidazole-Ligated Ruthenium Complexes That Engage in Proton-Coupled Electron-Transfer Reactions in Solution. *Inorg. Chem*. **2017**, *56*, 6419-6428.
21. Huynh, M. H. V.; Meyer, T. J. Proton-Coupled Electron Transfer. *Chem. Rev*. **2007**, *107*, 5004-5064.
22. Ali, C.; Banaszak, M.; Astumian, R. D.; Stoddart, J. F.; Grzybowski, B. A. Great Expectations: Can Artificial Molecular Machines Deliver on Their Promise? *Chem. Soc. Rev*. **2012**, *41*, 19-30.

23. Juris, A.; Balzani, V.; Barigelletti, F.; Campagna, S.; Belser, P.; Von Zelewsky, A. Ru (II) Polypyridine Complexes: Photophysics, Photochemistry, Eletrochemistry, and Chemiluminescence. *Coord. Chem. Rev*. **1988**, *84*, 85-277.

24. Balzani, V.; Juris, A.; Venturi, M.; Campagna, S.; Serroni, S. Luminescent and Redox-Active Polynuclear Transition Metal Complexes. *Chem. Rev*. **1996**, *96*, 759-833.

25. Sauvage, J.-P.; Collin, J. P.; Chambron, J. C.; Guillerez, S.; Coudret, C.; Balzani, V.; Barigelletti, F.; De Cola, L.; Flamigni, L. Ruthenium(II) and Osmium(II) Bis(terpyridine) Complexes in Covalently-Linked Multicomponent Systems: Synthesis, Electrochemical Behavior, Absorption Spectra, and Photochemical and Photophysical Properties. *Chem. Rev*. **1994**, *94*, 993-1019.

26. Medlycott, E. A.; Hanan, G. S. Designing Tridentate Ligands for Ruthenium (II) Complexes with Prolonged Room Temperature Luminescence Lifetimes**.** *Chem. Soc. Rev*. **2005**, *34*, 133-142.

27. Medlycott, E. A.; Hanan, G. S. Synthesis and Properties of Mono- and Oligo-Nuclear Ru (II) Complexes of Tridentate Ligands: The Quest for Long-Lived Excited States at Room Temperature. *Coord. Chem. Rev.* **2006**, *250*, 1763-1782.

28. Wang, X.; Guerzo, A.; Baitalik, S.; Simon, G.; Shaw, G. B.; Chen, L. X.; Schmehl, R. H. The Influence of Bridging Ligand Electronic Structure on the Photophysical Properties of Noble Metal Diimine and Triimine Light Harvesting Systems. *Photosynth. Res.* **2006**, *87*, 83-103.

29. Schubert, U. S.; Eschbaumer, C. Macromolecules Containing Bipyridine and Terpyridine Metal Complexes: Towards Metallosupramolecular Polymers. *Angew. Chem. Int. Ed.* **2002**, *41*, 2892-2896.

30. De Silva, A. P.; Gunaratne, H.Q.N.; McCoy, C.P. A Molecular Photoionic AND Gate Based on Fluorescent Signaling. *Nature*. **1993**, *364*, 42-44.

31. De Silva, A. P.; Fox, D. P.; Huxley, A. J. M.; Moody, T. S. Combining Luminescence, Coordination and Electron Transfer for Signaling Purposes. *Coord. Chem. Rev*., **2000**, *205*, 41-57.

32. Ling, J.; Daly, B.; Silverson, V. A. D.; de Silva, A. P. Taking Baby Steps in Molecular Logic-Based Computation. *Chem. Commun.*, **2015**, *51*, 8403-8409.

33. Daly, B.; Ling, J.; de Silva, A. P. Current Developments in Fluorescent PET (Photoinduced Electron Transfer) Sensors and Switches. *Chem. Soc. Rev.*, **2015**, *44*, 4203-4211.
34. Andréasson, J.; Pischel, U. Smart Molecules at Work Mimicking Advanced Logic Operations. *Chem. Soc. Rev.*, **2010**, *39*, 174-188.
35. Carvalho, C. P.; Dominguez, Z.; Da Silva, J. P.; Pischel, U. A Supramolecular Keypad Lock. *Chem. Commun*., **2015**, *51*, 2698-2701.
36. Andreasson, J.; Pischel, U. Molecules with a Sense of Logic: A Progress Report. *Chem. Soc. Rev*., **2015**, *44*, 1053-1069.
37. Schmittel, M.; Mal, P.; de los Rios, A. Multiport Logic Operations Triggered by Protonation-a Trisphenanthroline as a 3-input AND-NOR-OR Circuit, *Chem. Commun*., **2010**, *46*, 2031-2033.
38. Biswas, P. K.; Saha, S.; Gaikwad, S.; Schmittel, M. Reversible Multicomponent AND Gate Triggered by Stoichiometric Chemical Pulses Commands the Self-Assembly and Actuation of Catalytic Machinery. *J. Am. Chem. Soc.*, **2020**, *142*, 7889-7897.
39. Szaciłowski, K. Digital Information Processing in Molecular Systems. *Chem. Rev*., **2008,** *108*, 3481-3548.
40. Szaciłowski, K.; Macyk, W.; Stochel, G.; Light-Driven OR and XOR Programmable Chemical Logic Gates. *J. Am. Chem. Soc*., **2006**, *128*, 4550-4551.
41. Said, A. I.; Georgiev, N. I.; Bojinov, V. B. A Fluorescent Bichromophoric "Off-On-Off" pH Probe as a Molecular Logic Device (Half-Subtractor and Digital Comparator) Operating by Controlled PET and ICT Processes. *Dyes and Pigments*, **2019**, *162*, 377-384.
42. Georgiev, N. I.; Yaneva, I. S.; Surleva, A. R.; Asiri, A. M.; Bojinov, V. B. Synthesis, Sensor Activity and Logic Behavior of a Highly Water-Soluble Naphthalimide Derivative. *Sensors and Actuators B*, **2013**, 54-63.
43. Georgiev, N. I.; Sakr, A. R. Bojinov, V. B. Design and Synthesis of a Novel PET and ICT Based 1,8-Naphthalimide FRET Bichromophore as a Four-Input Disabled-Enabled-OR Logic Gate. *Sensors and Actuators B*, **2015**, *221*, 625-634.

44. Magri, D. C.; Spiteri, J. C. Proof of Principle of A Three-Input AND–INHIBIT–OR Combinatorial Logic Gate Array. *Org. Biomol. Chem*. **2017**, *15*, 6706-6709.
45. Mardanya, S.; Mondal, D.; Karmakar, S.; Baitalik, S. Smart Ruthenium and Osmium Complexes Mimic the Complicated Functions of Traffic Signal and Memory Device. *Sens. Actuators B: Chem*. **2017**, *239*, 635-641.
46. Cui, B. B.; Tang, J. H.; Yao, J.; Zhong, Y. W. A Molecular Platform For Multistate Near-Infrared Electrochromism and Flip-Flop, Flip-Flap-Flop, and Ternary Memory. Angew. Chem. Int. Ed. **2015**, *54*, 9192-9197.
47. Shao, J. Y.; Yao, C. J.; Cui, B. B.; Gong, Z. L.; Zhong, Y. W. Electropolymerized Films of Redox-Active Ruthenium Complexes for Multistate Near-Infrared Electrochromism, Ion Sensing, and Information Storage. *Chin. Chem. Lett*. **2016**, *27*, 1105-1114.
48. Szaciłowski, K. Molecular Logic Gates Based on Pentacyanoferrate Complexes: From Simple Gates to Three-Dimensional Logic Systems. *Chem. Eur. J.* **2004**, *10*, 2520-2528.
49. Artrith, N.; Butler, K. T.; Coudert, F. X.; Han, S.; Isayev, O.; Jain, A.; Walsh, A. Best Practices in Machine Learning for Chemistry. *Nat. Chem*. **2021**, *13*, 505-508.
50. Mater, A. C.; Coote, M. L. Deep Learning in Chemistry. *J. Chem. Inf. Model*. **2019**, *59*, 2545-2559.
51. Pflüger, P. M.; Glorius, F. Molecular Machine Learning: the Future of Synthetic Chemistry? *Angew. Chem. Int. Ed.* **2020**, *59*, 18860-18865.
52. He, L.; Bai, L.; Dionysiou, D. D.; Wei, Z.; Spinney, R.; Chu, C.; Xiao, R. Applications of Computational Chemistry, Artificial Intelligence, and Machine Learning in Aquatic Chemistry Research. *Chem. Eng. J.* **2021**, *426*, 131810.
53. Gentili, P. L. A Strategy to Face Complexity: The Development of Chemical Artificial Intelligence. In Advances in Artificial Life, Evolutionary Computation, and Systems Chemistry; Rossi, F., Piotto, S., Concilio, S., Eds.; *Springer: Cham*, Switzerland; New York, NY, USA. **2017**, *708*, 151-160.
54. Zadeh, L. A. Toward Human Level Machine Intelligence-is It Achievable? the Need for a Paradigm Shift. *IEEE Comput. Intell. Mag*. **2008**, *3*, 11-22.

55. Zadeh, L.A. Outline of a New Approach to the Analysis of Complex Systems and Decision Processes. *IEEE Trans. Syst. Man Cyb*. **1973**, *3*, 28-44.
56. Conrad, M. Molecular Computing. *Adv. Comput*. **1990**, *31*, 235-324.
57. Zadeh, L. A. Fuzzy sets. In Fuzzy Sets, Fuzzy Logic, and Fuzzy Systems: Selected Papers by Lotfi A Zadeh, pp. *394-432*. **1996.**
58. Gentili, P. L. Boolean and Fuzzy Logic Gates Based on The Interaction of Flindersine with Bovine Serum Albumin and Tryptophan. *J. Phys. Chem. A.* **2008**, *112*, 11992-11997.
59. Gentili, P. L. The Fuzziness of the Molecular World and Its Perspectives. *Molecules.* **2018**, *23*, 2074.
60. Gentili, P.L. The Fundamental Fuzzy Logic Operators and Some Complex Boolean Logic Circuits Implemented by the Chromogenism of a Spirooxazine. *Phys. Chem. Chem. Phys.* **2011**, *13*, 20335-20344.
61. Gentili, P.L.; Giubila, M.S.; Heron, B.M. Processing Binary and Fuzzy Logic by Chaotic Time Series Generated by a Hydrodynamic Photochemical Oscillator. *Chem Phys Chem.* **2017**, *18*, 1831-1841.
62. Gentili, P.L.; Giubila, M.S.; Germani, R.; Romani, A.; Nicoziani, A.; Spalletti, A.; Heron; B.M. Optical Communication Among Oscillatory Reactions and Photo-Excitable Systems: Uv and Visible Radiation Can Synchronize Artificial Neuron Models. *Angew. Chem. Int. Ed.* **2017**, *56*, 7535-7540.
63. Schumann, A.; Adamatzky, A. The Double-Slit Experiment with Physarum Polycephalum and P-adic Valued Probabilities and Fuzziness. *Int J Gen Syst.* **2015**, *44*, 392-408.
64. Giri Nandagopal, M. S.; Selvaraju, N. Prediction of Liquid-Liquid Flow Patterns in a Y-junction Circular Microchannel Using Advanced Neural Network Techniques. *Ind. Eng. Chem. Res.* **2016**, *55*, 11346-11362.
65. Bingöl, D.; Inal, M.; Çetintaş, S. Evaluation of Copper Biosorption Onto Date Palm (Phoenix Dactylifera L.) Seeds with MLR and ANFIS Models. *Ind. Eng. Chem.Res* **2013**, *52*, 4429-4435.

66. İnal, M. Predicting the Conversion Ratio for the Leaching of Celestite in Sodium Carbonate Solution Using An Adaptive Neuro-Fuzzy Inference System. *Ind. Eng. Chem.Res* **2014**, *53*, 4975-4980.

67. Jang, J. S. R.; Sun, C. T. Neuro-Fuzzy Modeling and Control. *Proc. IEEE.* **1995**, *83*, 378-405.

68. Sugeno, M.; Yasukhiro, T. A Fuzzy-Logic-Based Approach to Qualitative Modeling. *IEEE Trans. Fuzzy Syst.* **1993**, *1*, 7-31.

69. Goswami, S.; Pramanick, R.; Patra, A.; Rath, S. P.; Foltin, M.; Ariando, A.; Williams, R. S. Decision trees within a molecular memristor. *Nature*. **2021**, *597*, 51-56.

70. Shiratori, K.; Bishop, L. D.; Ostovar, B.; Baiyasi, R.; Cai, Y. Y.; Rossky, P. J.; Link, S. Machine-learned decision trees for predicting gold nanorod sizes from spectra. *J. Phys. Chem. C*. **2021**, *125*, 19353-19361.

71. LeCun, Y.; Bengio, Y.; Hinton, G. Deep learning. *Nature*. **2015**, *521*, 436-444.

72. Pedretti, G.; Graves, C. E.; Serebryakov, S.; Mao, R.; Sheng, X.; Foltin, M.; Strachan, J. P. Tree-based machine learning performed in-memory with memristive analog CAM. *Nat. comm.* **2021**, *12*, 1-10.

73. Geurts, P.; Irrthum, A.; Wehenkel, L. Supervised learning with decision tree-based methods in computational and systems biology. *Molecular Biosystems*. **2009**, *5*, 1593-1605.

74. Swaney, D. L.; McAlister, G. C.; Coon, J. J. Decision tree–driven tandem mass spectrometry for shotgun proteomics. *Nat. Methods*. **2008**, *5*, 959-964.

75. Kalyanasundaram, K. Photophysics, Photochemistry and Solar Energy Conversion with Tris (bipyridyl) Ruthenium (II) and Its Analogs.*Coord. Chem. Rev.* **1982**, *46*, 159.

76. Scandola, F.; Indelli M. T. Second Sphere Donor Acceptor Interactions in Excited States of Coordination Compounds. Ruthenium (II) Bipyridine Cyano Complexes. *Pure Appl. Chem.* **1988**, *60*, 973.

77. Endicott, J. F.; Schlegel, H. B.; Uddin, M.J.; Seniveratne, D.S. MLCT excited states and charge delocalization in some ruthenium–ammine–polypyridyl complexes. *Coord.Chem. Rev.* 2002, *229*, 95-106.

78. Bar, M.; Pal, P.; Maity, D.; Baitalik, S. Heterobimetallic Ru-Os Complexes Function as Multichannel Sensors for Selected Anions by Taking Profit of Metal-Ligand Interaction. *Sensors and Actuators* B, **2018**, *266*, 493-505.

79. Bhaumik, C.; Maity, D.; Das, S.; Dutta, S.; Baitalik, S. Anion Sensing Studies of Luminescent Bis-tridentate Ruthenium (II) and Osmium (II) Complexes Based on Terpyridyl-Imidazole Ligand Through Different Channels. *Polyhedron* **2013**, *52*, 890-899.

80. Maity, D.; Bhaumik, C.; Mondal, D.; Baitalik, S. Ru (II) and Os(II) Complexes Based on Terpyridyl-Imidazole Ligand Rigidly Linked to Pyrene: Synthesis, Structure, Photophysics, Electrochemistry, and Anion-Sensing Studies. *Inorg. Chem.*, **2013**, *52*, 13941-13955.

81. Mardanya, S.; Karmakar, S.; Maity, D.; Baitalik, S. Multichromophoric Bimetallic Ru (II) Terpyridine Complexes Based on Pyrenyl-bis-phenylimidazole Spacer: Synthesis, Photophysics, Spectroelectrochemistry, and TD-DFT Calculations. *Inorg. Chem.*, **2014**, *53*, 12036-12049.

82. Kober, E.M.; Caspar, J.V.; Lumpkin, R. S.; Meyer, T. J. Application of the Energy gap Law to Excited-state Decay of Osmium (II)-Polypyridine Complexes: Calculation of Relative Nonradiative Decay Rates from Emission Spectral Profiles. *J. Phys. Chem.*, **1986**, *90*, 3722-3734.

83. Caspar, J. V.; Meyer, T. J. Application of the Energy Gap Law to Nonradiative, Excited-State Decay. *J. Phys. Chem.*, **1983**, *87*, 6-10.

84. Amini, A.; Harriman, A.; Mayeux, A. The Triplet Excited State of Ruthenium (II) Bis(2,2′:6′,2″-terpyridine): Comparison Between Experiment and Theory. *Phys. Chem. Chem. Phys***. 2004**, *6*, 1157-1164.

85. Gu, J.; Yan, Y.; Helbig, B. J.; Huang, Z.; Lian, T.; Schmehl, R. H. The Influence of Ligand Localized Excited States on the Photophysics of Second Row and Third Row Transition Metal Terpyridyl Complexes: Recent Examples and a Case Study. *Coord. Chem rev*, **2015**, *222-283*, 100-109.

86. Hammarström, L.; Barigelletti, F.; Flamigni, L.; Indelli, M. T.; Armaroli, N.; Calogero, G.; Guardigli, M.; Sour, A.; Collin, J.-P. ; Sauvage, J.-P. A Study on Delocalization of MLCT Excited States by Rigid Bridging Ligands in Homometallic Dinuclear Complexes of Ruthenium (II). *J. Phys. Chem. A* **1997**, *101*, 9061-9069.

87. Suresh, M.; Jose D. A.; Das, A. 2,2'-Bipyridyl-3,3'-diol as a Molecular Half-Subtractor. *Org. Lett*., **2007**, *9*, 441-444.

88. Coskun, A.; Deniz, E.; Akkaya, E. U. Effective PET and ICT Switching of Boradiazaindacene Emission: A Unimolecular, Emission-Mode, Molecular Half-Subtractor with Reconfigurable Logic Gates. *Org. Lett*., **2005**, *7*, 5187-5189.

89. Langford, S. J.; Yann, T. Molecular Logic: A Half-Subtractor Based on Tetraphenylporphyrin. *J. Am. Chem. Soc*., **2003**, *125*, 11198-11199.

90. Kumar, S.; Luxami, V.; Saini, R.; Kaur, D. Superimposed Molecular Keypad Lock and Half-Subtractor Implications in a Single Fluorophore. *Chem. Commun*., **2009**, 3044-3046.

91. Margulies, D.; Melman G.; Shanzer, A. A Molecular Full-Adder and Full-Subtractor, an Additional Step toward a Moleculator. *J. Am. Chem. Soc.*, **2006**, *128*, 4865-4871.

92. Kaur, N.; Kumar, S. Aminoanthraquinone-Based Chemosensors: Colorimetric Molecular Logic Mimicking Molecular Trafficking and a Set-Reset Memorized Device. *Dalton Trans*., **2012**, *41*, 5217-5224.

93. MacVittie, K.; Halamek, J.; Katz, E. Enzyme-Based D-Flip-Flop Memory System *Chem. Commun*., **2012**, *48*, 11742-11744.

94. Zhuang, H.; Zhou, Q.; Zhang, Q.; Li, H.; Li, N.; Xu, Q.; Lu, J. Effects of Aromatic Spacers on Film Morphology and Device Memory Performance Based on Imidazole-π–Triphenylamine Derivatives. *J. Mater. Chem. C*, **2015**, *3*, 416-422.

95. Mardanya, S. ; Karmakar, S. ; Mondal, D.; Baitalik, S. An Imidazolyl-Pyreno-Imidazole Conjugate As A Cyanide Sensor and a Set-Reset Memorized Sequential Logic Device. *Dalton Trans*., **2015**, *44*, 15994-16012.

96. Karmakar, S.; Mardanya, S.; Das, S.; Baitalik, S. Efficient Deep-Blue Emittier and Molecular-Scale Memory Device Based on Dipyridyl-Phenylimidazole-Terpyridine Assembly. *J. Phys. Chem. C.*, **2015**, *119*, 6793-6805.

97. Andrasson, J.; Straight, S. D.; Bandyopadhyay, S.; Mitchell, R. H.; Moore, T. A.; Moore A. L.; Gust, D. Molecular 2:1 Digital Multiplexer. *Angew. Chem. Int. Ed*., **2007**, *46*, 958-961.

98. Erbas-Cakmak, S.; Bozdemir, O. A.; Cakmak Y.; Akkaya, E. U. Proof of Principle for a Molecular 1 : 2 Demultiplexer to Function as an Autonomously Switching Theranostic Device. *Chem. Sci.*, **2013**, *4*, 858-862.

99. Xu, S.; Hao, Y.-X.; Sun, W.; Fang, C.-J.; Lu, X.; Li, M.-N.; Zhao, M.; Peng, S.Q.; Yan, C.-H. 2:1 Multiplexing Function in a Simple Molecular System. *Sensors*., **2012**, *12*, 4421-4430.

100. Verma, S.; Kar, P.; Das, A.; Ghosh, H. N. Photophysical Properties of Ligand Localized Excited State in Ruthenium (II) Polypyridyl Complexes: A Combined Effect of Electron Donor–Acceptor Ligand. *Dalton Trans*., **2011**, *40*, 9765-9773.

101. Ambroise, A.; Maiya, B. G. Ruthenium (II) Complexes of Redox-Related, Modified Dipyridophenazine Ligands: Synthesis, Characterization, and DNA Interaction. *Inorg. Chem*., **2000**, *39*, 4256-4263.

102. Ashford, D. L.; Stewart, D. J.; Glasson, C. R.; Binstead, R. A.; Harrison, D. P.; Norris, M. R.; Meyer, T. J. An Amide-Linked Chromophore–Catalyst Assembly for Water Oxidation. *Inorg. Chem*., **2012**, **51**, 6428-6430.

103. Sorsche, D.; Schaub, M.; Heinemann, F. W.; Habermehl, J.; Kuhri, S.; Guldi, D.; Rau, S. (). π-Stacking Attraction vs. Electrostatic Repulsion: Competing Supramolecular Interactions in a Tpphz-Bridged Ru (II)/Au (III) Complex. *Dalton Trans*., **2016**, *45*, 12846-12853.

104. Nag, S.; Ferreira, J. G.; Chenneberg, L.; Ducharme, P. D.; Hanan, G. S.; La Ganga, G.; Campagna, S. Changing the Role of 2, 2′-Bipyridine from Secondary Ligand to Protagonist in $[Ru(bpy)_2(N^- N)]^{2+}$ Complexes: Low-Energy, Red Emission from a Ruthenium (II)-to-2, 2′-Bipyridine ^{3}MLCT State. *Inorg. Chem*., **2011**, *50*, 7-9.

105. Li, G.; Hu, K.; Yi, C.; Knappenberger Jr, K. L.; Meyer, G. J.; Gorelsky, S. I.; Shatruk, M. (). Panchromatic Light Harvesting and Hot Electron Injection by Ru (II) Dipyrrinates on a TiO_2 Surface. *J. Phys. Chem. C*., **2013**, *117*, 17399-17411.

106. Beley, M.; Delabouglise, D.; Houppy, G.; Husson, J.; Petit, J.-P. Preparation and Properties of Ruthenium (II) Complexes of 2,2':6',2''-Terpyridines Substituted at the 4'-Position with Heterocyclic Groups. *Inorg. Chim. Acta.*, **2005**, *358*, 3075-3083.

107. Duati, M.; Tasca, S.; Lynch, F. C.; Bohlen, H.; Vos, J. G.; Stagni, S.; Ward, M. D. Enhancement of Luminescence Lifetimes of Mononuclear Ruthenium(II)-

Terpyridine Complexes by Manipulation of the σ-Donor Strength of Ligands. *Inorg. Chem.*, **2003**, *42*, 8377-8384.

108. Duati, M.; Fanni, S.; Vos, J. G. A New Luminescent Ru (Terpy) Complex Incorporating a 1, 2, 4-Triazole Based σ -Donor ligand. *Inorg. Chem. Commun.*, **2000**, *3*, 68-70.
109. Mizuno, T.; Wei, W.H.; Eller, L.R.; Sessler, J.L. Phenanthroline Complexes Bearing Fused Dipyrrolylquinoxaline Anion Recognition Sites: Efficient Fluoride Anion Receptors. *J. Am. Chem. Soc.*, **2002**, *124*, 1134-1135.
110. Anzenbacher Jr, P.; Tyson, D.S.; Jursiková, K.; Castellano, F.N. Luminescence Lifetime-Based Sensor for Cyanide and Related Anions. *J. Am. Chem. Soc.*, **2002**, *124*, 1134-1135.
111. Zapata, F.; Caballero, A.; Espinosa, A.; Tárraga, A.; Molina, P. Cation Coordination Induced Modulation of the Anion Sensing Properties of a Ferrocene-Imidazophenanthroline Dyad. *J. Org. Chem*., **2008**, *73*, 4034-4044.
112. Patil, S. K.; Ghosh, R.; Kennedy, P.; Mobin, S. M.; Das, D. Potential Anion Sensing Properties By a Redox and Substitution Series of $[Ru(bpy)_{3-n}(Hdpa)_n]^{2+,}$ n = 1-3; Hdpa = 2,2' -Dipyridylamine: Selective Recognition and Stoichiometric Binding Cyanide and Fluoride Ions. *RSC Adv.*, **2016**, *6*, 62310-62319.
113. Khatua, S.; Samanta, D.; Bats, J. W.; Schmittel, M. Rapid and Highly Sensitive Dual-Channel Detection of Cyanide by Bis-heteroleptic Ruthenium (II) Complexes. *Inorg. Chem.*, **2012**, *51*, 7075-7086.
114. Cui, Y.; Mo, H.J.; Chen, J.C.; Niu, Y.L.; Zhong, Y.R.; Zheng K. C., Ye, B.H. Anion-Selective Interaction and Colorimeter by an Optical Metalloreceptor Based on Ruthenium(II) 2,2′-Biimidazole: Hydrogen Bonding and Proton Transfer. *Inorg. Chem.*, **2007**, *46*, 6427-6436.
115. Cui, Y.; Niu, Y.L.; Cao, M.L.; Wang, K.; Mo, H. J.; Zhong, Y. R.; Ye, B.H. Ruthenium(II) 2,2′-Bibenzimidazole Complex as a Second-Sphere Receptor for Anions Interaction and colorimeter. Inorg. Chem., **2008**. *47*, 5616-5624.

116. Mo, H.J.; Niu, Y. L.; Zhang, M.; Qiao, Z.P.; Ye, B.H. Photophysical, Electrochemical and Anion Sensing Properties of Ru(II) Bipyridine Complexes with 2,2'-Biimidazole-Like Ligand. *Dalton Trans.*, **2011**, *40*, *8218*-8225.
117. Mo, H.J.; Chao, H. Y.; Ye, B. H. A Ruthenium Biimidazole-Like Anion Receptor with Two Chelating NH···O Intramolecular Hydrogen Bonds. *Inorg. Chem. Commun.*, **2013**, *35*, 100-103.
118. Mardanya, S.; Karmakar, S.; Maity, D.; Baitalik, S. Ruthenium (II) and Osmium (II) Mixed Chelates Based on Pyrenyl-Pyridylimidazole and 2,2′-Bipyridine Ligands as Efficient DNA Intercalators and Anion Sensors. *Inorg. Chem.*, **2015**, *54*, 513-526.
119. Das, S.; Karmakar, S.; Mardanya, S.; Baitalik. Synthesis, Structural Characterization, and Multichannel Anion and Cation Sensing Studies of a Bifunctional Ru (II) Polypyridyl-Imidazole Based Receptor. *Dalton Trans.*, **2014**, *43*, 3767-3782.
120. Mondal, D.; Bar, M.; Mukherjee, S.; Baitalik, S. Design of Ru (II) Complexes Based on Anthraimidazoledione-Functionalized Terpyridine Ligand for Improvement of Room-Temperature Luminescence Characteristics and Recognition of Selective Anions: Experimental and DFT/TD-DFT Study. *Inorg. Chem.*, **2016**, *55*, 9707-9724.
121. de Silva, P. A.; Gunaratne, N. H.; McCoy, C. P. A Molecular Photoionic AND Gate Based on Fluorescent Signalling. *Nature*., **1993**, *364*, 42-44.
122. Biancardo, M.; Bignozzi, C.; Doyle, H.; Redmond Gareth. A Potential and Ion Switched Molecular Photonic Logic Gate. *Chem. Commun*., **2005**, 3918-3920.
123. Liu, Y.; Li, M.; Zhao, Q.; Wu, H.; Huang, K.; Li. F. Phosphorescent Iridium (III) Complex with an N^O Ligand as a Hg^{2+}-Selective Chemodosimeter and Logic Gate *Inorg. Chem.*, **2011**, *50*, 5969-5977.
124. Suresh, M.; Ghosh, A.; Das, A. A Simple Chemosensor for Hg^{2+} and Cu^{2+} that Works as a Molecular Keypad Lock. *ChemComm*., **2008**, *33*, 3906-3908.
125. Fang, C. J.; Zhu, Z.; Sun, W.; Xu, C. H.; Yan, C. H. New TTF Derivatives: Several Molecular Logic Gates Based on Their Switchable Fluorescent Emissions. *New J. Chem.*, **2007**, *31*, 580-586.

126. Cui, B. B.; Tang, J. H.; Yao, J.; Zhong, Y. W. A Molecular Platform for Multistate Near-Infrared Electrochromism and Flip-Flop, Flip-Flap-Flop, and Ternary Memory. *Angew. Chem. Int. Ed*., **2015**, *54*, 9192-9197.
127. Deb, S.; Sahoo, A.; Mondal, P.; Baitalik, S. Analysis and Prediction of Anion-and Temperature Responsive Behaviours of Luminescent Ru (II)-Terpyridine Complexes by using Boolean, Fuzzy Logic, Artificial Neural Network and Adapted Neuro Fuzzy Inference Models. *Dalton Trans*., **2022**, *51*, 15601-15613.
128. Gentili, P. L. The Fundamental Fuzzy Logic Operators and Some Complex Boolean Logic Circuits Implemented by the Chromogenism of a Spirooxazine. *Phys. Chem. Chem. Phys*., **2011**, *13*, 20335-20344.
129. Sahu, S.; Sil, T. B.; Das, M.; Krishnamoorthy, G. A Single Fluorophore to Address Multiple Logic Gates. *Analyst*., **2015**, *140*, 6114-6123.
130. Deb, S.; Sahoo, A.; Baitalik, S. Harnessing Deep Neural Networks to Analyze Multi-Channel Anion Sensing Characteristics of a Ru (II)-Pyrazolyl-Bis (Benzimidazole) Complex. *Eur. J. Inorg. Chem*., **2023**, *26*, e202300009.

****

2.1. Introduction

Design of artificial antennae systems having the potential to harvest light over a large extent of visible spectrum is now a vibrant area of contemporary research.[1-10] A wide range of molecular ensembles incorporating porphyrins, metalloporphyrins as well as transition metal complexes have been designed for this purpose.[11-20] Low-spin d^6 metal complexes based on polyheterocyclic ligands were extensively investigated in this regard because of their outstanding photo-redox behaviors which in turn could be modulated systematically either via synthetic maneuvering or under the influence of external stimuli.[21-29] Among the most widely investigated complexes, particularly popular are ruthenium complexes derived from bipyridine (bpy) or phenanthroline (phen)-type of ligands. Majority of the complexes of this sort (such as $[Ru(bpy)_3]^{2+}$) absorb a substantial domain of the visible spectrum, possess long-lived excited states (>1μs), are stable following one-electron oxidation and reduction, and exhibit good photochemical stability. The equilibrated excited state of these complexes has been assigned as metal-to-ligand charge transfer (MLCT) state.[30-41] These complexes have already exhibit their efficacy in diverse applications involving dye sensitized solar cells, molecular-level machines, and multichannel optical sensors and switches.[42-52] Multimetallic complexes derived from appropriate bridging ligands are also of particular interest in the context of direction flow of energy and/or electron from one site of coordination to the other across the bridge. This can be achieved either through structural and electronic modification of the bridging ligand or by varying the metal centers and often can be visualized by examining their emission spectral characteristics. In addition to their strong absorbtivity and long-lived excited states, the polynuclear complexes also act as electron reservoirs for multiple electron transfer processes.[53,54] Hence, the features associated with bridging ligands such as length, rigidity, topology, conjugation and charge play crucial roles in constructing multimetallic complex architectures with desirable photo-redox behaviors.

Our objective in this work is to construct multi-metallic light harvesting chromophores based on ruthenium(II) metal as well as to investigate systematic alteration of the photo-redox behavior of the complex entity upon sequential incorporation of Ru^{2+} unit in the complex architecture. In order to achieve our objective, we designed herein a polypyridyl-imidazole based bridging ligand (**phen-H_2PhImz-bpy**) wherein a 1,10-

phenanthroline moiety is covalently coupled with 2-(4-(pyridine-2-yl)-1*H*-imidazole-5-yl)pyridine unit via phenyl-imidazole spacer (**Chart 2.1**). The bridge can offer a

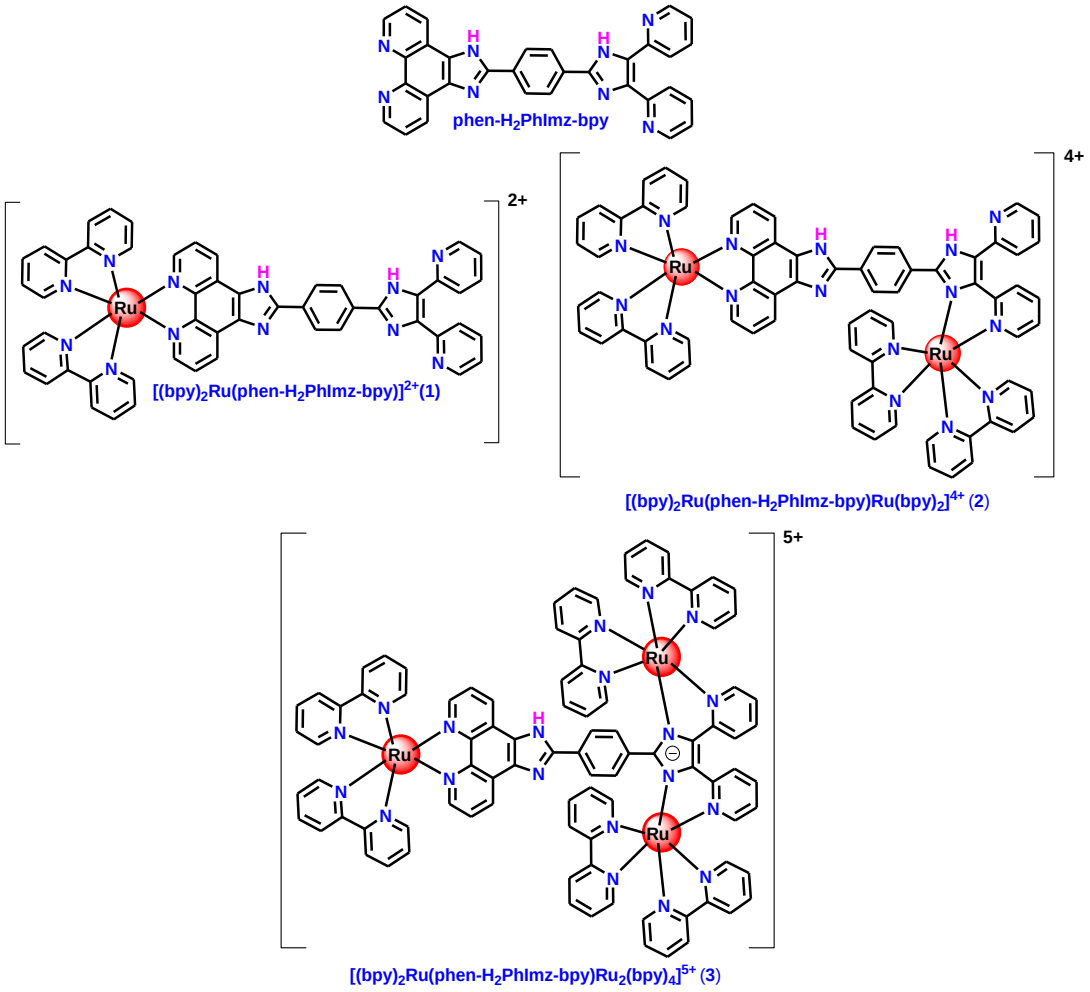

Chart 2.1. The structures of the bridging ligand and complexes.

maximum of three bidentate coordinating units situated in stereochemically distinct positions. The bridging ligand is employed here to synthesize mono-, bi-, as well as trimetallic Ru(II) complexes in combination with terminal bipyridine units as shown in Chart 2.1. Following synthesis, all the complexes have been thoroughly characterized by standard analytical tools and spectroscopic techniques. The physicochemical properties of the bridge as well as the Ru(II) complexes have been thoroughly investigated in this work via absorption, steady state and time-resolved emission spectroscopy as well as by cyclic voltammetry. The study is primarily aimed at exploration of structure-property relationships for electronic, photophysical and electrochemical characteristics in the

complexes. The main focus is concentrated on systematic modulation of MLCT absorption, emission as well as redox behavior of the complex entity upon gradual incorporation of Ru^{2+} unit in the complex backbone. In reality, sequential incorporation of Ru^{2+} metal in the bridging unit induced systematic change in the photo-redox behavior across the complex series. Accomplishment of well-defined structure-property relationship will lead to intelligent design of the complexes which are capable to absorb and emit light in required spectral domain which in turn could be useful to serve as potential building blocks in the context of light harvesting applications.

2.2. Experimental Section

2.2.1. Materials. Ruthenium trichloride ($RuCl_3 \cdot xH_2O$), terephaldehyde, 2,2′-bipyridine, 1,10-phenanthroline, 2,2′-pyridil and the solvents were purchased from Merck. *Cis*-$[Ru(bpy)_2Cl_2]\cdot 2H_2O$ was prepared following literature procedure.[55]

2.2.2. Synthesis of the Bridging Ligand. 2-(4-(4,5-di(pyridine-2-yl)-1*H*-imidazole-2-yl)phenyl)-1*H*-imidazo[4,5-*f*][1,10]phenanthroline (phen-H_2PhImz-bpy). A mixture of 4-(1*H*-imidazo[4,5-*f*][1,10]phenanthrolin-2-yl)benzaldehyde (0.32 g, 1.0 mmol), 2,2′-pyridil (0.21 g, 1.0 mmol), and ammonium acetate (2.3 g, 0.03 mol) were taken in acetic acid (25 mL) and was refluxed for 2h. The resulting solution upon pouring on crushed ice produces a yellow colored precipitate which was filtered and washed thoroughly with water. The compound was purified upon recrystallization from a methanol-chloroform (1:1, v/v) mixture and the desired compound was collected as microcrystalline yellow solid (198 mg, yield 40%), mp >300 °C. Anal. Calcd. for $C_{32}H_{20}N_8$: C, 74.23; H, 3.89; N, 21.65. Found: C, 74.18; H, 3.91; N, 21.61. ^{1}H NMR (300 MHz, DMSO-d_6, δ/ppm): 13.82 (s, 1H, imidazole NH), 8.78 (d, 2H, *J*=3.9 Hz, $2H_1$), 8.74 (d, 4H, *J*=6.0 Hz, $2H_6$+$2H_3$), 8.14-8.24 (m, 4H, $2H_8$+$2H_9$), 7.88 (m, 4H, $2H_4$+H_5), 7.69-7.73 (m, 2H, $2H_7$), 7.61 (t, 2H, *J*=6.0 Hz, $2H_2$), ESI-MS (positive, CH_3CN) *m/z* = 517.26 (100 %) [(phen-H_2PhImz-bpy)+H^+].

2.2.3. Synthesis of the Metal Complexes. The complexes were prepared under oxygen and moisture free dinitrogen using standard Schlenk techniques.

$[(bpy)_2Ru(phen\text{-}H_2PhImz\text{-}bpy)](ClO_4)_2\cdot H_2O$ (1). $[Ru(bpy)_2Cl_2]\cdot 2H_2O$ (0.52 g, 1.0 mmol) was dispersed in 30 mL of ethanol and solid $AgClO_4$ (0.45 g, 2.1 mmol) was

added to it and refluxed for 1h with continuous stirring under argon protection. The white precipitate of AgCl that formed was filtered quickly and to the filtrate containing $[Ru(bpy)_2(EtOH)_2]^{2+}$ was added solid powder of the bridging ligand (H_2L) (0.52 g, 1.0 mmol) and refluxed for 6h, during which time the color changed from red-violet to orange-yellow. The solid compound that was formed during the process was collected by filtration and purified through column chromatography (silica gel) using a mixture of acetonitrile-toluene (1:1, v/v) as the eluent. Upon evaporating the major fraction of the eluent to a small volume (~10 mL), an orange-red compound was obtained which was further purified upon recrystallization from acetonitrile-methanol (1:2 v/v) mixture in the presence of feebly acidic condition (2 drops of 10^{-4} M aqueous $HClO_4$). Yield: 85 mg (43%). Anal. Calcd. for $C_{52}H_{38}N_{12}Cl_2O_9Ru$: C, 54.43; H, 3.34; N, 14.65. Found: C, 54.39; H, 3.32; N, 14.60. ^{1}H NMR (400 MHz, DMSO-d_6, δ/ppm): 14.50 and 14.35 (s, 2H, NH imidazole), 9.13 (d, 3H, J=8.0Hz,3$H_{3''}$), 8.88-8.82 (m, 5H, $H_{3''}$+2H_1+2H_6), 8.53 (t, 4H, J=8.0 Hz, 4$H_{4'}$), 8.21 (t, 3H, J=8.0 Hz, 2H_3+$H_{6'}$), 8.12-8.07 (m, 6H, 3$H_{6'}$+2H_8+H_9), 7.95 (t, 2H, J=8.40 Hz, H_9+H_5) 7.84 (d, 3H, J=5.2Hz, H_5+2H_4), 7.62-7.57 (m, 5H, 2H_7+2H_2+$H_{5'}$), 7.34 (t, 3H, J=6.4 Hz, 3$H_{5'}$), ESI-MS (positive, CH_3CN) $[(bpy)_2Ru(phen\text{-}H_2PhImz\text{-}bpy)]^{3+}$ (m/z=310.45), $[(bpy)_2Ru(phen\text{-}H_2PhImz\text{-}bpy)]^{2+}$ (m/z=465.08) and $[(bpy)_2Ru(phen\text{-}H_2PhImz\text{-}bpy)]^{+}$ (m/z = 929.54).

$[(bpy)_2Ru(phen\text{-}H_2PhImz\text{-}bpy)Ru(bpy)_2](ClO_4)_4\cdot 2H_2O$ (2). Finely powered form of complex **1** (0.20 g, 0.11 mmol) was dispersed in 30 mL of ethanol and solvated ruthenium(II) precursor complex, $[Ru(bpy)_2(EtOH)_2]^{2+}$ (obtained upon stoichiometric reaction between $[Ru(bpy)_2Cl_2]^{2+}$ and $AgClO_4$ in ethanol) was added to it and the resulting mixture was refluxed in slightly acidic condition under argon protection for 8h. On cooling down to room temperature, an intense red colored precipitate formed which was collected by filtration. The precipitate was dissolved in small amount of acetonitrile and then loaded into a silica gel column and eluted with solvents with different polarities. The principal fraction on rotary evaporation to a small volume (~5 mL) gives rise to the desired product. Further purification was achieved upon recrystallization from an acetonitrile-methanol (1:1, v/v) mixture in the presence of slightly acidic condition (2 drops of aqueous 10^{-4} M $HClO_4$). (Yield 90 mg 58%). Anal. Calcd. for $C_{72}H_{56}N_{16}Cl_4O_{18}Ru_2$: C, 48.63; H, 3.17; N, 12.60. Found: C, 48.53; H, 3.13; N, 12.55. ^{1}H NMR

(400 MHz, DMSO-d_6, δ/ppm): 14.40 and 14.21 (s, 2H, NH imidazole), 9.08 (d, 2H, *J*=8.4Hz, $2H_{3''}$), 8.88-8.82 (m, 9H, $6H_{3''}+2H_1+2H_6$), 8.69 (d, 1H, *J*=7.6 Hz, H_6), 8.64 (d, 1H, *J*=8.0 Hz, H_3), 8.31 (s, 1H, H_3), 8.23 (t, 3H, *J*=7.8 Hz, $3H_{4'}$), 8.11-8.00 (m, 5H, $3H_{4'}+2H_{6'}$), 7.99-7.90 (m, 2H, $2H_{4'}$), 7.85 (d, 4H, *J*=5.6 Hz, $2H_4+2H_5$), 7.72-7.69 (t, 2H, *J*=6.2 Hz, $2H_8$), 7.59 (d, 8H, *J*=4 Hz, $2H_2+4H_{6'}+2H_9$), 7.52 (t, 3H, *J*=8.2 Hz, $H_{6'}+2H_7$), 7.40 (t, 1H, *J*=6.8 Hz, $H_{5'}$), 7.35 (t, 6H, *J*=6.0 Hz, $5H_{5'}+H_{6'}$), 7.28 (t, 2H, *J*=7.6 Hz, $2H_{5'}$), ESI-MS (positive, CH_3CN) $[(bpy)_2Ru(phen\text{-}H_2PhImz\text{-}bpy)Ru(bpy)_2]^{4+}$ (m/z=335.86), $[(bpy)_2Ru(phen\text{-}H_2PhImz\text{-}bpy)Ru(bpy)_2]^{3+}$ (m/z = 447.81) and $[(bpy)_2Ru(phen\text{-}H_2PhImz\text{-}bpy)Ru(bpy)_2]^{2+}$ (m/z = 670.72).

$[(bpy)_2Ru(phen\text{-}HPhImz\text{-}bpy)Ru_2(bpy)_4](ClO_4)_5\cdot 4H_2O$ (3). $[Ru(bpy)_2(EtOH)_2]^{2+}$ and complex 2 (0.05 g, 0.10 mmol) were mixed in 1:1 molar ratio and the mixture was refluxed in presence of triethylamine (0.45g, 0.40 mmol) under argon protection for 8h. On reaching at room temperature, a red-violet compound that deposited was collected by filtration and purified by silica gel column eluting with acetonitrile-water (10:1, v/v) mixture. Upon removal of acetonitrile, the desired compound gets precipitated and filtered. The compound was again recrystallized from 1:1 (v/v) acetonitrile-water mixture. (Yield 78 mg 60%). Anal. Calcd. for $C_{92}H_{75}N_{20}Cl_5O_{24}Ru_3$: C, 47.50; H, 3.25; N, 12.04. Found: C, 47.45; H, 3.23; N, 11.99. ^{1}H NMR (400 MHz, DMSO-d_6, δ/ppm): 14.00 (s, 1H, NH imidazole), 9.25 (d, 2H, *J*=7.6Hz, $2H_{3''}$), 8.86-8.82 (m, 4H, $4H_{3''}$), 8.77 (t, 2H, *J*=7.8 Hz, $2H_1$), 8.62-8.58 (m, 7H, $6H_{3''}+H_6$), 8.49 (d, 1H, *J*=8.4 Hz, H_6), 8.29 (t, 1H, *J*=5.4 Hz, $H_{4'}$), 8.23-8.20 (t, 4H, *J*=7.4 Hz, $2H_3+2H_{4'}$), 8.11-8.05 (m, 13H, $9H_{4'}+2H_{6'}+2H_9$), 8.00-7.97 (m, 4H, $H_4+3H_{6'}$), 7.84 (d, 3H, *J*=6.0 Hz, H_4+2H_5), 7.73 (t, 1H, *J*=6.4 Hz, H_8), 7.60 (d, 6H, *J*=5.6 Hz, $6H_{6'}$), 7.50 (t, 7H, *J*=6.2 Hz, $2H_2+2H_{5'}+2H_7+H_8$), 7.35 (t, 7H, *J*=5.6 Hz, $6H_{5'}+H_{6'}$), 7.27 (t, 4H, *J*=6.4 Hz, $4H_{5'}$). ESI-MS (positive, CH_3CN) $[(bpy)_2Ru(phen\text{-}HPhImz\text{-}bpy)Ru_2(bpy)_4]^{4+}$ (m/z=438.78), $[(bpy)_2Ru(phen\text{-}HPhImz\text{-}bpy)Ru_2(bpy)_4]^{3+}$ (m/z= 618.13) and $[(bpy)_2Ru(phen\text{-}HPhImz\text{-}bpy)Ru_2(bpy)_4]^{2+}$ (m/z=977.88).

Alternative route for the synthesis of $[(bpy)_2Ru(phen\text{-}HPhImz\text{-}bpy)Ru_2(bpy)_4](ClO_4)_5\cdot 4H_2O$ (3). A mixture of $[Ru(bpy)_2(EtOH)_2]^{2+}$ (0.00 g, 0.75 mmol), powered phen-H_2PhImz-bpy ligand (0.15 g, 0.25 mmol) and triethylamine (0.05 g, 0.5 mmol) in 50 mL of ethanol-water (1:1) was refluxed for overnight under argon

protection. The resulting solution was filtered to remove unreacted ligand and suspended particle and the filtrate on gradual evaporation gives rise to a red-violet solid. The solid was filtered and successively purified through silica gel column chromatography and recrystallization techniques as mentioned earlier. Yield 145 mg (55%).

Caution! Perchlorate salts of the metal complexes are explosive and should be handled in small amount with extreme care.

2.2.4. Physical Measurements. Elemental analyses of the compounds were performed with a Vario-Micro V2.0.11 elemental (CHNSO) analyzer. NMR spectra were collected on a Bruker 400 MHz spectrometer in DMSO-d_6 for both the ligand and metal complexes. High resolution mass spectroscopy was performed on a Waters Xevo G2 QTOf mass spectrometer.

Electronic absorption spectra were obtained with a Shimadzu UV 1800 spectrophotometer at room temperature. Quartz cuvettes with a 1 cm path length and a 3 cm^3 volume were used for all measurements.

Emission spectra were recorded on Perkin-Elmer LS55 fluorescence spectrophotometer. The room temperature (298 K) spectra were obtained using a 1 cm path length quartz cell. For all measurements, same slit widths for excitation and emission were maintained. Quantum yields were determined in freeze–thaw–pump degassed solutions of the complexes by a relative method using $[Ru(bpy)_3]^{2+}$ in the same solvent as the standard. The quantum yields were calculated by using the equation (2),

$$\Phi_r = \Phi_{std} \frac{A_{std}}{A_r} \frac{I_r}{I_{std}} \frac{\eta_r^2}{\eta_{std}^2} \qquad (2)$$

where Φ_r and Φ_{std} are the quantum yields of unknown and standard samples at λ_{ex} = 450 nm, A_r and A_{std} (<0.1) are the solution absorbances at the excitation wavelength (λ_{ex}), I_r and I_{std} are the integrated emission intensities, and η_r and η_{std} are the refractive indices of the solvent. Experimental errors in the reported luminescence quantum yields were about 20%.

Time–correlated single–photon–counting (TCSPC) measurements were carried out to estimate the lifetime of the compounds. For TCSPC measurement, the

photoexcitation was made at 370 nm for the bridging ligand and 440 nm for the Ru(II) complexes using a picoseconds diode laser (IBH Nanoled–07) in an IBH Fluorocube apparatus. The fluorescence decay data were collected on a Hamamatsu MCP photomultiplier (R3809) and were analyzed by using IBH DAS6 software.

The electrochemical measurements were carried out with a BAS 100B electrochemistry system. A three–electrode assembly (BAS) comprising a Pt (for oxidation) or glassy carbon (for reduction) working electrode, Pt auxiliary electrode, and an aqueous Ag/AgCl reference electrode was used. The cyclic voltammetric (CV) and square wave voltammetric (SWV) measurements were carried out at 25°C in acetonitrile solution of the complex (*ca.* 1 mmol dm^{-3}) and the concentration of the supporting electrolyte (TEAP) was maintained at 0.1 mol dm^{-3}. The potentials recorded were automatically compensated to *iR* drop in the cell. All of the potentials reported in this study were referenced against the Ag/AgCl electrode, which under the given experimental conditions gave a value of 0.36 V for the ferrocene/ferrocenium couple.

Experimental uncertainties were as follows: absorption maxima, ±2 nm; molar absorption coefficients, 10%; emission maxima, ±5 nm; excited–state lifetimes, 10%; luminescence quantum yields, 20%; redox potentials, ±10 mV.

2.3. Results and Discussion

2.3.1. Ligand Synthesis. The precursor, 4-(1*H*-imidazo[4,5-*f*][1,10] phenanthrolin-2-yl)benzaldehyde was obtained initially upon refluxing 1:1 molar ratio of terephthaldehyde and 1,10-phenanthroline-5,6-dione in CH_3COOH and NH_4OAc media. The said precursor upon treatment with 2,2'-pyridil in 1:1 molar ratio under the same reaction condition gives rise to the desired ligand in appreciable yield. The compounds are purified by column chromatography and recrystallization techniques.

2.3.2. Complex Synthesis. The procedure that is adopted for the synthesis of mono, bi-, and trinuclear Ru(II) complexes are sketched in Scheme 2.1. The use of solvated Ru(II) precursor, $[(bpy)_2Ru(EtOH)_2]^{2+}$ is advantageous over *cis*-$[(bpy)_2RuCl_2]$ itself in terms of both reaction time and yield. The key mononuclear complex is obtained in reasonably good yield upon treating $[(bpy)_2Ru(EtOH)_2]^{2+}$ with excess bridging ligand, phen-H_2PhImz-bpy in refluxing ethanol and purified through column chromatography

and recrystallization. The mononuclear complex (**1**) possess a vacant bipyridine-type coordination motif which on treatment with $[(bpy)_2Ru(EtOH)_2]^{2+}$ under slightly acidic condition produces binuclear complex (**2**). Acidic condition is maintained during the course of the reaction to arrest the dissociation of imidazole NH proton in the pyridyl-imidazole unit which became sufficiently acidic upon coordination to the Ru(II) centers. The binuclear complex (**2**) upon removal of the said imidazole NH proton again provides a pyridyl-imidazolate type of coordination motif. Thus, the trinuclear complex (**3**) can easily be prepared upon treating **2** with $[(bpy)_2Ru(EtOH)_2]^{2+}$ in basic condition. Trinuclear complex can also be directly prepared from the bridging ligand upon treating with little excess of three equivalents of $[(bpy)_2Ru(EtOH)_2]^{2+}$ under basic condition. All the complexes are purified through the use of column chromatography and recrystallization techniques and thoroughly characterized.

2.3.3 Mass Spectra. All the complexes are characterized through ESI mass spectrometry. Experimental spectra together with simulated isotopic patterns of the complexes are displayed in Figure 2.1. Each spectrum consists of many informative peaks and the correlation between experimentally observed and calculated isotopic pattern is very good. ESI mass spectrum of the mononuclear complex (**1**) displays three abundant peaks at m/z = 310.45, 465.08 and 929.54. The peak at m/z = 929.54 corresponds to the mono-positive ion of the type $[(bpy)_2Ru(phen\text{-}H_2PhImz\text{-}bpy)]^{+}$, another one at m/z = 465.08 corresponds to the bi-positive ion of the type $[(bpy)_2Ru(phen\text{-}H_2PhImz\text{-}bpy)]^{2+}$ (100%), while the remaining peak at m/z = 310.45 is due to tri-positive cation of the form $[(bpy)_2Ru(phen\text{-}H_3PhImz\text{-}bpy)]^{3+}$ (100%). The presence of tri-positive cation indicates the protonation of one of the imidazole nitrogen atoms in phen-H_2PhImz-bpy bridging unit. The binuclear complex (**2**) also exhibits three abundant peaks at m/z =335.86, 447.81 and 670.72 corresponding to $[(bpy)_2Ru(phen\text{-}H_2PhImz\text{-}bpy)\ Ru(bpy)_2]^{4+}$ (100%), $[(bpy)_2Ru(phen\text{-}HPhImz\text{-}bpy)Ru(bpy)_2]^{3+}$ (100%), and $[(bpy)_2Ru(phen\text{-}PhImz\text{-}bpy)Ru\ (bpy)_2]^{2+}$ species, respectively (Figure 2.1). The trinuclear complex (**3**) again displays three abundant peaks with their maximum at m/z = 438.78, 618.13, and 977.88, confirming the presence $[(bpy)_2Ru(phen\text{-}PhImz\text{-}bpy)Ru_2(bpy)_4]^{4+}$ (100%), $[(bpy)_2Ru(phen\text{-}PhImz\text{-}bpy)Ru_2(bpy)_4(ClO_4)]^{3+}$ (100%) and $[(bpy)_2Ru(phen\text{-}PhImz\text{-}bpy)Ru_2(bpy)_4(ClO_4)_2]^{3+}$ (100%) cations, respectively (Figure 2.1). It is

observed that many of the fragmented ions in bi- and tri-nuclear complexes display successive loss of imidazole NH proton and/or counter perchlorate ion keeping the main complex core intact and therefore assignments of the peaks became easier. As already observed, the correspondence between observed and simulated isotopic patterns is very good for all the complexes.

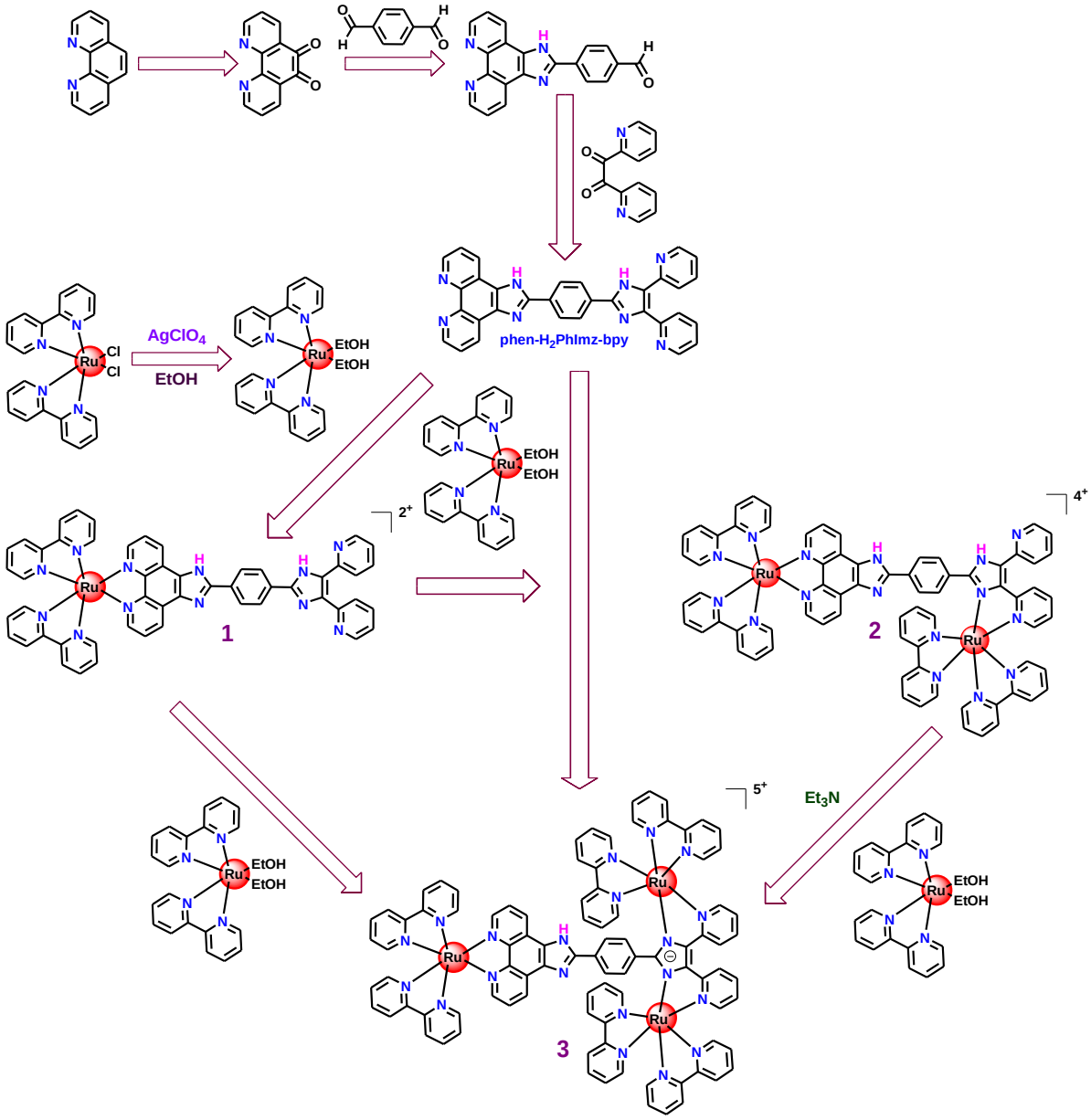

Scheme 2.1. Synthesis of bridging ligand and different Ru(II) complexes.

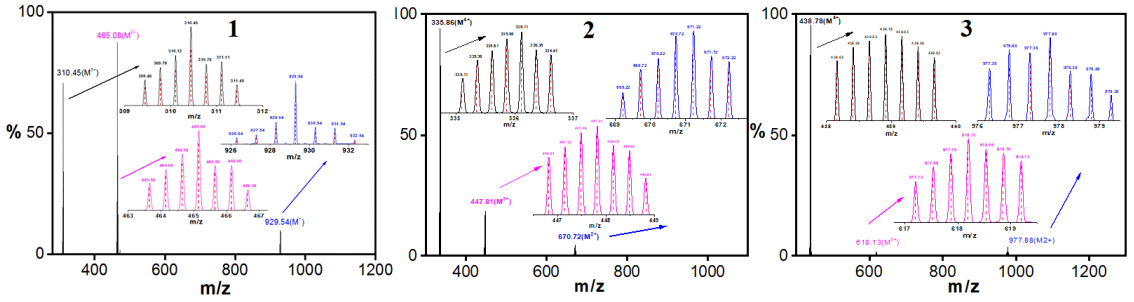

Figure 2.1. ESI (positive) mass spectrum for the complex cations of **1-3** in MeCN showing both observed and simulated isotopic distribution patterns.

2.3.4 Proton NMR Spectra. ^{1}H NMR spectra of the compounds (phen-H_2PhImz-bpy ligand as well as all three Ru(II) complexes) were acquired in DMSO-d_6 and presented in Figure 2.2. The spectra, in general, display complicated pattern due to appearance of large number of signals within the aromatic region. In addition, substantial overlaps also occur among them. In spite of their complex nature, all the peaks in the spectra were tentatively assigned with the help of their {^{1}H–^{1}H} COSY NMR spectra as well as by comparing the spectra of related Ru(II) complexes. Proton numbering scheme along with their assignment are also presented in Figure 2.2. The protons associated with bpy unit in the complexes are tentatively assigned by taking into account the chemical shift order of H_3> H_4 ≥ H_5> H_6. Furthermore, H_3 and H_6 are usually appeared as doublets, while H_4 and H_5 appeared either as triplet or doublet of doublet. The values of coupling constant among the different protons are $J_{3,4}$ and $J_{4,5}$ ≈ 8 Hz, $J_{5,6}$ ≈ 5 Hz, and $J_{3,5}$ and $J_{4,6}$ ≈ 1.2 Hz.[56, 57] Phen- H_2PhImz-bpy ligand exhibits a peak at 13.8 ppm due to its imidazole NH protons. These said NH signals shift towards down-field region upon complexation as shown in Figure 2.2.

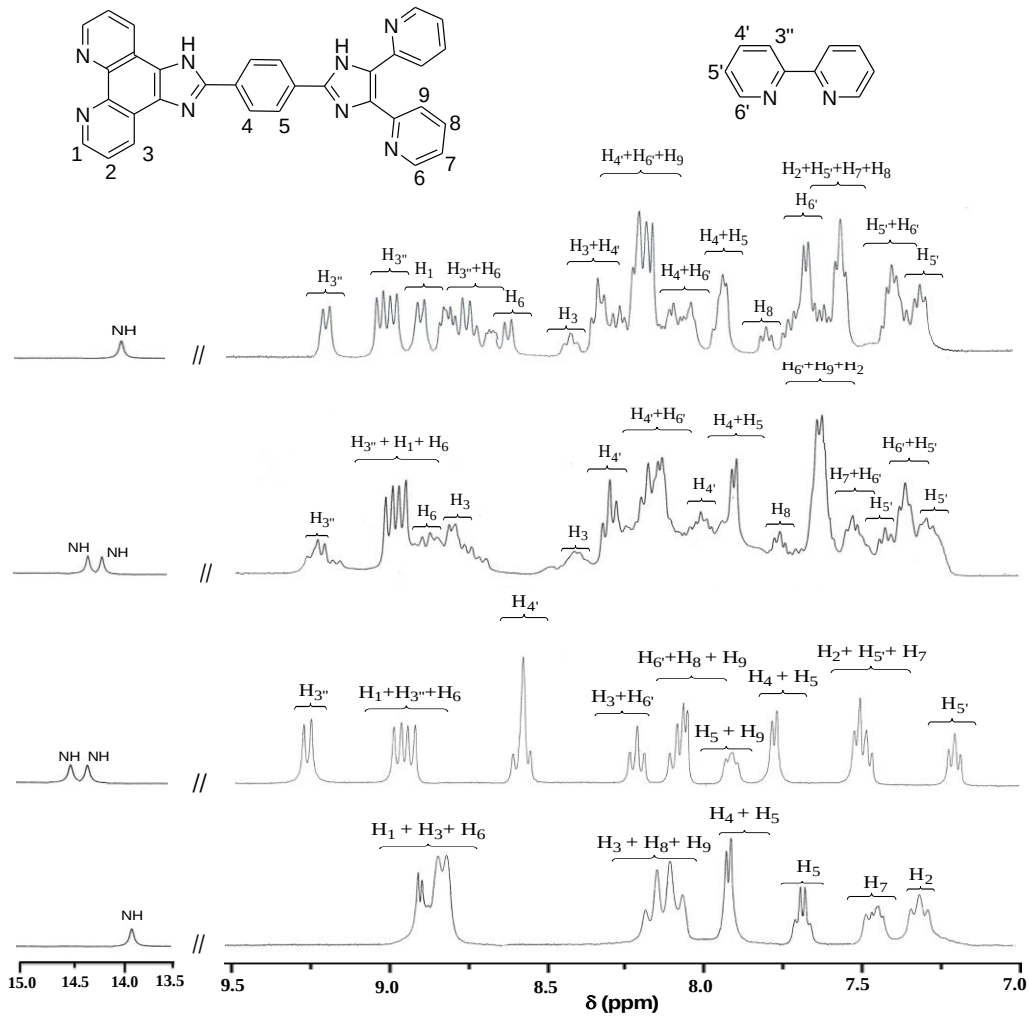

Figure 2.2. ^{1}H NMR spectra of the ligand (phen-H_2PhImz-bpy) and complexes **1**-**3** in DMSO-d_6.

2.3.5 UV-Vis Absorption Spectra. Absorption spectrum of the bridging ligand is recorded in DMSO (Figure 2.3a), while the spectra of the complexes are acquired in three different solvents (MeCN, DMSO, and H_2O) and displayed in Figure 2.4. The spectral data are provided in Table 2.1. The spectra of the complexes consist of three principal absorption features. The absorptions below 300 nm are mainly ligand-centered $\pi \rightarrow \pi^*$ transitions, at ~350 nm corresponds to intra-ligand charge transfer (ILCT) transition, while above 400 nm in the visible domain are due to metal-to-ligand charge transfer (MLCT) absorptions.

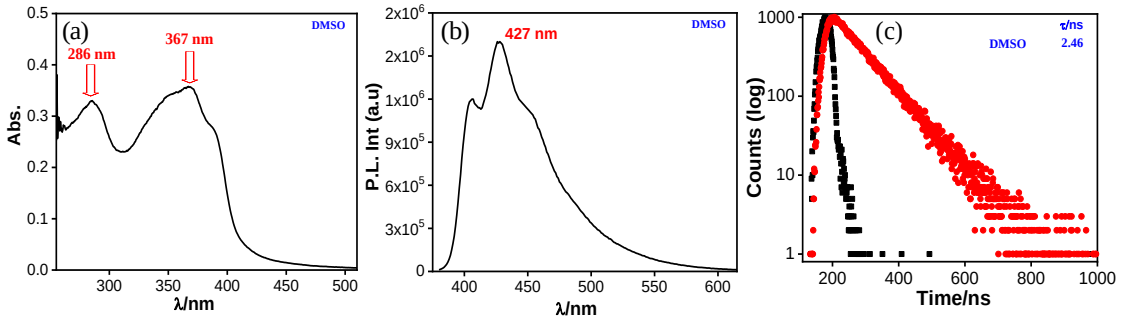

Figure 2.3. UV-vis absorption (a) and emission (λ_{ex}=367 nm) (b) spectrum of phen-H_2PhImz-bpy ligand in DMSO. (c) Excited state decay profile following pulsed excitation with 370 nm NanoLED. Inset shows the lifetime value.

2.3.6 Emission Spectra. The bridging ligand displays structured emission in DMSO upon excitation at 367 nm (Figure 2.3b) having lifetime of 2.46 ns (Figure 2.3c), while the complexes exhibit broad emission band upon excitation at their ^{1}MLCT absorption band(s) at room temperature in all three studied solvents (MeCN, DMSO, and H_2O) {Figure 2.4d-f}. The relevant spectral data are listed in Table 2.1. Emission in all three complexes arises due to radiative deactivation of their lowest ^{3}MLCT excited states that generates following rapid intersystem crossing from ^{1}MLCT excited states upon absorption of light. The emission characteristics for this family of chromophores {such as $Ru(bpy)_3^{2+*}$} are also strongly influenced by non-radiative decay (k_{nr}) that induces the involvement of thermal population followed by very rapid non-radiative deactivation via low-lying ligand-field (^{3}MC) excited states. It is clearly observed that there is a gradual red-shift of the emission maximum with systematic incorporation of Ru^{2+}center onto the complex backbone in all three studied solvents (Table 2.1). The emission spectra of the complexes are also acquired at 77K in EtOH-MeOH (4:1, v/v) glass (Figure 2.5a). Substantial enhancement of emission intensity and quantum yield takes place for all the three complexes which is typical for the ^{3}MLCT emitters. In line with the spectra at RT, systematic red-shift of emission maximum also takes place at 77K upon sequential inclusion of the metal in the complex architecture. Zero-zero spectroscopic energy (E_{00}) of the complexes is determined from their 77K emission maxima. The spectra display

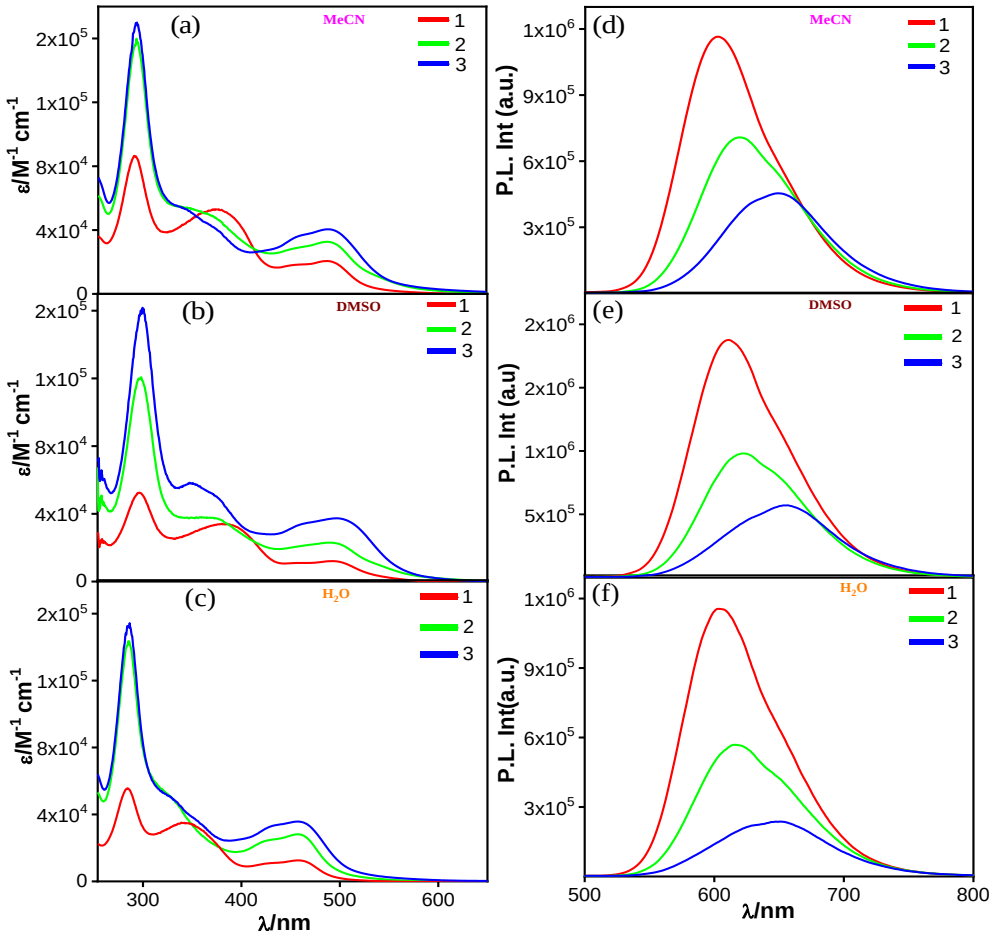

Figure 2.4. UV-vis absorption (a-c) and emission (λ_{ex}=461 nm) (d-f) spectra of **1**-**3** in MeCN, DMSO and H_2O.

vibrational progression with separation of 1135 cm^{-1} for complex **1**, 1152 cm^{-1} for complex **2** and 1178 cm^{-1} for complex **3**, indicating aromatic stretching vibration of ligand (Figure 2.6). Emission lifetime measurements are carried out by time-correlated single photon counting (TCSPC) method following excitation at 444 nm. The decay profiles of the complexes in different solvents are presented in Figure 2.7. The lifetime of the complexes depends heavily on the nature of the solvents and in general it is observed that the lifetime of the complexes increases substantially upon passing from MeCN→DMSO→H_2O. On the other hand, the lifetime is found to decrease (with few exceptions) gradually on passing from monomer→dimer→trimer.

Table 2.1. Photophysical Data of Complexes **1-3**.

Com -plex		Absorption λ_{max}/ nm (ε,$M^{-1}cm^{-1}$)	Luminescence				
			λ_{max} / nm	τ/ ns	Φ	k_r/s^{-1}	k_{nr}, $/s^{-1}$
1	**MeCN (298K)**	461(21000),428(br) (19200),385(sh)(39400),360 (54200),287(88000),240(466 00)	604	τ=150	1.42×10^{-2}	9.5×10^{4}	6.6×10^{6}
2		460(33500),430(br) (30150),356(sh)(50300),288 (159200),244(70300)	620	τ_1=54.3 (17%) τ_2=124.2 (83%)	1.15×10^{-2}		
3		460(41100),430(br)(36400), 360(sh)(41000), 331(sh)(53500),289(170000)	655	τ=92	8.43×10^{-3}	9.1×10^{4}	1.1×10^{7}
1	**DMSO (298K)**	466(12300),372 (34680),290(52600)	613	τ=445	3.1×10^{-2}	6.9×10^{4}	2.1×10^{6}
2		467(23200),360(sh)(37100), 291(120200)	622	τ=412	2.5×10^{-2}	6.1×10^{4}	2.3×10^{6}
3		469(37500),432(br)(33900), 360(sh)(49300),336 (58400),291(161000)	660	τ=186	1.07×10^{-2}	5.7×10^{4}	5.3×10^{6}
1	**H_2O (298K)**	462(13400),428(br)(11800), 346(36100),284(56100)	605	τ=496	2.1×10^{-2}	4.1×10^{4}	1.9×10^{6}
2		460(29300),422(br)(25500), 332(sh)(49500),286(143200)	617	τ_1=164 (66%) τ_2=425 (34%)	1.35×10^{-2}		
3		461(36600),427(br)(33200), 355(sh)(36300),329(sh)(502 00),285(153400)	651	τ_1=127 (76%) τ_2=353 (24%)	5.1×10^{-3}		
1	**EtOH-MeOH (4:1) (77K)**		574	7.42µs	0.036	4.8×10^{3}	1.3×10^{5}
2			594	6.11µs	0.035	5.7×10^{3}	1.5×10^{5}
3			623	3.58 µs	0.038	1.0×10^{4}	2.7×10^{5}

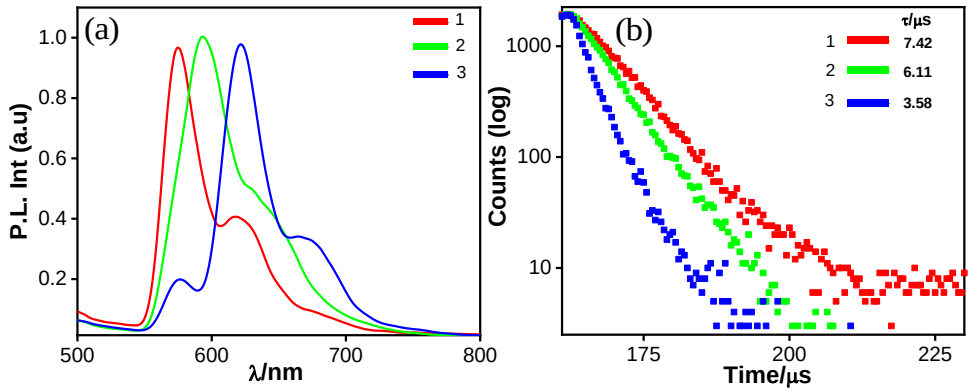

Figure 2.5. Normalized emission spectra (λ_{ex}=460 nm) (a) and excited state decay profiles following pulsed excitation with 450 nm NanoLED of **1-3** in EtOH-MeOH (4:1, v/v) glass at 77 K. The inset to figure b indicates the lifetime values.

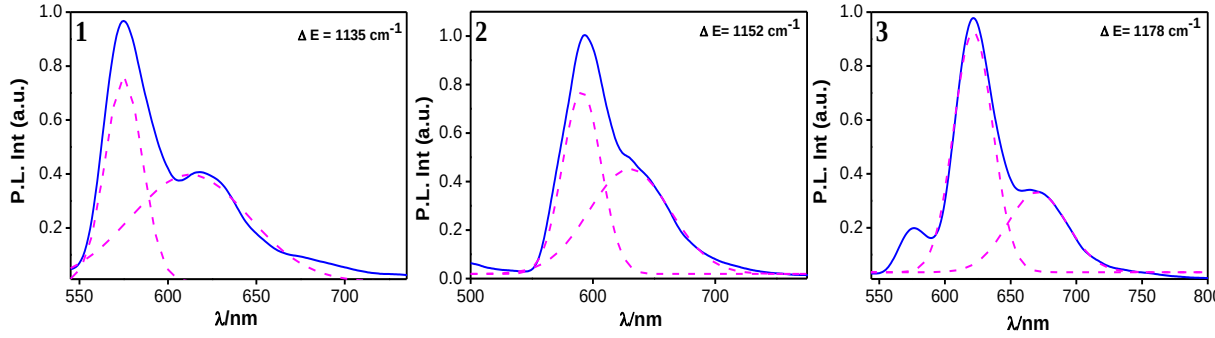

Figure 2.6. Experimental (solid line) and deconvoluted (dotted line) emission spectra of **1-3** in EtOH-MeOH (4:1 v/v) at 77K. The inset shows the values of vibrational spacing.

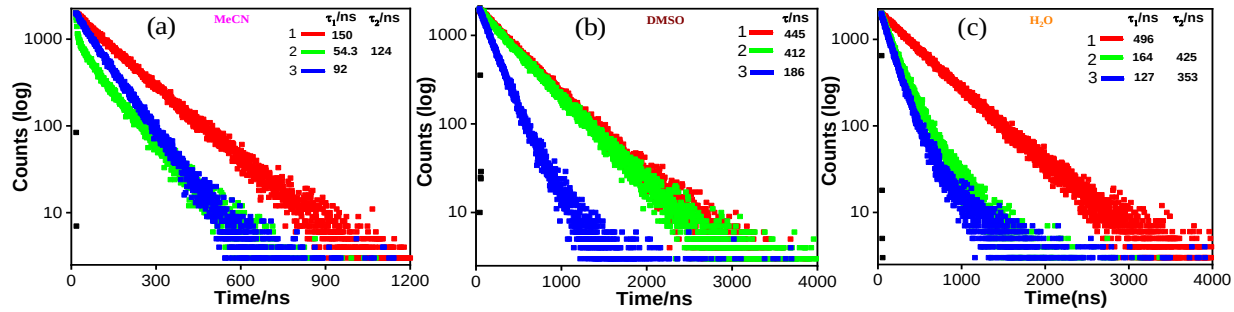

Figure 2.7. Decay cures of **1-3** upon excitation with 450 nm NanoLED in MeCN (a), DMSO (b), H_2O (c) at RT. The insets show the lifetimes.

2.3.7 Electrochemistry. The redox behaviors of **1-3** are studied in acetonitrile (0.1 M TEAP supporting electrolyte, TEAP=tetraethyl ammonium perchlorate) through cyclic voltammetry and pertinent electrochemical data are presented in Table 2.2. The

CVs of the complexes are displayed in Figure 2.8. The mononuclear complex (**1**) displays a reversible oxidation couple with $E_{1/2}$ = 1.40 V and four reversible/quasi-reversible/irreversible reduction waves in negative potential domain (0 to -2.0 V). Thus, the couple with $E_{1/2}$ = 1.40 V corresponds to $Ru^{3+/2+}$ oxidation process, while multiple couples in the negative potential window correspond to successive reductions of both bridging phen-HPhImz-phen-HPhImz-bpy and terminal bpy ligands. By comparing the $E_{1/2}$ value of 1.40 V for parent $[Ru(phen)_3]^{2+}$ in MeCN, it can be concluded that the Ru^{2+} ion coordinated to the phenanthroline (phen) coordinating motif of the bridging ligand is being oxidized in complex **1**. The binuclear complex (**2**), on the other hand, displays two successive reversible $Ru^{3+/2+}$ oxidations having $E_{1/2}$ values of 1.18 and 1.32 V with almost equal current height. It is anticipated that the Ru^{2+}-center coordinated to the bpy-type site of pyridyl-imidazole motif in phen-H_2PhImz-bpy bridge is oxidizing at lower potential, while that with higher potential is due to the Ru^{2+}-center coordinated to the phen site of

Table 2.2. Redox data[a] of **1-3** in MeCN.

Compounds	Oxidation[b] $E_{1/2}$(ox)/V	Reduction[c] $E_{1/2}$(red)/V
1	1.4	-1.3, -1.52, -1.9
2	1.18, 1.32	-1.40, -1.68, -1.93
3	1.05, 1.33	-1.42, -1.57, -1.82, -2.01

[a] The potentials are referenced against Ag/AgCl electrode with $E_{1/2}$ =0.36 V for the Fc/Fc^+ couple. [b] Reversible oxidation process in Pt working electrode. [c] $E_{1/2}$ values obtained by SWV with glassy carbon electrode.

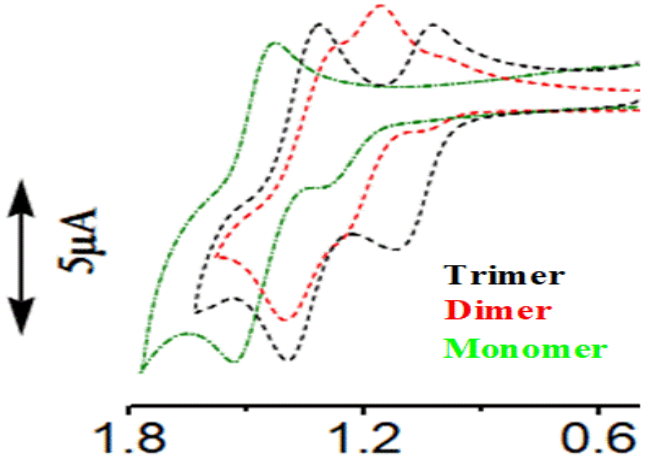

Figure 2.8. Overlay of CVs of **1-3** in acetonitrile showing oxidation in positive potential domain.

the bridge. Coordination of additional $Ru(bpy)_2^{2+}$ unit to the vacant bpy site of **1** lowers the LUMOs of phen-H_2PhImz-bpy bridge in **2**, thereby facilitates the shift of ligand-centered reductions to more positive potentials (Table 2.2). The trinuclear complex (**3**) also exhibits two consecutive reversible $Ru^{3+/2+}$ oxidations with $E_{1/2}$ values of 1.05 and 1.33 V. It is to be noted that current height of the peak at 1.33 V is almost double to that of 1.05 V. Thus, the couple with $E_{1/2}$ =1.33 V corresponds to simultaneous oxidations of two Ru^{2+} centers (one coordinated to phen- and another to bpy-type site of phen-H_2PhImz-bpy), while the couple with its $E_{1/2}$ value of 1.05 V most probably corresponds to the oxidation of Ru^{2+}-center coordinated to the pyridyl-imidazolate motif in the mono-deprotonated form of the bridging ligand (phen-HPhImz-bpy). The multiple quasi-reversible and/or irreversible waves that are observed in the negative potential domain for complex **3** are due to the reductions of coordinated phen-HPhImz-bpy bridging as well as terminal bpy ligands.

2.4 Discussions

The focus of investigation is concentrated on MLCT absorption, emission as well as the redox behavior of the complex entity with respect to gradual incorporation of Ru^{2+} unit in the complex backbone. Although the MLCT absorption maxima remain almost invariant, systematic augmentation of molar extinction coefficients occurs on passing across **1→2→3** in all the studied solvents (Figure 2.9). This is quite expected due to the additively of chromophoric units within the complex architecture. In contrast to absorption phenomena, gradual red-shift of the emission maximum together with decrease of Φ and τ takes place upon successive incorporation of the metal unit in the complex architecture. To this end, we plotted the emission energy (E_{max}), Φ and τ of the complexes as a function of number of Ru^{2+} unit in the complex backbone and reasonably good correlation is found in all three solvents (Figure 2.10). The plot of ln τ^{-1} *vs.* emission energy of the complexes in all three solvents is also presented in Figure 2.11. The plot indicates that diminution in lifetime with the number of metals incorporated in the bridging ligand is qualitatively correlated with energy gap law trend. It was demonstrated earlier that the Stokes shift could be thought of a crude estimate of nonradiative decay for conjugated organic frameworks. Systematic variation in Stokes shift with Φ and τ will guide us for tuning the electronic and vibrational (non-radiative relaxation) behaviors of

the complexes. Hence, we have measured the Stokes shift of the complexes by taking the difference of energy of their absorption and emission peak maximum in all three solvents and plotted the Φ and τ of the complexes as a function of their Stokes shifts (Figure 2.12). The graphs in Figure 2.12 clearly show good correlation between emission quantum yield/lifetime and Stokes shift. A linear fit to the data points is presented; the slope indicates the effect of the change of nuclearity in the complex architecture. The value of Stokes shift is found to increase systematically on passing across mononuclear→ binuclear→trinuclear. The argument that the Stokes shift is an estimate of the nonradiative decay rate could lead to the proposition that the complex with least Stokes shift would have the highest anticipated emission intensity/quantum yield, presuming the radiative rate being constant. The room temperature emission energies of complexes are also plotted as a function of their respective $\Delta E_{1/2}$ value ($\Delta E_{1/2}$ is the difference between the ground state $Ru^{3+/2+}$ oxidation and first ligand-based reduction potential) (Figure 2.13). Good linear correlation is observed in acetonitrile with systematic lowering of emission energy upon sequential incorporation of Ru^{2+} unit in the complex backbone. The band gap which could be defined as the difference between the first reduction and oxidation peaks of the complexes is also estimated from their redox data. Now, the band gap is plotted as function of number of metals in the complex architecture (Figure 2.13). A good linear correlation is observed with systematic decrease

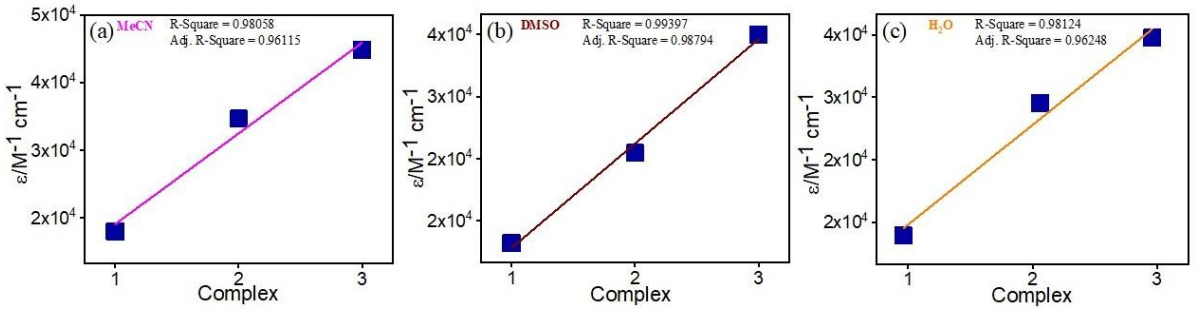

Figure 2.9. Variation of molar extinction coefficient (ε) with the nuclearity of the complexes in MeCN, DMSO and H_2O.

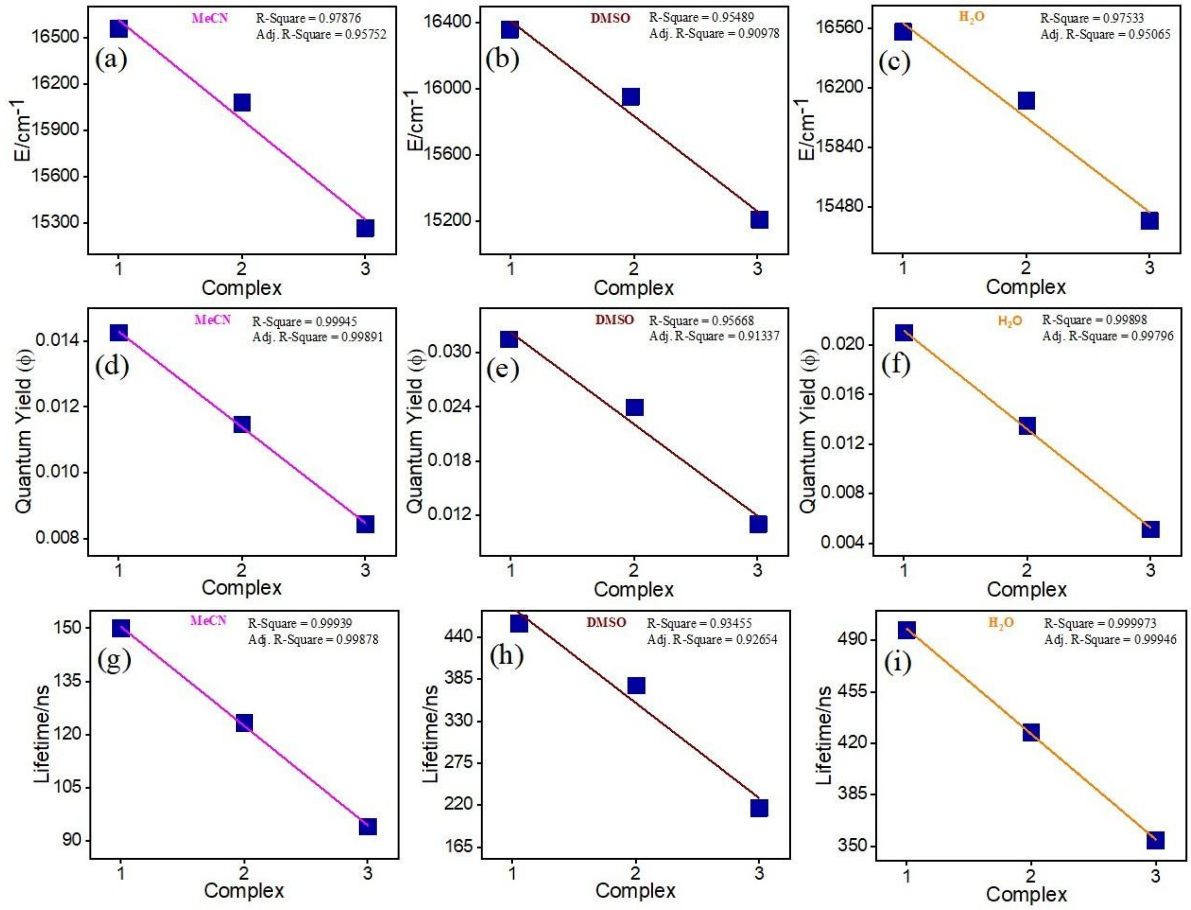

Figure 2.10. Plot of the emission energy (a-c), quantum yield (d-f) and lifetime (g-i) of the complexes as a function of number of Ru^{2+} unit.

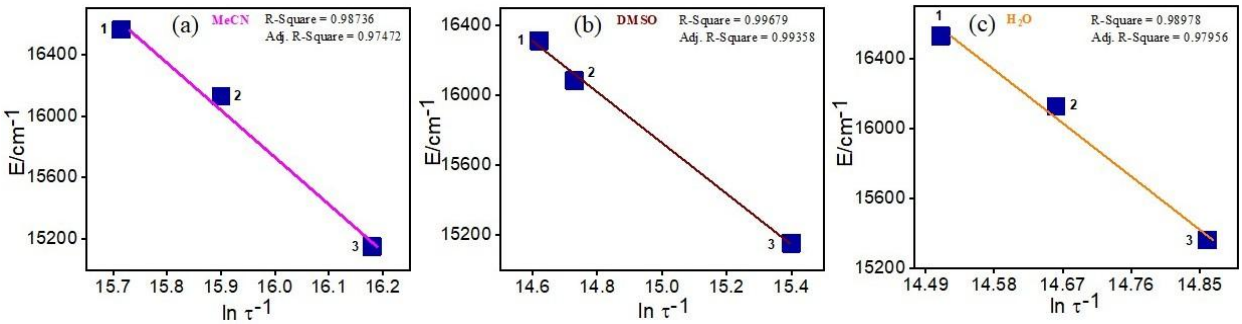

Figure 2.11. Plot of $\ln \tau^{-1}$ *vs.* emission energy of **1-3** in MeCN, DMSO and H_2O.

of band gap energy upon sequential incorporation metal in the complex architectures. It is to be noted that the energy gap law, equating the increase in the non-radiative rate as the band gap is reduced, is a common empirical guide as to the excited state dynamics of metal-based complexes.

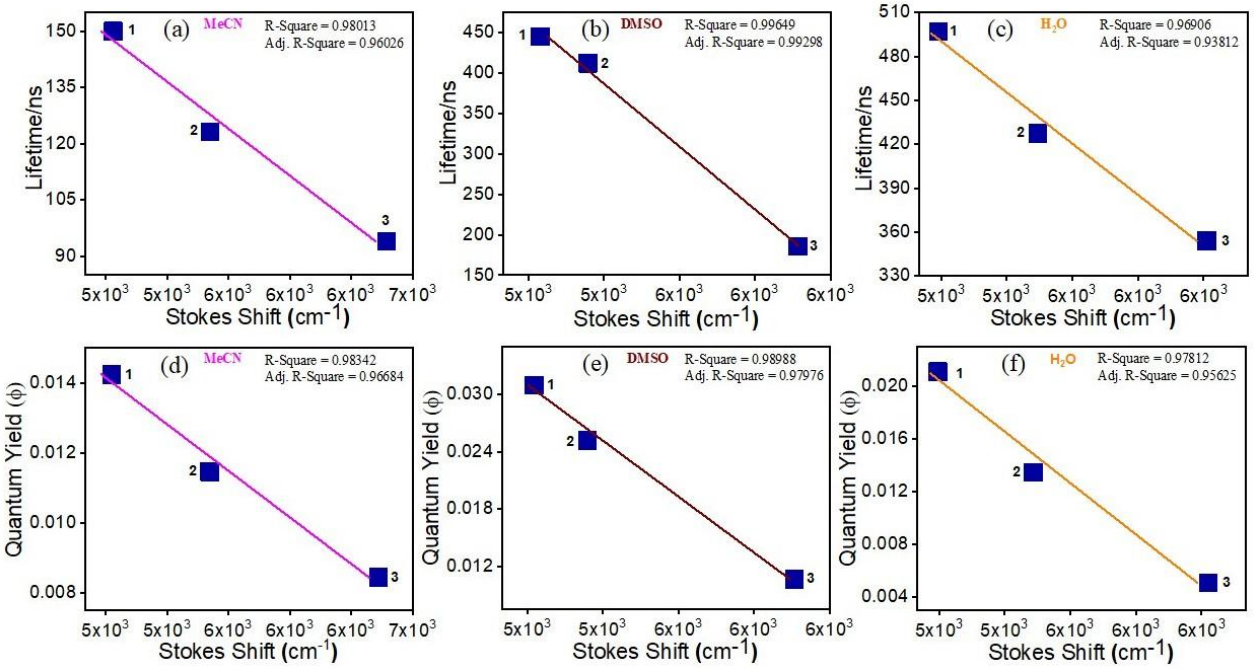

Figure 2.12. Plots of Stokes shift *vs.* lifetime (a-c) and emission quantum yield (d-e) of the complexes **1-3** in MeCN, DMSO and H_2O.

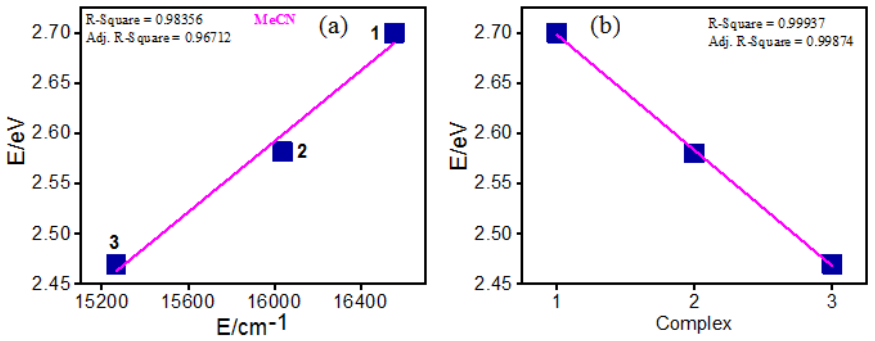

Figure 2.13. (a) Plot of emission energy of **1-3** ($\bar{\nu}_{em}$) as a function of their respective $\Delta E_{1/2}$ values in MeCN. (b) Band gap *vs.* number of Ru^{2+} unit in the complex architecture.

2.5. Conclusions

With regard to our desire for fabricating multi-metallic light harvesting chromophores, a polypyridyl-imidazole based bridging ligand having three bidentate coordinating sites has been designed and also utilized for the synthesis of monometallic, bimetallic as well as trimetallic Ru(II) complexes in combination with terminal bipyridine units. The focus of investigation is concentrated on systematic modulation of MLCT absorption, emission as well as redox behavior of the complex entity upon gradual incorporation of Ru^{2+} unit in the complex backbone. To this end, absorption and emission spectroscopic behaviors of

all the complexes have been thoroughly studied in three different solvents including water. Electrochemical characteristics of the complexes are investigated in acetonitrile only. Even though the MLCT absorption maxima remain almost invariant, systematic augmentation of molar extinction coefficients occurs on passing across monomer→ dimer→trimer in all the studied solvents. On the other hand, the emission energy, quantum yield and lifetime of the complexes is found to decrease systematically with the number of Ru^{2+} unit in the complex backbone and a good linear correlation is observed in each case. Good correlation is also observed between emission energies of complexes with their respective $\Delta E_{1/2}$ value. Thus, the present study establishes structure-property relationships for a series of systematically varied ruthenium complexes via a thorough investigation of the electronic absorption and emission spectral and electrochemical characteristics. In essence, the complexes have the desirable characteristics to act as potential building blocks for diverse light harvesting applications.

2.6. References

1. Lewis, N. S.; Nocera, D. G. Powering the Planet: Chemical Challenges in Solar Energy Utilization. *PNAS*. **2006**, *103*, 15729-15735.
2. Takeda, H.; Koike, K.; Inoue, H.; Ishitani, O. Development of an Efficient Potocatalytic System for CO_2 Reduction using Rhenium(I) Complexes Based on Mechanistic Studies. *J. Am. Chem. Soc.* **2008**, *130*, 2023-2031.
3. Ardo, S.; Meyer, G. J. Photodriven Heterogeneous Charge Transfer with Transition-Metal Compounds Anchored to TiO_2 Semiconductor Surfaces. *Chem. Soc. Rev.* **2009**, *38*, 115-164.
4. Brennaman, M. K.; Dillon, R. J.; Alibabaei, L.; Gish, M. K., Dares, C. J.; Ashford, D. L.; House, R. L.; Meyer. G. J.; Papanikolas, J. M.; Meyer, T. J. Finding the Way to Solar Fuels with Dye-Sensitized Photoelectrosynthesis Cells. *J. Am. Chem. Soc*. **2016**, *138*, 13085-13102.
5. Alibabaei, L.; Sherman, B. D.; Norris, M. R.; Brennaman, M. K.; Meyer, T. J. Visible Photoelectrochemical Water Splitting into H_2 and O_2 in a Dye-Sensitized Photoelectrosynthesis Cell. *PNAS*. **2015**, *112*, 5899-5902.
6. Shan, B.; Nayak, A.; Brennaman, M. K.; Liu, M.; Marquard, S. L.; Eberhart, M. S.; Meyer, T. J. Controlling Vertical and Lateral Electron migration using a bifunctional chromophore assembly in dye-sensitized photo electrosynthesis cells. *J. Am. Chem. Soc.* **2018**, *140*, 6493-6500.
7. Swierk, J. R.; Mallouk, T. E. Design and Development of Photoanodes for Water-Splitting Dye-Sensitized Photoelectrochemical Cells. *Chem Soc Rev*. **2013**, *42*, 2357-2387.
8. Gust, D.; Moore, T. A.; Moore, A. L. Solar Fuels via Artificial Photosynthesis. *Acc. Chem. Res.* **2009**, *42*, 1890-1898.
9. Kim, Y.; Das, A.; Zhang, H.; Dutta, P. K. Zeolite Membrane-Based Artificial Photosynthetic Assembly for Long-Lived Charge Separation. *J. Phys. Chem. B.* **2005**, *109*, 6929-6932.

10. Verma, S.; Kar, P.; Banerjee, T.; Das, A.; Ghosh, H. N. Sequential Energy and Electron Transfer in Polynuclear Complex Sensitized TiO2 Nanoparticles. *J. Phys. Chem. Lett*. **2012**, *3*, 1543-1548.
11. Frischmann, P. D.; Mahata, K.; Würthner, F. Powering the Future of Molecular Artificial Photosynthesis with Light-Harvesting Metallosupramolecular Dye Assemblies. *Chem. Soc. Rev.* **2013**, *42*, 1847-1870.
12. Kalyanasundaram, K.; Graetzel, M. Artificial Photosynthesis: Biomimetic Approaches to Solar Energy Conversion and Storage. *Curr. Opin. Biotechnol*. **2010**, *21*, 298-310.
13. Song, W.; Chen, Z.; Brennaman, M.; Concepcion, J.; Patrocinio, A.; Murakami Iha, N.; Meyer, T. Making Solar Fuels by Artificial Photosynthesis. *Pure Appl. Chem*. **2011**, *83*, 749-768.
14. Nocera, D. G. Chemistry of Personalized Solar Energy. *Inorg. Chem*. **2009**, *48*, 10001-10017.
15. Wasielewski, M. R. Self-Assembly Strategies for Integrating Light Harvesting and Charge Separation in Artificial Photosynthetic Systems. *Acc. Chem. Res.* **2009**, *42*, 1910-1921.
16. Barigelletti, F.; Flamigni, L. Photoactive Molecular Wires Based on Metal Complexes. *Chem. Soc. Rev*. **2000**, *29*, 1-12.
17. Sun, L. C.; Hammarstrom, L.; Akermark, B.; Styring, S. Towards Artificial Photosynthesis: Ruthenium-Manganese Chemistry for Energy Production. *Chem. Soc. Rev.* **2001**, *30*, 36-49.
18. Tyson, D. S.; Luman, C. R.; Castellano, F. N. Photodriven Electron and Energy Transfer from a Light-Harvesting Metallodendrimer. *Inorg. Chem.* **2002**, *41*, 3578-3586.
19. Serroni, S.; Juris, A.; Campagna, S.; Venturi, M.; Denti, G.; Balzani, V. Tetranuclear Bimetallic Complexes of Ruthenium, Osmium, Rhodium, and Iridium. Synthesis, Absorption Spectra, Luminescence, and Electrochemical Properties. *J. Am. Chem. Soc.* **1994**, *116*, 9086-9091.

20. Bassani, D. M.; Lehn, J. M.; Serroni, S.; Puntoriero, F.; Campagna, S. Homo and Heterometallic [2× 2] Grid Arrays Containing Ru^{II}, Os^{II}, and Fe^{II} Subunits and their Mononuclear Ru^{II} and Os^{II} Precursors: Synthesis, Absorption Spectra, Redox Behavior, and Luminescence Properties. *Chem. Eur. J.* **2003**, *9*, 5936-5946.

21. Juris, A.; Balzani, V.; Barigelletti, F.; Campagna, S.; Belser, P.; Von Zelewsky, A. Ru(II) Polypyridine Complexes: Photophysics, Photochemistry, Eletrochemistry, and Chemiluminescence. *Coord Chem Rev*. **1988**, *84*, 85-277.

22. Balzani, V.; Juris, A.; Venturi, M.; Campagna, S.; Serroni, S. Luminescent and Redox-Active Polynuclear Transition Metal Complexes. *Chem. Rev*. **1996**, *96*, 759-833.

23. Sauvage, J. P.; Collin, J. P. J.; Chambron, C.; Guillerez, S.; Coudret, C.; Balzani, V.; Barigelletti, F.; De Cola, L.; Flamigni, L. Ruthenium(II) and Osmium(II) Bis (Terpyridine) Complexes in Covalently-Linked Multicomponent Systems: Synthesis, Electrochemical Behavior, Absorption Spectra, and Photochemical and Photophysical Properties. *Chem. Rev*. **1994**, *94*, 993-1019.

24. Constable, E. C. 2, 2′: 6′, 2 ″-Terpyridines: From Chemical Obscurity to Common Supramolecular Motifs. *Chem. Soc. Rev*. **2007**, *36*, 246-253.

25. Medlycott, E. A.; Hanan, G. S. Synthesis and Properties of Mono-and Oligo-Nuclear Ru (II) Complexes of Tridentate Ligands: The Quest for Long-Lived Excited States at Room Temperature. *Coord. Chem. Rev*. **2006**, *250*, 1763-1782.

26. Schubert, U. S.; Eschbaumer, C. Macromolecules Containing Bipyridine and Terpyridine Metal Complexes: Towards Metallosupramolecular Polymers. *Angew. Chem., Int. Ed*. **2002**, *41*, 2892- 2896.

27. Hofmeier, H.; Schubert, U. S. Recent Developments in the Supramolecular Chemistry of Terpyridine-Metal Complexes. *Chem. Soc. Rev.* **2004**, *33*, 373-399.

28. Wang, X.; Guerzo, A.; Baitalik, S.; Simon, G.; Shaw, G. B.; Chen, L. X.; Schmehl, R. H. The Influence of Bridging Ligand Electronic Structure on the Photophysical Properties of Noble Metal Diimine and Triimine Light Harvesting Systems. *Photosynth. Res.* **2006**, *87*, 83-103.

29. Wong K. M-C.; Yam, V. W. W. Self-Assembly of Luminescent Alkynylplatinum (II) Terpyridyl Complexes: Modulation of Photophysical Properties Through Aggregation Behavior. *Acc. Chem. Res*. **2011**, *44*, 424-434.
30. Singh, H.; Tiwari, K.; Tiwari, R.; Pramanik, S. K.; Das, A. Small Molecule as Fluorescent Probes for Monitoring Intracellular Enzymatic Transformations. *Chem. Rev*. **2019**, *119*, 11718-11760.
31. Ghosh, H. N.; Banerjee, T.; Biswas, A. K.; Das, A.; Ganguly, B. Superior Grafting and State-of-the-Art Interfacial Electron Transfer Rates for Newly Designed Geminal Dicarboxylate Bound Ruthenium (II)–and Osmium (II)–Polypyridyl Dyes on TiO2 Nanosurface. *J. Phys. Chem. C*. **2014**, *118*, 3864-3877.
32. Walker, M. G.; Ramu, V.; Meijer, A. J. H. M.; Das, A.; Thomas, J. A. A Ratiometric Sensor for DNA Based on a Dual Emission Ru (dppz) Light-switch Complex. *Dalton Trans*. **2017**, *46*, 6079-6086.
33. Banerjee, T.; Kaniyankandy, S.; Das A.; Ghosh, H. N. Newly Designed Resorcinolate Binding for Ru (II)–and Re (I)–Polypyridyl Complexes on Oleic Acid Capped TiO2 in Nonaqueous Solvent: Prolonged Charge Separation and Substantial Thermalized 3MLCT Injection. *J. Phys. Chem. C*. **2013**, *117*, 3084-3092.
34. Banerjee, T.; Kaniyankandy, S.; Das A.; Ghosh, H. N. Synthesis, Steady-State, and Femtosecond Transient Absorption Studies of Resorcinol Bound Ruthenium (II)-and Osmium (II)-Polypyridyl Complexes on Nano-TiO2 Surface in Water. *Inorg. Chem*. **2013**, *52*, 5366-5377.
35. Karmakar, S.; Maity, D.; Mardanya, S.; Baitalik, S. Multichromophoric Bimetallic Ru(II) Terpyridine Complexes Based on Pyrenyl-bis-phenylimidazole Spacer: Synthesis, Photophysics, Spectroelectrochemistry, and TD-DFT Calculations. *Inorg. Chem*. **2014**, *53*, 12036-12049.
36. Mardanya, S.; Karmakar, S.; Mondal, D.; Baitalik, S. Homo and Heterobimetallic Ruthenium (II) and Osmium (II) Complexes Based on a Pyrene-biimidazolate

Spacer as Efficient DNA-binding Probes in The Near-infrared Domain. *Inorg. Chem*. **2016**, *55*, 3475-3489.

37. Saha, D.; Das, S.; Bhaumik, C.; Dutta, S.; Baitalik, S. Monometallic and Bimetallic Ruthenium (II) Complexes Derived From 4, 5-bis (benzimidazol-2-yl) Imidazole (H3Imbzim) and 2, 2′-Bipyridine as Colorimetric Sensors for Anions: Synthesis, Characterization, and Binding Studies. *Inorg. chem*. **2010**, *49*, 2334-2348.
38. Maity, D.; Bhaumik, C.; Mardanya, S.; Karmakar, S.; Baitalik, S. Light Harvesting and Directional Energy Transfer in Long-Lived Homo-and Heterotrimetallic Complexes of Fe^{II}, Ru^{II}, and Os^{II}. *Chem. – Eur. J*. **2014**, *20*, 13242–13252.
39. Baitalik, S.; Dutta, B.; Nag, K. Spectroscopic and Redox Properties of Rh(III)Ru(II) and Ru(II)Ru(II) Complexes Derived From 2, 2′-Bipyridine, Pyrazole-3, 5-Bis (Benzimidazole) and 1, 2, 4-Triazole-3, 5-Dicarboxylic Acid as Bridging Ligands. *Polyhedron*. **2004**, *23*, 913-919.
40. Mardanya, S.; Karmakar, S.; Maity, D.; Baitalik, S. Ruthenium (II) and Osmium (II) Mixed Chelates Based On Pyrenyl–Pyridylimidazole and 2, 2′-Pipyridine Ligands as Efficient DNA Intercalators and Anion Sensors. *Inorg. Chem*. **2015**, *54*, 513-526.
41. Deb, S.; Sahoo, A.; Pal, P.; Baitalik, S. Exploitation of The Second Coordination Sphere to Promote Significant Increase of Room-Temperature Luminescence Lifetime and Anion Sensing In Ruthenium–Terpyridine Complexes. *Inorg. Chem*. **2021**, *60*, 6836-6851.
42. Grätzel, M. Photoelectrochemical Cells. *Nature*. **2001**, *414*, 338-344.
43. O'regan, B.; Grätzel, M. A Low-cost, High-Efficiency Solar Cell Based On Dye-Sensitized Colloidal TiO_2 Films. *Nature*. **1991**, *353*, 737-740.
44. Kuriki, R.; Sekizawa, K.; Ishitani, O.; Maeda, K. Visible Light Driven CO_2 Reduction With Carbon Nitride: Enhancing The Activity Of Ruthenium Catalysts. *Angew. Chem., Int. Ed. Engl*. **2015**, *54*, 2406-2409.

45. Zong, R.; Thummel, R. P. A New Family Of Ru Complexes For Water Oxidation. *J. Am. Chem. Soc*. **2005**, *127*, 12802-12803.

46. Das, S.; Karmakar, S.; Saha, D.; Baitalik, S. A Combined Experimental and DFT/TD-DFT Investigation Of Structural, Electronic, and Cation-Induced Switching of Photophysical Properties Of Bimetallic Ru (II) and Os (II) Complexes Derived From Imidazole-4, 5-Dicarboxylic Acid and 2, 2′-Bipyridine. *Inorg. chem*. **2013**, *52*, 6860-6879.

47. Karmakar, S.; Mardanya, S.; Maity, D.; Baitalik, S. Polypyridyl-Imidazole Based Os (II) Complex As Optical Chemosensor For Anions and Cations and Multi-Readout Molecular Logic Gates and Memory Device: Experimental and DFT/TDDFT Study. *Sens. Actuators B: Chem*. **2016**, *226*, 388-402.

48. Pal, P.; Mukherjee, S.; Maity, D.; Baitalik, S. Synthesis, Structural Characterization, and Luminescence Switching of Diarylethene-Conjugated Ru (II)-Terpyridine Complexes by Trans–Cis Photoisomerization: Experimental and DFT/TD-DFT Investigation. *Inorg. chem*. **2018**, *57*, 5743-5753.

49. Karmakar, S.; Mardanya, S.; Pal, P.; Baitalik, S. Design Of Multichannel Osmium-Based Metalloreceptor For Anions And Cations By Taking Profit From Metal–Ligand Interaction And Construction Of Molecular Keypad Lock And Memory Device. *Inorg. Chem*. **2015**, *54*, 11813-11825.

50. Paul, A.; Sahoo, A.; Bhattacharya, S.; Baitalik, S. Anion And Temperature Responsive Molecular Switches Based On Trimetallic Complexes Of Ru (II) And Os (II) That Demonstrate Advanced Boolean And Fuzzy Logic Functions. *Inorg. Chem.* **2022**, *61*, 3186-3201.

51. Sahoo, A.; Ahmed, T.; Deb, S.; Baitalik, S. Neuro-Fuzzification Architecture for Modeling of Electrochemical Ion-Sensing Data of Imidazole-Dicarboxylate-Based Ru (II) Bipyridine Complex. *Inorg. Chem.* **2022**, *61*, 10242-10254.

52. Ghosh, H. N.; Das, A. Implications of Strongly Coupled Catecholate-Based Anchoring Functionality of a Sensitizer Dye Molecule Toward Photoinduced Electron Transfer Dynamics. *Adv. Inorg. Chem*. **2023**, *81*, 305-343.

53. Paul, A.; Bar, M.; Deb, S.; Baitalik, S. Long-Lived Trimetallic Complexes of Fe (II), Ru (II), and Os (II) Based On a Heteroditopic Bipyridine–Terpyridine Bridge: Synthesis, Photophysics, and Electronic Energy Transfer. *Inorg. Chem*. **2019**, *58*, 10065-10077.

54. Paul, A.; Ganguly, T.; Bar, M.; Baitalik, S. Controlling The Direction of Intercomponent Energy Transfer by Appropriate Placement of Metals in Long-Lived Trinuclear Complexes of Fe (II), Ru (II), and Os (II). *Inorg*. *Chem*., **2020**, *60*, 412-422.

55. Sullivan, B. P.; Meyer, T. J. Mixed Phosphine 2,2'-Bipyridine Complexes of Ruthenium**.** *Inorg. Chem.* **1978**, *17*, 3334-3341.

56. Baitalik, S.; Flörke, U.; Nag, K. Mononuclear and Binuclear Ruthenium (II) Complexes Containing 2, 2'-Bipyridine or 1, 10-Phenanthroline and Pyrazole-3, 5-bis (Benzimidazole), Synthesis, Structure, Isomerism, Spectroscopy and Proton-Coupled Redox Activity. *Inorg. Chem.* **1999**, *38*, 3296-3308.

57. Constable, E. C.; Seddon, K. R. A Deuterium Exchange Reaction Of The Tris-(2, 2′-Bipyridine) Ruthenium (II) Cation: Evidence For The Acidity Of The 3, 3′-Protons. *J. Chem. Soc., Chem. Commun*. **1982**, 34-36.

****

3.1. Introduction

Artificial Intelligence (AI) has made significant inroads into the field of chemical systems, offering new ways to optimize processes, discover novel materials, and gain deeper insights into molecular interactions. AI tools are increasingly prevalent and applied across a wide range of disciplines, including chemistry, materials science, and biology.[1-9] A primary emphasis in contemporary research is the creation of smart materials and examine their multi-faceted physicochemical information (including sensing, bio-sensing, and imaging) for better applicability.[10-19] However, there has been limited progress in various related fields of AI, including fuzzy logic[20-25], artificial neural networks (ANNs)[26-30], Adaptive Neuro-Fuzzy Inference Systems (ANFIS)[31-35], robotics, and evolutionary computation. Creating a robust, dependable and extensive database has the potential to broaden up the scope of machine learning applications. There is now a significant focus on nurturing the fertile ground of AI that deals with uncertain and imprecise inputs.

Herein, we will execute the anion sensing characteristics of a new array of polypyridyl-imidazole based Ru(II)-bipyridine complexes as reported in chapter 2 (**Chart 3. 1**)[36] and thereafter apply adaptive neuro-fuzzy inference system based AI tools for accurate prediction of the experimental data as well as appropriate modeling of the sensing characteristics of the complexes. The motivation behind choosing anion sensing characteristics is because of their crucial roles in chemical and biological events. Because of the omnipresence of anions in various chemical and biochemical systems, we are interested to design highly sensitive and selective anion sensors for their utilization in fields of anion scaffolds, sensors, catalysts and many more. We are particularly interested to sense F^- because of its duplicitous nature and also due to its relevance in biology and environment. The main reason for selecting Ru(II) complexes is due to their rich and versatile photophysical properties that in turn, could provide multiple channels for detection of the anions. Thus, this sort of complexes could be utilized as the potential building blocks for the fabrication of molecular switches and devices when exposed to appropriate external stimuli, including anions and acid. For fine tuning of photophysical as well as sensing characteristics, we have systematically altered the number of Ru(II) unit in the complex architecture. Herein, we have employed monometallic, bimetallic as well as trimetallic complexes. The design protocol offers one and/or two imidazole NH protons in the periphery of the complexes which are capable to interact with incoming anions via hydrogen bonding and/or complete proton transfer.[37-44] As will be demonstrated, spectral characteristics of the metalloreceptors undergo substantial alteration when exposed to basic anions like F^- and CN^- in acetonitrile, whereas only CN^- in water. The observed spectral change is ascribed to initial

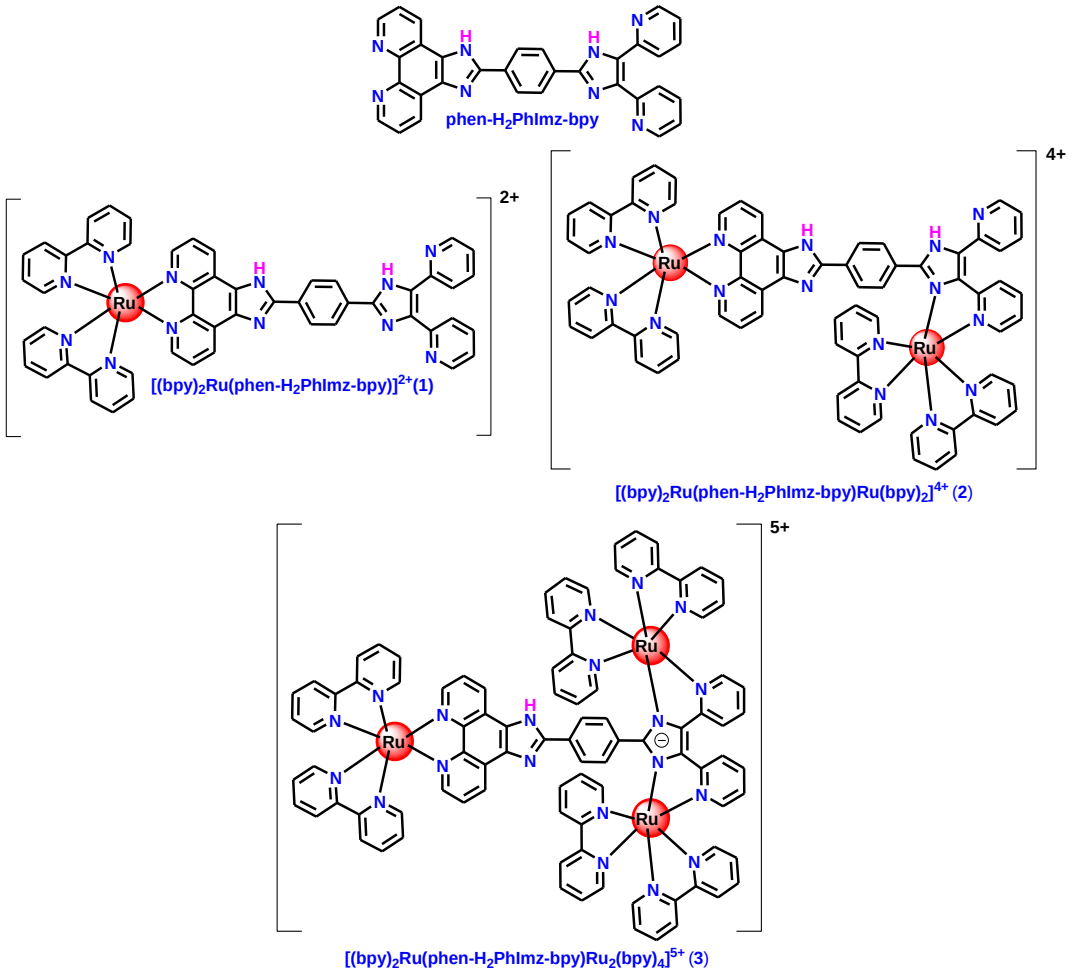

Chart 3.1. The structures of polypyridyl-imidazole based Ru(II)-bipyridine receptors.

hydrogen bonding among NH proton(s) and anions followed by complete removal of the said protons in presence of excess anions. Notably, the deprotonation of the metalloreceptors by anion, and subsequent refurbishment to their original state through addition of acid, is a reversible process that can be iterated numerous times.

Interestingly, the metalloreceptors can exhibit advanced Boolean logic functions by leveraging their spectral responses when exposed to anions and acid.[45-52] The operation of Boolean logic (BL) relies on altering the output signal in-between the two limits, viz. false (0) and true (1).[53-58] Conversely, the majority of real systems consist of numerous intermediary states. To address the intermediate states, the Adaptive Neuro-Fuzzy Inference System (ANFIS) is expected to be a potential alternative. It is an AI based computational modeling approach that blends the principles of artificial neural networks (ANN) and fuzzy logic (FL).[31-35] ANFIS is used for modeling and

approximating complex systems, especially those with nonlinear functions and uncertain characteristics. It consists of layers that include fuzzification of input data into fuzzy sets, defining IF-THEN rules relating input and output variables, inference using these rules, and defuzzification to obtain a numerical output. ANFIS combines the power of neural networks for pattern recognition and fuzzy logic for handling uncertainty, making it a versatile tool for tasks like system identification, control, and prediction in various fields. It is trained by adjusting parameters iteratively using optimization techniques until it accurately represents the relationships among the predicted and experimental outputs. Herein, we also impose the hybrid-optimization method-based ANFIS system for fabricating an infinite-valued logic algorithm via the use of the spectral outputs of the receptors under the influence of anion and acid. It is of interest to note that the membership function plays a crucial role in the training phase of ANFIS as they define the fuzzy sets that characterize the linguistic variables used in the system. These fuzzy sets are essential because they capture the imprecision and uncertainty often present in real-world data. As membership function plays a crucial role, it's appropriate selection is of pivotal importance for accurate modeling and prediction. To this end, we have implemented as much as five widely used membership functions, viz. *trimf, trapmf, gbellmf, gaussmf, and pimf* for execution of the ANFIS models. Furthermore, we have conducted a comparative evaluation of their performances against experimental results, aiming to enhance the modeling accuracy of the sensing behaviors of the metalloreceptors. It is to be noted that execution of ANFIS models on molecular and supramolecular systems upon variation of membership functions are extremely rare in the literature.[31-35]

3.2. Experimental Section

3.2.1. Materials. The synthesis and thorough characterization of all the three Ru(II)-bipyridine derived from polypyridyl-imidazole based bridging ligand; (**phen-H_2PhImz-bpy**) has been reported in chapter 2.[36]

3.2.2. Physical Measurements. The details of different equipments used and experimental process to measure absorption and luminescence spectral behaviors have already been discussed in chapter 2.

For a typical absorption and emission titration experiment, aliquots of $HClO_4$ (0.1 M) were added incrementally to a 2.5 mL solution of the complexes (1.0×10^{-5} M).

3.2.3. Computational Method.

Adaptive Neuro-Fuzzy Inference System (ANFIS). The network framework of the ANFIS is illustrated in Scheme 3.1 in the main text. It consists of five connected layers

(excluding input layer) which is common for the two input dimensions, P and Q, both of which possess three fuzzy sets, viz. C1C2C3 for P, while D1D2D3 for Q input. We have chosen A number of inputs and B number of fuzzy set to represent each input which in turn implies A×B number of nodes in Layer1. In Layer 2, all the nodes are interconnected with the membership function output of each input node, yielding a total of B^A node in Layer 2. Layer 3 and 4 possess the same number of nodes as that of Layer 2. Layer 5, on the other hand, possess only one node representing the output of the network. Upon considering each input as a node, the total number of nodes in the architecture will be A + A×B + 3×B^A + 1. In ANFIS, only the membership function parameters in Layer1 and inputs weight in Layer 4 are to be predicted by training. Upon implication of the triangular membership function (trimf) which is represented by three parameters, we need to assess 3×B×A premise parameters in Layer 1 and A×B^A consequent weight parameters in Layer 4 (Scheme 3.1).

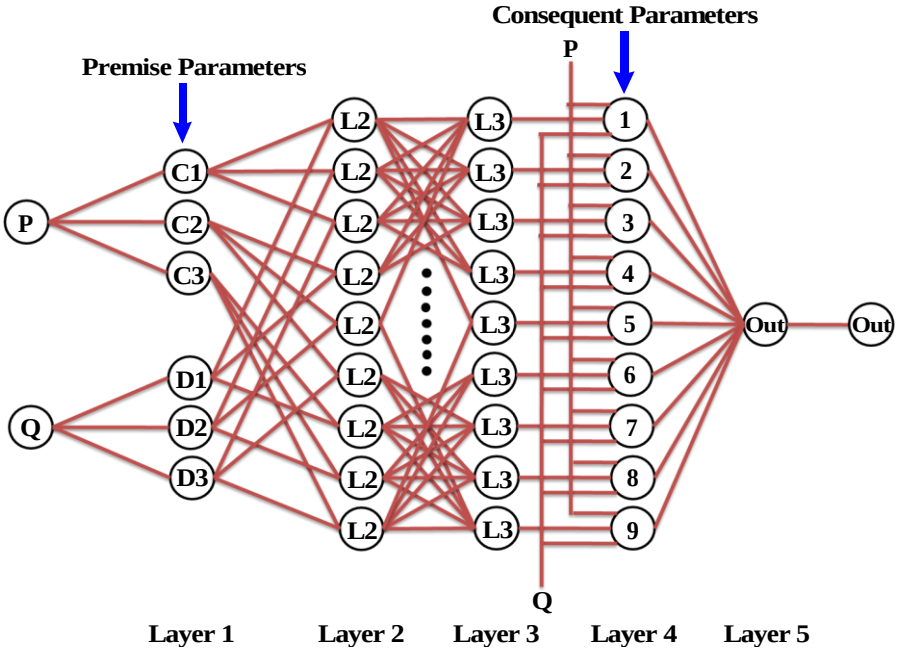

Scheme 3.1. Schematic sketch of ANFIS network comprising of two inputs, five layers and one output.

3.3. Results and Discussion

3.3.1. Anion-Responsive Behaviors. Taking benefit of the imidazole NH motif(s), anion sensing characteristics of the complexes **1-3** are studied systematically in both acetonitrile and

water by using various optical channels. Tetrabutylammonium salt of the anions (F^-, Cl^-, Br^-, I^-, $H_2PO_4^-$, SCN^- and CN^-) is used in this study. The reduction in MLCT absorption band intensity at ~460 nm along with enhancement of absorbance at ~500 nm region takes place only with F^- and CN^- in MeCN for all three complexes. In line with UV-vis absorption spectra, the decrease in emission intensity occurs in all cases, albeit in different extent, highest for **1**, least for **3** with an intermediate value for **2** in presence of the said anions. On passing from MeCN to H_2O, all the complexes selectively sense only CN^- and the degree of spectral change is also small relative to MeCN.

To acquire quantitative insight of the receptor-anion interplay, absorption and emission spectral titrations are executed for all three complexes in acetonitrile by gradual inclusion of F^- and CN^-. Clear-cut change is noticed in the spectral profile for each complex as shown in Figure 3.1a-c. The spectral profiles of the complexes are found to be almost same for both F^- and CN^-. Systematic intensification in absorbance at ~500 nm and at ~350 nm accompanied with gradual reduction in band intensity at ~460 nm and ~290 nm is observed in all cases, although the spectral pattern and extent of change differs from each other. Successive spectral lines are found to pass through distinct isosbestic points in each case. The emission spectral variation upon systematic incorporation of F^- or CN^- is already displayed in Figure 3.1d-f. Gradual diminution of emission intensity together with bathochromic shift takes place in all the three complexes, albeit the degree of change varies with number of Ru^{2+} unit in the complex backbone (604→625 nm for **1**; 620→645 nm for **2** and 655→669 nm for **3**). The equilibrium/binding constants of receptor-anion interplay are estimated by using both the absorption and emission titration profiles via equation 1 and tabulated in Table 3.1. Reasonably good parity is found among the binding constants, obtained by two different types of data sets. The lifetime is also measured upon incremental inclusion of F^- and the results are presented in Figure 3.2. With gradual addition of F^-, the lifetime of all the complexes is found to decrease systematically till saturation. It is to be noted that the nature of the decay change from mono- to bi-exponential form for both **1** and **2** in presence of F^- but remains mono-exponential for **3**.

$$\Delta A = \frac{\Delta\varepsilon b([\mathrm{H}] + [\mathrm{G}] + (1/K)) \pm \sqrt{\Delta\varepsilon^2 b^2\,([\mathrm{H}] + [\mathrm{G}] + (1/\mathrm{K}))^2 - 4\Delta\varepsilon^2 b^2\ [\mathrm{H}][\mathrm{G}]}}{2} \quad (1)$$

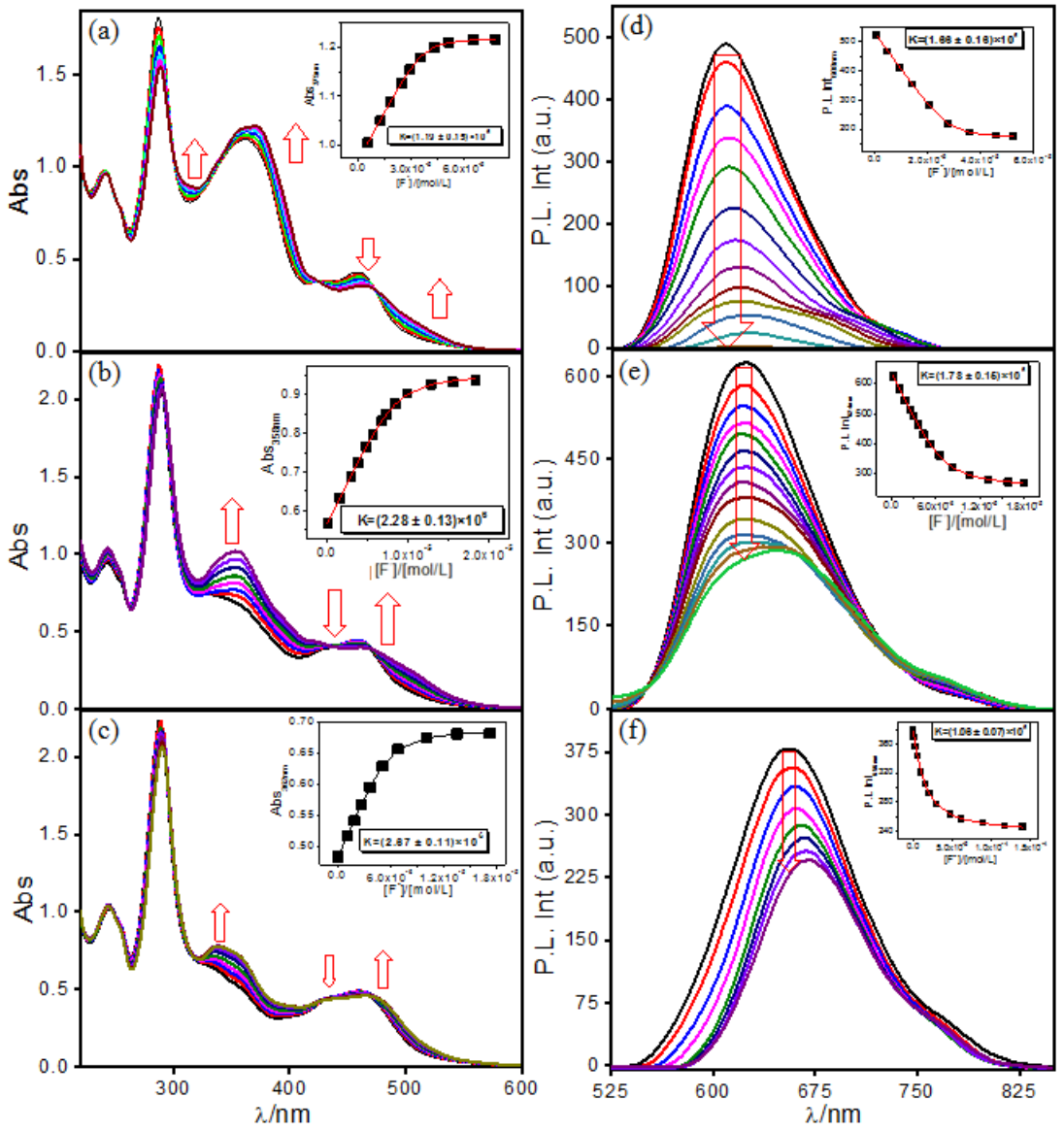

Figure 3.1. Absorption (a-c) and emission (λ_{ex}=450 nm) spectral (d-f) change for **1-3** in MeCN upon step-by-step addition of F^-. The insets display the fitting of the respective spectral data via equation 1 for estimation of the binding/equilibrium constants.

Table 3.1. Equilibrium/Binding Constant of Complexes **1-3** in MeCN and H_2O.

Anions	Complexes	Absorption	Emission
		K	K
F^- (in MeCN)	**1**	$1.2\pm0.15\times10^6$	$1.6\pm0.16\times10^6$
	2	$2.3\pm0.13\times10^6$	$1.8\pm0.15\times10^6$
	3	$2.7\pm0.11\times10^6$	$1.1\pm0.07\times10^6$
CN^- (in H_2O)	**1**	$1.5\pm0.53\times10^4$	$1.4\pm0.20\times10^4$
	2	$1.4\pm0.004\times10^4$	$1.3\pm0.28\times10^4$
	3	$1.1\pm0.10\times10^4$	$1.2\pm0.29\times10^4$

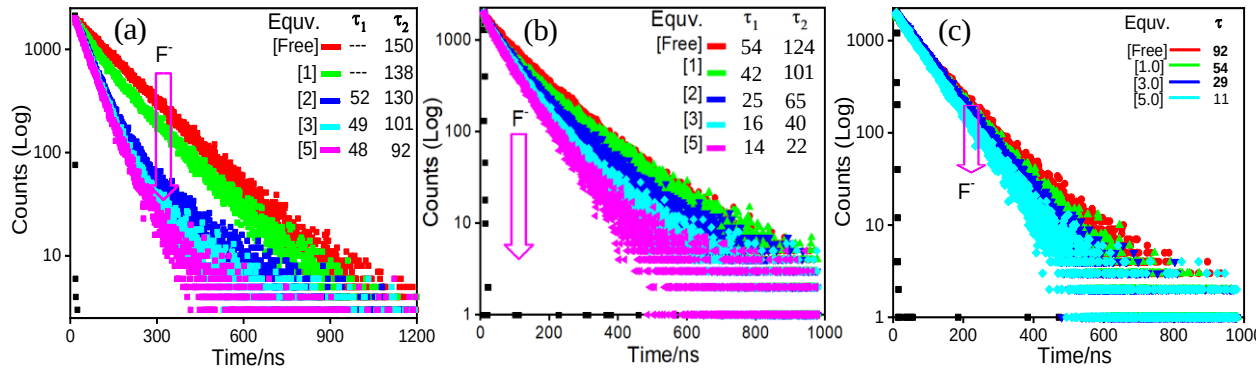

Figure 3.2. Change in luminescence decay of **1** (a), **2** (b) and **3** (c) in MeCN at RT upon step-by-step addition of F^- (up to 5.0 equiv). Insets show the respective lifetime values.

We have already pointed out that complexes are sensitive to only CN^- among the studied anions in water. Consequently, absorption and emission spectra of the complexes are acquired with systematic increase in CN^- concentration and displayed in Figure 3.3a-c. The spectral profiles are grossly similar with their MeCN counterpart. Of course, small but finite differences exist among the profiles in MeCN and H_2O. In the absorption spectral profiles of **1** and **2**, decrease in absorbance of the MLCT band at 462 nm takes place. By contrast, small increase in intensity of the said band is noticed in case of **3**. Small but finite red-shift of the MLCT band takes place for **1** and **2** but remains almost unaltered for **3**. The emission spectral variation of complexes upon systematic incorporation of CN^- is already displayed in Figure 3.3d-f. In-line with the behavior of the complexes in MeCN, systematic quenching of emission takes place in all three complexes together with small red-shift of peak maximum for **1** and **2** but not in case of **3**. The extent of red-shift in emission maximum along with its quenching is found to be much smaller in water compared with MeCN in all cases. The titration profiles are also employed to calculate equilibrium/binding constant (*K*) for complex-anion interaction process by using equation 1 and the values are listed in Table 3.1. The estimated values gathered from the emission titration profiles of the complexes, match reasonably well with that obtained from the absorption data.

3.3.2. Logic operations. In the preceding section, we have witnessed a substantial alteration in the spectral profiles of all the complexes in presence of specific anions. The spectral changes are reversible and restoration of their initial state is feasible with acid and the overall process is reversible and can be recycled many times. The spectral outputs are employed here for the fabrication of various advanced Boolean logic devices. Additionally, Adaptive Neuro-Fuzzy Inference System (ANFIS) could also be utilized to predict the experimental outputs as a function

of numerous combinations of the inputs as well as for proper understanding as well as appropriate modeling of sensing characteristics of the complexes.

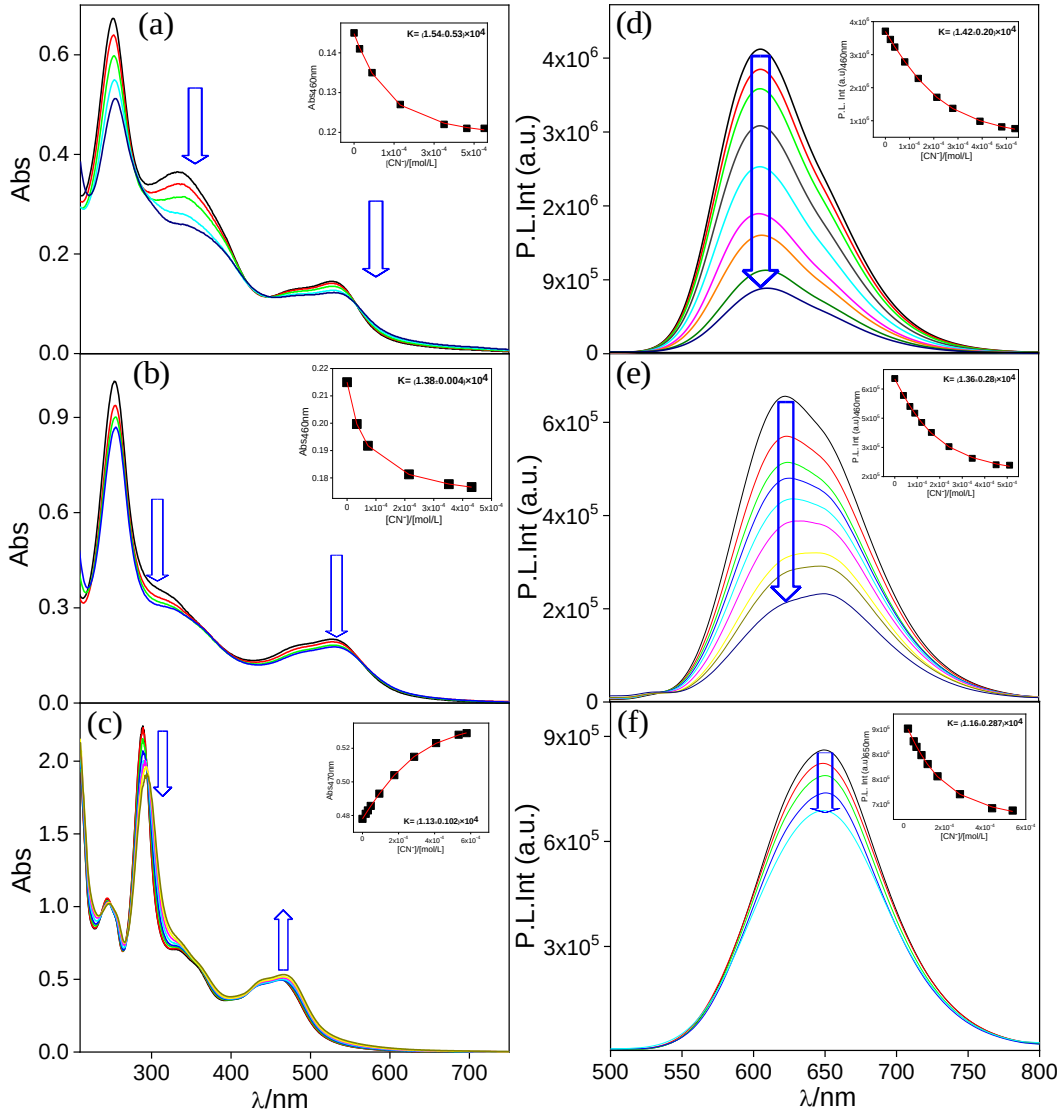

Figure 3.3. Absorption (a-c) and emission (λ_{ex}=450 nm) (d-f) spectral variation for **1-3** in H_2O upon step-by-step addition of CN^-. The insets display the fitting of the respective spectral data via equation 1 for estimation of the binding/equilibrium constants.

3.3.2.1. Implication Gate. This type of gate is a logical construction that combines the operations of the AND, OR, and NOT gates to implement an implication relationship between two inputs. If one input can imply or determine the other input, the implication gate produces the corresponding output. To mimic this type of logic, we have taken the emission intensity of complex **1** at 604 nm as the output signal as a function of F^- and H^+ inputs (Figure 3.4a). From the

truth table, we can observe that the system exhibits an ON state (1) in three out of four possible combinations of inputs (Figure 3.4b). Specifically, when both F^- and H^+ are either 0 or 1, the output emission response at 604 nm stays at the level much higher than the threshold, so that we can consider them as ON state. However, when F^- is 1, the emission intensity goes down below the threshold, indicating OFF state (0). Based on these observations, it is possible to interpret the behavior of the system as an implication relationship, where the presence of F^- implies a change in the output state from ON to OFF (Figure 3.4c).

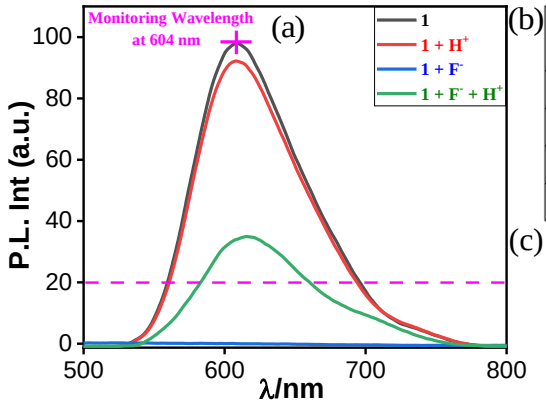

(b)

Input 1 (F^-)	Input 2 (H^+)	Output Emission Intensity at 604 nm
0	0	1 (high)
0	1	1 (high)
1	0	0 (low)
1	1	1 (high)

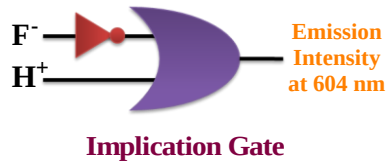

Figure 3.4. (a) Emission spectral change of **1** due to the addition of F^- and H^+. (b) Corresponding truth table. (c) Schematic presentation of an Implication gate.

3.4. Adaptive Neuro-Fuzzy Inference System (ANFIS)

It is a hybrid tool that combines the operations of both fuzzy logic and neural network. It was developed by Jang in the early 1990s as a method for adaptive reasoning and modeling.[59-62] It is capable of defining numerous in-between values within the two extremes, viz. 0 and 1, allowing for more nuanced representations and reasoning which is not possible in case of Boolean logic. ANFIS utilizes a learning algorithm to adjust the parameters of its fuzzy inference system based on input-output data. By incorporating neural network techniques, ANFIS can learn and adapt its fuzzy rules to make accurate predictions or decisions. It starts with a fuzzy inference system structure, typically represented by a set of if-then rules, which are commonly used in fuzzy logic. These rules define the relationships between input variables and output variables. The ANFIS model consists of several layers, viz. input-, fuzzification-, rule-, artificial neural network-, defuzzification-, and output layer, as presented in Figure 3.5. ANFIS is often used for modeling complex systems via prediction, classification, and controlling the tasks. It offers the ability to adapt as well as to learn from data upon employing the interpretability and linguistic reasoning of fuzzy logic. This makes ANFIS a powerful tool for handling uncertain and complex information

in various domains. Of course, choosing of appropriate membership functions is very crucial in ANFIS as they play key role in capturing the linguistic variables and fuzzy relationships between inputs and outputs. Additionally, the accuracy, interpretability, and overall performance of the ANFIS model is critically dependent on the type of membership function.

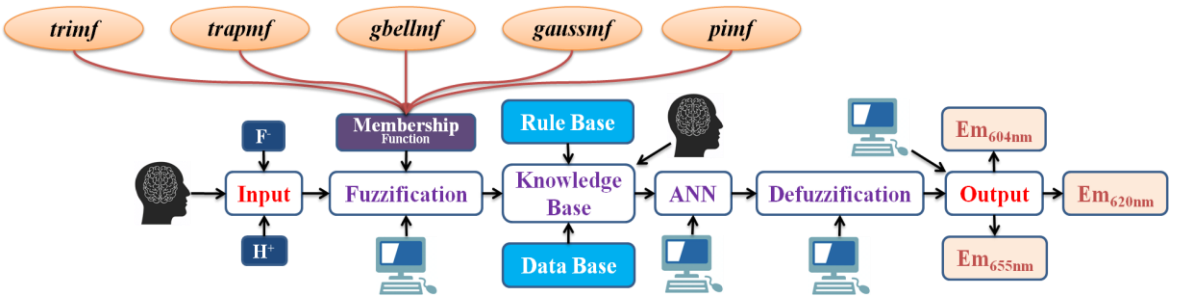

Figure 3.5. Layers of ANFIS models.

We used herein hybrid optimization method to train and fine-tune the parameters of the ANFIS model and have chosen five most popular membership functions, viz. *trimf, trapmf, gbellmf, gaussmf and pimf* for accurate prediction of the emission characteristics of complexes **1-3** in presence of anion (Figure 3.6).

3.5. Mathematical Formulation of Membership Functions

In adaptive neuro-fuzzy system, inclusion of a membership function (MF) is a crucial concept. Fuzzy logic is an extension of classical (or crisp) logic that allows the uncertainty and vagueness in decision-making and reasoning processes in a complex system. A fuzzy inference tool is the central part of any fuzzy logic system wherein fuzzification is the first step. Formally, a MF for a given fuzzy set A on the universe of discourse X is defined as μ_A: X $\rightarrow$ [0, 1], wherein each element of X is mapped to a value within 0 and 1. This value, designated as membership value or degree of membership, accesses the grade of membership of X to the fuzzy set A. Here, X being the universal set, while A is the fuzzy set derived from X. The fuzzy MF is the graphical display to rationalize the degree of membership of any value in a given fuzzy set. The X-axis in the graph designates the universe of discourse, while the Y-axis represents the degree of membership in the range between 0 and 1 (Figure 3.7).

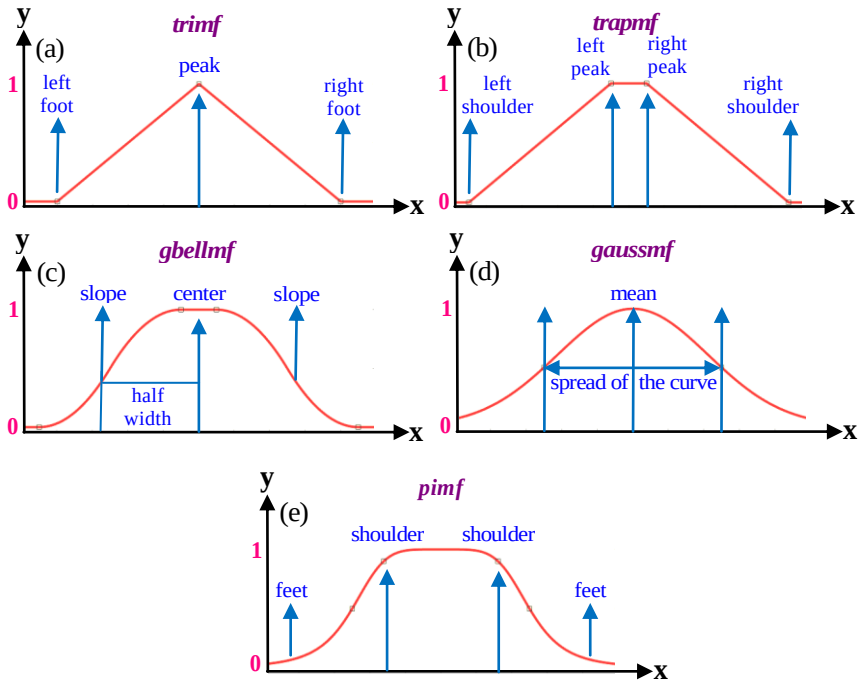

Figure 3.6. Shape and parameters of the five different membership function.

3.5.1. Triangular Membership Function (*trimf*): This is one of the extensively used and universally adopted MF in the fabrication of fuzzy controller. The triangle that fuzzifies the input could be expressed by three parameters, viz. a, b and c, wherein a and c defines the base, whereas b denotes the height of the triangle (Figure 3.7). The X-axis in the plot represents the input from the process, whereas the Y-axis designates respective fuzzy value.

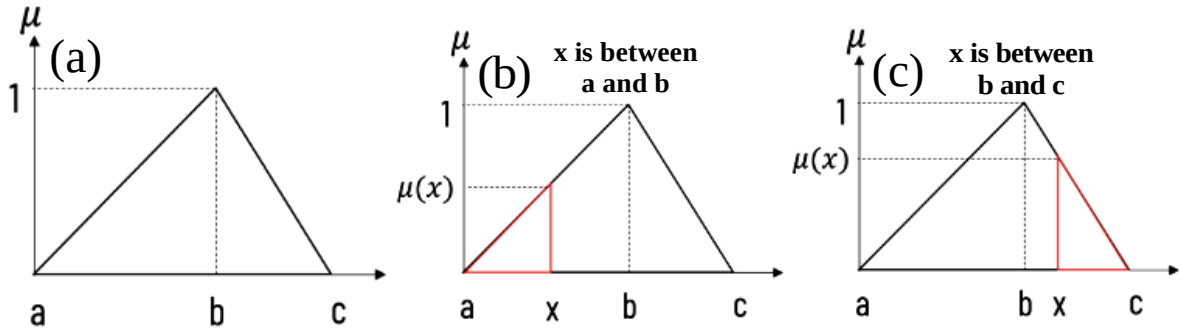

Figure 3.7. Graphical presentation for visualizing the degree of triangular membership function (*trimf*) of any value in a given fuzzy set.

Case I: If input x = b; the membership function, $\mu_{(x)} = 1$(Figure 3.7a).

Case II: If the input is either less than a or greater than c, then the value of the membership function ($\mu_{(x)}$) will be zero = 0 (when x < a or x > c) because the fuzzy set does not belong to the specified domain of the triangle.

Case III: If x lies in between a and b, its $\mu_{(x)}$ value varies within the domain of 0 and 1. If the value of x is near to a, its $\mu_{(x)}$ value will be close to 0. By contrast, if the value of x is near to b, its $\mu_{(x)}$ value will tend to 1 (Figure 3.7b). We can compute the fuzzy value of x using a similar triangle rule, $\mu_{(x)} = (x - a) / (b - a)$, when $a \leq x \leq b$

Case IV: If x lies in between b and c, its $\mu_{(x)}$ value again alters in the range between 0 and 1. If it is near to b, its $\mu_{(x)}$ value is close to 1, and if x is near to c, its $\mu_{(x)}$ value gets close to 0 (Figure 3.7c). We can compute the fuzzy value of x using a similar triangle rule,

$\mu_{(x)} = (c - x) / (c - b)$, when $b \leq x \leq c$

For the ease of operation flexibility, we can combine all the aforementioned four cases into a single equation.

$\mu_{combined} = \max [\min \{(x - a) / (b - a), (c - x) / (c - b)\}, 0]$

The mathematical formulations of the other four membership functions are given below,

3.5.2. Trapezoidal membership function. The trapezoidal membership function is defined by four parameters: a, b, c and d. Span b to c represents the highest membership value that element can take. And if x is between (a, b) or (c, d), then it will have a membership value between 0 and 1 (Figure 3.8a).

We can apply the triangle MF if elements are in between a to b or c to d.

It is quite obvious to combine all together as,

$\mu_{trapezoidal} (x; a, b, c) = 0$ when $x \leq a$

$\mu_{trapezoidal} (x; a, b, c) = (x - a) / (b - a)$ when $a \leq x \leq b$

$\mu_{trapezoidal} (x; a, b, c) = (d - x) / (d - c)$ when $c \leq x \leq d$

$\mu_{trapezoidal} (x; a, b, c) = 0$ when $b \leq x$

$\mu_{combined} = \max [\min \{(x - a) / (b - a), (d - x) / (d - c)\}, 0]$

3.5.3. Gaussian membership function. A Gaussian MF is specified by two parameters {m, σ} and can be defined as follows. In this function, m represents the mean / center of the gaussian curve and σ represents the spread of the curve (Figure 3.8b). This is a more natural way of representing the data distribution, but due to mathematical complexity, it is not much used for fuzzification.

$\mu_{gaussian} (x; m, \sigma) = e^{-1/2 (x- m/\sigma)2}$

3.5.4. Generalized bell-shaped function. It is also called Cauchy MF. A generalized bell MF is specified by three parameters {a, b, c} and can be defined as follows (Figure 3.8c).

Slope at x = + b/2a

Slope at y = - b/2a

$\mu_{bell} (x; a, b, c) = 1 / \{1+ |(x-c)/a|^{2b}\}$

3.5.5. Pi-membership function. Pi membership function is named after it's shape. It is determined by 4 parameters (a, b, c and d) i.e. two feets and two shoulders (Figure 3.8d).

a, b, c, and d are specific points in the universe of discourse X, with a < b < c < d.

The value of $\mu_A(x)$ is 1 in the interval [a, b], representing full membership to the fuzzy set A.

The value of $\mu_A(x)$ is 0 in the intervals $(-\infty, a)$ and (b, c) and (c, ∞), indicating no membership to the fuzzy set A.

The value of $\mu_A(x)$ linearly varies from 1 to 0 in the intervals [a, b] and [b, c], representing the gradual transition from full membership to no membership.

$\mu_{pi}(x; a, b, c, d) = 1$, when $x \in [a, b]$

$\mu_{pi}(x; a, b, c, d) = (x - b) / (a - b)$, when $x \in [b, d]$

$\mu_{pi}(x; a, b, c, d) = 0$, otherwise.

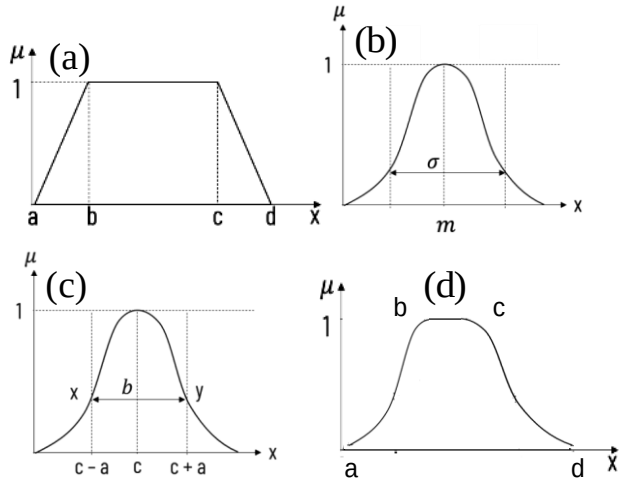

Figure 3.8. Graphical way of visualizing the degree of trapezoidal (a), gaussian (b), generalized bell shaped (c) and pi-shaped (d) membership function of any value in a given fuzzy set.

There are many membership functions in fuzzy logic but the most popular and widely used five membership functions are *trimf, trapmf, gbellmf, gaussmf and pimf*. We have used F^- as input 1, H^+ as input 2 and intensity of emission maximum at 604 nm, 620 nm and 655 nm of **1**, **2** and **3**, respectively as the three outputs (Figure 3.9).

The *trimf* is one of the simplest and most commonly employed membership functions. It has a triangular shape, defined by three parameters, viz. left foot, the peak and the right foot (Figure 3.6a). It is often used when there is a moderate degree of uncertainty or gradual transition between two fuzzy sets. In line with *trimf*, the trapezoidal membership function (*trapmf*) has four parameters, viz. left foot and the left shoulder as well as the right shoulder and the right foot (Figure 3.6b). It is used when the transition between fuzzy sets is less gradual and more defined. Generalized bell-shaped membership function has a symmetric bell-shaped curve and is often

used when there is a need to model symmetric membership degrees around a central value. It is characterized by parameters that define the center, slope and width of the bell curve (Figure 3.6c). The Gaussian membership function has a bell-shaped curve and is often used when the

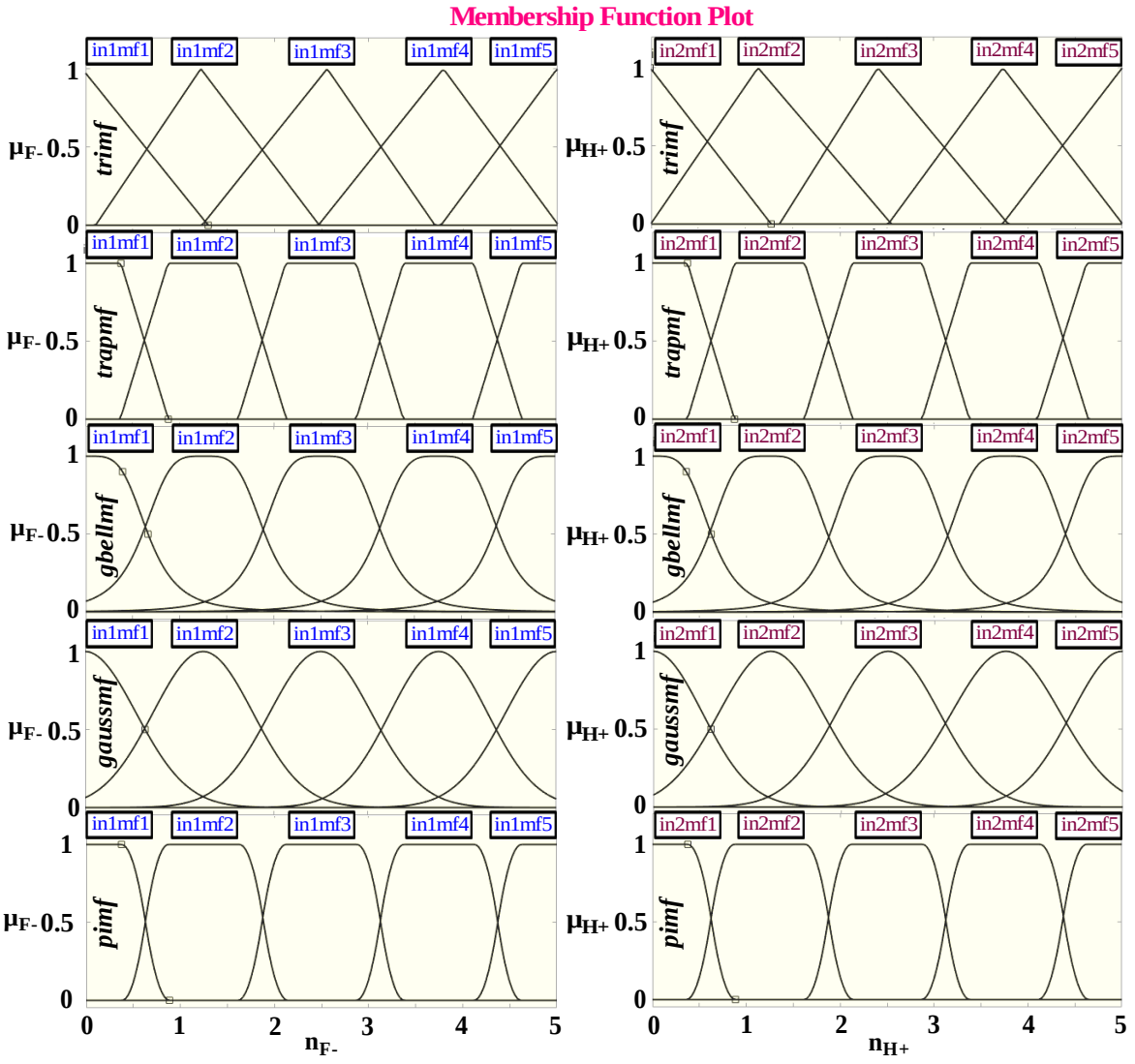

Figure 3.9. Schematic diagram of ANFIS on the basis of Sugeno's method (consisting five different membership functions).

fuzziness is distributed around a central value. It is characterized by two parameters: the mean and the spread of the curve (Figure 3.6d). Pi membership function is named after its shape. It is determined by 4 parameters, viz. two feets and two shoulders (Figure 3.6e).

3.5.6. Optimization with ANFIS. ANFIS model is applied here to foresee the variation of emission response as function of varying quantities of F^- and H^+ that involves fuzzification,

knowledge base, ANN, and defuzzification layers (Figure 3.5). 80% of total data is taken for training while the rest is used for testing for each of the different membership functions-assisted hybrid optimization process in ANFIS. The learning process continues up to 100 epochs with diminution of root mean square error (RMSE) (Figure 3.10). The RMSE values of the five different membership-assisted ANFIS models are given in Table 3.2. Taking into consideration 2 inputs and 5 membership functions each, the network will yield $5^2 = 25$

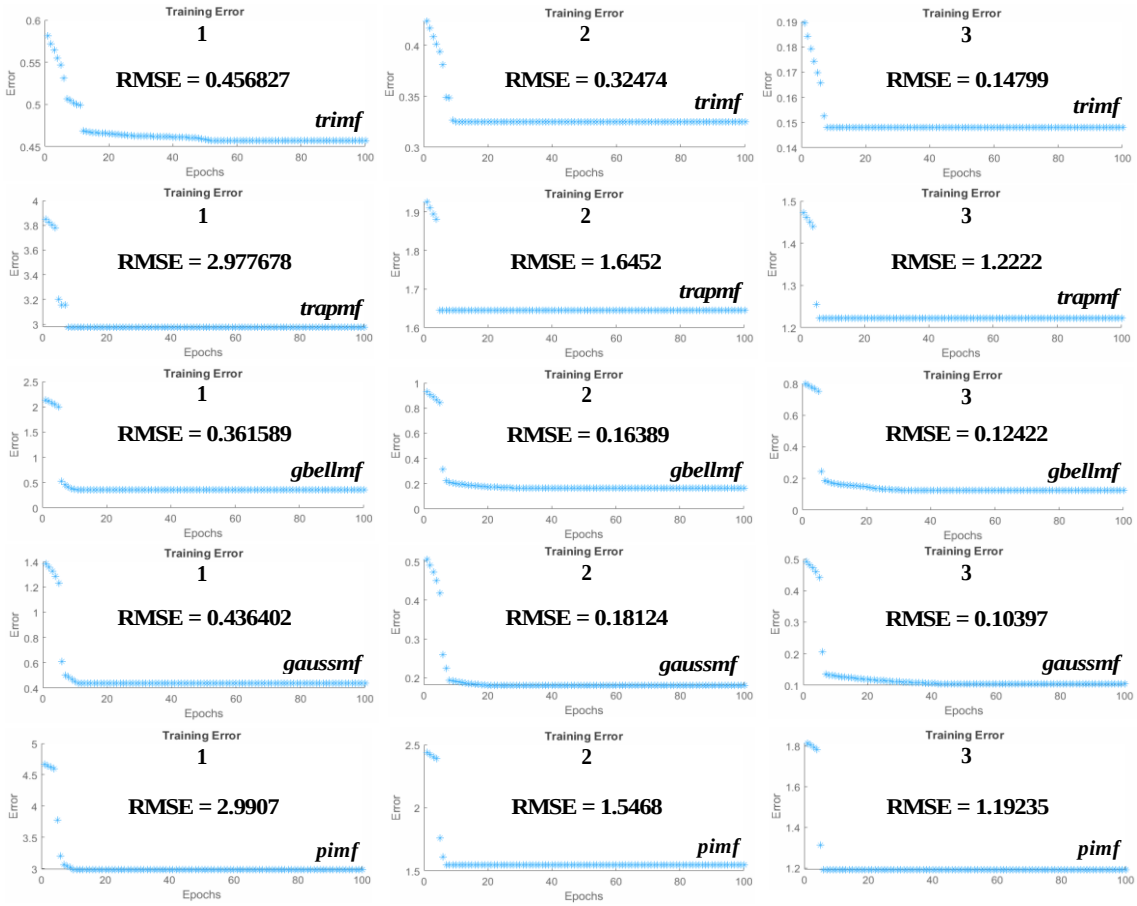

Figure 3.10. Data training process of complexes **1-3** with ANFIS for two inputs and three outputs consisting of five different membership functions.

Table 3.2. Generated RMSE Values from the ANFIS Models Consisting of Five Different Membership Functions.

Complex	Root Mean Square Error (RMSE)				
	trimf	*trapmf*	*gbellmf*	*gaussmf*	*pimf*
1	0.45682	2.97767	0.36158	0.43640	2.99071
2	0.32474	1.64521	0.16389	0.18124	1.54682
3	0.14799	1.22221	0.12422	0.10397	1.19235

rules and their corresponding 25 output membership functions. Root means square error (RMSE) values of *gbellmf* assisted ANFIS models of complex **1** and **2** and *gaussmf* assisted ANFIS model of complex **3** are the lowest (0.361589, 0.16389 and 0.10397) implying that the model is running precisely. The experimental and ANFIS model output values of complex **1-3** are given in Table 3.3.

Table 3.3. Experimental Data along with ANFIS Outputs Based on Different Membership Functions.

(a)

Complex 1		Emission Intensity at 604 nm					
Input 1 (F^-)	Input 2 (H^+)	Expt. Data	Membership Functions				
			trimf	*trapmf*	*gbellmf*	*gaussmf*	*pimf*
0.7	4.3	80.01	79.41	79.51	80.11	79.83	91.63
1.9	3.1	57.03	56.23	56.52	57.14	56.31	58.47
4.3	0.7	10.16	12.71	12.51	10.96	12.65	4.11
3.1	1.9	32.92	33.81	34.23	32.81	34.02	32.78
2.1	2.9	52.02	52.52	53.12	52.17	52.56	47.63

(b)

Complex 2		Emission Intensity at 620 nm					
Input 1 (F^-)	Input 2 (H^+)	Expt. Data	Membership Functions				
			trimf	*trapmf*	*gbellmf*	*gaussmf*	*pimf*
0.7	4.3	88.46	88.82	89.11	88.70	88.92	93.42
1.9	3.1	76.85	77.93	77.92	76.76	78.03	78.83
4.3	0.7	47.42	51.83	51.73	47.57	51.85	47.33
3.1	1.9	66.76	67.23	66.83	66.72	66.93	66.17
2.1	2.9	76.82	76.32	73.42	76.6	76.53	73.93

(c)

Complex 3		Emission Intensity at 655 nm					
Input 1 (F^-)	Input 2 (H^+)	Expt. Data	Membership Functions				
			trimf	*trapmf*	*gbellmf*	*gaussmf*	*pimf*
0.7	4.3	90.34	90.03	90.12	90.11	90.32	91.53
1.9	3.1	82.02	83.13	83.14	83.12	81.89	83.81
4.3	0.7	62.13	64.07	64.12	64.13	62.17	60.53
3.1	1.9	74.52	73.72	73.71	73.61	74.47	73.11
2.1	2.9	80.57	81.13	78.63	81.21	80.37	79.03

The emission response as a cumulative function F^- and H^+ is also portrayed in a 3D plot (Figure 3.11). Figure 3.12a and 12b clearly shows that with decreasing the range of data, the RMSE values also decreases in each of the five different membership functions-assisted ANFIS model and from this we can conclude that *gbellmf* and *gaussmf* are the two best membership function to predict sensing behaviour of complex **1-3** quite accurately. Generated ANFIS structure with five membership functions for each of the two inputs is given in Figure 3.12c.

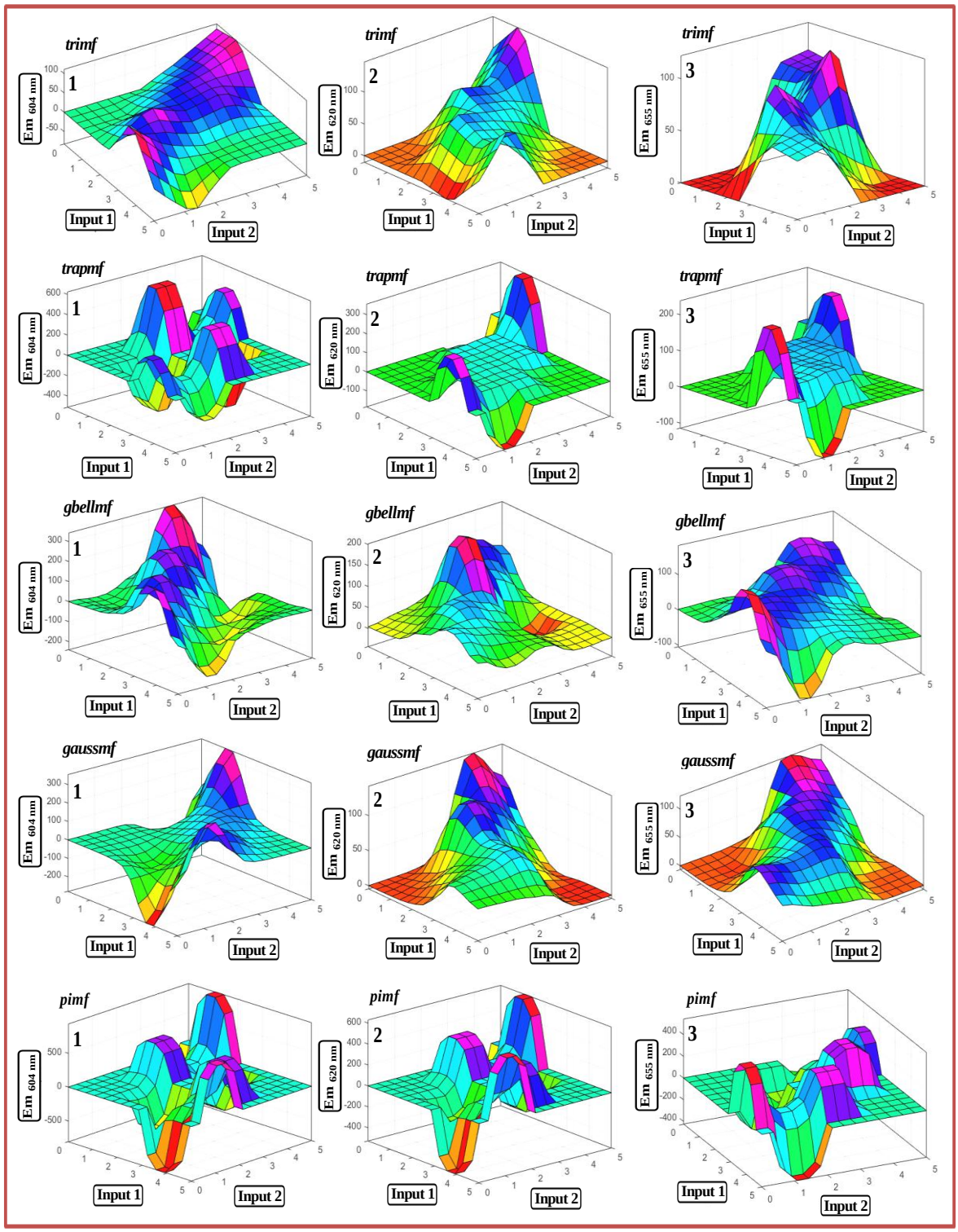

Figure 3.11. Variation of emission intensity of **1-3** (with triangular, trapezoidal, generalized bell shaped, Gaussian and pi-shaped membership function) in presence of input 1 (F^-) and input 2 (H^+) portrayed in 3D plot.

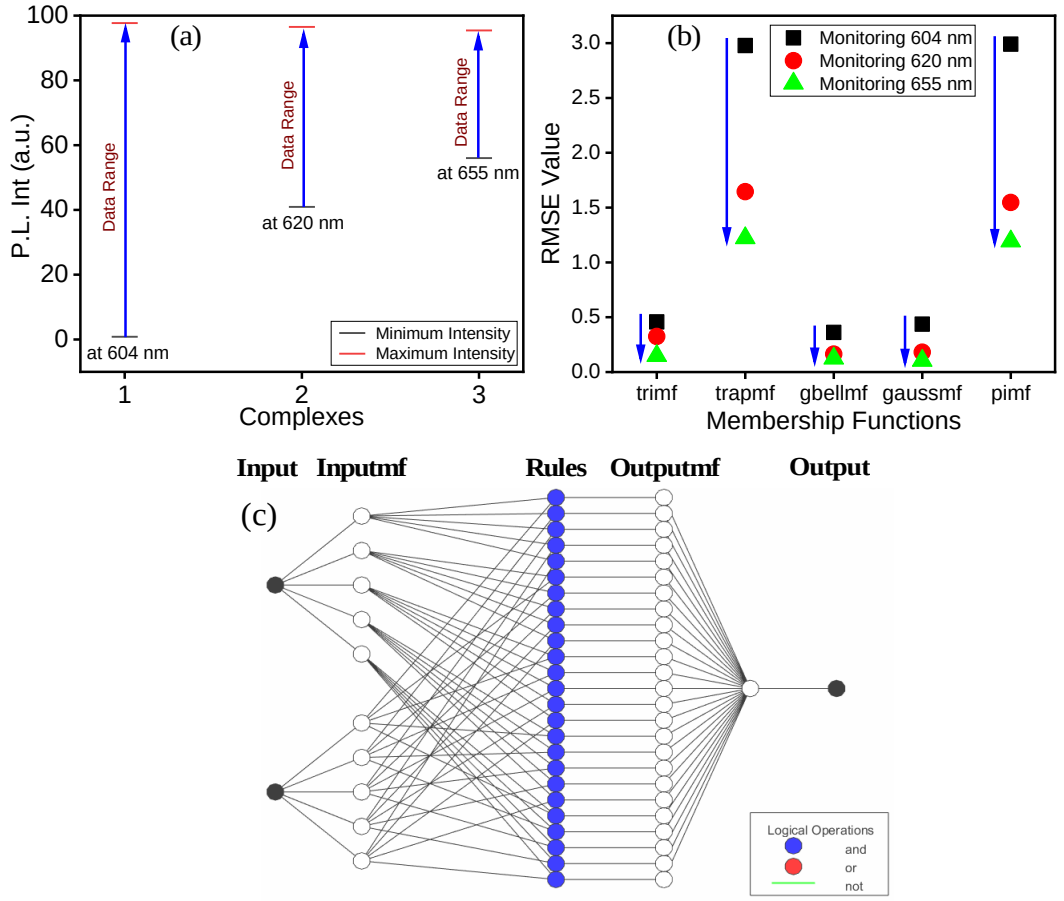

Figure 3.12. (a) Emission intensity data range of **1-3**. (b) ANFIS generated root mean square error (RMSE) values of **1-3** after operating with different types of membership functions. (c) Generated ANFIS structure.

3.6. Conclusions

In continuation with our persistent research focus on delving into molecular-level computation and implication of machine learning and other artificial intelligence tools in chemistry, we utilized herein anion- and acid-responsive behaviors of a new array of Ru(II)-bipyridine complexes based on polypyridyl-imidazole bridging ligand. All the complexes possess imidazole NH proton(s) in their secondary coordination sphere that could be deprotonated by specific anion resulting in substantial alteration of their photophysical characteristics. We have chosen Ru(II)-polypyridine complexes as our choice due to their versatile and tuneable photophysical and electrochemical properties which in turn could lead to fabrication of prospective molecular sensors and switches when exposed to appropriate external stimuli. The absorption and both steady state and time-resolved emission spectral characteristics of the metalloreceptors underwent substantial modulation in presence of basic anions like F^- and CN^-. Incipient hydrogen bonding

followed by anion-induced deprotonation is responsible for the observed change in the spectral properties. Notably, the deprotonation of the metalloreceptors by specific anions, followed by restoration to their initial states by acid is feasible and process could be reiterated multiple cycles.

The metalloreceptors exhibit sophisticated Boolean logic functions, such as implication- logic gates, by harnessing their spectral responses through appropriate utilization of different inputs, including anions and acid. It is to be noted that carrying out extensive sensing experiments involving the manipulation of analyte concentrations across a broad spectrum is frequently a time-consuming, labor-intensive, and expensive process. In order to address these challenges, we have applied artificial intelligence (AI)-based tools for proper prediction as well as understanding the complete sensing characteristics of the metalloreceptors. In this work, we have designed an amalgamated neuro-fuzzy system that incorporates five widely used membership functions (*trimf*, *trapmf*, *gbellmf*, *gaussmf*, and *pimf*) into an adaptive neuro-fuzzy inference system (ANFIS) for accurate prediction of the experimental data. This approach is employed to develop an algorithm for infinite-valued logic by using the emission spectral output of the receptors when subjected to anions and acid. Herein, we also conducted a comparison among the results produced by five ANFIS models, each of which was constructed using different membership functions. The model outputs are subsequently employed for modeling the protonation-deprotonation behaviors of the metalloreceptors. The satisfactory RMSE values observed for ANFIS models, in particular with *gaussmf* and *gbellmf* membership functions, suggest that the predicted values of sensing data from these models are remarkably accurate and show a significant degree of resemblance to the experimental data. Therefore, membership function assisted artificial intelligence-based neuro-fuzzification approach holds promise as a potential model for ion sensing data in the context of the current Ru(II)-based metalloreceptors.

3.7. References

1. Artrith, N.; Butler, K. T.; Coudert, F. X.; Han, S.; Isayev, O.; Jain, A.; Walsh, A. Best Practices in Machine Learning for Chemistry. *Nat. Chem.*, **2021**, *13*, 505-508.
2. Mater, A. C.; Coote, M. L. Deep Learning in Chemistry. *J. Chem. Inf. Model* **2019**, *59*, 2545-2559.
3. Pflüger, P. M.; Glorius, F. Molecular Machine Learning: The Future of Synthetic Chemistry?. *Angew. Chem., Int. Ed.* **2020**, *59*, 18860-18865.
4. He, L.; Bai, L.; Dionysiou, D. D.; Wei, Z.; Spinney, R.; Chu, C.; Lin, Z.; Xiao, R. Applications of Computational Chemistry, Artificial Intelligence, and Machine Learning in Aquatic Chemistry Research. *Chem. Eng. J.* **2021**, *426*, 131810.
5. Zadeh, L. A. Toward Human Level Machine Intelligence-Is It Achievable? The Need for a Paradigm Shift. *IEEE Comput. Intell. Mag.* **2008**, *3*, 11-22.
6. Szaciłowski, K. Digital Information Processing in Molecular Systems. *Chemical Reviews* **2008**, *108*, 3481-3548.
7. Zadeh, L. A. Outline of a New Approach to the Analysis of Complex Systems and Decision Processes. *IEEE Transactions on systems, Man, and Cybernetics*, **1973**, *3*, 28-44.
8. Conrad, M. Molecular Computing. *Adv. Comput.***1990**, *31*, 235-324.
9. Wlaźlak, E.; Przyczyna, D.; Gutierrez, R.; Cuniberti, G.; Szaciłowski, K. Towards Synthetic Neural Networks: Can Artificial Electrochemical Neurons be Coupled with Artificial Memristive Synapses?. *Jpn. J. Appl. Phys.* **2020**, *59*, SI0801.
10. Szaciłowski, K. Molecular Logic Gates Based on Pentacyanoferrate Complexes: From Simple Gates to Three-Dimensional Logic Systems. *Chem. Eur. J.* **2004**, *10*, 2520-2528.
11. Adamatzky, A.; Costello, B. D. L. Experimental Logical Gates in a Reaction-Diffusion Medium: The XOR Gate and Beyond. *Phys. Rev. E: Stat., Nonlinear, Soft Matter Phys.* **2002**, *66*, 046112.
12. Adamatzky, A.; Tegelaar, M.; Wosten, H. A.; Powell, A. L.; Beasley, A. E.; Mayne, R. On Boolean Gates in Fungal Colony. *Biosystems* **2020**, *193*, 104138.
13. Adamatzky, A.; Jones, J.; Mayne, R.; Tsuda, S.; Whiting, J. Logical Gates and Circuits Implemented in Slime Mould. *Advances in Physarum Machines: Sensing and Computing with Slime Mould*, **2016**, 37-74.
14. Khatua, S.; Samanta, D.; Bats, J. W.; Schmittel, M. Rapid and Highly Sensitive Dual-Channel Detection of Cyanide by Bis-Heteroleptic Ruthenium (II) Complexes. *Inorg. Chem.* **2012**, *51*, 7075-7086.

15. Shu, Q.; Birlenbach, L.; Schmittel, M. A Bis (Ferrocenyl) Phenanthroline Iridium (III) Complex as a Lab-on-a-Molecule for Cyanide and Fluoride in Aqueous Solution. *Inorg. Chem.* **2012**, *51*, 13123-13127.
16. Schmittel, M.; Qinghai, S. A Lab-on-a-Molecule for Anions in Aqueous Solution: Using Kolbe Electrolysis and Radical Methylation at Iridium for Sensing. *Chem. Commun.* **2012**, *48*, 2707−2709.
17. Gale, P. A. Anion Receptor Chemistry. *Chem. Commun*. **2011**, *47*, 82-86.
18. Sessler, J. L.; Davis, J. M. Sapphyrins: Versatile Anion Binding Agents. *Acc. Chem. Res.* **2001**, *34*, 989−997.
19. Chen, K.; Schmittel, M. A Triple-Channel Lab-on-a-Molecule for Triple-Anion Quantification Using an Iridium(III)-Imidazolium Conjugate. *Chem. Commun.* **2014**, *50*, 5756−5759.
20. Gentili, P. L. The Fuzziness of the Molecular World and Its Perspectives. *Molecules*, **2018**, *23*, 2074.
21. Gentili, P. L. The Fundamental Fuzzy Logic Operators and Some Complex Boolean Logic Circuits Implemented by the Chromogenism of a Spirooxazine. *Phys. Chem. Chem. Phys.* **2011**, *13*, 20335-20344.
22. Gentili, P. L.; Giubila, M. S.; Heron, B. M. Processing Binary and Fuzzy Logic by Chaotic Time Series Generated by a Hydrodynamic Photochemical Oscillator. *ChemPhysChem.* **2017**, *18*, 1831-1841.
23. Gentili, P. L.; Giubila, M. S.; Germani, R.; Romani, A.; Nicoziani, A.; Spalletti, A.; Heron, B. M. Optical Communication among Oscillatory Reactions and Photo-Excitable Systems: UV and Visible Radiation Can Synchronize Artificial Neuron Models. *Angew. Chem., Int. Ed.*, **2017**, *56*, 7535-7540.
24. Gentili, P. L.; Perez-Mercader, J. Quantitative Estimation of Chemical Microheterogeneity through the Determination of Fuzzy Entropy. *Front. Chem.* **2022**, *10*, 950769.
25. Schumann, A.; Adamatzky, A. The Double-Slit Experiment with Physarum Polycephalum and P-Adic Valued Probabilities and Fuzziness. *Int. J. Gen. Syst.* **2015**, *44*, 392-408.
26. Korshunova, M.; Ginsburg, B.; Tropsha, A.; Isayev, O. OpenChem: A Deep Learning Toolkit for Computational Chemistry and Drug Design. *J. Chem. Inf. Model.* **2021**, *61*, 7-13.

27. Lu, J.; Zhang, Y. Unified Deep Learning Model for Multitask Reaction Predictions with Explanation. *J. Chem. Inf. Model.* **2022**, *62*, 1376-1387.
28. Singh, K.; Munchmeyer, J.; Weber, L.; Leser, U.; Bande, A. Graph Neural Networks for Learning Molecular Excitation Spectra. *J. Chem. Theory Comput.* **2022**, *18*, 4408-4417.
29. Yao, K.; Herr, J. E.; Brown, S. N.; Parkhill, J. Intrinsic Bond Energies from a Bonds-in-Molecules Neural Network. *J. Phys. Chem. Lett.* **2017**, *8*, 2689-2694.
30. Cho, E. H.; Deng, X., Zou, C.; Lin, L. C. Machine Learning-Aided Computational Study of Metal–Organic Frameworks for Sour Gas Sweetening. *J. Phys. Chem. C*, **2020**, *124*, 27580-27591.
31. İnal, M. Predicting the Conversion Ratio for the Leaching of Celestite in Sodium Carbonate Solution Using an Adaptive Neuro-Fuzzy Inference System. *Ind. Eng. Chem. Res.* **2014**, *53*, 4975-4980.
32. Bingöl, D.; Inal, M.; Çetintaş, S. Evaluation of Copper Biosorption onto Date Palm (Phoenix Dactylifera L.) Seeds with MLR and ANFIS Models. *Ind. Eng. Chem. Res.* **2013**, *52*, 4429-4435.
33. Brown, K. A.; Brittman, S.; Maccaferri, N.; Jariwala, D.; Celano, U. Machine Learning in Nanoscience: Big Data at Small Scales. *Nano Letters* **2019**, *20*, 2-10.
34. Sahoo, A.; Ahmed, T.; Deb, S.; Baitalik, S. Neuro-Fuzzification Architecture for Modeling of Electrochemical Ion-Sensing Data of Imidazole-Dicarboxylate-Based Ru (II)–Bipyridine Complex. *Inorg. Chem.* **2022**, *61*, 10242-10254.
35. Sahoo, A.; Baitalik, S. Fuzzy Logic, Artificial Neural Network and Adaptive Neuro-Fuzzy Inference Methodology for Soft Computation and Modeling of Ion Sensing Data of a Terpyridyl-Imidazole Based Bifunctional Receptor. *Front. Chem.* **2022**, *10*, 864363.
36. Sahoo, A.; Bar, M.; Biswas, R.; Abedin, T.; Baitalik, S. Modulation of Ground and Excited State Properties of Ruthenium Complexes through Sequential Incorporation of Metal into a Polypyridyl-Imidazole Bridging Ligand. *Dalton Trans.* **2023**, *52*, 15896-15906.
37. Cametti, M.; Rissanen, K. Recognition and Sensing of Fluoride Anion. *Chem. Commun.* **2009**, *20*, 2809-2829.
38. Gale, P. A.; García-Garrido, S. E.; Garric, J. Anion Receptors Based on Organic Frameworks: Highlights From 2005 and 2006. *Chem. Soc. Rev.* **2008**, *37*, 151-190.
39. Gale, P. A.; Gunnlaugsson, T. Preface: Supramolecular Chemistry of Anionic Species Themed Issue. *Chem. Soc. Rev.* **2010**, *39*, 3595-3596.

40. Amendola, V.; Bonizzoni, M.; Esteban-Gomez, D.; Fabbrizzi, L.; Licchelli, M.; Sancenon, F.; Taglietti, A. Some Guidelines for the Design of Anion Receptors. *Coord. Chem. Rev.* **2006**, *250*, 1451-1470.
41. Marin-Hernandez, C.; Santos-Figueroa, L. E.; Moragues, M. E.; Raposo, M. M. M.; Batista, R. M.; Costa, S. P.; Pardo, T.; Martínez-Máñez, R.; Sancenon, F. Imidazoanthraquinone Derivatives for the Chromofluorogenic Sensing of Basic Anions and Trivalent Metal Cations. *J. Org. Chem.* **2014**, *79*, 10752-10761.
42. Steed, J. W.; Coordination and Organometallic Compounds as Anion Receptors and Sensors. *Chem. Soc. Rev.*, **2009**, *38*, 506-519.
43. Manez, R. M.; Sancenon, F. Fluorogenic and Chromogenic Chemosensors and Reagents for Anions. *Chem. Rev*. **2003**, *103*, 4419-4476.
44. Bowman-James, K. Alfred Werner Revisited: The Coordination Chemistry of Anions. *Acc. Chem. Res*. **2005**, *38*, 671-678.
45. Schmittel, M.; Mal, P.; de los Rios, A. Multiport Logic Operations Triggered by Protonation-a Tris-Phenanthroline as a 3-Input AND-NOR-OR Circuit. *Chem. Commun.* **2010**, *46*, 2031−2033.
46. Chen, K.; Schmittel, M. An Iridium(III) Complex as a Versatile Platform for Molecular Logic Gates: An Integrated Full Subtractor and 1:2 Demultiplexer. *Anal. Bioanal. Chem.* **2016**, *408*, 7077−7083.
47. Biswas, P. K.; Saha, S.; Gaikwad, S.; Schmittel, M. Reversible Multicomponent AND Gate Triggered by Stoichiometric Chemical Pulses Commands the Self-Assembly and Actuation of Catalytic Machinery. *J. Am. Chem. Soc*. **2020**, *142*, 7889−7897.
48. Mizuno, T.; Wei, W.-H.; Eller, L. R.; Sessler, J. L. Phenanthroline Complexes Bearing Fused Dipyrrolylquinoxaline Anion Recognition Sites: Efficient Fluoride Anion Receptors. *J. Am. Chem. Soc*. **2002**, *124*, 1134−1135.
49. Hargrove, A. E.; Nieto, S.; Zhang, T.; Sessler, J. L.; Anslyn, E. V. Artificial Receptors for the Recognition of Phosphorylated Molecules. *Chem. Rev*. **2011**, *111*, 6603−6782.
50. Martínez-Máñez, R.; Sancenón, F. Fluorogenic and Chromogenic Chemosensors and Reagents for Anions. *Chem. Rev.* **2003**, *103*, 4419−4476.
51. Omana, M.; Papasso, G.; Rossi, D.; Metra, C. A Model for Transient Fault Propagation in Combinatorial Logic. 9th IEEE On-Line Testing Symposium, **2003**, 111−115.
52. Zhang, Y.; Liu, W.; Zhang, W.; Yu, S.; Yue, X.; Zhu, W.; Zhang, D.; Wang, Y.; Wang, J. DNA-Mediated Gold Nanoparticle Signal Transducers for Combinatorial Logic Operations and Heavy Metal Ions Sensing. *Biosens. Bioelectron*. **2015**, *72*, 218−224.

53. Das, S., Saha, D.; Bhaumik, C.; Dutta, S.; Baitalik, S. Ru (II) And Os (II) Mixed-Chelates Derived from Imidazole-4, 5-Dicarboxylic Acid and 2, 2′-Bipyridine as Colorimetric Sensors for Anions: Synthesis, Characterization and Binding Studies. *Dalton Trans.* **2010**, *39*, 4162-4169.
54. Margulies, D.; Melman, G.; Felder, C. E.; Arad-Yellin, R.; Shanzer, A. Chemical Input Multiplicity Facilitates Arithmetical Processing. *J. Am. Chem. Soc.* **2004**, *126*, 15400-15401.
55. Margulies, D.; Felder, C. E.; Melman, G.; Shanzer, A. A Molecular Keypad Lock: A Photochemical Device Capable of Authorizing Password Entries. *J. Am. Chem. Soc.* **2007**, *129*, 347-354.
56. Deb, S.; Sahoo, A.; Ahmed, T.; Baitalik, S. Stimuli-Responsive Molecular Switches and Logic Devices Based on Ru (II)–Terpyridyl–Imidazole Coordination Motif. *J. Phys. Chem. B* **2021**, *125*, 8919-8931.
57. Paul, A.; Sahoo, A.; Bhattacharya, S.; Baitalik, S. Anion and Temperature Responsive Molecular Switches Based on Trimetallic Complexes of Ru (II) and Os (II) that Demonstrate Advanced Boolean and Fuzzy Logic Functions. *Inorg. Chem.* **2022,** *61*, 3186-3201.
58. Bhattacharya, S.; Sahoo, A.; Baitalik, S. Human Brain-Inspired Chemical Artificial Intelligence Tools for the Analysis and Prediction of the Anion-Sensing Characteristics of an Imidazole-Based Luminescent Os (II)-Bipyridine Complex. *Dalton Trans.* **2023**, *52*, 6749-6762.
59. MATLAB 2018a, The MathWorks, Inc., Natick, Massachusetts, United States.
60. Mamdani. E. H. Application of Fuzzy Logic to Approximate Reasoning Using Linguistic Synthesis. *IEEE Trans. Comput.* **1977**, *100*, 1182-1191.
61. Jang, J. S.; Sun, C. T. Neuro-Fuzzy Modeling and Control. *Proc. IEEE* **1995**, *83*, 378-406.
62. Sugeno, M.; Yasukawa, T. A Fuzzy-Logic-Based Approach to Qualitative Modeling. *IEEE Trans. Fuzzy Syst.* **1993**, *1*, 7.

****

4.1. Introduction

The machine learning (ML) and various artificial intelligence (AI) tools are now widely been employed in diverse fields in chemistry, materials sciences and biology.[1-9] One of the most important foci of the present-day research is to design smart materials and to analyze their diverse physicochemical data (such as sensing) for the diagnostic grounds. But relatively little advancement has been made in other subsidiary domains of AI, such as fuzzy, ANNs, ANFIS, robotics, and evolutionary computation.[10-19] Fabrication of reliable and comprehensive database could expand the ML to a boarder domain of applications. Significant emphasis is now been put forward to flourish the fertile area of AI with vague and imprecise inputs.

One of the major aspects of the present work is to mimic advanced Boolean and Fuzzy logic functions at the molecular level upon judicious use of their spectral and electrochemical responses upon the influence of suitable external stimuli. The processing of information at the molecular level is a vibrant area of research and rational executions of appropriate logic functions by smart molecules is a great challenge for the researchers.[20-28] In the present study, we have utilized an imidazole-dicarboxylate based Ru(II)-bipyridine complex possessing a number of dissociable protons in its secondary coordination sphere for this purpose (**Chart 4.1**).[29,30] The motivation of choosing Ru(II)-polyheterocyclic complex is because of its very rich and tunable photophysical and electrochemical behaviors which in turn gives rise to construction of potential molecular switches and devices in presence of suitable external stimuli such as light, anions, cations, acid and base.[31-41] The absorption, emission and electrochemical behavior of the metalloreceptor is significantly modulated upon the influence of basic anions (such as F^-, AcO^- and $H_2PO_4^-$) as well as by changing the pH.[42-47] Interestingly, the deprotonation of the metalloreceptor by selected anions or by alkaline pH followed by its restoration to its original form by acid or acidic pH is reversible and could be repeated many cycles. The metalloreceptor is capable to demonstrate several advanced Boolean logic functions through the use of its spectral and electrochemical responses upon the influence of anions, acid and solution of appropriate pH).[48-56] The beauty of the present system is the use of its electrochemical responses (cyclic and square wave voltammetric signals) compared with the absorption and emission spectral response of our previously reported receptors.

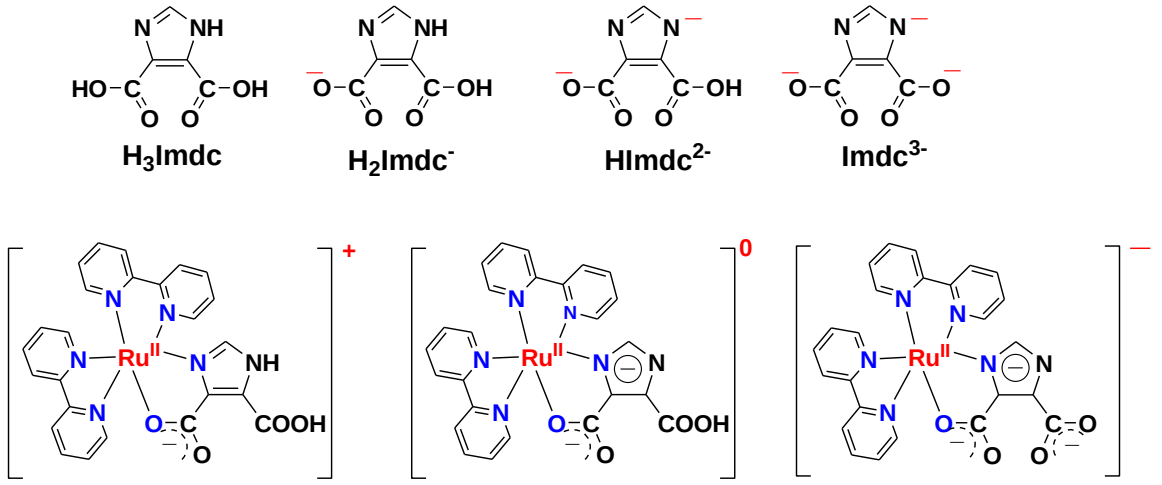

Chart 1. Chemical structures of different protonation states of the complex.

The operation of a Boolean logic (BL) banks on spreading of the output at the two extremes, either "0" or "1".[48-56] Most of the real systems, on the other hand, are composed of several in-between states. To address the intervening conditions, fuzzy logic (FL) is expected to be a potential choice. The enthusiasm in picking out the FLS depends on the notion that the conceptualization and decision-taking action in human brain is exceptionally complex to be accurately expressed and thought to act as mechanized fine-tuning administer for countless number of intermediate stages with different degrees of truths. FLS comprises of non-linear mapping of the input vectors to the scalar outputs. In this work, we also enforce FL to generate an infinite-valued logic algorithm by using the electrochemical output of the receptor upon the action of anions, acid and solution of appropriate pH.

Execution of extensive sensing experiments upon changing the analyte concentration within a wide range is usually tedious as well as exorbitantly expensive. To get rid of these difficulties, we employed here several soft computing tools, viz. ANNs, FL and ANFIS to predict the experimental data. An ANN is a network stimulated by the central nervous system of the animals, primarily the brain. ANNs are often employed to guess functions which could rely on huge number of unknown inputs. Two principal categories of neural networks, viz. recurrent (RNN) and feed-forward (FFN) are commonly applied to represent a complex system. RNN comprises of connections between units yielding a directed cycle and generates an internal state of the network which permits it to show dynamic temporal

conduct. RNN is mainly employed to depict the dynamic organizations. But considering the static nature of our system, we employed FNN in the present study. FNN is the simplest and convenient category of network where the information passes into a particular direction, proceeds, from the input nodes, via the hidden notes, and finally to the output nodes. It is to be noted that no loops are associated with FNN. Additionally, due to its high efficiency in forecasting static system, we implemented advanced feed-forward back propagation network, namely, ANN-function fitting (ANN-FF) network for deeper understanding and forecasting of the system.

As mentioned earlier, FL is employed to learn numerous input parameters of realistic networks and fruitfully implemented in the control engineering domain. Amalgamation of FL with neutral networks leads to the generation of ANFIS which often gives rise to noteworthy results. NNs have the good capability to grasp from the data but usually quite difficult to better understand the actual meaning related to each neuron and its weight. In comparison to NNs, the models relying on fuzzy-logic are readily understandable as FL adopts linguistic languages and IF-THEN law. In contrary to NNs, FLs are unable to learn by itself. To learn and identify FLs, one needs to accept methodologies from other domains, viz. statistics, system identification etc. As the NNs are capable to learn, it is quite logical to combine these two methodologies and the consolidated technique that combines FL with the learning capability of NNs is termed as neuro-fuzzy networks. The skeleton of ANFIS possesses the same components as the fuzzy interference system with the exception of NN block. Herein, we also compared of the results of Fuzzy, ANN and ANFIS models with the experimental results for appropriate modeling of the sensing behavior of the metalloreceptor.

4.2. Experimental Section

4.2.1. Materials. Reagent grade chemicals obtained from commercial sources were used as received. Solvents were purified and dried according to standard methods.[35] 4,5-imidazole dicarboxylic acid and tetrabutylammonium (TBA) salt of the anions were purchased from Sigma-Aldrich. *Cis*–$[Ru(bpy)_2Cl_2]\cdot 2H_2O$[36] was prepared by the literature method. $AgClO_4$ was prepared from silver carbonate and perchloric acid and recrystallized from benzene.

4.2.2. Preparation of the metal complexes. The complexes were prepared under oxygen and moisture free dinitrogen using standard Schlenk techniques.

Caution! $AgClO_4$ and perchlorate salts of the metal complexes used in this study are potentially explosive and therefore should be handled with care in small quantities.

$[(bpy)_2Ru(H_2Imdc)](ClO_4)\cdot 2H_2O$. To a stirred suspension of cis–$[Ru(bpy)_2Cl_2]\cdot 2H_2O$ (0.52 g, 1 mmol) in ethanol (50 mL) was added solid $AgClO_4$ (0.42 g, 2 mmol). After 0.5 h, the precipitated AgCl was removed by filtration and the filtrate containing $[Ru(bpy)_2(EtOH)_2]^{2+}$ was treated with powdered H_3Imdc (0.19 g, 1.2 mmol) and 1 ml of 1 mmol dm^{-4} of $HClO_4$. The mixture was heated under reflux for 8 h with continuous stirring after which it was filtered to remove the unreacted solid. The filtrate was concentrated to approximately 20 mL and kept overnight at 5° C. The orange red crystals that deposited were collected by filtration and recrystallized from methanol–water (4:1) containing a few drops of 1 mmol dm^{-4} of $HClO_4$; yield 0.42 g (60%). Anal. Found: C, 42.53; H, 3.41; N, 11.73, Calc. for $C_{25}H_{23}N_6ClO_{10}Ru$: C, 42.65; H, 3.29; N, 11.94 %. IR(KBr) υ (cm^{-1}): 3400, 3093, 1718, 1603, 1580, 1543, 1498, 1463, 1445, 1421, 1377, 1268, 1245, 1090, 1023, 762, 729, 623. ^{1}H NMR data {300 MHz, DMSO-d_6, TMS, δ (ppm), see scheme 1 for atom numbering}: 16.80 (s, 1H, COOH), 14.38 (s, 1H, NH)), 8.79 (d, 1H, *J* = 8.0 Hz, H(3)), 8.74 (d, 1H, *J* = 8.0 Hz, H(3)), 8.72-8.68 (m, 2H, H(6)+H(3)), 8.62 (d, 1H, *J* = 8.0 Hz, H(3)), 8.22 (d, 1H, *J* = 5.0 Hz, H(6)), 8.19-8.14 (m, 2H, H(4)), 7.98 (t, 1H, *J* = 8.0 Hz, H(4)), 7.89 (t, 1H, *J* = 8.0 Hz, H(4)), 7.86 (s, 1H, H(7)), 7.77 (t, 1H, *J* = 6.5 Hz, H(5)), 7.74 (d, 1H, *J* = 5.5 Hz, H(6)), 7.66 (t, 1H, *J* = 7.0 Hz H(5)), 7.64 (d, 1H, *J* = 6.0 Hz, H(6)), 7.36 (t, 1H, *J* = 6.5 Hz, H(5)), 7.26 (t, 1H, *J* = 6.5 Hz, H(5)). ESI-MS (positive, CH_3CN) *m/Z* = 568.79 (100 %) $[(bpy)_2Ru(H_2Imdc)]^+$. UV-VIS [CH_3CN; λ_{max}, nm (ε, $dm^3\,mol^{-1}cm^{-1}$)]: 485 (8950), 440 (5740), 345 (8770), 291 (56 470), 243 (29 500).

4.2.3. Physical Measurements. The details of different equipments used and experimental process to measure absorption, luminescence and electrochemical spectral behaviors have been presented in chapter 2.

pH measurements were carried out with a series of MeCN-aqueous buffer (3:2) solutions containing the same amount of the complex and pH adjusted in the range 2–12. Robinson-Britton buffer were used in the study. The pH measurements were made with a

Beckman Research Model pH meter. The pH meter responded reproducibly to the variation of hydrogen ion concentration and as such, the pH meter readings were referred to as pH.

Experimental uncertainties were as follows: absorption maxima, ±2 nm; molar absorption coefficients, 10%; emission maxima, ±5 nm; excited–state lifetimes, 10%; luminescence quantum yields, 20%; redox potentials, ±10 mV.

4.2.4. Computational Methods. The details of computational methods of ANFIS have already been discussed in chapter 3.

4.2.4.1. Artificial Neural Networks (ANNs). An artificial neural network is a network stimulated by the central nervous system of the animals, primarily the brain. ANNs are often employed to guess functions which could rely on huge number of unknown inputs. Among the two principal categories of neural networks, viz. recurrent (RNN) and feed-forward (FFN), we employed FNN in the present study due to static nature of our system. FNN is the simplest and convenient category of network where the information passes into a particular direction, proceeds, from the input nodes, via the hidden notes, and finally to the output nodes. Additionally, due to its high efficiency in forecasting static system, we implemented advanced feed-forward back propagation network, namely, ANN-function fitting (ANN-FF) network for deeper understanding and forecasting of the system.

Artificial neural network model consists of 2 inputs, 5 hidden layers and 1 output. In ANN-FF, the relation between the input and output is assumed to be a function, which is approximated using the experimental data. The network diagram of the ANN-FF for the system can be found in Figure 4.10b. It can fit multidimensional mapping problems arbitrarily well when consistent data and enough neurons are designed in the hidden layer. For function fitting of the problem, a neural network is needed to map between a data set of numeric inputs and a set of numeric targets. Hence, each pattern is assigned a number (e.g., 1, 2, 3, 4, etc.).

In this study, a neural network for function fitting was coded in MATLAB 2018. The input data present the network, while the target data define the desired network output. The current intensity outputs upon the action of 31 different combinations of two inputs (input 1=H^+ and input 2=F^-) were taken. Thus, the 31×2 matrix represents the static input data of 31 samples involving 2 inputs, while 31×1 matrix represents the static

output data (at 0.71V) of one element. Now, the 31 samples are divided into 3 sets of data. 70% of the data are conferred for the training and the network is corrected according to its error. Now the learning algorithm and the number of neurons in the hidden layer were optimized. 15% data are employed to compute the network generalization and to halt training. When generalization stops improving, the data validation takes place. The remaining 15% data give an independent estimate of the network performance during and after the training, called testing data (Figure 4.9a).

4.3. Results and Discussion

4.3.1. Overview of Photo-Redox as well as Anion- and pH-Sensing Behavior of the Meatallorecptor. Synthesis, characterization and photo-redox behaviors as well as anion- and pH sensing aspects of $([bpy)Ru(Imdc)]^{+}$ has been reported by our group.[29,30] A concise overview of the photophysical, electrochemical and sensing behavior of the complex is again outlined here for the sake of the readers (Table 4.1). The complex displays an intense absorption peak at 485 nm and a shoulder at 440 nm in MeCN due to Ru(d)→bpy (π^*) charge transfer (MLCT) transitions and several intense bands in the UV region arising out of internal transitions of the H_2Imdc^- ligand as well as π–π^* transitions of bpy moieties. The complex also displays an emission band at 690 nm from radiative deactivation of its ^{3}MLCT state having lifetime (τ)=55 ns and quantum yield (Φ)=5.4×10^{-4} at RT. By virtue of the presence of imidazole NH and carboxylic acid moieties in its outer coordination sphere, the metalloreceptor interacts strongly with F^-, AcO^- and $H_2PO_4^-$ among the other studied anions (Cl^-, Br^-, I^-, NO_3^-, and ClO_4^-) resulting in significant alteration in its absorption, emission and redox behaviors. Titration experiments were carried out to obtain quantitative perception of receptor-anion interaction event (Figure 4.1). One-step change is observed in each case in presence of F^-, AcO^- and $H_2PO_4^-$. In the absorption spectra, gradual decrease in MLCT band at 485 nm occurs and at its expense a band at ~525 nm evolves and increases in intensity up to 1 equiv of the anions (Figure 4.1a). The emission intensity of the band at 690 nm enhanced substantially accompanied with a red-shift to 740 nm upon addition of the said anions (Figure 4.1b). The complex exhibits a reversible oxidation wave with $E_{1/2}$ = 0.96 V in MeCN due to Ru^{III}/Ru^{III} process, while two successive reversible waves at $E_{1/2}$ = -1.45 and -1.77 V because of the reduction of two bpy units (Figure 4.2). Upon incremental

Table 4.1. The Photophysical and Electrochemical Data of the Three Different Forms of the Complex (**1**$^+$, **1** and **1**$^-$).

Compounds	λ_{max} (ε, in $M^{-1}cm^{-1}$)	λ_{emi}, nm at RT	Quantum Yield (ϕ)	Experimental Redox potential (Volt)	
				$E_{1/2}$ (ox)	$E_{1/2}$(red)
1$^+$	485 (8950), 440 (5740), 345(8770), 291 (56470), 243 (29500).	690	5.4×10^{-4}	0.96	-1.45, -1.77
1	525 (9050), 465 (5100), 355 (9700), 294 (52470), 244 (26800).	740	3.0×10^{-3}	0.71	-1.43, -1.70
1$^-$	544 (9260), 485 (6300), 358 (11900), 297 (47750), 247 (29650).	770	1.3×10^{-3}	0.52	-1.42, -1.65

addition of F^-, the current intensity of the couple at 0.96 V gradually deceases and at its expense a new couple that generates at 0.71 V gradually intensified and at saturation the couple at 0.96 V is totally replaced by the new couple at 0.71 V.

In spite of the presence of two dissociable protons (NH and COOH), the metalloreceptor displays one-step change in presence of basic anions as the free COOH proton in the complex is engaged in intramolecular hydrogen bonding with O-atom of the coordinated CO_2^- moiety. In order to abstract the COOH proton from the complex backbone, we also studied previously the effect of pH (2-12) on the photo-redox behaviors of the complex in MeCN-H_2O buffer. The complex underwent two-step changes in the studied pH range according to equation (1) and the progressive change is reflected in its absorption and emission spectral profiles.

$$\mathbf{[(bpy)_2Ru(H_2Imdc)]^+ \underset{H^+}{\overset{K_1}{\rightleftharpoons}} [(bpy)_2Ru(HImdc)]^0 \underset{H^+}{\overset{K_2}{\rightleftharpoons}} [(bpy)_2Ru(Imdc)]^-} \quad \text{----(1)}$$

The first change occurs within the pH range of 4-8 with gradual red-shift of MLCT absorption bands and significant enhancement of emission band at 710 nm without alteration of the band maximum. The second step change takes place within the pH domain of 8-12 with further red-shift of MLCT absorption maxima and quenching of emission together with red-shift from 710 to 760 nm.

The oxidation potential of the complex was also measured within the pH range of 2-12. It was observed that $E_{1/2}$ value remains constant (0.96 V) when pH is either lower than 3 or

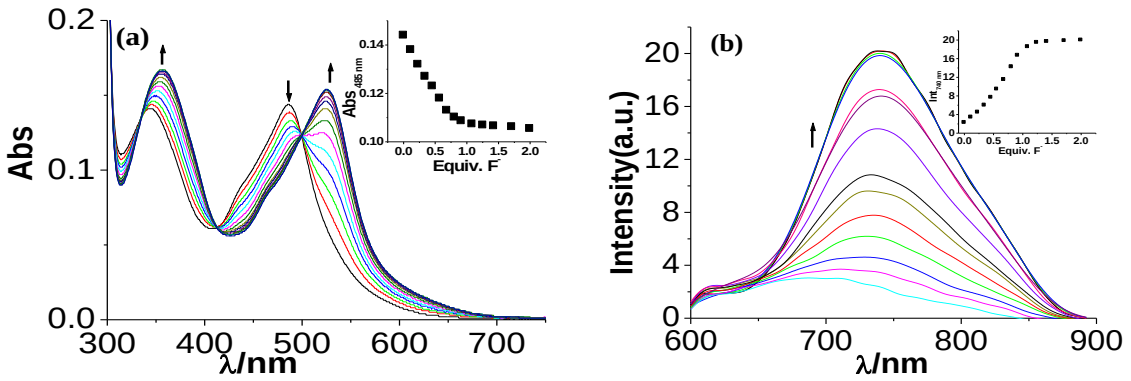

Figure 4.1. Absorption and emission spectral change of $[(bpy)_2Ru(H_2Imdc)]^+$ ($\mathbf{1}^+$) (a and b, respectively) upon gradual addition of F^- in MeCN.

higher than 11, suggesting that the electron-transfer reaction is not coupled with proton transfer. In the pH domain of 3.0-11.0, the slope of $E_{1/2}$ vs pH profile is ~ -60 mV/pH, indicating the occurrence of two consecutive one-proton and one-electron transfer process. The experimental outcomes indicate the anticipated trend of gradual decrease of $E_{1/2}$ value with increase in pH. The original $E_{1/2}$ value of 0.96 V of the complex gets substantially lowered (0.52 V) upon complete deprotonation at pH 11. Thus, the absorption, emission and redox experiments suggest that the basic anions (such as F^- and AcO^-) interact firmly with the complex in 1:1 stoichiometry, although such interaction is either feeble or absent in presence of the other studied anions (Cl^-, Br^-, I^-, NO_3^- and ClO_4^-). It appears that the imidazole N–H group initially interacts with F^-, AcO^- and $H_2PO_4^-$ through N–H----X^- hydrogen bonding and excess of X^- induces further lengthening of the N–H bond which ultimately splits through proton transfer reaction. In case with pH measurements, two successive deprotonation processes take place (initially from NH- and thereafter from COOH groups) with gradual increase of pH. Interestingly, the deprotonation of the metalloreceptor by selected anions or by alkaline pH followed by its restoration to its original form by acid or acidic pH is reversible and could be repeated many cycles. In the next section, we will demonstrate that the metalloreceptor is capable of

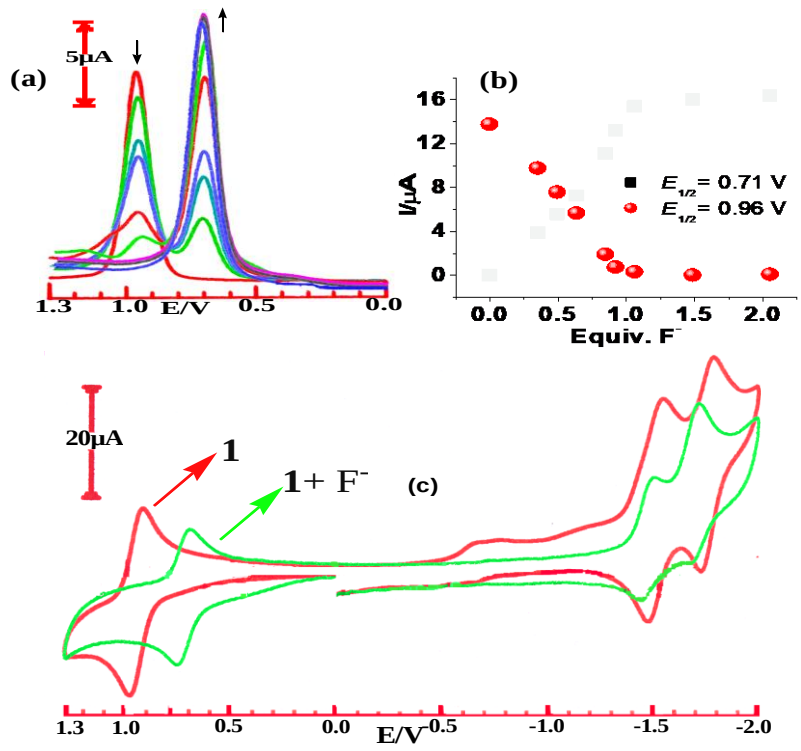

Figure 4.2. SWVs and CVs of receptor **1** (a and c) obtained upon incremental addition of TBAF to their CH_3CN solutions. The changes in the current intensities of **1** as a function of equivalents of F^- ion added are shown in (b).

mimicking the functions of several advanced Boolean logic functions, viz. three input OR gate, combinatorial logic gates, set-reset flip-flop logic and complicated function of traffic signal by employing its absorption- and emission spectral or electrochemical responses through proper use of different inputs (anions, acid and solution of appropriate pH). In order to minimize the time and expenses associated with performing very exhaustive sensing experiments by changing the analyte concentration within a vast range, we will also employ soft computing approaches like ANNs, Fuzzy-logic and ANFIS to predict the experimental data.

4.3.2. Three input OR gate. OR gate is one of the seven basic logic gates (AND, OR, XOR, NOT, NAND, NOR, and XNOR). To demonstrate the function of an OR gate, we have chosen both the emission intensity at 750 nm and absorbance at 525 nm as the output signal and F^-, AcO^- as well as $H_2PO_4^-$ as the three different anionic inputs (Figure 4.3 and 4.4). In presence of any of these three inputs, the emission intensity as well as the absorbance overcome the threshold barrier and generate the "ON" state (1). We can also

see the action of an OR gate in analog circuits (Figure 4.4e). The presence of any of the three inputs allows the current to pass through the circuit. By contrast, the absence of all three inputs will not allow the current to flow through the circuit.

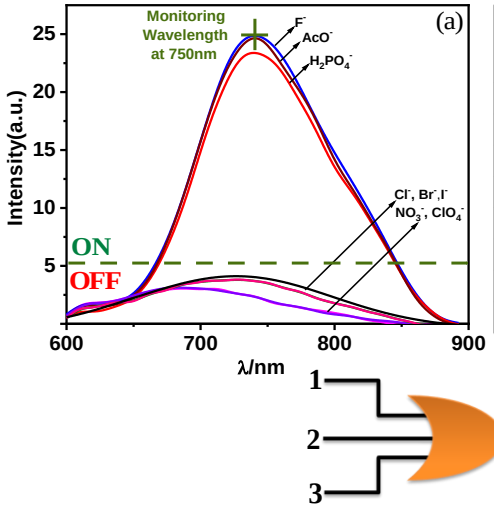

(b)

Input 1 (F^-)	Input 2 (AcO^-)	Input 3 ($H_2PO_4^-$)	Output Emission at 750nm
0	0	0	0 (low)
0	0	1	1(high)
0	1	0	1(high)
0	1	1	1(high)
1	0	0	1(high)
1	0	1	1(high)
1	1	0	1(high)
1	1	1	1(high)

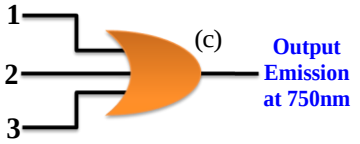

Figure 4.3. (a) The emission of spectrum **1** in CH_3CN in presence of selected anions. (b) Truth table of the OR gate. (c) Schematic representation of OR logic system.

4.3.3. Traffic Signaling. Trafficking is a process where information at molecular level is transferred from one channel to other in a controlled manner. This phenomenon is also important and applicable in daily life or inside the living organisms. In both transportation of ions in cellular system or crossing roads in daily life, a particular order is strictly conserved. To mimic molecular trafficking operation, we have chosen three different pH as the inputs, viz. pH 3 (In 1), pH 7 (In 2) and pH 10 (In 3). It has been observed that the extent as well as the direction of potential change in CV varies considerably upon various combinations of the inputs (Figure 4.5). The $E_{1/2}$ of the complex at 0.96 V is taken here as the output signal. The originated CVs at pH 3, pH 7 and pH 10 are designated as green, yellow and red signals, respectively. In Figure 4.5a, the high potential value (0.96 V) at pH 3 (green) allows the traffic to move. The intermediate potential (0.71V) at pH 7 signals the traffic to be stopped, while the low potential (0.45 V) in presence of pH 10 indicates the "traffic stop" state of the trafficking mechanism (Figure 4.5a).

4.3.4. Set-Reset Flip-Flop Logic. It is a consecutive binary logic circuit comprising of pair of cross-linked NOR gates. Here, H^+ plays the role of input 1, while F^-

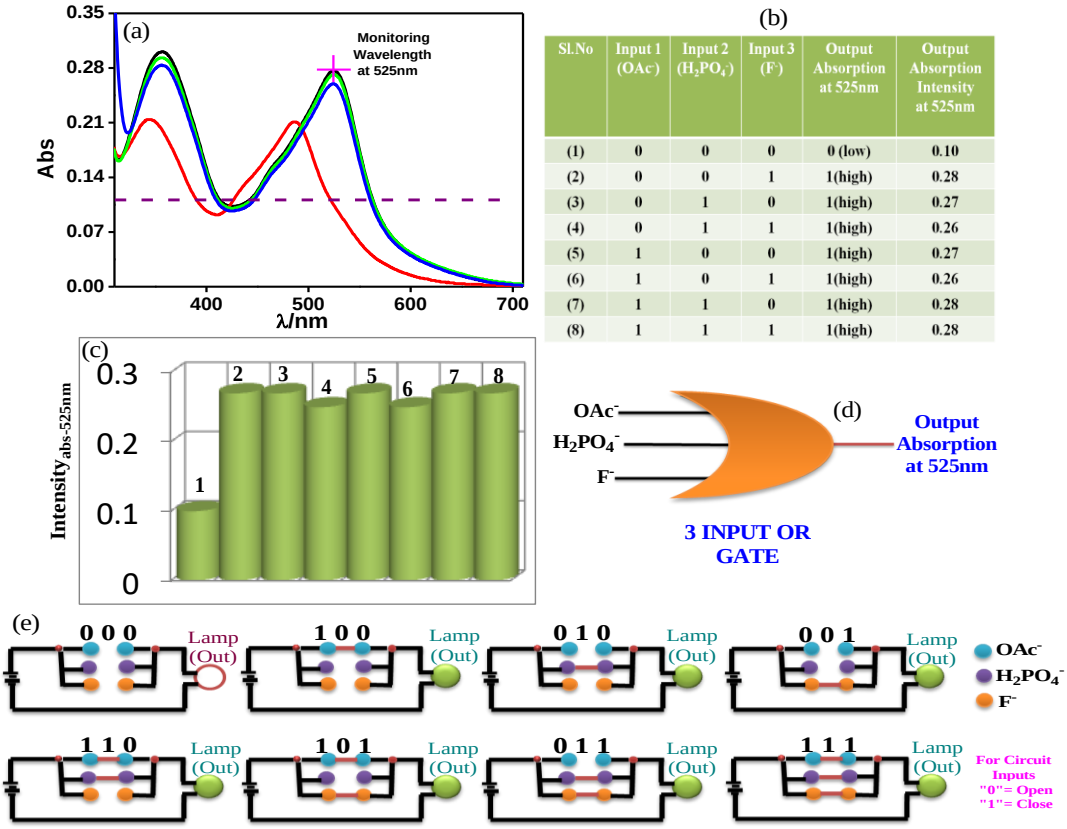

Sl.No	Input 1 (OAc^-)	Input 2 ($H_2PO_4^-$)	Input 3 (F^-)	Output Absorption at 525nm	Output Absorption Intensity at 525nm
(1)	0	0	0	0 (low)	0.10
(2)	0	0	1	1(high)	0.28
(3)	0	1	0	1(high)	0.27
(4)	0	1	1	1(high)	0.26
(5)	1	0	0	1(high)	0.27
(6)	1	0	1	1(high)	0.26
(7)	1	1	0	1(high)	0.28
(8)	1	1	1	1(high)	0.28

Figure 4.4. (a) The change in absorption spectrum of $\mathbf{1}^+$ in presence of OAc^-, $H_2PO_4^-$ and F^- in MeCN. (b) Truth table of the 3 input OR gate. (c) Histogram representing the variation in absorption intensity under different combinations of anionic inputs. (d) Schematic representation of 3 input OR gate. (e) Analog circuits for 3 input OR gate.

acts as input 2 and the current intensity at 0.71 and 0.96 V is treated as output 1 and output 2, respectively (Figure 4.6). In absence of both the inputs, the current intensity lies above the threshold barrier and designates the "ON" state (1). The presence of only F^- gives rise to the ON-state at 0.71V but OFF-state at 0.96 V. But addition of H^+ leads to the reverse behavior, viz. ON-state at 0.96 V but OFF-state at 0.71 V (Figure 4.6c). Hence, the "writing-reading-erasing-reading" of the electrochemical responses of the receptor mimic the function of set-reset flip-flop logic device (Figure 4.6d).

4.3.5. Fuzzy Logic Operations. Fuzzy logic was initiated with the proposition of fuzzy set theory by Lotfi Zadeh in 1965. It is an extension of classical set theory. In Boolean algebraic system, two crisp states (either '0' or '1') are used and the system is very efficient in differentiating true (1) and false (0) interactions. BL can't define any

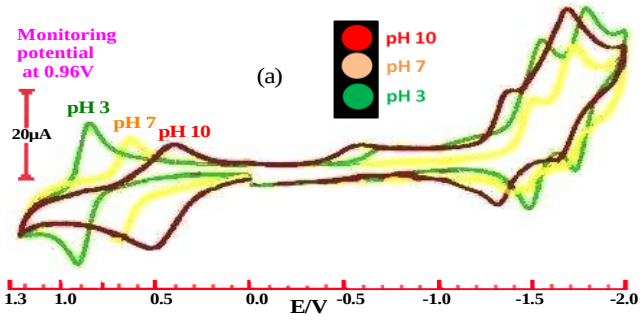

(b)

Input 1 pH 3	Input 2 pH 7	Input 3 pH 10	Monitoring Output Potential at 0.96V
0	0	0	0 (low)
0	0	1	0 (low)
0	1	0	0 (low)
0	1	1	0 (low)
1	0	0	1 (high)
1	0	1	0 (low)
1 (1st)	1 (2nd)	0	0 (low)
1	1	1	0 (low)

Figure 4.5. (a) The CVs of $\mathbf{1}^{+}$, **1**, and $\mathbf{1}^{-}$ in MeCN. (b) Truth table of the traffic signal at different pH.

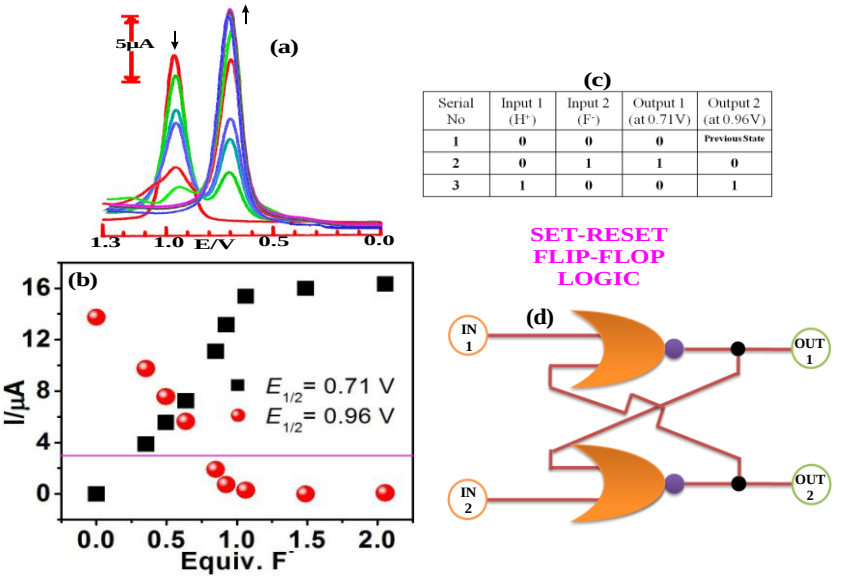

Figure 4.6. (a) The SWVs of receptor $\mathbf{1}^{+}$ in MeCN as a function of F^{-}. The variations of current intensities upon variation of F- are displayed figure b. The truth table and schematic representation of set-reset flip-flop logic is shown is figure c and d, respectively.

in-between values. But in real world, we often encounter complex situations that can't be defined by either "true" or "false" methodology. FL, on the other hand, provides a valuable flexibility and can define the intermediate states. Hence, FL is expected to be a potential alternative to handle the inconclusive information with regard to unclear and vagueness of many important chemical reactions.[57] FLS is composed of nonlinear mapping of input crisp data vector $(\bar{x})$ into scalar crisp output (y) and could be quantitatively expressed by the function: $y = f(\bar{x})$.

As shown in Figure 4.7, the electrochemical change of **1** varies to a great extent under the influence of H^+ (input 1) and F^- (input 2). Taking into account the large degree of change and in absence of exact values, the variables here could be expressed in terms of a few linguistic parameters of the triangular molecular functions (*trimf*), viz. low, medium, and high.[58] The effect of varying concentrations of H^+ and F^- on the current intensity of **1** could be displayed in terms of fuzzy sets (Figure 4.8). A collection of different IF-THEN statements comprising the inference rules are generated. The IF-portion refers to the predecessors, and the THEN-portion refers to the consequence. The gradual decrease in current intensity at 0.96 V and concomitant evolution at 0.71 takes place in presence of F^-, while the reverse situation takes place if H^+ is added. To this end, FL is executed onto **1** upon scanning the current intensity with varying amounts of H^+ and F^- ions. The possible combinations of H^+ and F^- yield 15 rules. Additionally, the change in current intensity upon cooperative activity of H^+ and F^- is sketched in a three-dimensional plot (Figure 4.8e,f).

4.3.6. Artificial Neural Network (ANN). As mentioned in the introduction, the FNN is the simplest and convenient category of network where the information passes into a particular direction, proceeds, from the input nodes, via the hidden notes, and finally to the output nodes. Additionally, due to its high efficiency in forecasting the static system, we implemented advanced feed-forward back propagation network, namely, ANN-function fitting (ANN-FF) network for deeper understanding and forecasting of the system. We used Levenberg-Marquardt algorithm for training purpose. In this study, the ANN-FF is coded in MATLAB 2018 (Detailed procedure has been discussed in "Computational Methods" section). It clearly shows that at 0.71 V, the model's best validation performance is

0.0038557 up to epoch 28 (Figure 4.9a), while 7.8478 up to epoch 1 in case of the monitoring current at 0.96V. The enhancement of green colored line after epoch 28

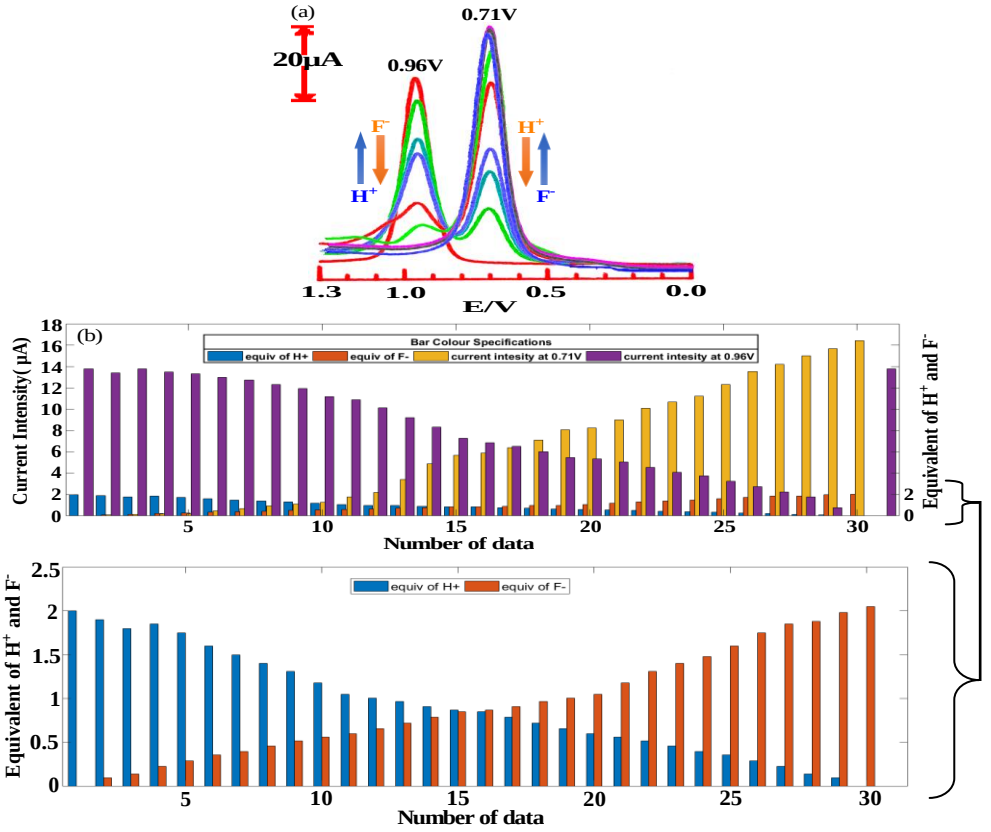

Figure 4.7. (a) SWVs of receptor **1** due to incremental addition of H^+ and F^-. (b) Histogram of current intensity in presence of 31 different combinations of H^+ and F^-.

suggests that the increment of the mean squared error (mse) and training gets halted. Figure 4.9b represents the histogram of the errors among the target and predicted values after training process. The Y-axis represents the number of samples in the database which exists in a particular bin. The bins are equally spaced intervals which are utilized to sort data on the graph. It is to be noted that the zero-error point is located under the bin centred at 0.009337 and -0.03577 for 0.71V and 0.96 V, respectively, while the total error of the network ranges from -0.2609 (leftmost bin) to 0.3096 (rightmost bin) for 0.71V and from -2.54 to 4.256 for 0.96V. The regression value (R) close to unity implies good correspondence between output and target and also indicates that the model is performing very well (Figure 4.10a). The training state of the ANN model up to epoch 34 is provided in Figure 4.11 for 0.71V. The schematic network representation for ANN-FF system is also provided in Figure 4.10b.

4.3.7. Adaptive Neuro-Fuzzy Inference System (ANFIS). It is a combination of fuzzy and neural network to overcome the drawback of individual ones and often yields

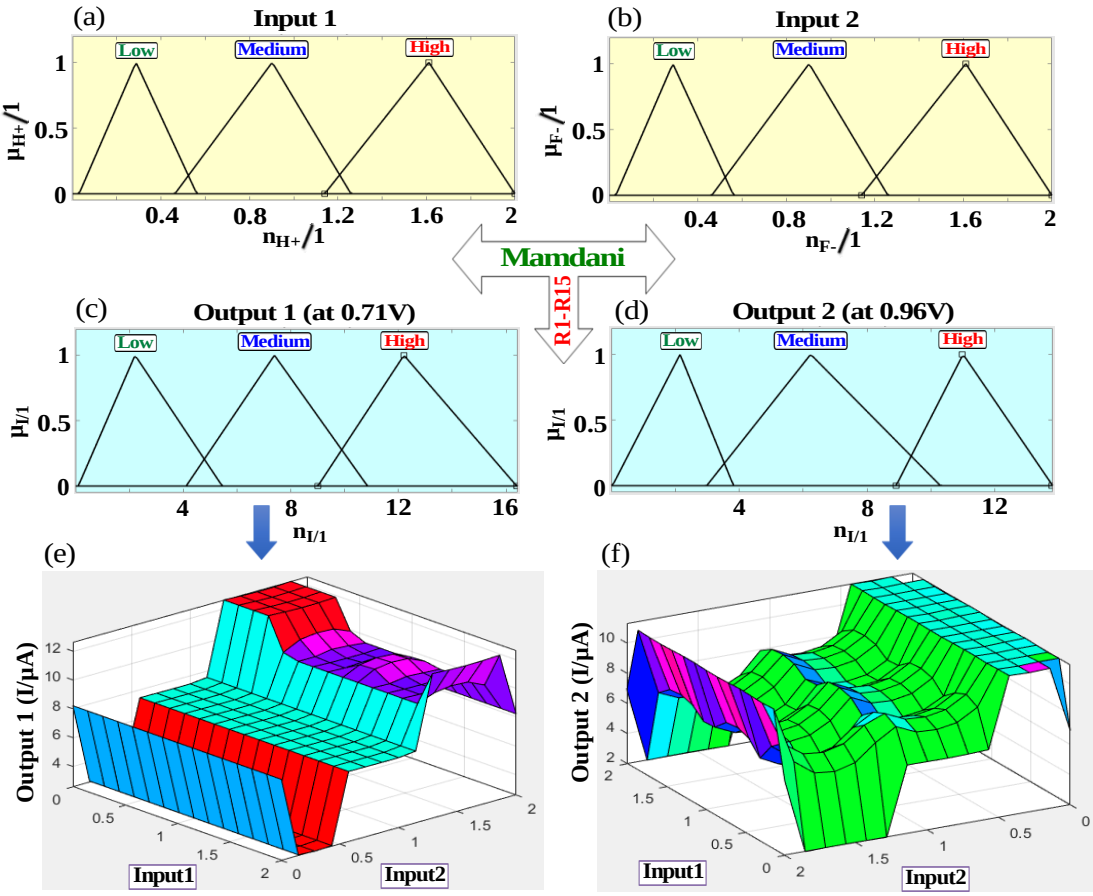

Figure 4.8. Sketch of FLS based on fuzzy inference rules upon scanning the CVs of $\mathbf{1}^+$ as a function of H^+ and F^-. The variables are decomposed in five fuzzy sets. (a) H^+: (1) low (trimf μ_{low}, [0.0295 0.287 0.5615]); (2) medium (trimf μ_{medium}, [0.463 0.9027 1.259]) (3) high (trimf μ_{high}, [1.14 1.611 2.01]). (b) F^-: (1) low (trimf μ_{low}, [0.0295 0.287 0.5615]); (2) medium (trimf μ_{medium}, [0.463 0.9027 1.258]) (3) high (trimf μ_{high}, [1.14 1.611 2.02]). (c) Current intensity at 0.71V (Output1): (1) low (trimf μ_{low}, [0.1017 2.211 5.451]); (2) medium (trimf μ_{medium}, [4.11 7.39 10.85]); (3) high (trimf μ_{high}, [9.004 12.2 16.39]). (d) Current intensity at 0.96V (Output2): (1) low (trimf μ_{low}, [0.0364 2.15 3.82]); (2) medium (trimf μ_{medium}, [2.983 6.233 10.29]); (3) high (trimf μ_{high}, [8.92 11.01 13.8]). 3D plot representing the alteration of current intensity upon the action of H^+ and F^- (e, f).

significant results.[57-59] Robustness, solidity and high generalization capability of ANFIS model provides a room for applications that involve crisp inputs and outputs. The network framework of ANFIS is sketched in Figure 4.12. It consists of five connected

layers (excluding input layer) which is common for two input dimensions, P and Q, both of which possess three fuzzy sets, viz. C1C2C3 for P, while D1D2D3 for Q input. The

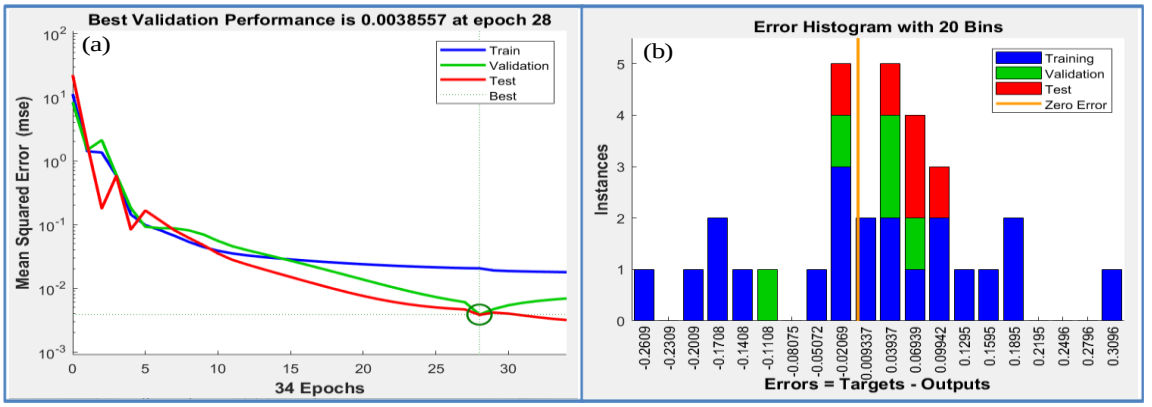

Figure 4.9. (a)The performance of the designed ANN model. (b) Error histogram of designed ANN model.

(a)

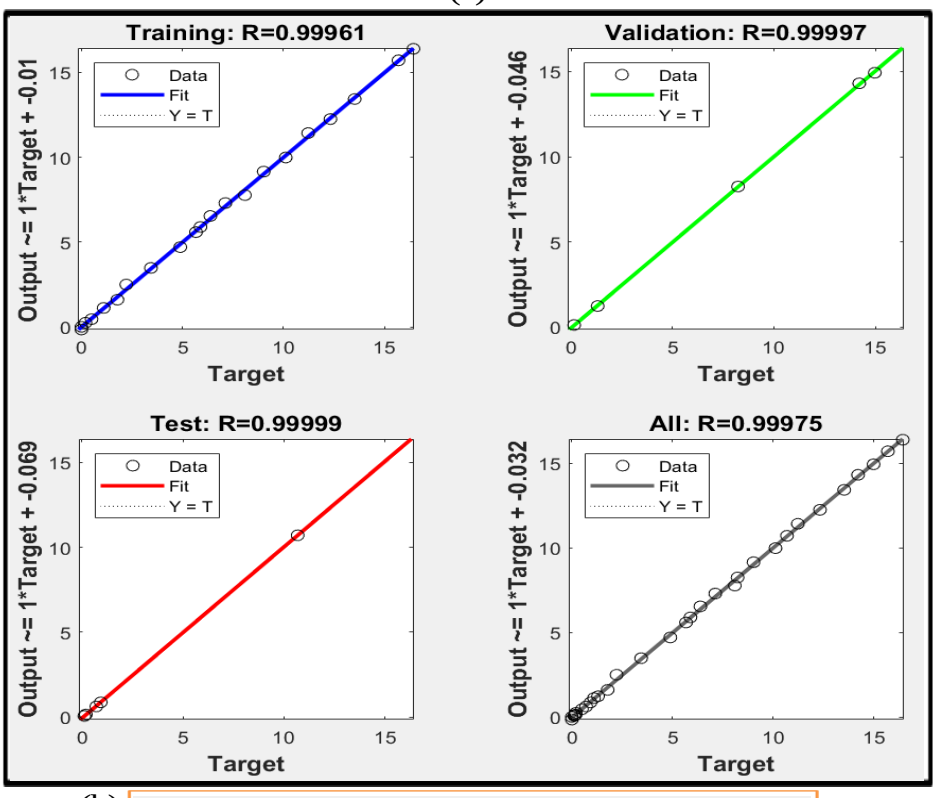

(b)

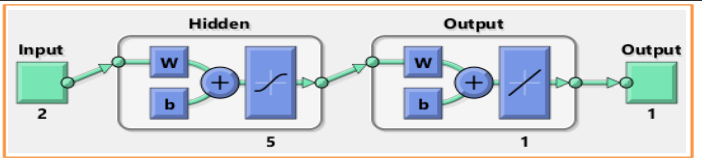

Figure 4.10. (a) Comparison of the results obtained by linear regression and ANN model. (b) Generated ANN scheme consisting of 2 inputs, 5 hidden layers and 1 output.

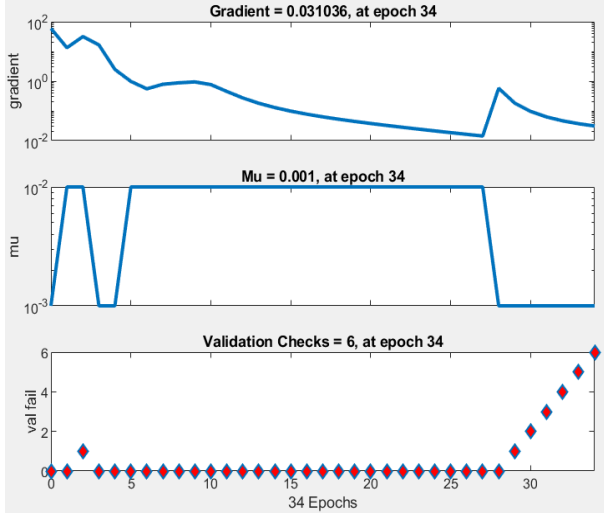

Figure 4.11. Training state of the ANN model of **1** at (0.71V) up to epoch 34.

detailed description of the individual layers is summarized in Chapter 3. In spite of the fact that the ANFIS network is quite exhaustive and possesses too many interrelations for high number of fuzzy set and input variables, the majority of them is not trainable and thus yields only a limited number of trainable parameters. Hence, the degrees of freedom for the ANFIS is relatively small compared with an equivalent ANN system. In ANFIS, only the membership function parameters in Layer1 and inputs weight in Layer 4 are to be predicted by training.

The fundamental structure of the output predictor model developed by using ANFIS to predict the current intensities upon the action of inputs (F^- and H^+) comprises of four important parts, viz. fuzzification, knowledge base, artificial neural network, and defuzzification blocks (**Scheme 4.1**).

To develop the system, we used 70% data for the training purpose and the rest 30% data for the testing purpose at the monitoring potential of 0.71V. Figure 4.13b indicates that the training error is gradually reduced up to 50 epochs suggesting that the system is learning in each step. The presence of two inputs and 3 membership functions for each input will generate 3^2= 9 rules for the system (Figure 4.14). The feasible consolidation of H^+ and F^- yields two outputs, each consisting of 9 rules, on the basis of Sugeno's method (Figure 4.14). The ANFIS predicted results showing relationship between two inputs and the output are graphically presented in 3D plots (Figure 4.15a,b).

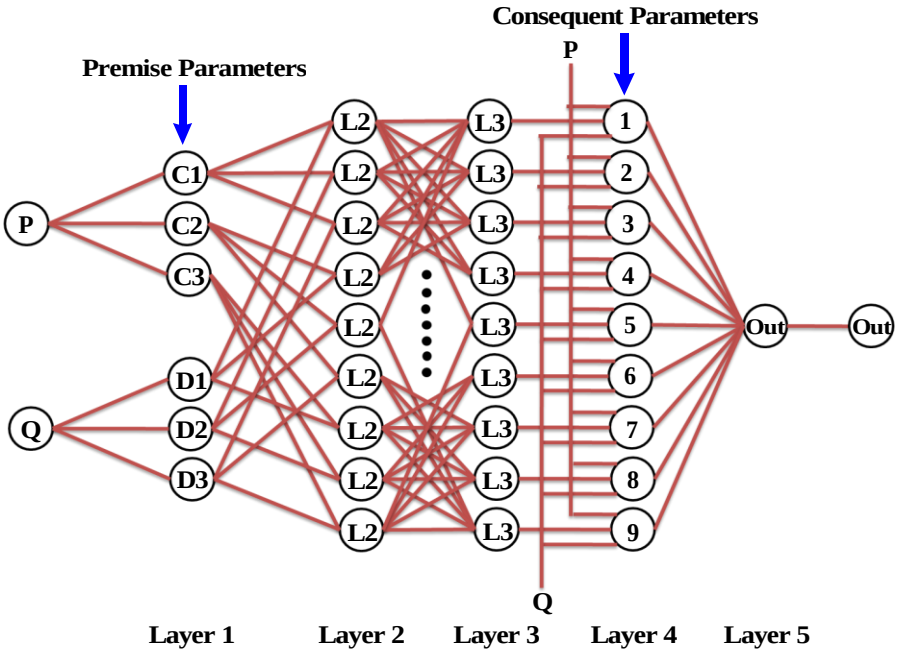

Figure 4.12. Schematic sketch of ANFIS network comprising of two inputs, five layers and one output.

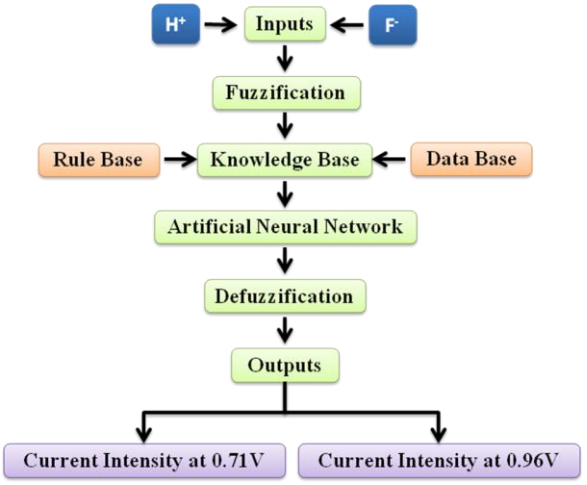

Scheme 4.1. Block diagram of the ANFIS for predicting the output in presence of inputs.

The generated ANFIS network architectures are also portrayed in Figure 4.15c,d on the basis of 9 rules. Table 4.2 summarizes the output values that are obtained upon incorporation of different input values in the rule viewer of FLS and command section of ANN model in MATLAB R2018a. Table 4.2 clearly indicates that the difference between experimental and FL output is greater than the difference among experimental and ANN output. This is because of the neural network's inability to explain decision (lack of

transparency) and fuzzy logic's weakness of learning. The efficacy of the ANFIS model could be statically measured by the root mean squared error (RMSE) values.

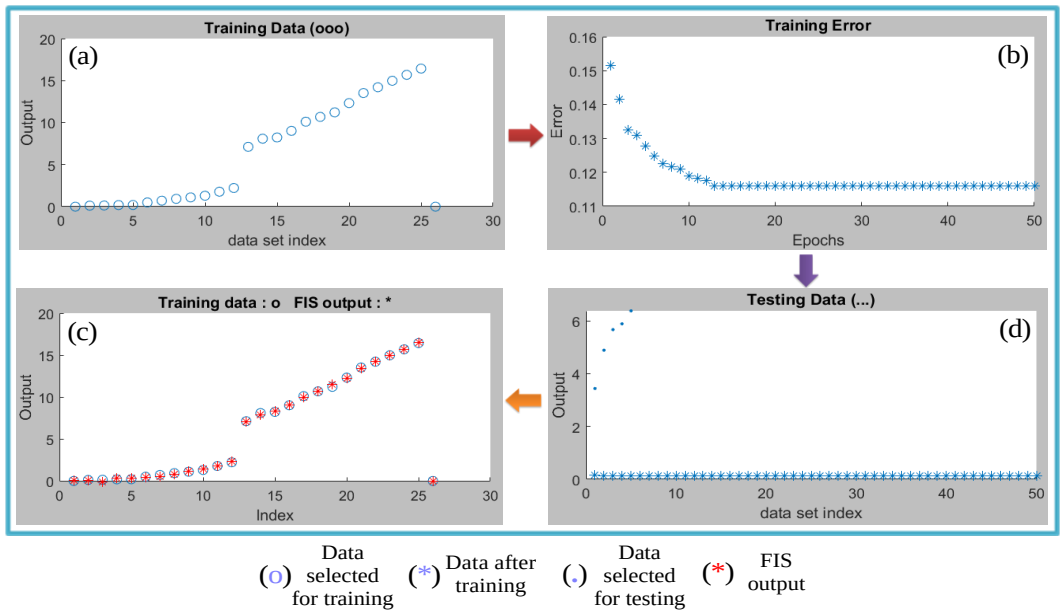

Figure 4.13. (a) Selected training data to create the ANFIS network. (b) Gradual reduction of training error up to 50 epochs. (c) Combination of training and output data. (d) Testing data after training process.

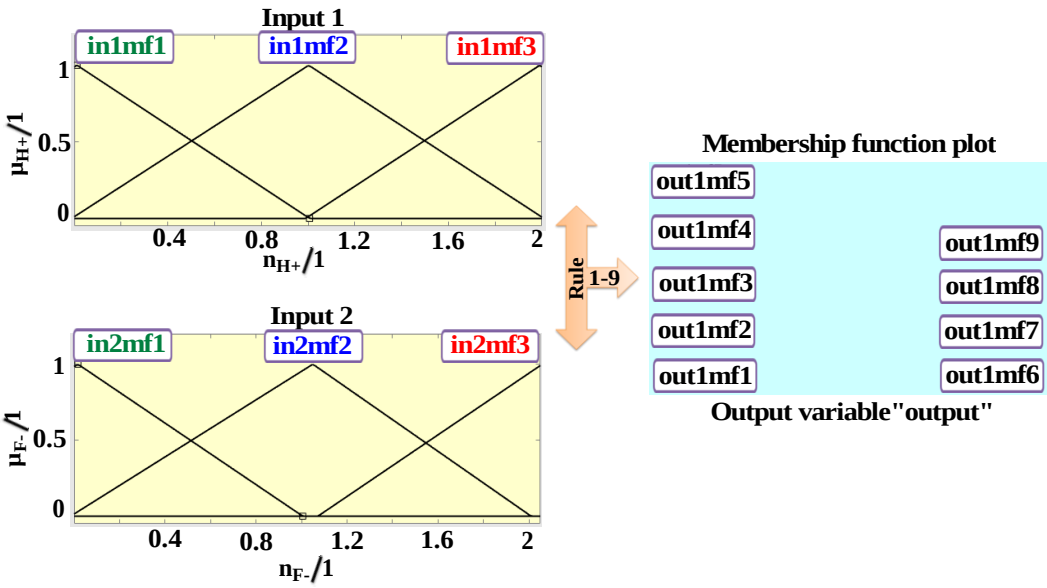

Figure 4.14. Schematic display of ANFIS at 0.71V obeying 9 rules.

The testing RMSE value of 0.115961 for 0.71V and 0.118894 for 0.96V clearly indicate that the model is working efficiently. The mse and R values of ANN models as well as

RMSE values of ANFIS models are also provided in Table 4.3. It is observed that the ANFIS generated outputs are closer to the experimental outputs. So, it is more

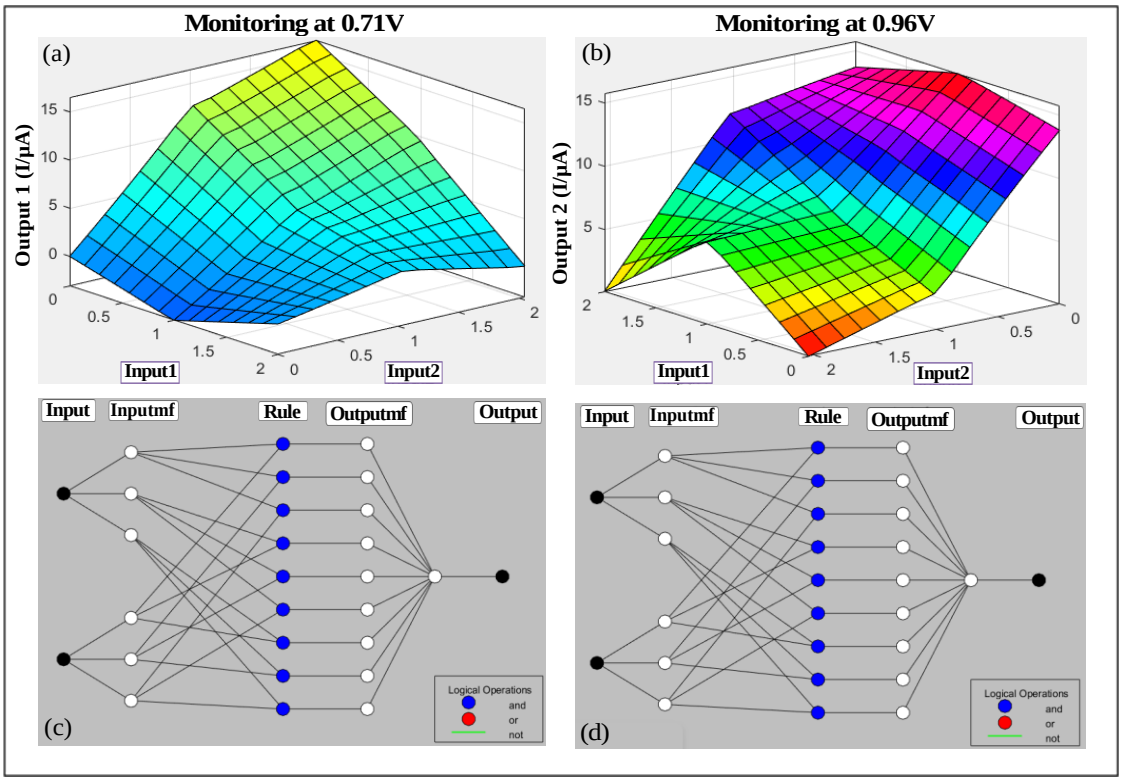

Figure 4.15. The variation of current intensity in presence of H^+ and F^- is portrayed in a 3D plot (a, b). Generated ANFIS structures for two outputs (c, d).

accurate optimization system than fuzzy and neural network. The comparison as well as the deviation of the experimental data to those of Fuzzy, ANN and ANFIS outputs is presented in Table 4.2 and Figure 4.16a and 4.16b.

Table 4.2. Experimental, Fuzzy, ANN and ANFIS Generated Outputs in Presence of 6 different Combinations of Inputs.

No of Data	Equiv of H^+	Equiv of F^-	Experimental Data		Fuzzy Output		ANN Output		ANFIS Output	
			at 0.71V	at 0.96V	at 0.71V	at 0.96V	at 0.71V	at 0.96V	at 0.71V	at 0.96V
1	1.75	0.29	0.20	13.34	2.59	11.21	0.24	13.38	0.36	13.31
2	1.18	0.56	1.31	11.21	7.38	8.42	1.22	12.81	1.43	11.41
3	0.66	1.00	8.09	5.46	7.45	8.07	7.72	3.85	7.85	5.51
4	0.40	1.48	11.22	3.74	12.61	6.27	11.42	1.34	11.5	3.79
5	1.85	0.23	0.19	13.49	2.62	11.2	0.14	13.45	0.33	13.4
6	1.05	0.61	1.78	10.89	7.47	8.96	1.61	12.56	1.81	10.8

Table 4.3. Mean Square Errors (MSE) and Regression (R) Values of ANN Models as well as Root Mean Square Errors (RMSE) of ANFIS models.

Monitoring Current Intensity at	ANN Model		ANFIS Model
	Mean Square Error (mse)	Regression (R)	Root Mean Square Error (RMSE)
0.71V	$1.5141e^{-2}$	$9.9975e^{-2}$	0.115961
0.96V	$5.7030e^{-0}$	$9.5299e^{-1}$	0.118894

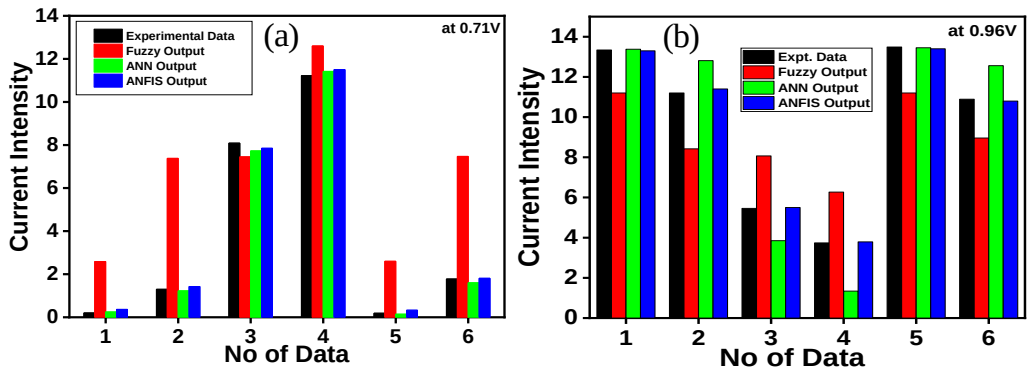

Figure 4.16. The histograms represent the comparison between the experimental output data to those of FL, ANN and ANFIS generated outputs.

4.4. Conclusions

In continuation with our ongoing research interest to explore molecular level computation as well as the usage of machine learning and other artificial intelligence tools, we utilized an imidazole-dicarboxylate based Ru(II)-bipyridine complex possessing a number of dissociable protons in its secondary coordination sphere. The motivation of choosing Ru(II)-polyheterocyclic complex is because of its rich and tuneable photophysical and

electrochemical behaviors which in turn gives rise to construction of potential molecular switches and devices in presence of suitable external stimuli such as anions, acid and base. The absorption, emission and electrochemical behavior of the metalloreceptor were significantly modulated upon the influence of basic anions (such as F^-, AcO^- and $H_2PO_4^-$) as well as by altering the pH of the solution. Interestingly, the deprotonation of the metalloreceptor by selected anions or by alkaline pH followed by its restoration to its original form by acid or acidic pH is reversible and could be repeated many cycles. The metalloreceptor is capable to demonstrate several advanced Boolean logic functions, viz. three input OR gate, set-reset flip-flop logic and complicated function of traffic signal by employing its spectral and electrochemical responses through proper use of different inputs (anions, acid and solution of appropriate pH). In this work, we also enforce fuzzy logic for creating an infinite-valued logic algorithm by using the electrochemical output of the receptor upon the action of anions, acid and solution of appropriate pH. Performing very detailed sensing experiments upon varying the concentration of the analytes within a broad domain is often time consuming, laborious as well as expensive. To get rid of these difficulties, we employed several soft computing approaches such as ANNs, Fuzzy-logic or ANFIS to predict the experimental data. Interestingly, the Fuzzy, ANN and ANFIS can predict the experimental data quite accurately. Herein, we also compared the outputs of Fuzzy, ANN and ANFIS methods and the outputs are utilized for modeling of the protonation-deprotonation behaviors of the metalloreceptor. The statistical performance indicators (such as MSE, RMSE) suggest that the predicted values of the electrochemical sensing data by ANFIS models are quite good and comparable to the experimental data. Hence, the adopted computational intelligence-based approach can be considered as a potential ion sensing data model for the present Ru(II)-based metalloreceptor.

4.5. References

1. Artrith, N.; Butler, K. T.; Coudert, F. X.; Han, S.; Isayev, O.; Jain, A.; Walsh, A. Best Practices in Machine Learning for Chemistry. *Nat. Chem.***2021**, *13*, 505-508.
2. Mater, A. C.; Coote, M. L. Deep Learning in Chemistry. *J. Chem. Inf. Model.* **2019**, *59*, 2545-2559.
3. Pflüger, P. M.; Glorius, F. Molecular Machine Learning: The Future of Synthetic Chemistry? *Angew. Chem. Int. Ed.* **2020**, *59*, 18860-18865.
4. He, L.; Bai, L.; Dionysiou, D. D.; Wei, Z.; Spinney, R.; Chu, C.; Xiao, R. Applications of Computational Chemistry, Artificial Intelligence, and Machine Learning in Aquatic Chemistry Research. *Chem. Eng. J.* **2021**, *426*, 131810.
5. Gentili, P. L. A strategy to face complexity: The Development of Chemical Artificial Intelligence. In Advances in Artificial Life, Evolutionary Computation, and Systems Chemistry; Rossi, F., Piotto, S., Concilio, S., Eds.; Springer: Cham, Switzerland; New York, NY, USA. **2017**, 708, 151-160.
6. Zadeh, L. A. Toward Human Level Machine Intelligence-is it Achievable? The Need for a Paradigm Shift. *IEEE Comput. Intell. Mag.* **2008**, *3*, 11-22.
7. Szaciłowski, K. Digital Information Processing in Molecular Systems. *Chem. Rev.* **2008**, *108*, 3481-3548.
8. Zadeh, L.A. Outline of a New Approach to the Analysis of Complex Systems and Decision Processes. *IEEE Trans. Syst. Man Cyb.* **1973**, *3*, 28-44.
9. Conrad, M. Molecular Computing. *Adv. Comput.* **1990**, 31, 235-324.
10. Zadeh, L. A. Fuzzy Sets. In Fuzzy Sets, Fuzzy Logic, and Fuzzy Systems: Selected Papers by Lotfi A Zadeh, pp. 394-432. **1996.**
11. Gentili, P. L. Boolean and Fuzzy Logic Gates Based on the Interaction of Flindersine with Bovine Serum Albumin and Tryptophan. *J. Phys. Chem. A*. **2008**, *112*, 11992-11997.
12. Gentili, P. L. The Fuzziness of the Molecular World and its Perspectives. *Molecules*. **2018**, *23*, 2074.
13. Gentili, P.L. The Fundamental Fuzzy Logic Operators and Some Complex Boolean Logic Circuits Implemented by the Chromogenism of a Spirooxazine. *Phys. Chem. Chem. Phys.* **2011**, *13*, 20335-20344.

14. Gentili, P.L.; Giubila, M.S.; Heron, B.M. Processing Binary and Fuzzy Logic by Chaotic Time Series Generated by a Hydrodynamic Photochemical Oscillator. *ChemPhysChem.* **2017**, *18*, 1831-1841.
15. Gentili, P.L.; Giubila, M.S.; Germani, R.; Romani, A.; Nicoziani, A.; Spalletti, A.; Heron; B.M. Optical Communication among Oscillatory Reactions and Photo-Excitable Systems: UV And Visible Radiation can Synchronize Artificial Neuron Models. *Angew. Chem. Int. Ed.* **2017**, *56*, 7535-7540.
16. Schumann, A.; Adamatzky, A. The Double-Slit Experiment with Physarum Polycephalum and P-Adic Valued Probabilities and Fuzziness. *Int J Gen Syst.* **2015**, *44*, 392-408.
17. Giri Nandagopal, M. S.; Selvaraju, N. Prediction of Liquid–Liquid Flow Patterns in a Y-Junction Circular Microchannel using Advanced Neural Network Techniques. *Ind. Eng. Chem. Res.* **2016**, *55*,11346-11362.
18. Bingöl, D.; Inal, M.; Çetintaş, S. Evaluation of Copper Biosorption onto Date Palm (Phoenix Dactylifera L.) Seeds with MLR and ANFIS Models. *Ind. Eng. Chem.Res* **2013**, *52*, 4429-4435.
19. İnal, M. Predicting the Conversion Ratio for the Leaching of Celestite in Sodium Carbonate Solution using an Adaptive Neuro-Fuzzy Inference System. *Ind. Eng. Chem.Res* **2013**, *52*, 4429-4435. **2014**, *53*, 4975-4980.
20. de silva, A.P.; Gunaratne, H. Q. N.; McCoy, C.P. A Molecular Photoionic AND Gate Based on Fluorescent Signaling. *Nature.* **1993**, *364*, 42-44.
21. Ling, J.; Daly, B.; Silverson, V. A. D.; de Silva, A. P. Taking Baby Steps in Molecular Logic-Based Computation. *Chem. Commun.* **2015**, *51*, 8403-8409.
22. de Silva, A. P.; McClenaghan, N. D. Molecular-Scale Logic Gates. *Chem. Eur. J.* **2004**, *10*, 574-586.
23. de Silva. A. P. Molecular Logic Gate Arrays. *Chem. Asian J.* **2011**, *6*, 750-766.
24. Szaciłowski, K. Molecular Logic Gates Based on Pentacyanoferrate Complexes: from Simple Gates to Three-Dimensional Logic Systems. *Chem. Eur. J.* **2004**, *10*, 2520-2528.
25. Szaciłowski, K.; Wojciech, M.; Grażyna, S. Light-driven OR and XOR Programmable Chemical Logic Gates. *J. Am. Chem. Soc.* **2006**, *128*, 4550-4551.

26. Adamatzky, A.; Costello, B. D. L. Experimental Logical Gates in a Reaction-Diffusion Medium: The XOR Gate and Beyond. *Phys. Rev. E.* **2002**, *66*, 046112.
27. Adamatzky, A.; Tegelaar, M.; Wosten, H. A.; Powell, A. L.; Beasley, A. E.; Mayne, R. On Boolean Gates in Fungal Colony. *Biosystems*. **2020**, *193*, 104138.
28. Adamatzky, A.; Jones, J.; Mayne, R.; Tsuda, S.; Whiting, J. Logical Gates and Circuits Implemented in Slime Mould. *Advances in Physarum Machines.* **2016**, 37-74.
29. Das, S.; Saha, D.; Bhaumik, C.; Dutta, S.; Baitalik, S. Ru (II) and Os (II) Mixed-Chelates Derived from Imidazole-4, 5-Dicarboxylic Acid and 2, 2′-Bipyridine as Colorimetric Sensors for Anions: Synthesis, Characterization and Binding Studies. *Dalton Trans*. **2010**, *39*, 4162-4169.
30. Das, S.; Saha, D.; Karmakar, S.; Baitalik, S. Effect of pH on the Photophysical and Redox Properties of a Ruthenium (II) Mixed Chelate Derived from Imidazole-4, 5-Dicarboxylic Acid and 2,2′-Bipyridine: An Experimental and Theoretical Investigation. *J. Phys. Chem. A.* **2012**, *116*, 5216-5226.
31. Khatua, S.; Samanta, D.; Bats, J. W.; Schmittel, M. Rapid and Highly Sensitive Dual-Channel Detection of Cyanide by Bis-Heteroleptic Ruthenium(II) Complexes**.** *Inorg. Chem.* **2012**, *51*, 7075-7086.
32. Shu, Q.; Birlenbach, L.; Schmittel, M. A Bis (Ferrocenyl) Phenanthroline Iridium(III) Complex as a Lab-On-A-Molecule for Cyanide and Fluoride In Aqueous Solution. *Inorg. Chem.* **2012**, *51*, 13123-13127.
33. Schmittel, M.; Qinghai, S. A Lab-On-A-Molecule for Anions in Aqueous Solution: Using Kolbe Electrolysis and Radical Methylation at Iridium for Sensing. *Chem. Commun*., **2012**, *48*, 2707-2709.
34. Sessler, J. L.; Gale, P. A.; Cho, W. S. Anion Receptor Chemistry. *Royal Society of Chemistry*, Cambridge, U.K., **2006**.
35. Sessler, J. L.; Davis, J. M. Sapphyrins: Versatile Anion Binding Agents. *Acc. Chem. Res.* **2001**, *34*, 989-997.
36. Bhaumik, C.; Das, S.; Saha, D.; Dutta, S.; Baitalik, S. Synthesis, Characterization, Photophysical and Anion-Binding Studies of Luminescent Heteroleptic Bis-Tridentate Ruthenium(II) Complexes Based on 2,6-Bis(Benzimidazole-2-

Yl)Pyridine and 4'-Substituted 2,2':6',2" Terpyridine Derivatives. *Inorg. Chem.* **2010,** *49*, 5049-5062.

37. Mondal, D.; Bar, M.; Mukherjee, S.; Baitalik, S. Design of Ru (II) Complexes Based on Anthraimidazoledione-Functionalized Terpyridine Ligand for Improvement of Room-Temperature Luminescence Characteristics and Recognition of Selective Anions: Experimental and DFT/TD-DFT Study. *Inorg. Chem*. **2016**, *55*, 9707-9724
38. Bar, M.; Deb, S.; Paul A.; Baitalik, S. Stimuli-Responsive Luminescent Bis-Tridentate Ru(II) Complexes toward the Design of Functional Materials. *Inorg. Chem.* **2018,** *57*, 12010-12024.
39. Deb, S.; Sahoo, A.; Pal, P.; Baitalik, S. Exploitation of The Second Coordination Sphere to Promote Significant Increase of Room-Temperature Luminescence Lifetime and Anion Sensing in Ruthenium-Terpyridine Complexes. *Inorg. Chem.* **2021**, *60*, 6836-6851.
40. Mondal, D.; Biswas, S.; Paul, A.; Baitalik, S. Luminescent Dinuclear Ruthenium Terpyridine Complexes with a Bis-Phenylbenzimidazole Spacer. *Inorg. Chem.* **2017**, *56*, 7624-7641.
41. Chen, K.; Schmittel, M. A Triple-Channel Lab-On-A-Molecule for Triple-Anion Quantification using an Iridium(III)-Imidazolium Conjugate. *Chem. Commun*. **2014**, *50*, 5756-5759.
42. Schmittel, M.; Mal, P.; de los Rios, A. Multiport Logic Operations Triggered by Protonation-A Tris-Phenanthroline as a 3-Input AND-NOR-OR Circuit, *Chem. Commun*. **2010**, *46*, 2031-2033.
43. Chen, K.; Schmittel, M. An Iridium(III) Complex as a Versatile Platform for Molecular Logic Gates: an Integrated Full Subtractor and 1:2 Demultiplexer. *analytical and bioanalytical chemistry*, **2016**, *408*, 7077-7083.
44. Biswas, P. K.; Saha, S.; Gaikwad, S.; Schmittel, Michael. Reversible Multicomponent AND Gate Triggered by Stoichiometric Chemical Pulses Commands the Self-Assembly and Actuation of Catalytic Machinery. *J. Am. Chem. Soc.* **2020**, *142*, 7889-7897.

45. Mizuno, T.; Wei, W. H.; Eller, L. R.; Sessler, J. L. Phenanthroline Complexes Bearing Fused Dipyrrolylquinoxaline Anion Recognition Sites: Efficient Fluoride Anion Receptors. *J. Am. Chem. Soc*. **2002**, *124*, 1134-1135.
46. Hargrove, A. E.; Nieto, S.; Zhang, T.; Sessler, J. L.; Anslyn, E. V. Artificial Receptors for the Recognition of Phosphorylated Molecules. *Chem. Rev.* **2011**, *111*, 6603-6782.
47. Martínez-Máñez, R.; Sancenón, F. Fluorogenic and Chromogenic Chemosensors and Reagents for Anions. *Chem. Rev.* **2003**, *103*, 4419-4476.
48. Mukherjee, S.; Sahoo, A.; Deb, S.; Baitalik, S. Light and Cation-Criven Optical Switch Based on a Stilbene-Appended Terpyridine System for the Design of Molecular-Scale Logic Devices. *J. Phys. Chem. A*. **2021**, *125*, 8261-8273.
49. Mondal, D.; Bar, M.; Maity, D.; Baitalik, S. Anthraimidazoledione-Terpyridine-Based Optical Chemosensor for Anions and Cations that Works as Molecular Half Subtractor, Key-Pad Lock, and Memory Device. *J. Phys. Chem. C.* **2015**, *119*, 25429-25441.
50. Omana, M.; Papasso, G.; Rossi, D.; Metra, C. A Model for Transient Fault Propagation in Combinatorial Logic. In *9th IEEE On-Line Testing Symposium*. **2003**. 111-115.
51. Zhang, Y.; Liu, W.; Zhang, W.; Yu, S.; Yue, X.; Zhu, W.; Wang, J. DNA-Mediated Gold Nanoparticle Signal Transducers for Combinatorial Logic Operations and Heavy Metal Ions Sensing. *Biosens. Bioelectron.* **2015**, *72*, 218-224.
52. Goldsworthy, V.; LaForce, G.; Abels, S.; Khisamutdinov, E. F. Fluorogenic RNA aptamers: A Nano-Platform for Fabrication of Simple and Combinatorial Logic Gates. *Nanomaterials*. **2018**, *8*, 984.
53. Magri, D. C.; Spiteri, J. C. Proof of Principle of a Three-Input AND–INHIBIT–OR Combinatorial Logic Gate Array. *Org. Biomol. Chem.* **2017**, *15*, 6706-6709.
54. Mardanya, S.; Mondal, D.; Karmakar, S.; Baitalik, S. Smart Ruthenium and Osmium Complexes Mimic the Complicated Functions of Traffic Signal and Memory Device. *Sens. Actuators B: Chem.* **2017**, *239*, 635-641.

55. Cui, B. B.; Tang, J. H.; Yao, J.; Zhong, Y. W. A Molecular Platform for Multistate Near-Infrared Electrochromism and Flip-Flop, Flip-Flap-Flop, and Ternary Memory. *Angew. Chem. Int. Ed.* **2015**, *54*, 9192-9197.
56. Shao, J. Y.; Yao, C. J.; Cui, B. B.; Gong, Z. L.; Zhong, Y. W. Electropolymerized Films of Redox-Active Ruthenium Complexes for Multistate Near-Infrared Electrochromism, Ion Sensing, and Information Storage. *Chin. Chem. Lett*. **2016**, *27*, 1105-1114.
57. Mamdani, E. H. Application of Fuzzy Logic to Approximate Reasoning using Linguistic Synthesis. *IEEE Trans. Comput*. **1977**, *26*, 1182-1191.
58. Jang, J. S. R.; Sun, C. T. Neuro-Fuzzy Modeling and Control. *Proc. IEEE.* **1995**, *83*, 378–405.
59. Sugeno, M.; Yasukhiro, T. A Fuzzy-Logic-Based Approach to Qualitative Modeling. *IEEE Trans. Fuzzy Syst.* **1993**, *1*, 7-3.

****

5.1. Introduction

Machine learning (ML) is now a very influential implement in materials research. The technological advances of ML are now evident in almost all disciplines of science and technology.[1-9] Upon appropriate usage of powerful computing and high-throughput experimentation, ML has established its credentials to speed up the scientific research and technological growth. Although the acceptance of data-driven methods for materials development is stimulating, the forecasts and internal functioning of ML models should also make chemical sense. Classical ML comprises of different algorithms taking advantage of which one could learn from the existing data set and then exploit that learning for prediction of new dataset. Deep learning (DL), on the other hand, are based on artificial neural networks (ANN) wherein manifold layers of processing are utilized to take out increasingly advanced level features from the data. Due to the alteration in how structures are devised and exploited, interpreting classical and deep learning tools frequently needs diverse methods. Taking into consideration some exceptions, the DL methods usually acquire structured inputs, whereas classical ML works on unstructured data. Several definitions as well as debates exist with regard to a good interpretable model. A model could be regarded as an interpretable model when its function could be recognized by a human. The decision tree (DT)-based model might be regarded as an interpretable model since its functioning could be easily understood upon inspecting the arrangement of the tree. By contrast, a deep NN-based model could not be interpretable upon inspection.

To quantify or explain some observation either through experiment or by theory is always time consuming. To minimize the time and the mean square error (mse), we will utilize the existing data-set by machine learning and could formulate new data set upon regression. In this work, we employed both the classical and deep learning methods to understand as well as to predict complete anion-responsive behaviors of two of our reported emissive Ru(II)-terpyridine complexes as shown in **Chart 5.1**.[10]

The inspiration in selecting Ru(II) complexes is due to their unique combination of photophysical and redox properties which could be systematically modulated under the influence of different stimuli (such as anion, acid and base) and ultimately can lead to the fabrication of potential molecular sensors and switches.[11-16] The outer coordination

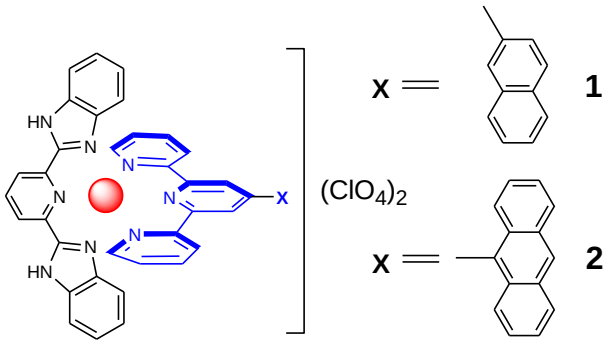

Chart 5.1. Chemdraw structures of the complexes

sphere of the complexes is decorated with two imidazole NH moieties and taking benefits of which we thoroughly studied their anion sensing characteristics.[10] Significant alteration of absorption, emission spectral as well as electrochemical and spectro-electrochemical responses of the complexes take place upon the action of selected anions. Incipient hydrogen bonding among the NH motifs and anions followed by anion-promoted deprotonation occurs in presence of basic anions. Fascinatingly, the deprotonation of the complexes by basic anions such as F^- and AcO^-, followed by their refurbishment to the initial state by acid is reversible and repetitive by many cycles.

In the following section, we will use their spectral, electrochemical and spectroelectrochemical outputs upon the action of anions to mimic the roles of YES-NOT and set-reset flip-flop logic gates.[17-30] We will also apply machine learning tools such as ANNs, ANFIS, and Decision tree (DT) regression to analyze the experimental data and also to predict lots of intermediate states. Thus, we can reduce the time and expenditures associated with execution of comprehensive sensing experimentations.

ANN is inspired through central nervous system of human brain and capable to venture the enormous number of unspecified states. Recurrent (RNN) and function fitting (ANN-FF) networks are frequently used.[31-39] In the present work, ANN-FF procedure has been employed due to the static nature of our system and because of its ability to understand and forecast the complex systems. Although ANN is quite competent to grasp the data but not so competent with respect to understand the meaning of every neuron and its load. By contrast, the Fuzzy logic (FL)-based tool is superior in terms of understanding as it works through lingual language and IF-THEN rule. But the lacuna of FLs is their inability to learn by itself. To be trained through FLs, one requires to use of

the techniques from other area such as statistics and system identification. As the NNs are efficient in learning, it would be advantageous to amalgamate FL and NN and the amalgamated technique, termed as ANFIS, is better over the individual ones. The construction of ANFIS possesses the same machinery as the FL with the exclusion of NN block.

Among the diverse learning tools, the DT-based methods turn out as nonparametric methods having the exclusive feature of uniting interpretability, efficacy and accuracy.[40-45] DTs emulate human thinking and thereby help the data scientists to recognize and interpret the results. A DT resembles well a tree. The base of the tree is the root node from where a series of decision nodes flow that helps the decisions to be made. The leaf nodes are generated from the decision nodes which signify the consequences of the decisions. Schematic presentation together with the depiction of each part of a DT will be presented in the next section. We applied here DT regression analysis to predict the current intensities (dependent variables) at different voltages (0.48V and 1.11V) upon the change in the concentration of acid (H^+) and anion (AcO^-) (independent variable). In this work, we will also compare the outcomes of ANN, ANFIS and DT methods with those of the experimental results.

5.2. Experimental Section

5.2.1. Materials. Reagent grade chemicals obtained from commercial sources were used as received. Solvents were purified and dried according to standard methods. 2,2':6',2''–Terpyridine (tpy), 2,6–pyridinedicarboxylic acid, 1,2-phenylenediamine and the tetrabutylammonium (TBA) salt of the anions were purchased from Sigma-Aldrich. 4′-(2-naphthyl)-2,2′:6′,2″-terpyridine (tpy-Naph) and 4′-(9-anthryl)-2,2′:6′,2″-terpyridine (tpy-An),[46,47] were synthesized according to the literature procedures. [Ru(H_2pbbzim)Cl_3] and [(H_2pbbzim)Ru(tpy)](ClO_4)$_2$ were previously reported by us.[48]

5.2.2. General Procedure for Preparation of Heteroleptic Ruthenium(II) Complexes [(H_2pbbzim)Ru(tpy-Ar)](ClO_4)$_2$ (1-2). [(H_2pbbzim)$RuCl_3$] (75 mg, 0.14 mmol) was suspended into ethylene glycol (25 mL) and heated at 100°C with continuous stirring under nitrogen. To the suspension was added 0.15 mmol of different tpy-Ar ligand and the reaction mixture were again heated at 180°C for 12 h. The resulting deep

red solution was cooled to room temperature and the perchlorate salt of the complexes were precipitated by pouring the solution into an aqueous solution of $NaClO_4 \cdot H_2O$ (1.0 g in 10 mL of water). The precipitate was filtered, washed several times with cold water and then dried under vacuum. The compound was then purified by silica gel column chromatography using acetonitrile as the eluent. The eluents were reduced to about 5 mL and to it was then added aqueous solution of $NaClO_4 \cdot H_2O$ when a red micro crystalline compound deposited. The precipitate was collected and washed several times with cold water. Further purification was carried out by recrystallization of the compound from a mixture of MeCN and MeOH (1:2 v/v) in the presence of a few drops of aqueous 10^{-4} M perchloric acid.

$[(H_2pbbzim)Ru(tpy\text{-}Naph)](ClO_4)_2 \cdot H_2O$ (1). Yield: 60%. Anal. Calcd. for $C_{44}H_{32}N_8Cl_2O_9Ru$: C, 53.45; H, 3.26; N, 11.33. Found: C, 53.42; H, 3.29; N, 11.31. ^{1}H NMR {500 MHz, DMSO-d_6, δ/ppm}: 9.65 (s, 2H, H3′), 9.14 (s, 1H, H13), 8.99 (d, 2H, *J* = 8.0 Hz, H3), 8.74 (d, 2H, *J* = 8.0 Hz, H17), 8.64 (d, 1H, *J* = 8.5 H7), 8.58 (t, 1H, *J* = 8.0 Hz, H16), 8.31 (d, 1H, *J* = 8.5 Hz, H8), 8.21 (d, 1H, *J* = 7.5 Hz, H9), 8.13 (d, 1H, *J* = 7.5 Hz, H12), 7.93 (t, 2H, *J* = 7.2 Hz, H4), 7.72-7.69 (m, 2H, 1H10+1H11), 7.62 (d, 2H, *J* = 8.5 Hz, H6), 7.47 (d, 2H, *J* = 5.5 Hz, H18), 7.26-7.21 (m, 4H, 2H5+2H19), 6.98 (t, 2H, *J* = 8.0, H20), 6.07 (d, 2H, *J* = 8.5, H21). ESI–MS (positive, CH_3CN) *m/z* = 386.05 (100%) $[(H_2pbbzim)Ru(tpy–Naph)]^{2+}$; 871.11 (7%) $[(H_2pbbzim)Ru(tpy–Naph)(ClO_4)]^+$; 771.14 (45%) $[(Hpbbzim)Ru(tpy–Naph)]^+$. UV-vis [$CH_2Cl_2$; λ_{max} / nm (ε / $M^{-1}cm^{-1}$)]: 495 (12200), 406 (3700), 354 (27750), 337 (27250), 316 (35900), 285(32050).

$[(H_2pbbzim)Ru(tpy\text{-}An)](ClO_4)_2 \cdot 2H_2O$ (2). Yield: 50 %. Anal. Calcd. for $C_{48}H_{36}N_8Cl_2O_{10}Ru$: C, 54.55; H, 3.43; N, 10.60 Found: C, 54.54; H, 3.45; N, 10.59. ^{1}H NMR {500 MHz, DMSO-d_6, δ/ppm}: 9.32 (s, 2H, H3′), 8.98 (s, 1H, H11), 8.74-8.69 (m, 4H, 2H3+2H17), 8.58 (t, 1H, *J* = 8.0 Hz, H16), 8.37 (d, 2H, *J* = 9.0 Hz, H10), 8.08 (d, 2H, *J* = 9.0 Hz, H7), 7.82-7.77 (m, 4H, 2H4+2H9), 7.72 (t, 2H, *J* = 7.2Hz, H8), 7.66 (d, 2H, *J* = 8.0 Hz, H18), 7.52 (d, 2H, *J* = 5.5 Hz, H6), 7.34 (t, 2H, *J* = 7.5 Hz, H19), 7.21 (t, 2H, *J* = 6.5 Hz, H5) 7.17 (t, 2H, *J* = 7.5 Hz, H20), 6.30 (d, 2H, *J* = 8.0 Hz, H21). ESI-MS (positive, CH_3CN) *m/z* = 411.07 (100%) $[(H_2pbbzim)Ru(tpy\text{-}An)]^{2+}$; 921.13 (6%) $[(H_2pbbzim)Ru(tpy\text{-}An)(ClO_4)]^+$; 821.17 (25%) $[(Hpbbzim)Ru(tpy\text{-}An)]^+$**.** UV-vis [$CH_2Cl_2$; λ_{max} / nm (ε / $M^{-1}cm^{-1}$)]: 503 (15750), 354 (44950), 318 (59000), 276(71900).

5.2.3. Physical Measurements. The details of different equipments used and experimental process to measure absorption and luminescence spectral behaviors have already been presented in chapter 2 and 3.

The details of computational methods of ANFIS and ANN have already been discussed in chapter 3 and 4.

5.2.4. Computational Details of Decision Tree Regression (DTR). We have used decision tree regression for the computational prediction of our chemical data using the python programming language. Chemical data followed by its header has been imported, using the 'pandas' library. Then, the datasets are split into two parts, viz. train and test, using the 'scikit-learn' library function 'train_test_split'. Thereafter, we fitted the dataset with decision tree regression using the Scikit-learn library function 'DecisionTreeRegressor'. We have got an optimized depth of the tree by calculating the training accuracy. We have taken one-less depth from the maximum depth corresponding to maximum accuracy to avoid decision tree over fitting. We have plotted the decision tree with the optimized depth of the tree.

5.3. Results and Discussion

5.3.1. A Brief Survey of Photophysical, Electrochemical, Spectroelectrochemical and Anion Sensing Behaviours of the Complexes. The synthesis, characterization and the physicochemical characteristics of the complexes were already reported by us. A brief recapitulation of their photo-redox, spectro-electrochemical and anion responsive properties is again delineated here for the benefit of the readers. The compounds display broad and intense bands in the visible domain assignable as the overlapping {Ru→tpy-Ar(π^*) and Ru→H_2pbbzim(π^*)} MLCT transitions. A weak and broad peak in the range of 600-700 nm is also observed due to Ru→tpy-Ar (π^*) singlet to triplet transitions. Additionally, intense peaks in the UV domain are observed because of π-π* transitions of aromatic and heteroaromatic motifs. The complexes exhibit a broad emission band {680 nm (**1**) and 677 nm (**2**)} in dichloromethane (DCM) at room temperature (RT) having lifetime {15 ns (**1**) and 6.5 ns (**2**)} and quantum yield {2.1×10^{-3} (**1**) and 0.85×10^{-3} (**2**)} because of the deactivation of their ^{3}MLCT (^{3}Ru→tpy-Ar (π^*) state. The complexes undergo one reversible Ru^{II}/Ru^{III}

oxidation within the domain of +1.5 V and up to four quasi-reversible reductions up to the region of -2.4 V.

The anion sensing behaviours of the complexes were also previously investigated via absorption and emission spectroscopy as well as by SWV. Titration measurements were also performed to acquire quantitative insight about complex-anion interplay. Two-stage changes were noticed in their spectral profiles in presence of F^- and AcO^-, while one-stage change is observed with $H_2PO_4^-$. Other anions induce practically no change in their spectral profiles. Systematic decrease in the MLCT band (490 nm) together with concomitant evolution of a band at the longer wavelength region (515 nm) takes place and saturation takes place with 4 equiv of F^-. Considerable quenching of emission accompanied with red-shift of emission maximum takes place in presence of F^- and AcO^-, whereas substantial augmentation with no shift in band maximum occurs with HSO_4^- and $H_2PO_4^-$. SWV shows gradual decrease in Ru^{II}/Ru^{III} peak current at 1.11 V with concomitant growth of current at 0.48 V in presence of the said anions and at saturation the peak at 1.11 V is completely replaced by the peak at 0.48 V. Spectroelectrochemical experiments show that the MLCT bands in the complexes gradually diminished with concomitant evolution of LMCT bands in the longer wavelength region during the course of oxidation.

It seems that the N-H motifs at first commune with anions (X^-) via N-H----X^- hydrogen bonding interaction and excess of X^- encourages further expansion of the N–H bond which eventually ruptures through complete proton removal. $H_2PO_4^-$, on the other hand, interacts only through hydrogen bonding and no proton removal is expected to takes place. Moreover, the deprotonation of the complexes by basic anions such as F^-, and AcO^- followed by its refurbishment to its initial state by acid is reversible and repetitive by many cycles. In the following section, we will use the spectral, electrochemical and spectroelectrochemical responses of complexes upon the action of anions to mimic the roles of YES-NOT and set-reset flip-flop logic gates. We will also apply ML tools such as ANNs, ANFIS, and Decision tree (DT) to analyze and forecast the experimental data and thus can reduce the time and expenditures connected with execution of comprehensive sensing experimentations.

5.3.2. YES (transfer) and NOT (not transfer) Logic System. In this case, we have chosen the emission spectral response of **1** upon the action of F^- ion. We have monitored two emission maxima (678 nm and 768 nm) as the outputs. Figure 5.1a clearly shows that in absence of F^-, the system exhibits its emission intensity only at 678 nm above the threshold and no emission at 768 nm indicating "ON" state (1) at 678 nm and "OFF" state (0) at 768 nm. By contrast, when F^- is added, the emission maximum at 678 nm quenched below the threshold, while the maximum at 768 nm reached above the threshold barrier, indicating the "OFF" state (0) at 678 nm and "ON" state (1) at 768 nm. Hence, upon monitoring the two output signals in absence and presence of F^-, we implemented a one-input and two-outputs YES (transfer) and NOT (not transfer) logic system (Figure. 5.1d).

5.3.3. Set-Reset Flip-Flop Logic. It is successive binary logic operator mimicked by a couple of cross-linked NOR gates. The applied potential of 0.05 and 1.09 V in the

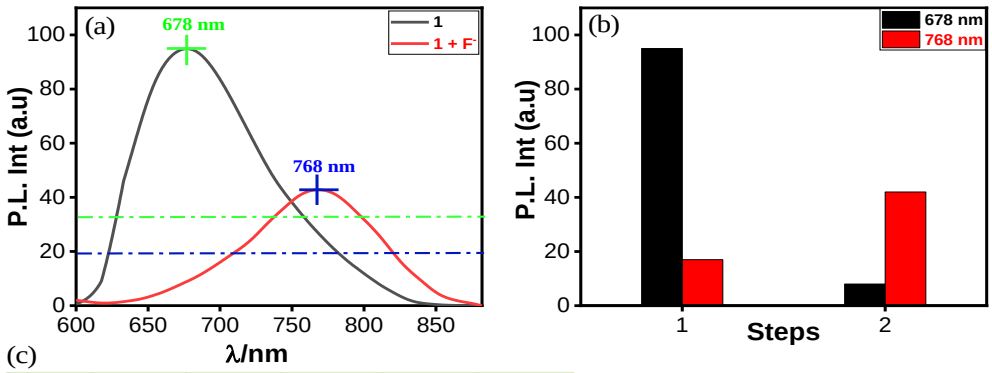

Steps	Input(F^-)	Output Emission at 678 nm	Output Emission Intensity at 678 nm	Output Emission at 768 nm	Output Emission Intensity at 768 nm
1	0	1(high)	95	0(low)	17
2	1	0(low)	8	1(high)	42

Figure 5.1. (a) Emission spectrum of **1** in absence and presence of F^- ion in MeCN-DCM (1:9 v/v) solution. (b) Histogram of emission intensities in absence and presence of F^-. (c) Represents the truth table of "YES" and "NOT" logic operations. (d) Represents the schematic diagram of these logic operations.

spectroelectrochemical measurements is allocated as input 1 and input 2, respectively. The "write-read-erase-read" cycle was also documented via spectroelectrochemistry. The absorbance at 706 nm was treated as the monitoring output 1, while at 468 nm as the

output 2 (Figure 5.2a). In every cycle, the potentials were applied to realize the "Write" (In 2, *E* = 1.09 V) or "Erase" (In 1, *E* = 0.05 V) process. In the "Write" process, the applied potential was +1.09 V (where the input combination is 0 1) and a high "Out 1" signal (1) and a low "Out 2" (0) signals were obtained and accordingly the output combination is 1 0. During the "Erase" process, the applied potential was +0.05 V (where the input combination is 1 0) and a low "Out 1" signal and a high "Out 2" signals were obtained and the output combination is 0 1 (Figure 5.2c). Hence, the "writing-reading-erasing-reading" of the absorption spectral response of the complex upon the application of suitable electrochemical potential mimic the function of set-reset flip-flop logic (Figure 5.2b). 1, 1 state is forbidden in set-reset flip flop. The flip flop does not get damaged in forbidden state (1, 1). It is called forbidden because there is no definitive guarantee of a fixed output.

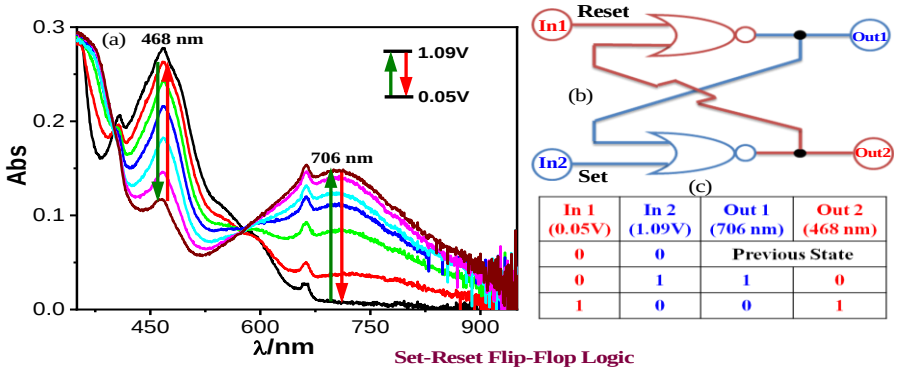

In 1 (0.05V)	In 2 (1.09V)	Out 1 (706 nm)	Out 2 (468 nm)
0	0	Previous State	
0	1	1	0
1	0	0	1

Figure 5.2. (a) Absorption spectral response of **2** during oxidation. (b) Schematic display and (c) truth table of the Flip-Flop logic.

5.3.4. Artificial Neural Network (ANN). As already pointed out ANN is one of the easiest and most suitable networks which facilitate the transfer of information into a specific way (from the input nodes through the hidden-, and eventually onto the output nodes). Furthermore, because of its high efficacy in predicting stationary system, we applied herein the ANN-FF grid to better understand (execution of the model via MATLAB 2018). Figure 5.3a and 5.3b show the variation of the current height of the Ru^{II}/Ru^{III} couple at 1.11 and 0.48 V upon incremental addition of AcO^-. Histogram in Figure 5.3c represents the current intensity at 0.48V and 1.11V upon simultaneous addition of H^+ and OAc^-. It is evident that at 0.48 V, the network's best authentication

achievement is 0.0014236 up to epoch 19 (Figure 5.4a), while 0.014952 up to epoch 5 at the observing current at 1.11V (Figure 5.4b). As evidenced by the advancement of the validation spectra (green line), the lowering of mean squared error (mse) along with progress of training gets halted after epoch 19 (for 0.48V) and 5 (for 1.11V) representing the current intensity at 0.48V and 1.11V due to addition of various combinations of H^+ and OAc^-. Figure 5.5 signifies the error histogram between the target and output. The Y-axis signifies the quantity of samples that occurs in a specific bin. The zero-error point is positioned underneath the bin centered at 0.005072 and 0.005877 for 0.48V and 1.11V, respectively, although the over-all error span from -0.1187 to 0.1165 for 0.48V and from -0.1967 to 0.2844 for 1.11V (Figure 5.5a and 5.5b). The value of regression (R) near to unity infers decent correlation and good performance of the model (Figure 5.6). The training status of the networks up to epoch 19 and 5 for 0.48V and 1.11V respectively was observed.

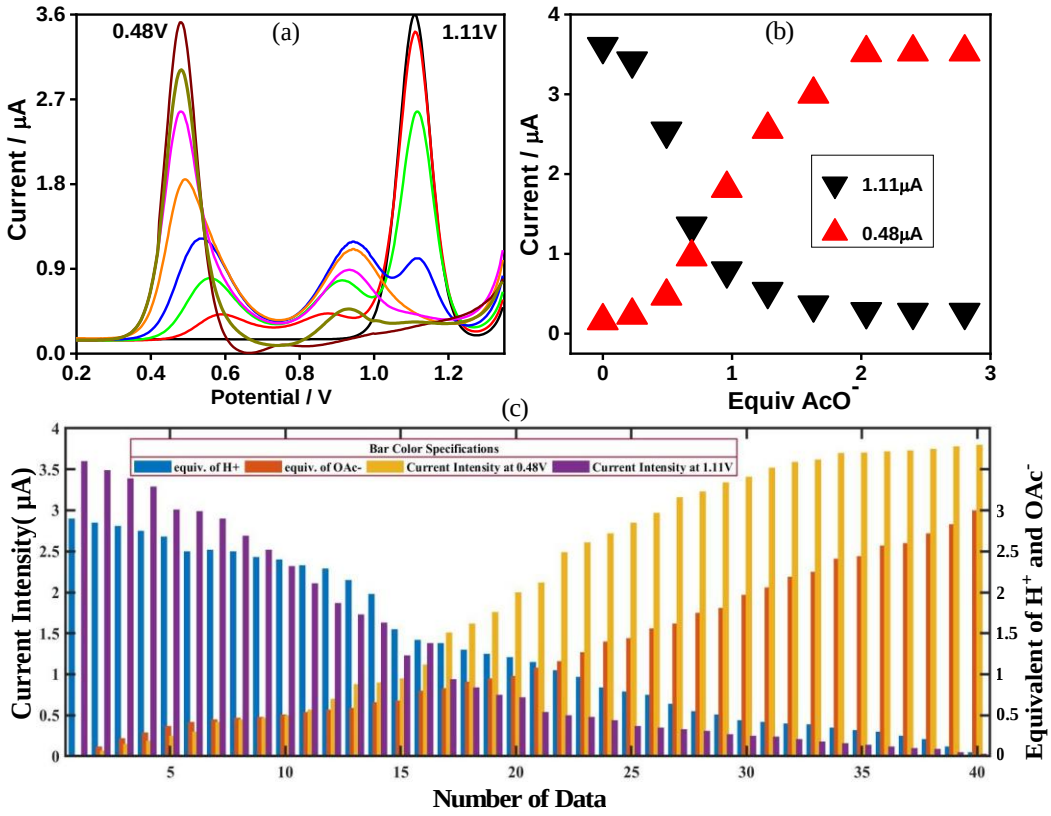

Figure 5.3 SWVs (a) of **2** in MeCN obtained upon incremental addition of AcO^-. (b) The changes in the current intensities due to incremental addition of AcO^-. (c) Histogram

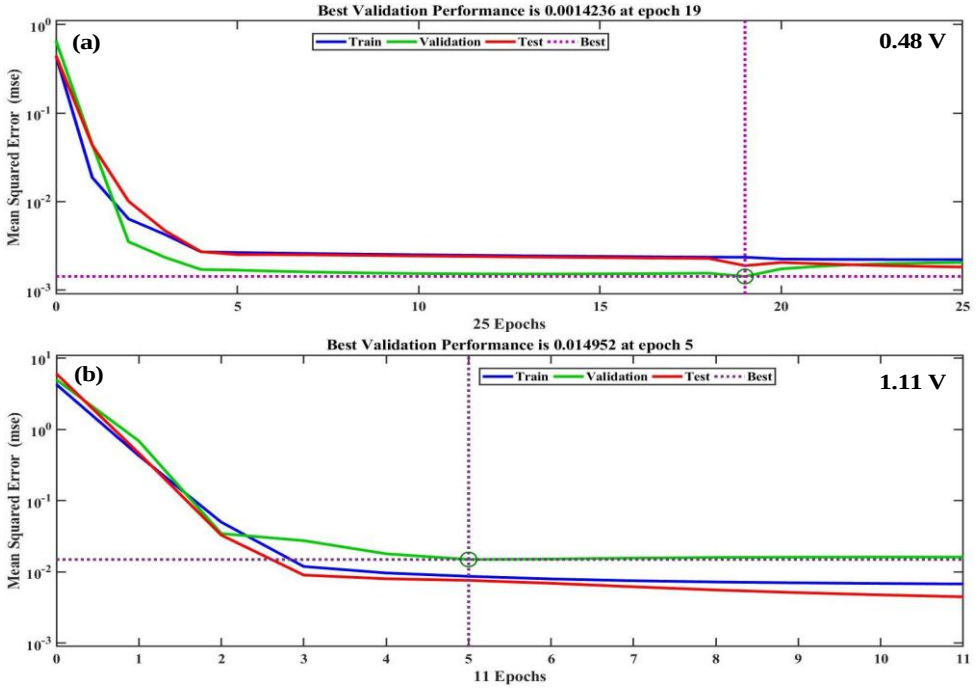

Figure 5.4 (a) and (b) represents the performance of the ANN at 0.48V and 1.11V, respectively.

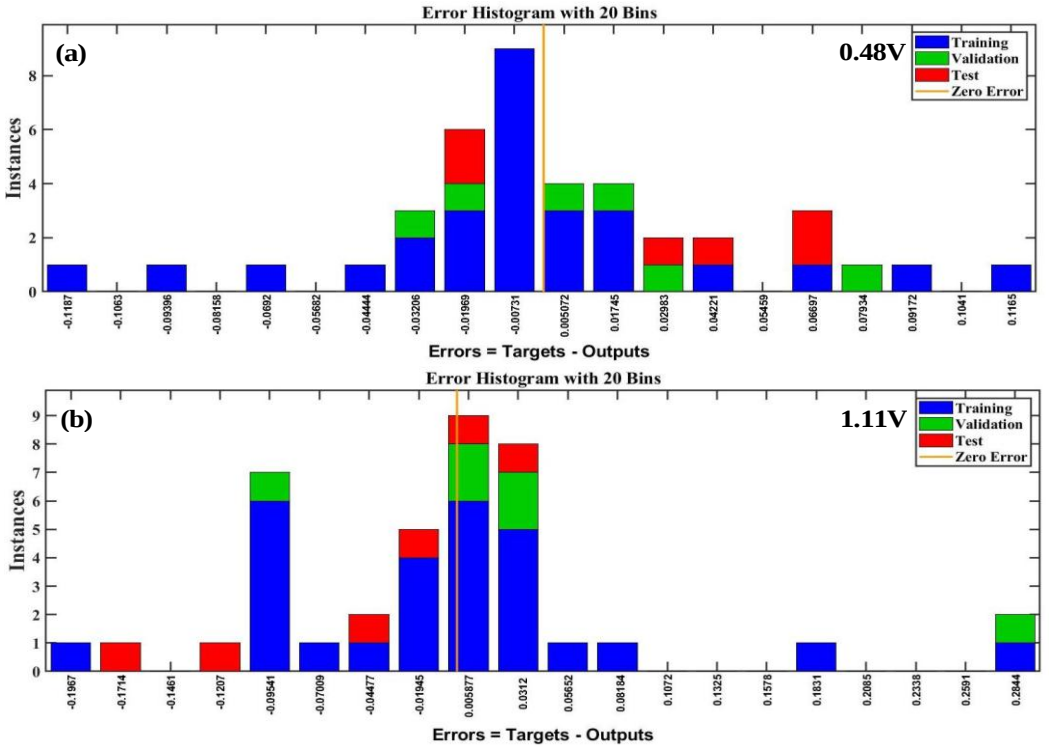

Figure 5.5 (a) and (b) represents the error histogram of ANN monitoring 0.48V and 1.11V respectively.

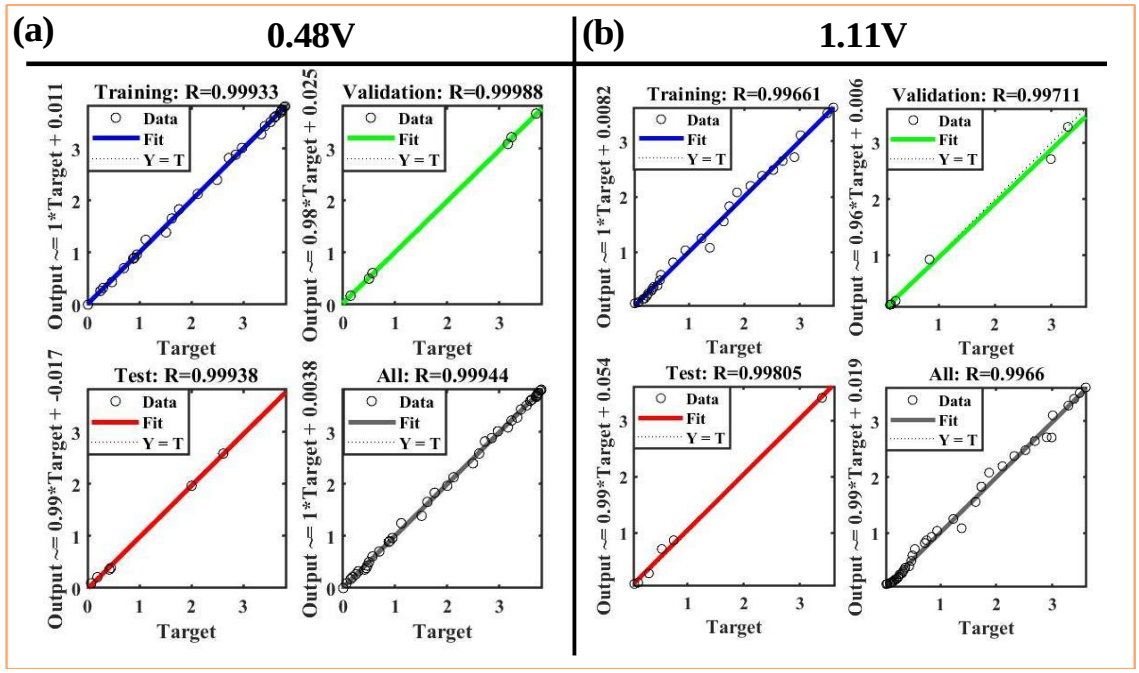

Figure 5.6 The regression analysis of the outcomes of ANN at 0.48 V (a) and 1.11 V (b).

5.3.5. Adaptive Neuro-Fuzzy Inference System (ANFIS). This is an amalgamation of FL and NN to succeed the disadvantage of each one and usually produces noteworthy results.[49,50] Sturdiness and better generality of ANFIS network offers a scope for applications which include crisp inputs and outputs. A schematic sketch of ANFIS network is provided. The basic architecture of the output forecaster model established by ANFIS to envisage the variation of current as a function of H^+ and OAc^- comprises of four vital steps (fuzzification, knowledge base, ANN, and defuzzification slabs.

To devise the network, 70% data were used for training, while the remaining 30% for testing and authentication. Figure 5.7b shows that the error is progressively decreased up to 20 epochs. Combination of 2 inputs and 3 membership functions for each will create 3^2= 9 IF-THEN rules. The outputs that are obtained by Sugeno's technique upon implication of 2 inputs and 3 membership functions are presented in Figure 5.8. The ANFIS forecasted outcomes displaying the connection among the inputs and outputs are displayed in 3D plots (Figure 5.9a and 5.9b). The created ANFIS network based on the 9 rules are also depicted in Figure 5.9c and 5.9d. The mean squared error (mse) and regression (R) statistical parameters of ANN as well as root mean squared error (RMSE)

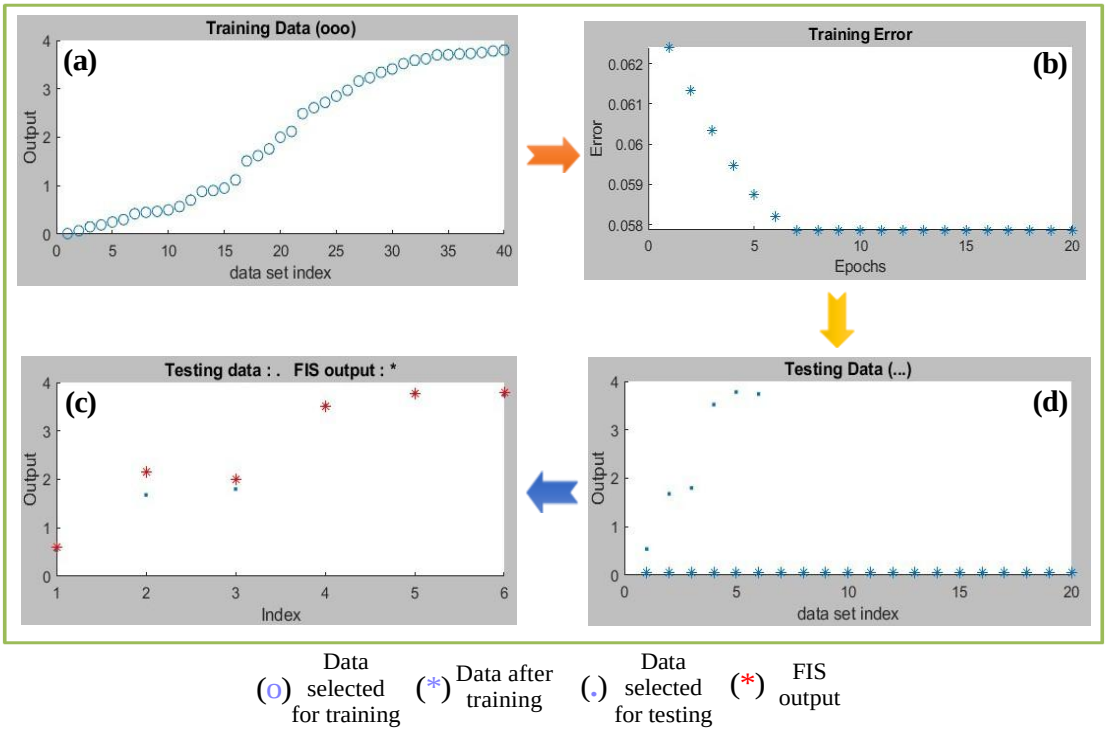

Figure 5.7 (a) Selected training data to create the ANFIS network. (b) Gradual reduction of training error up to 20 epochs. (c) Testing data after training process. (d) Combination of testing and output data.

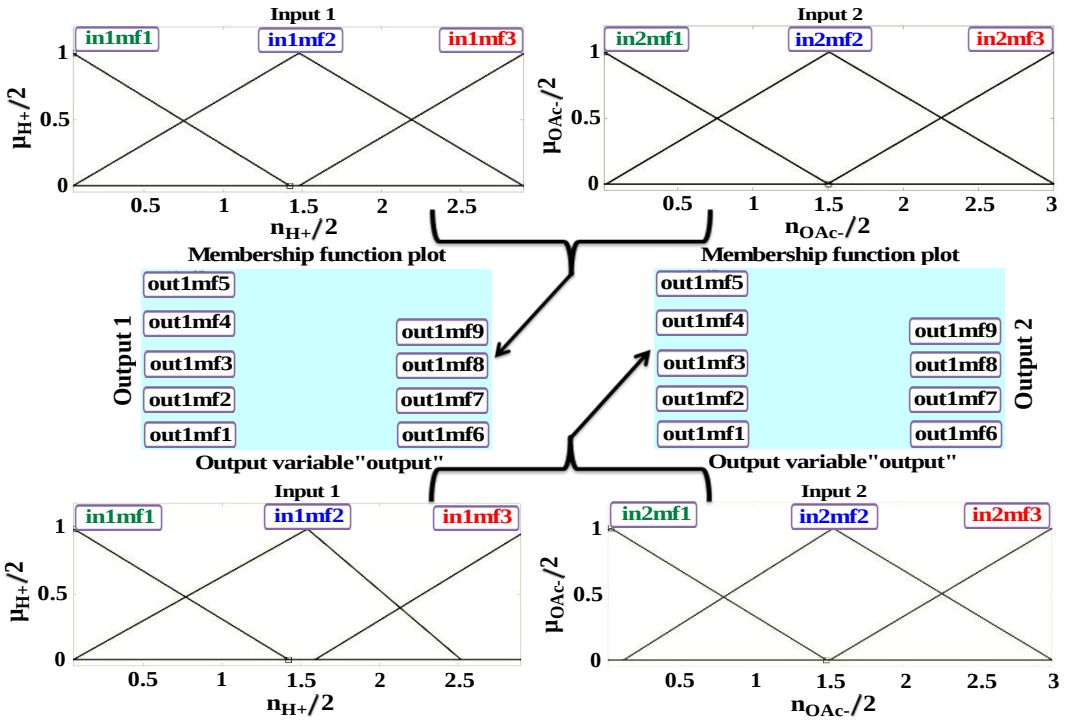

Figure 5.8 The outcomes of ANFIS at 0.48V and 1.11V following 9 rules.

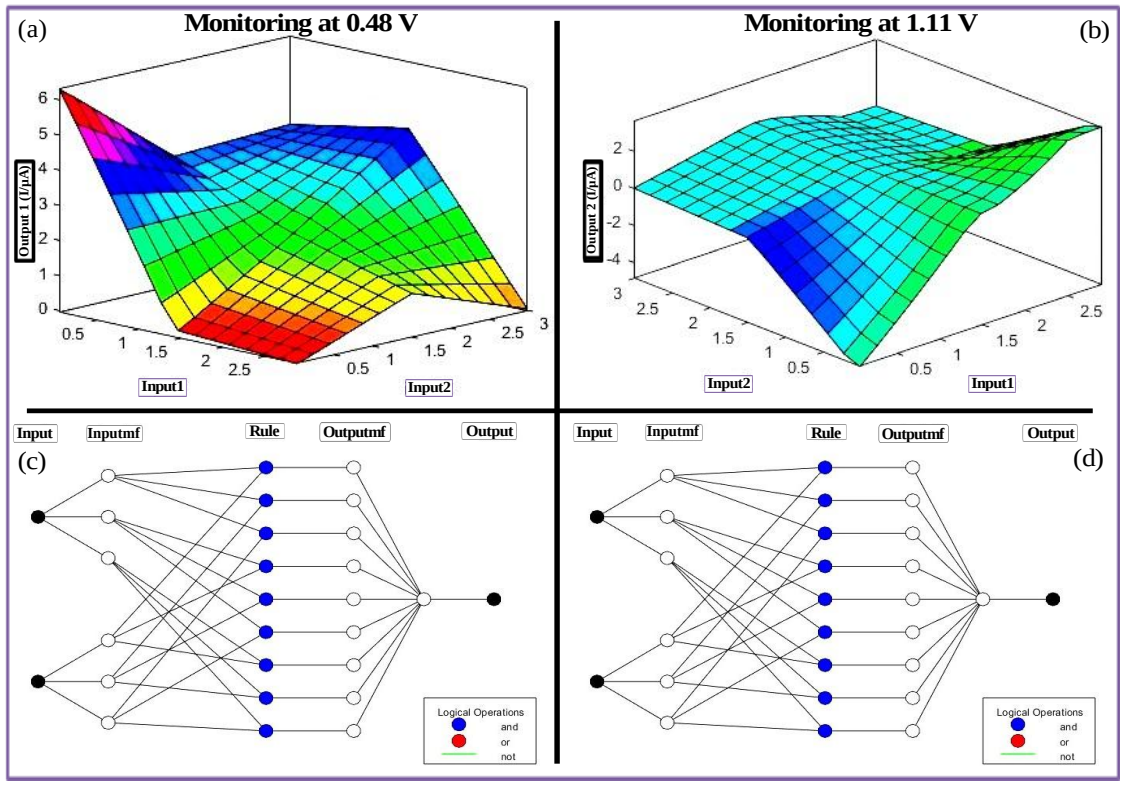

Figure 5.9 3D plots of alteration of current with H^+ and OAc^- (a and b). The resulted ANFIS structures for the outputs (c, d).

and Average Testing Errors (ATE) of ANFIS are presented inTable 5.1. The RMSE value of 0.057865 for 0.48V and 0.077117 for 1.11V clearly suggest that the model is working quite competently (Table 5.1). It is observed that the outputs derived from both the models are closer to the experimental values. But our main objective is to minimize the mse values close to zero. Hence, we employed the supervised learning algorithm and executed the decision tree regression modeling for better prediction of experimental data.

Table 5.1. Mean Square Errors (MSE) and Regression (R) Values of ANN Models as well as Root Mean Square Errors (RMSE) and Average Testing Error of ANFIS Models

Monitoring Current Intensity at	ANN Model		ANFIS Model	
	Mean Square Error (mse)	Regression (R)	Root Mean Square Error (RMSE)	Average Testing Error
0.48V	$6.62977e^{-2}$	$9.82857e^{-1}$	0.057865	0.21287
1.11V	$4.80689e^{-2}$	$9.97999e^{-1}$	0.077117	0.20675

5.3.6. Regression with Decision Tree (DTR). We have already made a brief description of the decision tree in the introduction part. Schematic presentation of a DT together with the description of each part is presented in Figure 5.10. DT is a type of supervised ML method which is employed to predict the observation (dependent variables) based on a given feature (independent variables) that supports the observation by "if-else" algorithm. Decision tree classifier (DTC) functions with quantitative categorical variables, such as Yes (1) or No (0). Decision tree regression (DTR), on the other hand, works with quantitative continuous variables with precision. Herein, we are interested to foresee the current intensities (dependent variables) on different voltages (0.48V and 1.11V) upon the influence of changing concentration of H^+ and AcO^- (independent variable). As our desire is to determine the absolute current intensities, we employed here the DTR technique. We fabricate an in-house DTR programme with the help Python language as it offers a wide range of libraries and ML which could be employed for processing of the chemical data. Additionally, most of the Python's popular libraries are free as well as open source. The libraries that we have employed in this work are: (i) Pandas for handling and processing of the data set, (ii) Matplotlib for plotting and (iii) Scikit-Learn for scientific computing and ML tools. Initially, we posses some experimental data sets that are employed for the training and testing purpose. Thereafter, we fit the training data set in the DTR to fabricate a model, taking advantage of which we can foresee the observations by unknown features (testing data).

Finally, we optimize the accuracy of our model based on R-square value or score. To obtain maximum accuracy (without over fitting), we also fit our training data with the DTR model. By using the outcome of the DTR model, we also create a DT which is displayed in Figure 5.11. The accomplishment and the statistical performance indicators of the DT model are provided in Figure 5.12 and Table 5.2, respectively. Compilation of model outputs and experimental data is presented in Table 5.3 and Figure 5.13a and 5.13b.

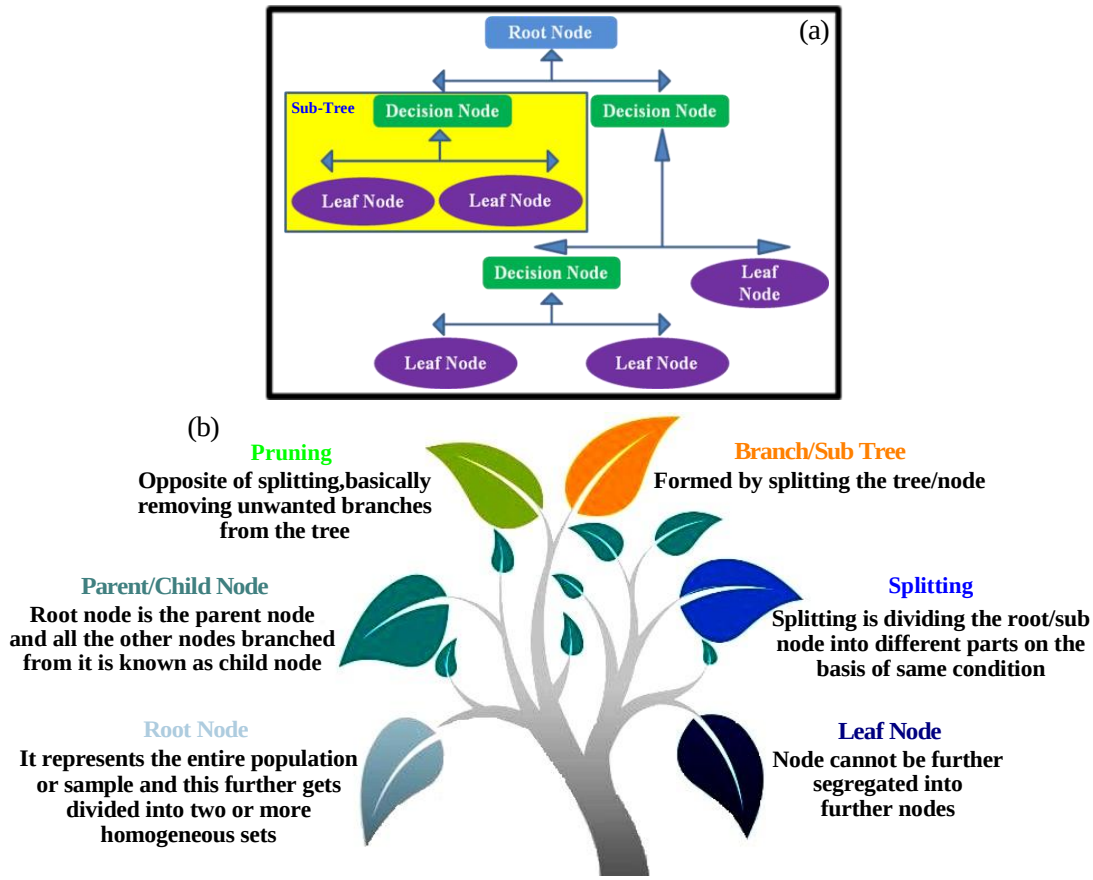

Figure 5.10 Schematic presentation of a decision tree (a) together with the description of each part (b).

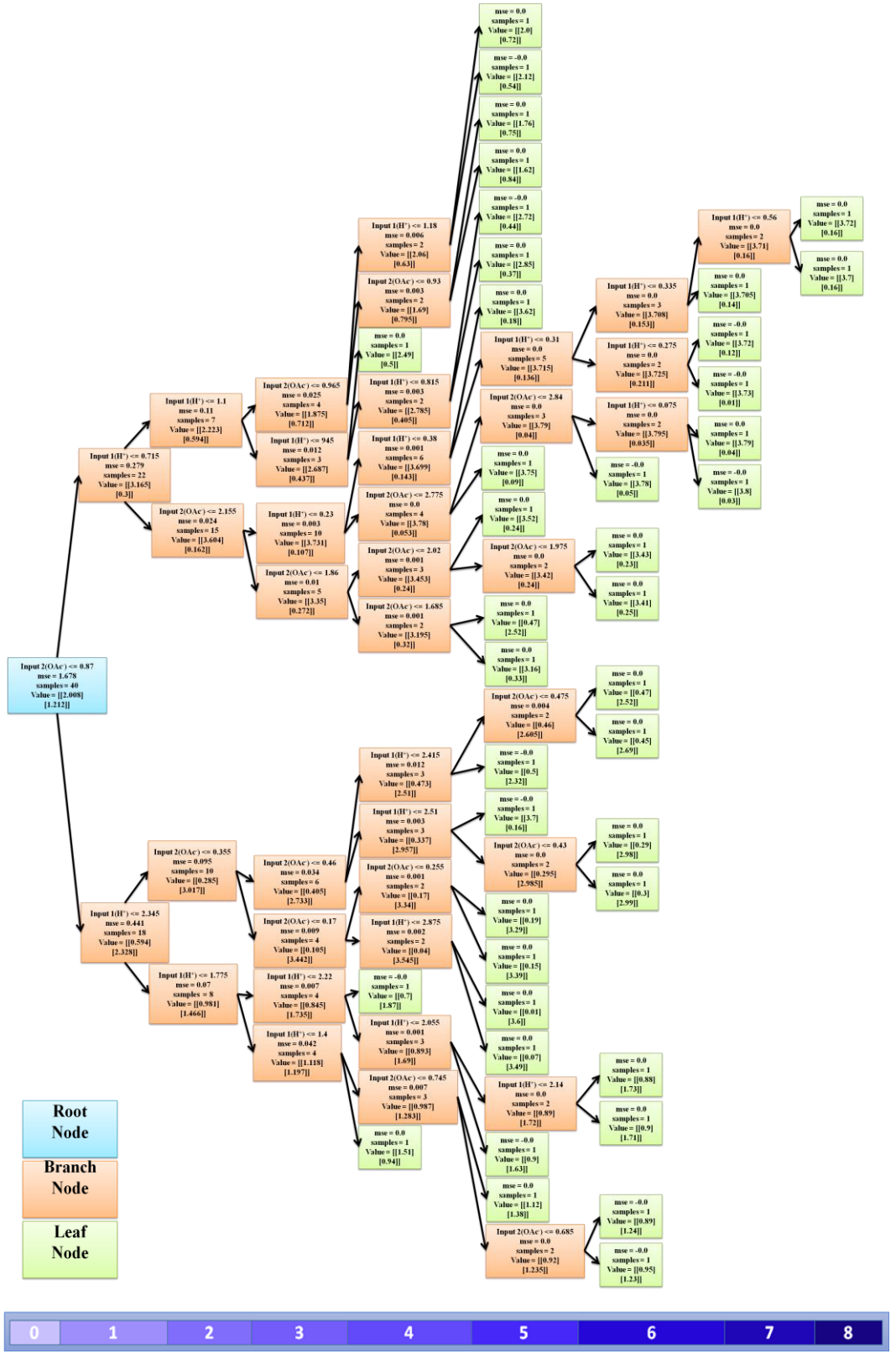

Figure 5.11 Schematic presentation of the decision tree.

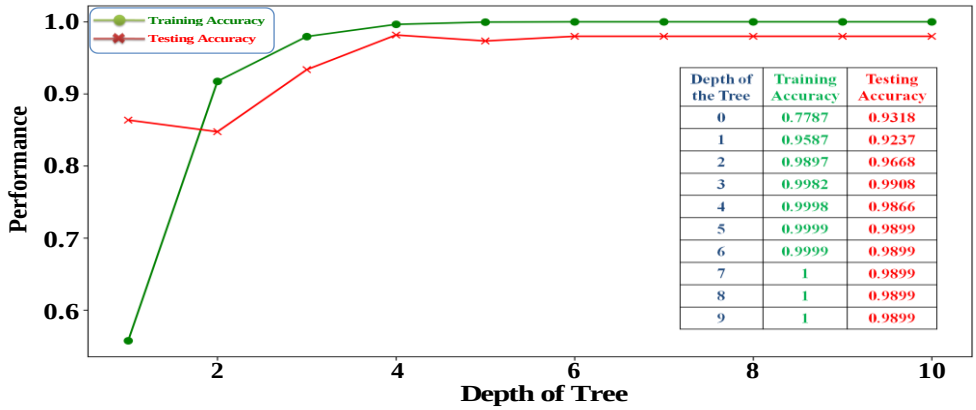

Depth of the Tree	Training Accuracy	Testing Accuracy
0	0.7787	0.9318
1	0.9587	0.9237
2	0.9897	0.9668
3	0.9982	0.9908
4	0.9998	0.9866
5	0.9999	0.9899
6	0.9999	0.9899
7	1	0.9899
8	1	0.9899
9	1	0.9899

Figure 5.12 Performance of the decision tree up to depth 9.

Table 5.2. Statistical Performance Indicators of Supervised Learning Based Decision Tree Regression Model

Decision Tree Regression	
R^2	0.9880
RMSE	0.9912
Training Accuracy (TrA)	1
Testing Accuracy (TeA)	0.9899
Error	TrA - TeA= 0.0101

Table 5.3. Comparison of Model Outputs and Experimental Data Derived from 6 Different Input Combinations.

No of data	Input 1 (H^+)	Input 2 (OAc^-)	Experimental Outputs		ANN Outputs		ANFIS Outputs		Decision Tree Assisted Outputs	
			Current Intensity at 0.48V	Current Intensity at 1.11V	Current Intensity at 0.48V	Current Intensity at 1.11V	Current Intensity at 0.48V	Current Intensity at 1.11V	Current Intensity at 0.48V	Current Intensity at 1.11V
1	2.37	0.56	0.54	2.13	0.60	2.25	0.59	2.23	0.5	2.32
2	1.1	0.89	1.68	0.81	2.30	0.79	2.16	0.33	1.62	0.84
3	1.24	1.1	1.8	0.67	1.76	0.76	1.99	0.81	2.12	0.58
4	0.46	2.09	3.52	0.27	3.52	0.19	3.51	0.23	3.52	0.24
5	0.18	2.7	3.78	0.07	3.76	0.09	3.77	0.07	3.75	0.08
6	0.14	2.89	3.74	0.09	3.77	0.08	3.81	0.07	3.79	0.09

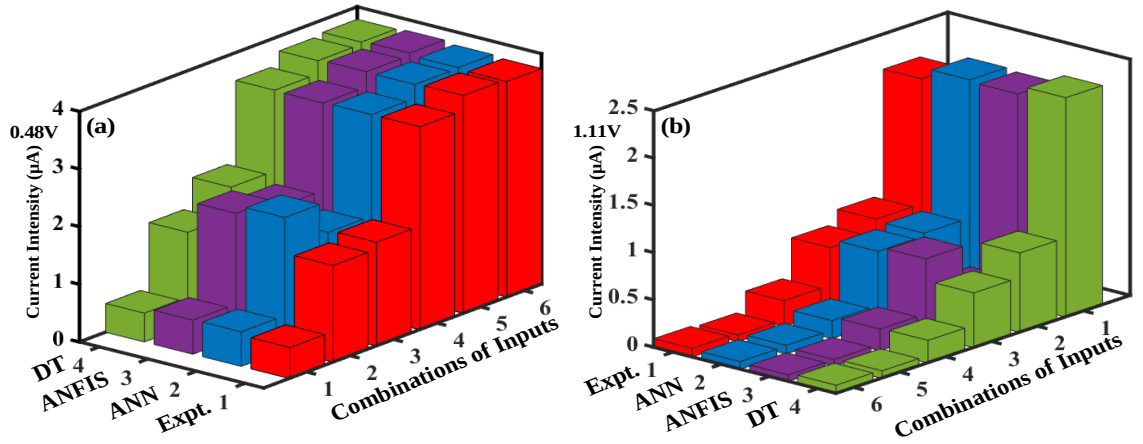

Figure 5.13. Histograms showing the comparison of the experimental outputs and the outcomes of ANN, ANFIS and DT models.

5.4. Conclusions

The technological developments of ML get recognized in almost all disciplines of science and technology in recent past. With regard to our sustained interest to explore the possibility of molecular level computation and implication of ML tools, we implemented both the classical and deep learning methods to understand and predict the anion-responsive behaviors of two heteroleptic Ru(II) complexes derived from two tridentate ligands, 2,6-bis (benzimidazole-2-yl)pyridine (H_2pbbzim) and substituted terpyridine ligands tpy-Ar with Ar = 2-naphthyl and 9-anthryl group. The inspiration in selecting Ru(II) complexes is due to their unique combination of photophysical and redox behaviors which in turn could be systematically modulated under the influence of different external stimuli and ultimately can lead to the fabrication potential molecular sensors and switches. The secondary coordination sphere of the complexes is decorated with two imidazole NH moieties and taking benefits of these NH motifs, the anion sensing characteristics of the complexes were thoroughly studied. Significant alteration of absorption, emission spectral as well as electrochemical and spectroelectrochemical responses of the complexes take place upon the action of selected anions. Incipient hydrogen bonding among the NH motifs and anions followed by anion-promoted deprotonation occurs in presence of basic anions. Moreover, the deprotonation of the complexes by basic anions such as F^-, and AcO^- followed by its refurbishment to its initial

state by acid is reversible and repetitive by many cycles.

We have utilized the spectral, electrochemical and spectroelectrochemical outputs of complexes upon the influence of anions to mimic the operations of YES-NOT and set-reset flip-flop logic gates. We also applied machine learning tools such as ANNs, ANFIS, and DT regression to analyze and foresee the experimental data and thus can reduce the time and expenditures connected with execution of comprehensive sensing experimentations. The model output of ANN, ANFIS and DT methods are also compared with the experimental results for better visualization. Among the three models, the outcomes derived from DT regression analysis turns out to be excellent with almost zero error. Thus, the applied machine learning based tools could be regarded as prospective anion sensing data model for the present Ru(II) complexes.

5.5. References

1. Artrith, N.; Butler, K. T.; Coudert, F. X.; Han, S.; Isayev, O.; Jain, A.; Walsh, A. Best Practices in Machine Learning for Chemistry. *Nat. Chem.* **2021**, *13*, 505-508.
2. Mater, A. C.; Coote, M. L. Deep Learning in Chemistry. *J. Chem. Inf. Model.* **2019**, *59*, 2545-2559.
3. Pflüger, P. M.; Glorius, F. Molecular Machine Learning: The Future of Synthetic Chemistry? *Angew. Chem. Int. Ed.* **2020**, *59*, 18860-18865.
4. He, L.; Bai, L.; Dionysiou, D. D.; Wei, Z.; Spinney, R.; Chu, C.; Xiao, R. Applications of Computational Chemistry, Artificial Intelligence, and Machine Learning in Aquatic Chemistry Research. *Chem. Eng. J.* **2021**, *426*, 131810.
5. Gentili, P. L. The Fuzziness of The Molecular World and Its Perspectives. *Molecules* **2018**, *23*, 2074.
6. Zadeh, L. A. Toward Human Level Machine Intelligence-Is It Achievable? The Need for a Paradigm Shift. *IEEE Comput. Intell. Mag.* **2008**, *3*, 11-22.
7. Szaciłowski, K. Digital Information Processing in Molecular Systems. *Chem. Rev.* **2008**, *108*, 3481-3548.
8. Zadeh, L.A. Outline of a New Approach to the Analysis of Complex Systems and Decision Processes. *IEEE Trans. Syst. Man Cyb.* **1973**, *3*, 28-44.
9. Conrad, M. Molecular Computing. *Adv. Comput.* **1990**, 31, 235-324.
10. Maity, D.; Das, S.; Mardanya, S.; Baitalik, S. Synthesis, Structural Characterization, and Photophysical, Spectroelectrochemical, and Anion-Sensing Studies of Heteroleptic Ruthenium(II) Complexes Derived from 4′-Polyaromatic-Substituted Terpyridine Derivatives and 2, 6-Bis (Benzimidazol-2-yl) Pyridine. *Inorg. Chem.*, **2013**, *52*, 6820-6838.
11. Sessler, J. L.; Gross, D. E.; Cho, W. S.; Lynch, V. M.; Schmidtchen, F. P.; Bates, G. W.; Light, M. E. and Gale, P. A. Calix [4] Pyrrole as a Chloride Anion Receptor: Solvent and Countercation Effects. *J. Am. Chem. Soc.*, **2006**, 128, 12281-12288.
12. Sessler, J. L.; Davis, J. M. Sapphyrins: Versatile Anion Binding Agents. *Acc. Chem. Res.* **2001**, *34*, 989-997.

13. Bhaumik, C.; Das, S.; Saha, D.; Dutta, S.; Baitalik, S. Synthesis, Characterization, Photophysical, and Anion-Binding Studies of Luminescent Heteroleptic Bis-Tridentate Ruthenium(II) Complexes Based on 2, 6-Bis (Benzimidazole-2-yl) Pyridine and 4′-Substituted 2, 2′: 6′, 2″ Terpyridine Derivatives. *Inorg. Chem.* **2010**, *49*, 5049-5062.

14. Mondal, D.; Bar, M.; Mukherjee, S.; Baitalik, S. Design of Ru(II) Complexes Based on Anthraimidazoledione-Functionalized Terpyridine Ligand for Improvement of Room-Temperature Luminescence Characteristics and Recognition of Selective Anions: Experimental and DFT/TD-DFT Study. *Inorg. Chem.* **2016**, *55*, 9707-9724.

15. Deb, S.; Sahoo, A.; Pal, P.; Baitalik, S. Exploitation of the Second Coordination Sphere to Promote Significant Increase of Room-Temperature Luminescence Lifetime and Anion Sensing in Ruthenium-Terpyridine Complexes. *Inorg. Chem.* **2021**, *60*, 6836-6851.

16. Mondal, D.; Biswas, S.; Paul, A.; Baitalik, S. Luminescent Dinuclear Ruthenium Terpyridine Complexes with a Bis-Phenylbenzimidazole Spacer. *Inorg. Chem.* **2017**, *56*, 7624-7641.

17. de silva, A. P.; Gunaratne, H. Q. N.; McCoy, C.P. A Molecular Photoionic AND Gate Based on Fluorescent Signaling. *Nature.* **1993**, *364*, 42-44.

18. Ling, J.; Daly, B.; Silverson, V. A. D.; de Silva, A. P. Taking Baby Steps in Molecular Logic-Based Computation. *Chem. Commun.* **2015**, *51*, 8403-8409.

19. Mondal, D.; Bar, M.; Maity, D.; Baitalik, S. Anthraimidazoledione-Terpyridine-Based Optical Chemosensor for Anions and Cations that Works as Molecular Half-Subtractor, Key-Pad Lock, and Memory Device. *J. Phys. Chem. C.* **2015**, *119*, 25429-25441.

20. Deb, S.; Sahoo, A.; Ahmed, T.; Baitalik, S. Stimuli-Responsive Molecular Switches and Logic Devices Based on Ru(II)-Terpyridyl-Imidazole Coordination Motif. *J. Phys. Chem. B.* **2021**, *125*, 8919-8931.

21. Paul, A.; Sahoo, A.; Bhattacharya, S.; Baitalik, S. Anion and Temperature Responsive Molecular Switches Based on Trimetallic Complexes of Ru (II) and Os

(II) that Demonstrate Advanced Boolean and Fuzzy Logic Functions. *Inorg. Chem.* **2022**, *61*, 3186-3201.

22. Mukherjee, S.; Sahoo, A.; Deb, S.; Baitalik, S. Light and Cation-Driven Optical Switch Based on a Stilbene-Appended Terpyridine System for the Design of Molecular-Scale Logic Devices. *J. Phys. Chem. A.* **2021**, *125*, 8261-8273.

23. Margulies, D.; Felder, C. E.; Melman, G. and Shanzer, A. A Molecular Keypad Lock: A Photochemical Device Capable of Authorizing Password Entries. *J. Am. Chem. Soc.* **2007**, *129*, 347-354.

24. Margulies, D.; Melman, G.; Felder, C. E.; Arad-Yellin, R. and Shanzer, A. Chemical Input Multiplicity Facilitates Arithmetical Processing. *J. Am. Chem. Soc.* **2004**, *126*, 15400-15401.

25. Margulies, D.; Melman, G. and Shanzer, A. A Molecular Full-Adder and Full-Subtractor, an Additional Step Toward a Moleculator. *J. Am. Chem. Soc.* **2006**, *128*, 4865-4871.

26. Szaciłowski, K. Molecular Logic Gates Based on Pentacyanoferrate Complexes: from Simple Gates to Three-Dimensional Logic Systems. *Chem. Eur. J.* **2004**, *10*, 2520-2528.

27. Szaciłowski, K.; Wojciech, M.; Grażyna, S. Light-Driven OR and XOR Programmable Chemical Logic Gates. *J. Am. Chem. Soc.* **2006**, *128*, 4550-4551.

28. Adamatzky, A.; Costello, B. D. L. Experimental Logical Gates in a Reaction-Diffusion Medium: The XOR Gate and Beyond. *Phys. Rev. E.* **2002**, *66*, 046112.

29. Adamatzky, A.; Tegelaar, M.; Wosten, H. A.; Powell, A. L.; Beasley, A. E.; Mayne, R. On Boolean Gates in Fungal Colony. *Biosystems*. **2020**, *193*, 104138.

30. Adamatzky, A.; Jones, J.; Mayne, R.; Tsuda, S.; Whiting, J. Logical Gates and Circuits Implemented in Slime Mould. *Advances in Physarum Machines.* **2016**, 37-74.

31. Gentili, P.L. The Fundamental Fuzzy Logic Operators and Some Complex Boolean Logic Circuits Implemented by the Chromogenism of a Spirooxazine. *Phys. Chem. Chem. Phys.* **2011**, *13*, 20335-20344.

32. Gentili, P. L.; Giubila, M. S.; Heron, B. M. Processing Binary and Fuzzy Logic by Chaotic Time Series Generated by a Hydrodynamic Photochemical Oscillator. *Chem Phys Chem.* **2017**, *18*, 1831-1841.

33. Gentili, P. L.; Giubila, M. S.; Germani, R.; Romani, A.; Nicoziani, A.; Spalletti, A.; Heron B. M. Optical Communication among Oscillatory Reactions and Photo-Excitable Systems: UV and Visible Radiation Can Synchronize Artificial Neuron Models. *Angew. Chem. Int. Ed.* **2017**, *56*, 7535-7540.

34. Gentili, P. L. and Micheau, J. C. Light and Chemical Oscillations: Review and Perspectives. *J. Photochem. Photobiol. C* . **2020**, *43*, 100321.

35. Sahoo, A.; Baitalik, S. Fuzzy Logic, Artificial Neural Network, and Adaptive Neuro-Fuzzy Inference Methodology for Soft Computation and Modeling of Ion Sensing Data of a Terpyridyl-Imidazole Based Bifunctional Receptor. *Frontiers in Chemistry*. **2022**, *10*, 864363.

36. Sahoo, A.; Ahmed, T.; Deb, S.; Baitalik, S. Neuro-Fuzzification Architecture for Modeling of Electrochemical Ion-Sensing Data of Imidazole-Dicarboxylate-Based Ru (II)-Bipyridine Complex. *Inorg. Chem.* **2022**, *61*, 10242-10254.

37. Mills, K.; Ryczko, K.; Luchak, I.; Domurad, A.; Beeler, C.; Tamblyn, I. Extensive Deep Neural Networks for Transferring Small Scale Learning to Large Scale Systems. *Chemical science*. **2019**, *10*, 4129-4140.

38. Curtis, C.; McKenna, M.; Pontes, H.; Toghani, D.; Choe, A.; Nance, E. Predicting in Situ Nanoparticle Behavior Using Multiple Particle Tracking and Artificial Neural Networks. *Nanoscale*. **2019**, *11*, 22515-22530.

39. Lv, H.; Chen, X. Intelligent Control of Nanoparticle Synthesis through Machine Learning. *Nanoscale*. **2022**, *14*, 6688-6708.

40. Goswami, S.; Pramanick, R.; Patra, A.; Rath, S. P.; Foltin, M.; Ariando, A.; Williams, R. S. Decision Trees within a Molecular Memristor. *Nature*. **2021**, *597*, 51-56.

41. Shiratori, K.; Bishop, L. D.; Ostovar, B.; Baiyasi, R.; Cai, Y. Y.; Rossky, P. J.; Link, S. Machine-Learned Decision Trees for Predicting Gold Nanorod Sizes from Spectra. *J. Phys. Chem. C*. **2021**, *125*, 19353-19361.

42. LeCun, Y.; Bengio, Y.; Hinton, G. Deep Learning. *Nature*. **2015**, *521*, 436-444.

43. Pedretti, G.; Graves, C. E.; Serebryakov, S.; Mao, R.; Sheng, X.; Foltin, M.; Strachan, J. P. Tree-Based Machine Learning Performed In-Memory with Memristive Analog CAM. *Nat. comm.* **2021**, *12*, 1-10.

44. Geurts, P.; Irrthum, A.; Wehenkel, L. Supervised Learning with Decision Tree-Based Methods in Computational and Systems Biology. *Molecular Biosystems*. **2009**, *5*, 1593-1605.

45. Swaney, D. L.; McAlister, G. C.; Coon, J. J. Decision Tree–Driven Tandem Mass Spectrometry for Shotgun Proteomics. *Nature methods*. **2008**, *5*, 959-964.

46. Gulyani, A.; Gopalan, R. S.; Kulkarni, G. U.; Bhattacharya, S. Twisted Aromatics, 9-Anthryl and 1-Pyrenyl Terpyridines Organize into Novel Multi-Directional 'Ladder-Like' Motifs in the Solid State. *J. Mol. Struc.* **2002**, *616*, 103.

47. Hargrove, A. E.; Nieto, S.; Zhang, T.; Sessler, J. L.; Anslyn, E. V. Artificial Receptors for the Recognition of Phosphorylated Molecules. *Chem. Rev.* **2011**, *111*, 6603.

48. Bhaumik, C.; Das, S.; Saha, D.; Dutta, S.; Baitalik, S. Synthesis, Characterization, Photophysical, and Anion-Binding Studies of Luminescent Heteroleptic Bis-Tridentate Ruthenium (II) Complexes Based on 2, 6-Bis (Benzimidazole-2-yl) Pyridine and 4′-Substituted 2, 2′: 6′, 2″ Terpyridine Derivatives. *Inorg. Chem.* **2010**, *49*, 5049.

49. Jang, J. S. R.; Sun, C. T. Neuro-Fuzzy Modeling and Control. *Proc. IEEE*. **1995**, *83*, 378-405.

50. Sugeno, M.; Yasukhiro, T. A Fuzzy-Logic-Based Approach to Qualitative Modeling. *IEEE Trans. Fuzzy Syst.* **1993**, *1*, 7-31.

****

6.1. Introduction

Tailored synthesis of molecules that can respond to external stimuli (such as ionic species) and causes extensive alteration of their physicochemical properties could be useful building constituents for diverse applications such as molecular sensors and switches.[1-14] This sort of molecular switches could also be important ingredients in the area of molecular computation. The idea of processing information at the molecular level was initiated by de Silva et al[15-17] and thereafter tremendous emphasis was provided to prepare useful molecular systems that can perform the operations of complicated logic functions which could ultimately yield highly efficient computers with small size that could not be achieved by conventional silicon-based devices.[18-21] Lots of efforts have already been provided to display the functions of fundamental logic gates together with high order functions, but molecular systems capable to demonstrate complicated and advanced logic functions as required in various circuits are relatively sparse in the literature.[22-30] So, there remains scope to synthesize smart molecular systems that on treatment with various external stimuli could generate multiple output signals for mimicking complicated logic functions.[31-36]

To this end, we synthesized a terpyridyl-imidazole receptor (**tpy-HImzPh$_3$NMe$_2$**) by incorporating NMe_2 group into the 4'-position of the terpyridine motif via phenyl-imidazole spacer for selective sensing of both cations and anions (**Chart 6.1**). In the synthetic planning of the receptor, a terpyridine motif is introduced for coordinating with metal ions, while the imidazole moiety for interacting with anions via hydrogen bonding interaction. Co-joining of strongly electron-donating NMe_2 groups in the phenyl-imidazole unit with terpyridyl electron acceptor unit yields ligand-to-ligand charge transfer (LLCT) probe whose photophysical properties could be significantly modulated by treating with selected anions, cations, acid as well as solvents of varying polarity. The receptor acts as multi-channel optical sensor for F^- and CN^- in organic solvent, while selective probe for CN^- in predominantly aqueous medium. Additionally, the receptor can visually recognize Fe^{2+} in presence of other bivalent 3d metals. By utilizing the optical spectral outputs upon the action of the ionic inputs, the receptor is capable to demonstrate NOT and YES Boolean logic operations. In addition to experiment, computational investigations using DFT and TD-DFT methods are also performed to acquire better

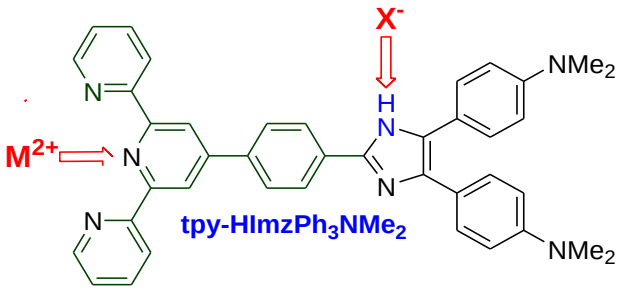

Chart 6.1. Chemdraw structure of the bifunctional receptor.

perception of the electronic structure of the probe and for appropriate assignment of the experimental spectral bands.

The operation of Boolean logic (BL) switches between two extremes, viz. '0' or '1' and very authoritative in distinction of true and false relations.[15-21] However, practical systems often composed of several intervening states in-between the two ends. The fuzzy logic system (FLS) could be a probable substitute of BL to address the intervening states [37-47]. We applied FLS on the present system to establish an infinite-valued logic system by considering the emission spectral response of the receptor under the influence of multiple external stimuli.

Machine learning (ML) and artificial intelligent (AI) tools are now-a-days used in all branches of science and technology and also play very crucial role in materials research. Through proper usage of powerful computational studies and high-throughput experimental works, ML has proved it credential to expedite the scientific research and technological growth. Time is extremely vital for each decision to take. Usually, a lot of time is consumed to gain a quantitative insight of a particular observation either via experiment or by computation. In order to diminish the time as well as the error, we will employ ML tools such as ANN[46-53] and ANFIS[54-59] and DTR[60-68] on the current dataset to understand as well as to anticipate the ion-responsive characteristics of the present receptor.

ANN network is inspired by human brain and may be useful to speculate the functions that rely on enormous number of unidentified factors. Amongst the two categories {recurrent (RNN) and feed-forward (FFN)}, we apply the ANN-function fitting (ANN-FF) network because of the static character of the present scheme and also due to its competence

in grasping and predicting a complex system. NNs usually possess good acquisitive aptitude from the data but not so competent with regard to understand the meaning of individual neuron and its weight. FL-based model, on the other hand, usually understand better as it functions through linguistic languages and IF-THEN rule but incapable to learn by itself. In order to overcome the lacuna of the individual one, we also applied herein ANFIS network (amalgamated form of NN and FL) for better understanding and prediction.

A model could be considered as an interpretable when its decision-making course might be recognized by a human. Decision tree-based regression might be regarded as an interpretable model as all of its "If-Else" rule-based decision-making course are easily understandable and could be visualized upon inspecting the path from root node to leaf node of the tree [60-68]. By contrast, a neural network based deep learning models could not be interpretable upon simple inspection. Hence, by exploiting its excellent interpretability, efficacy, and accuracy, we also applied herein DT-based tool for complete analysis and fully understand the ion-sensing behaviors of the receptor. Comparison was also made between the models' outputs and observed values for correct modeling of the ion sensing characteristics of the receptor.

6.2. Experimental Section

6.2.1. Materials. Chemicals and solvents were purchased from local suppliers. 4-formyl-2,2':6',2"-terpyridine(tpy-PhCHO) was prepared following reported procedures.[69]

6.2.2. Synthesis of the Ligand [(tpy-HImzPh$_3$(NMe$_2$)$_2$]. N,N dimethylbenzil (1.5 g, 2.45 mmol), tpy-PhCHO (0.825g 2.45mmol) and NH_4OAc (2.3 g, 30 mmol) were dissolved in CH_3COOH (10 mL) and refluxed for 3h. After cool down to RT, the resulting solution was poured into crushed ice (300 mL) and upon stirring a yellowish compound that deposited was filtered. The resulting solid was filtered and thoroughly washed with water. Purification of the compound was performed through column chromatography using $CHCl_3$ as the eluting solvent and finally through recrystallization from $CHCl_3$-MeOH (1:1) mixture Yield, 1.1 g, (73%).^{1}H NMR (400 MHz, DMSO-d_6, δ/ppm): 12.25 (s, 1H, NH(imidazole)), 8.75(s, 4H, $2H_3$+$2H_6$), 8.67(d, 2H, J=10.8 Hz, H_3), 8.26(d, 2H, J=11.6 Hz, H_8), 8.00-8.06 (m, 2H, H_7), 7.50-7.54(m, 2H, H_4), 7.38(d, 6H, J=11.6 Hz, H_5+H_9), 6.71 (d, 4H, J=12 Hz, H_{10}), 2.48(s,12H, Me). ESI-MS: m/z

614.34 ([L+H]$^+$). Anal. Calcd for $C_{40}H_{35}N_7$: C, 78.28; H, 5.75; N, 15.97. Found: C, 78.05; H, 5.82; N, 12.75.

6.2.3. Physical Measurements. The details of different equipments used and experimental process to measure absorption, luminescence and electrochemical spectral behaviors have been discussed in chapter 2.

The details of computational methods of ANFIS, ANN and DTR have already been discussed in chapter 3, 4 and 5 respectively.

6.2.4. X-ray Crystal Structure Determination. Crystals suitable for structure determination were obtained by diffusing toluene to a solution of **1** in MeCN-DCM (1:4, v/v). X–ray diffraction data for the crystal of **1** mounted on a glass fiber and coated with perfluoropolyether oil was collected on a Bruker–AXS SMART APEX II diffractometer at 296 K equipped with CCD detector using graphite–monochromated MoKα radiation (λ =0.71073 Å). The data were processed with SAINT and absorption corrections were made with SADABS.[70] The structures were solved by direct methods using SHELXT[71] program and refined by full matrix least-squares method based on F 2 by using SHELXL program through Olex-2.[72] The non hydrogen atoms were refined anisotropically, while the hydrogen atoms were placed with fixed thermal parameters at idealized positions. In the structure of **1**, two free water molecules remain in the crystal packing which was highly disordered and the structure was finally solved by removing the disordered water molecule by running the program SQUEEZE.[73] The electron density map also showed the presence of some unassignable peaks, which were removed by running the program SQUEEZE. The crystallographic figures have been generated using Diamond 3.1e software.[74] CCDC reference number: 2208591 for tpy-HImzPh_3NMe_2.

6.2.5. Computational Methods of DFT and TD-DFT. All calculations were performed with the Gaussian 09 program[75] employing the DFT method with Becke's three-parameter hybrid functional and Lee-Yang-Parr's gradient corrected correlation functional B3LYP level and of theory,[76,77] using 6-31g(d) basis set for the ligand. Geometries were fully optimized using the criteria of the respective programs. To compute the UV-vis transitions of the compounds, the singlet excited state geometries corresponding to the vertical excitations were optimized using the time-dependent DFT (TD-DFT) scheme starting with the ground state geometries optimized in solution

phase.[78,79] The excitation energies, computed in DCM were simulated by PCM model.[80,81] The geometries of the lowest energy singlet states of the compounds were also optimized in DCM by using TD-DFT method and employing the PCM models to calculate the emission energies. Orbital and fractional contribution analysis was done with Gauss View[82] and Gauss Sum 2.1.[83]

6.3. Results and Discussion

6.3.1. Synthesis and Characterization. Upon treating 1:1 molar ratio of dimethylaminobenzil and formylphenyl terpyridine (tpy-PhCHO) in AcOH and AcONa, the desired product is obtained in good yield. The receptor is purified through column chromatography followed by recrystalization from $CHCl_3$-MeOH mixture and characterized via elemental (C, H, N) analysis and ESI mass spectrometry as well as by ^{1}H NMR (Figure 6.3, 6.4). The solid-state structure of the receptor was also determined through single crystal X-ray crystallography.

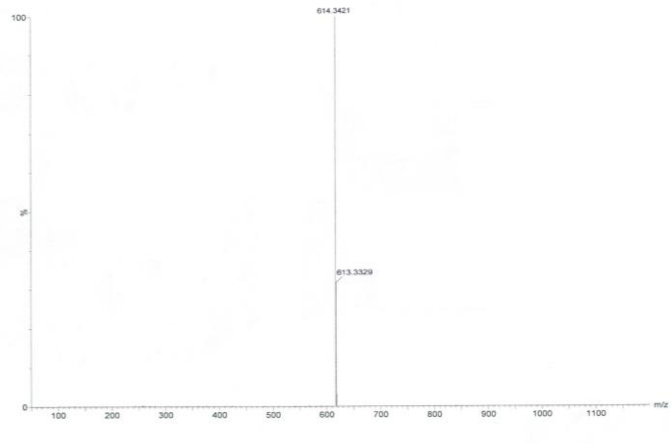

Figure 6.3. ESI (positive) mass spectrum for tpy-HImz$Ph_3(NMe_2)_2$ (m/z=614.34) ($[L+H]^+$) in MeCN.

6.3.2. X-ray Crystal Structure. The receptor crystallizes in the monoclinic form having space group of *C*2/c. The ORTEP plot of tpy-HImzPh_3NMe_2 is provided in Figure 6.5 and Table 6.1, while crystallographic data, selected bond distances and angles are presented in Table 6.2 and 6.3 respectively. Three pyridine units in the terpyridine motif assume *transoid* configuration across the interannular C-C bonds and thus minimizes

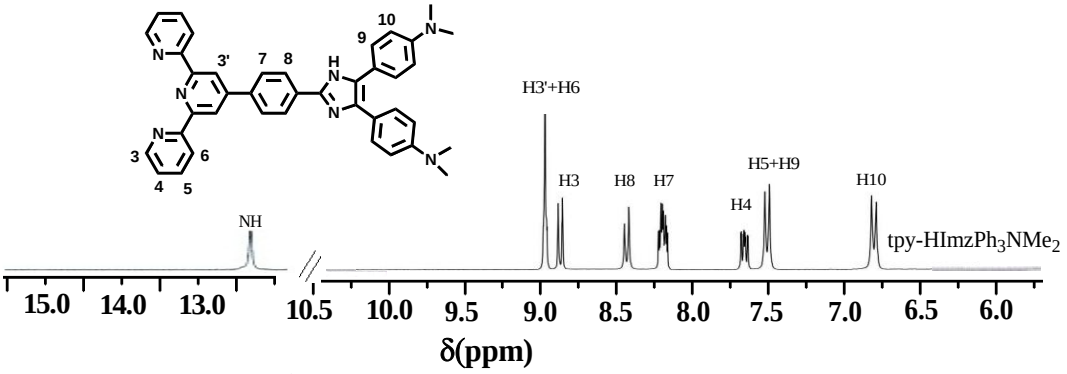

Figure 6.4. ^{1}H NMR spectrum of tpy-HImzPh$_3$(NMe$_2$)$_2$ in DMSO-d_6.

electrostatic interactions among the nitrogen lone pairs and the van der Waals interactions among the *meta* protons. It is of interest to watch that the imidazole NH proton is engaged in intermolecular hydrogen bonding with the N atom of a neighbouring tpy-HImzPh$_3$NMe$_2$ receptor with an N–H-----N distance of 2.172 A˚. Hence, it appears that the N-H motif of tpy-HImzPh$_3$NMe$_2$ has the ability to form adduct with incoming anionic guest through hydrogen bonding interaction.

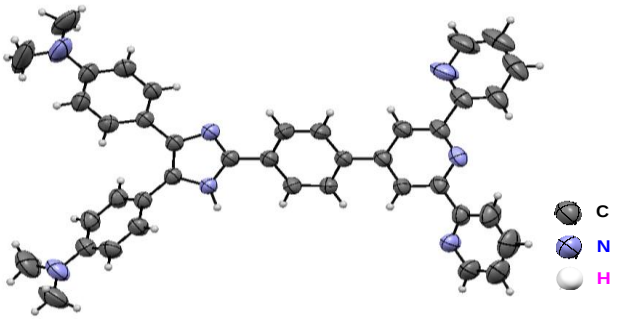

Figure 6.5. The ORTEP representation of tpy-HImzPh$_3$NMe$_2$ with 50% probability of thermal ellipsoids (CCDC reference number: 2208591).

6.3.3. Absorption and Emission Spectra. The spectral properties of the receptor are checked in different solvents and relevant results are provided in Table 6.4, Figure 6.6, and Figure 6.7. The receptor displays a strong absorption peak in the range of 386-408 nm due to intraligand charge transfer (ILCT) transition and another peak within the domain of 285-313 nm because of π-π^* transitions. Excitation to any of the bands gives rise to an intense emission band within 493-627 nm, having quantum yield (Φ) within 0.11-0.41 and lifetime (τ) between 2.0 ns and 4.0ns, dependent on the nature of solvent (Figure 6.7). Table 1 shows that small red-shift of spectral band takes place upon increase

in polarity of the solvents. The emission band displays a greater extent of solvatochromism relative to its absorption peak. Relatively large Stokes' shifts [(n_{abs}-n_{em})] of the emission band of the receptor are probably due to its enhanced charge-transfer character in the excited state. It is of interest to note that upon illumination of UV light, the emission color of the receptor alters between cyan and yellow as shown in the photograph (Figure 6.6a). The Commission Internationale de L'Eclairage (CIE) coordinates of the receptor in the studied solvents are displayed in Figure 6.6c.

Table 6.1. Crystallographic Data for tpy-HImzPh$_3$NMe$_2$.

CCDC reference number	2208591
Compound	tpy-HImzPh$_3$NMe$_2$
Formula	$C_{40}H_{35}N_7$
FW	617.530
T (K)	297 K
Cryst. Syst.	Monoclinic
Space group	C2/c
a (Å)	23.6456(9)
b (Å)	10.9809(4)
c (Å)	29.2135(11)
α (deg)	90
β (deg)	107.737(2)
γ (deg)	90
V (Å3)	7224.7(5)
Dc(g cm-3)	1.135
Z	8
μ (mm-1)	0.571
F(000)	2480.5
2θ range (deg)	7.86 to 150.6
Data/restraints/parameters	7152/0/432
GOF on F^2	1.092
Final R indexes [I>=2σ (I)]	R_1 = 0.0752, wR_2 = 0.1801
Final R indexes [all data]	R_1 = 0.0914, wR_2 = 0.1943
Largest diff. peak/hole / e Å^{-3}	0.29/-0.31

6.3.4. Anion Sensing Properties. We performed the sensing behavior of the receptor by taking advantage of its imidazole NH group via multiple channels, viz. absorption, emission, ^{1}H NMR spectroscopy as well as by time-correlated single photon counting techniques in both DCM and DMSO. Tetrabutylammonium (TBA) salts of F^-, Cl^-, Br^-, I^-, CN^-, $H_2PO_4^-$, AcO^-, NO_3^-, and ClO_4^- ions are employed for this purpose. The spectral profile of the receptor upon addition of 5 equiv of each of the studied anions in

Table 6.2. Selected Experimental Bond Distances (Å) for **tpy-HImzPh$_3$NMe$_2$.**

N5-C22	1.361(3)	C34-C35	1.368(3)
N5-C23	1.380(3)	C31-C30	1.379(3)
N2-C6	1.344(3)	C10-C9	1.379(3)
N2-C10	1.341(3)	C10-C11	1.487(3)
N4-C22	1.323(3)	C30-C27	1.394(4)
N4-C32	1.379(3)	C25-C26	1.383(3)
N1-C5	1.336(3)	C21-C20	1.369(3)
N1-C1	1.336(3)	C5-C4	1.383(3)
C33-C32	1.469(3)	C40-C39	1.397(4)
C33-C41	1.383(3)	C27-C26	1.376(4)
C33-C34	1.386(3)	C27-N6	1.388(3)
C22-C19	1.465(3)	C35-C39	1.379(4)
C19-C18	1.383(3)	N3-C11	1.330(4)
C19-C20	1.389(3)	N3-C15	1.333(4)
C7-C8	1.384(3)	C11-C12	1.365(4)
C7-C6	1.388(3)	N6-C28	1.430(5)
C8-C16	1.487(3)	N6-C29	1.417(5)
C8-C9	1.384(3)	C39-N7	1.399(3)
C23-C32	1.374(3)	C12-C13	1.398(4)
C23-C24	1.468(3)	C1-C2	1.355(4)
C16-C17	1.385(3)	C4-C3	1.377(5)
C16-C21	1.396(3)	N7-C01A	1.312(5)
C6-C5	1.481(3)	N7-C37	1.420(5)
C18-C17	1.383(3)	C13-C14	1.340(6)
C41-C40	1.372(3)	C2-C3	1.363(5)
C24-C31	1.386(3)	C14-C15	1.335(6)
C24-C25	1.382(3)		

Table 6.3. Selected Experimental Bond Angles (deg) for **tpy-HImzPh$_3$NMe$_2$.**

C23-N5-C22	107.60(18)	C11-C10-N2	116.6(2)
C10-N2-C6	117.69(19)	C11-C10-C9	121.0(2)
C32-N4-C22	105.49(18)	C10-C9-C8	120.5(2)
C1-N1-C5	117.6(2)	C27-C30-C31	121.0(2)
C41-C33-C32	121.44(19)	C26-C25-C24	121.7(2)
C34-C33-C32	121.9(2)	C20-C21-C16	121.4(2)
C34-C33-C41	116.6(2)	C6-C5-N1	117.03(19)
N4-C22-N5	111.34(19)	C4-C5-N1	121.3(3)
C19-C22-N5	123.67(19)	C4-C5-C6	121.6(2)
C19-C22-N4	124.9(2)	C39-C40-C41	120.6(2)
C18-C19-C22	122.4(2)	C26-C27-C30	117.0(2)
C20-C19-C22	119.8(2)	N6-C27-C30	121.2(3)
C20-C19-C18	117.8(2)	N6-C27-C26	121.8(3)
C6-C7-C8	120.1(2)	C21-C20-C19	121.3(2)
C16-C8-C7	122.23(18)	C27-C26-C25	121.7(2)
C9-C8-C7	116.9(2)	C39-C35-C34	121.0(2)
C9-C8-C16	120.8(2)	C15-N3-C11	117.8(3)
C32-C23-N5	105.18(18)	N3-C11-C10	116.8(2)
C24-C23-N5	121.22(18)	C12-C11-C10	121.8(3)
C24-C23-C32	133.55(19)	C12-C11-N3	121.4(3)
C17-C16-C8	121.7(2)	C28-N6-C27	120.1(3)
C21-C16-C17	117.1(2)	C29-N6-C28	117.4(3)
C33-C32-N4	120.07(18)	C35-C39-C40	117.6(2)
C23-C32-N4	110.39(18)	N7-C39-C40	121.5(3)
C23-C32-C33	129.53(19)	N7-C39-C35	120.9(3)
C7-C6-N2	122.4(2)	C13-C12-C11	117.9(4)
C5-C6-N2	116.38(19)	C2-C1-N1	124.5(3)
C5-C6-C7	121.2(2)	C3-C4-C5	119.2(3)
C17-C18-C19	120.9(2)	C01A-N7-C39	124.1(3)
C18-C17-C16	121.6(2)	C37-N7-C39	119.6(3)
C40-C41-C33	122.0(2)	C37-N7-C01A	116.1(3)
C31-C24-C23	121.68(19)	C14-C13-C12	120.6(4)
C25-C24-C23	121.71(19)	C3-C2-C1	117.8(3)
C25-C24-C31	116.6(2)	C15-C14-C13	117.2(3)
C35-C34-C33	122.2(2)	C2-C3-C4	119.5(3)
C30-C31-C24	122.0(2)	C14-C15-N3	125.1(4)
C9-C10-N2	122.4(2)		

Table 6.4. Photophysical Parameters in Various Solvent.

Solvent	Absorption λ_{max}/ nm (ε,$M^{-1}cm^{-1}$)	Luminescence		
		λ_{max}/ nm	τ/ns	Φ
Hexane	285(86100), 387(31400)	493	2.0	0.32
Toluene	313(br) (50500) 392(25300),	503	2.5	0.24
Chloroform	286(101900) 397(sh) (23300)	561	3.2	0.25
DCM	284(66500), 404(27100)	575	3.5	0.20
Acetone	389(25300)	602	2.5	0.11
MeCN	283(64000), 386(28300)	619	3.2	0.18
DMF	285(66000), 398(28900)	617	3.8	0.41
DMSO	286(65000) 408(28300)	627	4.0	0.36
Water	288(51000) 400(22000)	556	2.8	0.23

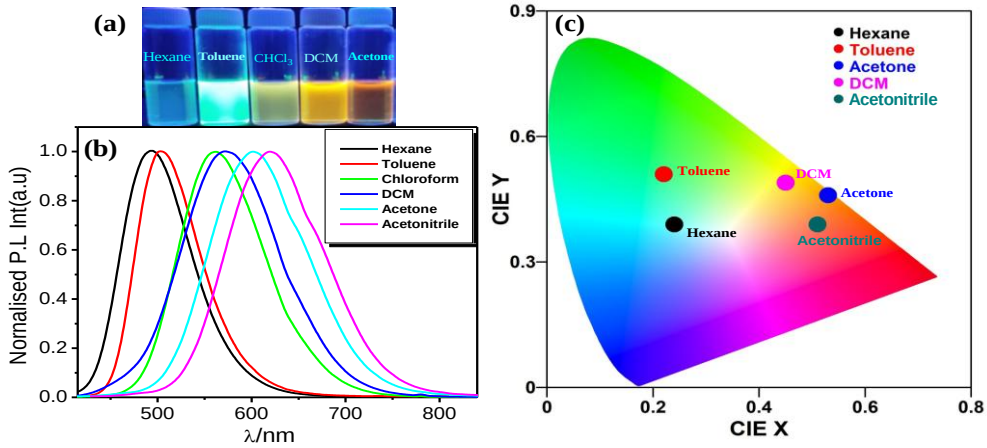

Figure 6.6. Visual color change upon illumination of UV light (a), normalized emission spectra (b), and CIE coordinates of the receptor in the different studied solvents (c).

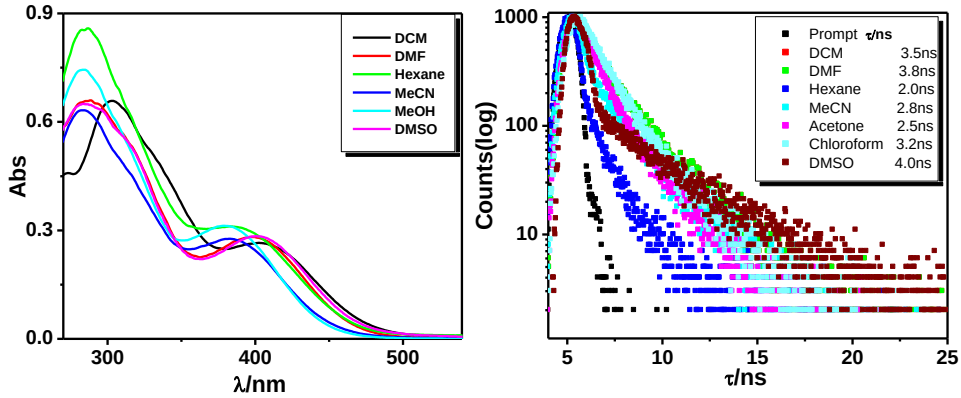

Figure 6.7. Changes in UV-vis spectrum and excited state decay profiles of receptor in different solvent.

DMSO is displayed in Figure 6.8. The spectral profiles of the receptor in two solvents are grossly similar with small variation in the band maxima. Among the anions, only F^- and CN^- bring about bathochromic shift of the absorption maximum (408→490 nm in DMSO, while 404→490 nm in DCM) as well as almost complete quenching of the emission intensity together with small red-shift (Figure 6.9).

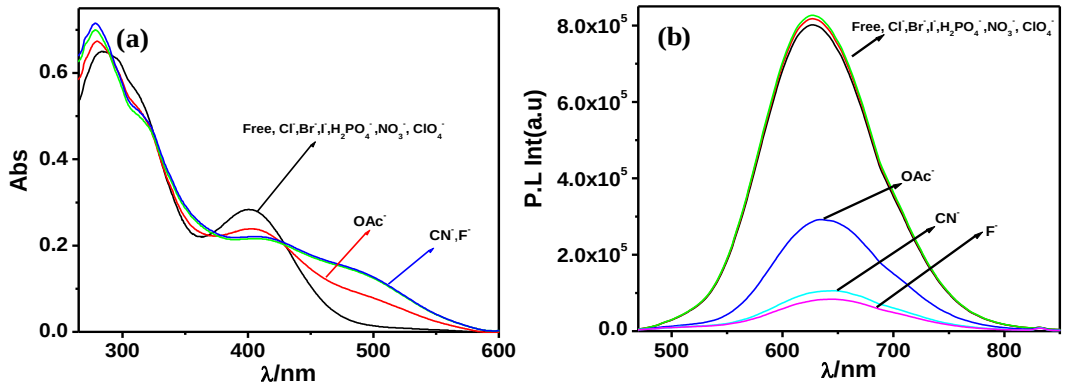

Figure 6.8. Change in absorption (a) and emission (b) spectral profile of the receptor in DMSO on addition of 5 equiv of different anions.

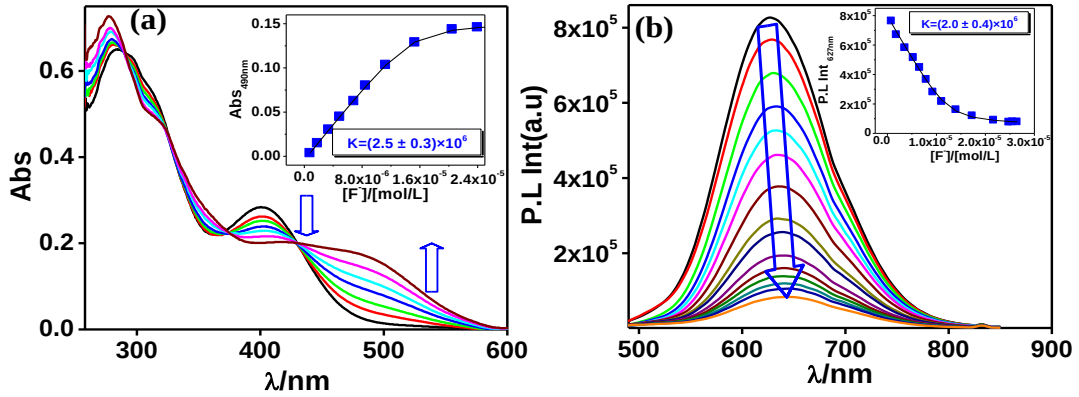

Figure 6.9. Change in UV-vis absorption (a) and luminescence (b) spectrum of **1** (1×10^{-5}M) in DMSO upon incremental addition of 0.1M of F^-. Insets display the fit of the experimental data to a 1:1 binding profile.

The original band at ~408 nm gets diminished systematically with concomitant development of a new peak at ~490 nm through well resolved isosbestic points in both DMSO and DCM solvents. The emission band (at 627 nm in DMSO and 575 nm in DCM) on the other hand, gets systematically quenched and saturation occurs with 2 equiv of the anions. The extent of spectral change with AcO^- is much less relative to both F^- and

CN^-. The red-shift of the spectral band is probably because of incipient hydrogen bonding followed by anion-promoted NH dissociation and subsequent spreading of the charge across the receptor backbone. In-line with steady state emission, the lifetime of the receptor also gradually decreases in presence of the said anions in both solvents (Figure 6.10). The binding constant (K_a) and limit of detection of the receptor towards F^- is also evaluated from the absorption and emission titration profile. The values of binding constant are grossly in the order of 10^6 and detection limit are in the order of 10^{-8} M (Table 6.5 and 6.6).

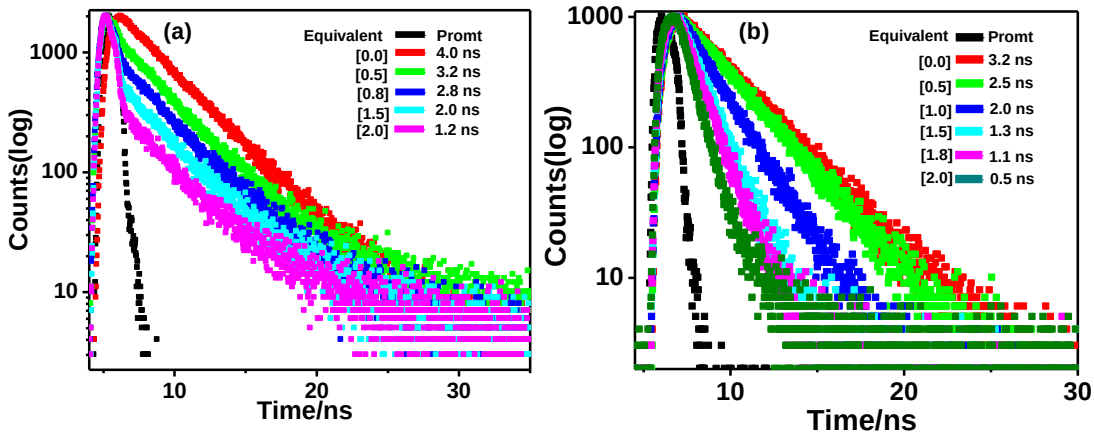

Figure 6.10. Change in excited state lifetime of the receptor in (a) DMSO and (b) DCM with gradual addition of F^-. Inset shows the corresponding lifetime values.

Table 6.5. Value of Binding Constants [a,b] (K) for **1** in DMSO at RT

From Absorption spectra	
F^-	$K=2.5\times10^6$
Fe^{2+}	$K=2.0\times10^6$
From Emission spectra	
F^-	$K=2.0\times10^6$
Fe^{2+}	$K=2.4\times10^6$

[a]t-Butyl salts of the respective anions were used for the studies. [b]Estimated errors were < 15 %

Table 6.6. Value of Limit of Detection of **1** in DMSO

Value of Limit of Detection of **1** in DMSO			
F^-		Fe^{2+}	
Absorption	Emission	Absorption	Emission
1.45×10^{-8}M	2.4×10^{-8}M	8.0×10^{-9}M	6.0×10^{-9}M

The competition experiments of tpy-HImzPh$_3$NMe$_2$ with F^- and CN^- in presence of other anions are also performed in DMSO through absorption and emission spectroscopic techniques. In both cases, substantial red-shift of the lowest energy absorption band as well as almost complete quenching of emission intensity is observed.

^{1}H NMR spectrum of the receptor is acquired in DMSO-d_6 upon step-by step addition of F^- and the overlaid spectra are displayed in Figure 6.11. The NH signal at 12.3 ppm gradually loses its intensity and eventually disappeared upon addition of 2.0 equiv of F^-. At the same time, the H_7-H_{10} protons adjacent to the imidazole motif are shifted gradually towards the up-field region. The tpy protons, on the other hand, remains almost unaltered in presence of F^-. Deprotonation of imidazole motif strongly indicates that F^- acts as the proton abstractor. The up-field movement of the H_7-H_{10} protons adjacent to the imidazole motif is probably because of increase in electron density at these centres caused by dissociation of NH proton followed by delocalization of the negative charge.

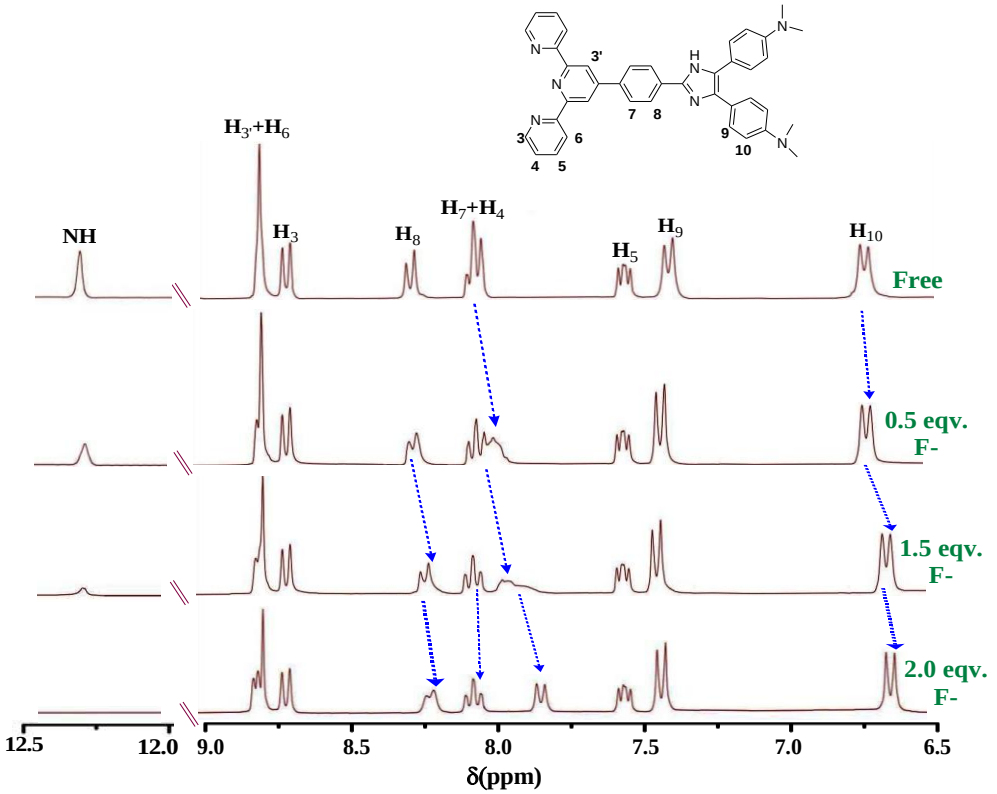

Figure 6.11. ^{1}H NMR spectrum of the receptor upon addition of F^- in DMSO-d_6.

For real practicability, the sensing experiments is also carried out in water. Because of solubility limitation in water, we used DMSO/H_2O (1:9 v/v) solution of the

receptor for performing sensing experiments. Previously, we observed that the receptor displays vivid response for F^-, CN^-, and AcO^- in DCM and DMSO without much selectivity. On the contrary, the receptor exhibits strong selectivity as well as sensitivity only for CN^- amongst all anions in predominantly water medium. The extent of change in the absorption spectral profile is relatively less in water compared to that of organic media. On the other hand, almost complete quenching of emission along with small blue-shift of emission maximum is noticed upon gradual addition of CN^- (10 equiv). The selectivity of the receptor for CN^- among the remaining anions (F^- and AcO^-) is most likely due to its smaller free energy of hydration ($\Delta G_h°$= -295 kJ/mol) compared with F^- ($\Delta G_h°$= -465 kJ/mol) and AcO^- ($\Delta G_h°$= -365 kJ/mol) Furthermore, CN^- functions as a strong base relative to F^- and AcO^- which is reflected in their p*K*a values (p*K*a = 9.0 for HCN) than HF (p*K*a = 3.17) and AcOH (p*K*a = 4.75) in water. [84]

6.3.5. Cation Sensing Properties. By virtue of the presence of the terpyridine motif, the receptor is able to interact with metal ions via coordination. The spectral profile of the receptor upon addition of 1 equiv of each of the studied cations in both DMSO and DCM are displayed in Figure 6.12. Among all the cations, only Fe^{2+} generates an intense band at 590 nm (for DMSO) and 576 (for DCM) together with sharp color change from yellow to deep violet due to Fe^{II}(d)→tpy(π*) charge transfer transition. It is to note that Fe^{3+} does induce any such color because of its inability to promote metal-to-ligand charge transfer transition (MLCT).

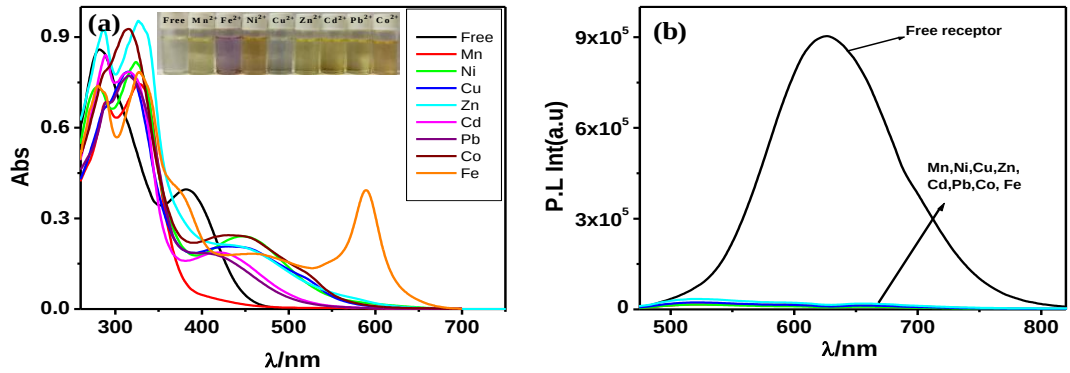

Figure 6.12. Change in absorption (a) and emission (b) spectral profile of the receptor in DMSO upon addition of different metal ions. Inset shows the visual color change.

The other ions (Mn^{2+}, Ni^{2+}, Cu^{2+}, Zn^{2+}, Cd^{2+}, Pb^{2+} and Co^{2+}), on the other hand, induce a peak in the spectral range of 414-450 nm because of intra-ligand charge transfer (ILCT) transition. The emission band at 627 nm (for DMSO) and at 575 nm (for DCM) diminishes in intensity in presence of all the cations. The spectral titrations are performed with Fe^{2+} in both DCM and DMSO and saturation takes place with 0.5 equiv of cation implying the generation of the complex adduct of the type $[Fe(tpy\text{-}HImzPh_3NMe_2)_2]^{2+}$ (**Chart 6.2**). Spectral titrations profile in DMSO is presented in Figure 6.13.

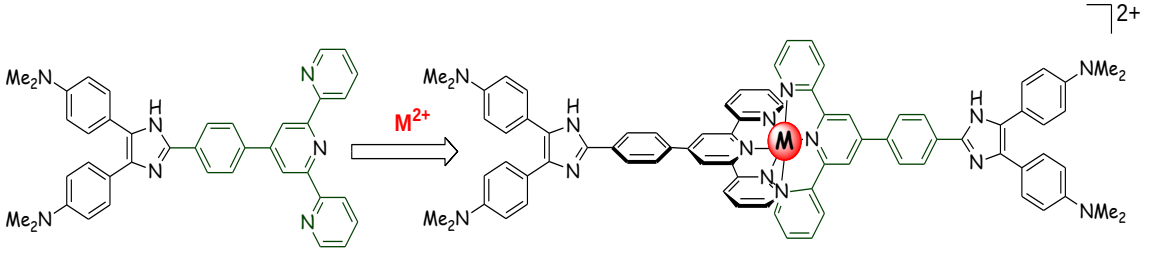

Chart 6.2

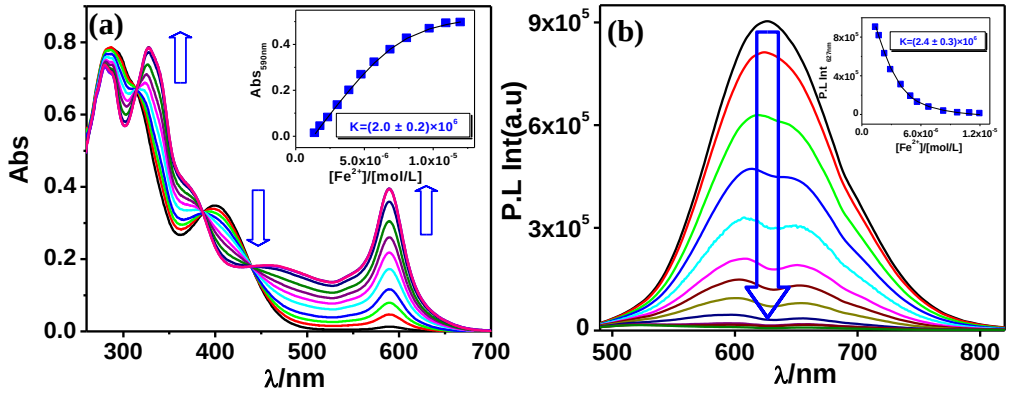

Figure 6.13. Change in UV-vis absorption (a) and luminescence (b) spectrum of **1** (1×10^{-5}M) in DMSO upon incremental addition of 0.1M Fe^{2+}. Insets display the fit of the experimental data to a 1:1 binding profile.

The composition of the resulting adduct was confirmed by acquiring its ESI mass spectrum (the peak at m/z = 641.26 corresponds to $[Fe(tpy\text{-}HImzPh_3NMe_2)_2]^{2+}$). In-line the anion sensing, the competition experiments of $tpy\text{-}HImzPh_3NMe_2$ with Fe^{2+} in presence of other studied cations are also carried out in DMSO via absorption and emission spectroscopy (Figure 6.14).

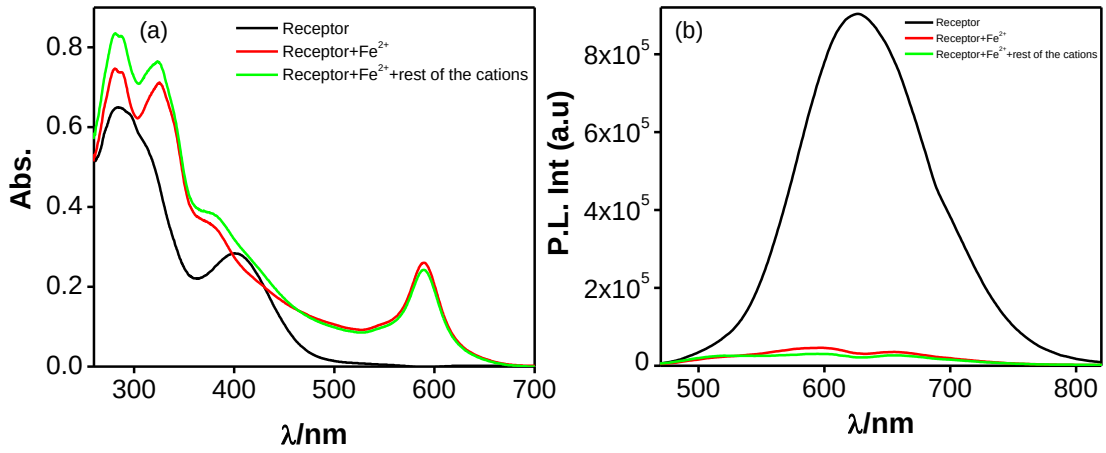

Figure 6.14. Change in absorption (a) emission (b) spectral profile of tpy-HImzPh$_3$NMe$_2$ in competition experiment of Fe^{2+} in presence of other cations in DMSO.

An intense absorption band at 590 nm and complete emission quenching is again observed with Fe^{2+} in presence of other cations.

The NMR spectrum of $[Fe(tpy\text{-}HImzPh_3NMe_2)_2]^{2+}$ complex is shown in Figure 6.15. It is observed that $H_{3'}$, H_6, H_7 and H_8 protons move to deshielded region whereas H_4, H_9 and H_{10} protons remain almost unaltered in the Fe complex. The H_3 proton of terpyridine moiety is affected most and shifts to a significantly up-field region because on complex formation, the said proton comes above the anisotropic ring current of pyridine ring of other terpyridine moiety. Binding constant (K_a) and detection limit of Fe^{2+}-receptor interaction was also evaluated from the absorption and emission titration profile. The values of binding constant are grossly in the order of 10^6, while the limit of detection is in the order of 10^{-9} M.

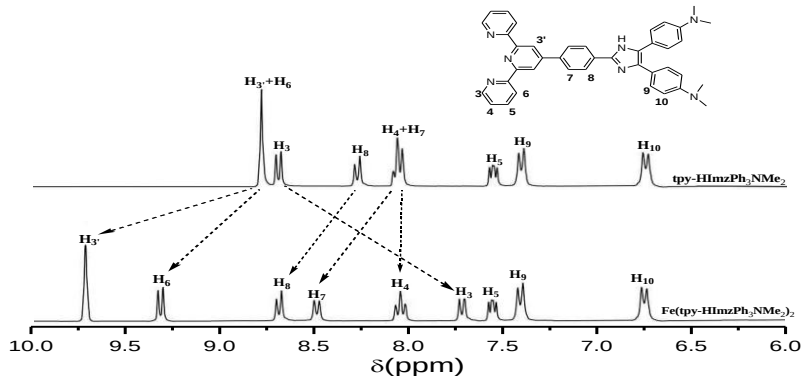

Figure 6.15. ^{1}H spectrum of the receptor and its Fe-complex in DMSO-d_6.

6.3.6. DFT and TD-DFT Investigation. Geometry optimization is performed on tpy-HImzPh$_3$NMe$_2$ as well as its deprotonated form (tpy-ImzPh$_3$NMe$_2$) in DCM by using Gaussian 09 program (Figure 6.16). The FMO sketch shows that with few exemptions, the HOMOs are mostly confined on dimethylamionobenzene and imidazole motifs, whereas the LUMOs are localized on the tpy unit (Figure 6.17 and 6.18). The charge distribution in both forms of the receptor could be envisioned from their respective ESP schemes, wherein the red and blue color designates the area of negative and positive charge, respectively (Figure 6.19).

TD-DFT calculations are also executed on the optimized geometries on both forms of the receptor in DCM to get their calculated absorption spectra. The correspondence among the calculated and experimental spectra is reasonably well.

The participation of the MOs in their longer-wavelength bands is depicted in Fig. Figure 6.20. The calculated lowest energy band at 413 nm (for tpy-HImzPh$_3$NMe$_2$) and at 530 nm for tpy-ImzPh$_3$NMe$_2$ is due to intra-ligand charge transfer from the dimethylaminobenzene-imidazole portion to the tpy unit, whereas the band at 365 nm is because of combined ILCT and π-π* transitions. The respective observed bands are 386 and 284 nm. Additionally, red-shift of the ILCT bands upon deprotonation is also observed by calculation.

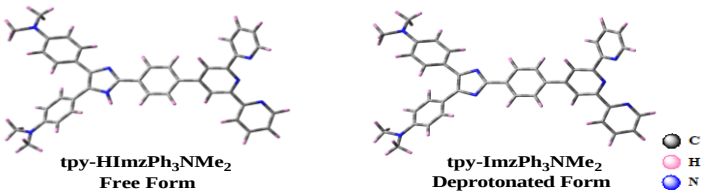

Figure 6.16. Ground state optimized geometry of free and deprotonated form of tpy-HImzPh$_3$NMe$_2$.

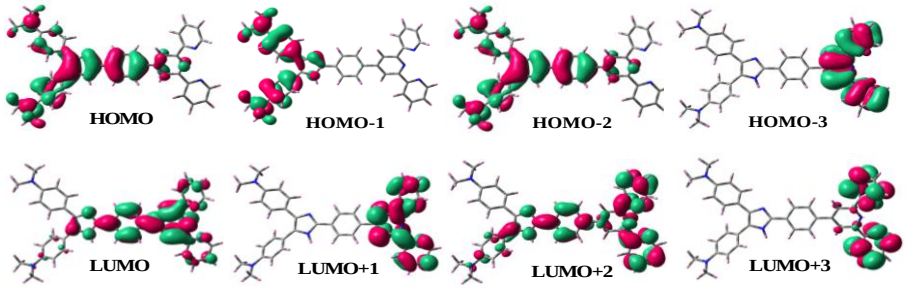

Figure 6.17. Schematic drawings of the selective frontier molecular orbital of tpy-HImzPh$_3$NMe$_2$ in DCM.

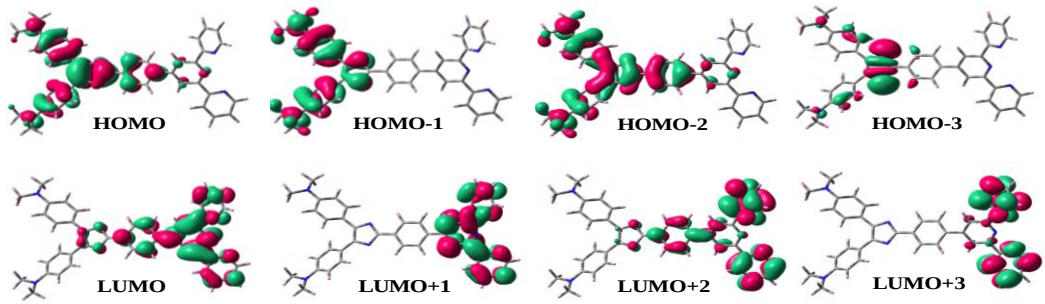

Figure 6.18. Schematic drawings of the selective frontier molecular orbital of deprotonated form of the receptor (tpy-ImzPh$_3$NMe$_2$) in DCM.

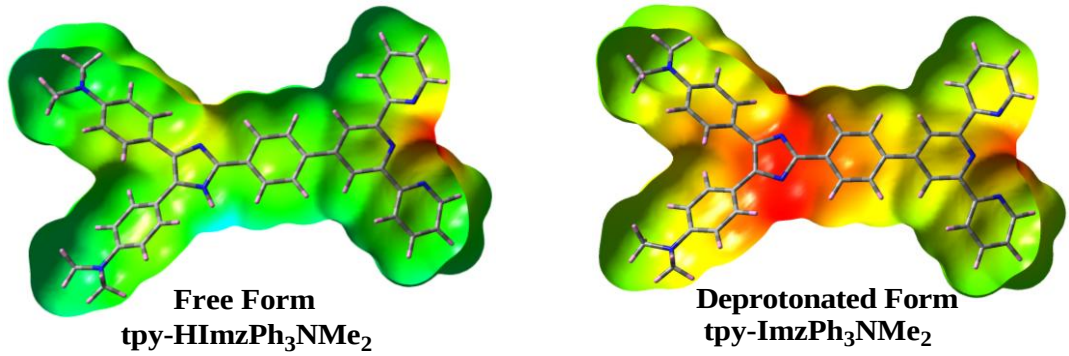

Figure 6.19. Electrostatic surface potential (ESP) plots of free and deprotonated form of tpy-HImzPh$_3$NMe$_2$ in DCM.

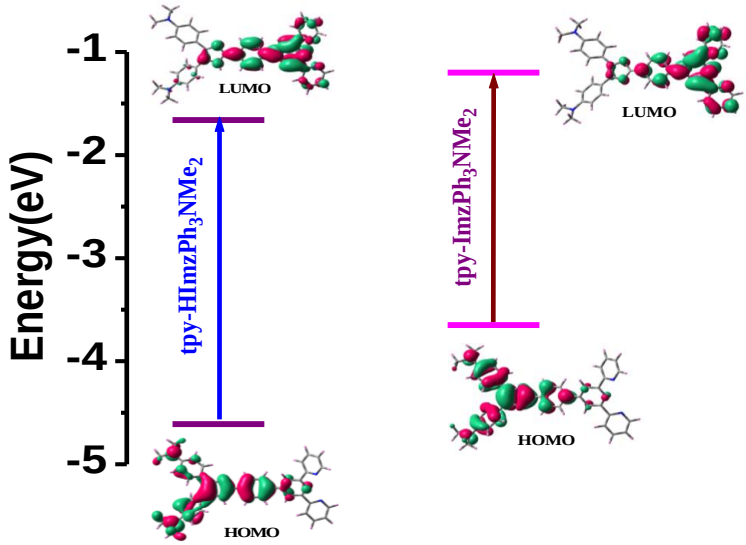

Figure 6.20. Calculated energy level diagram showing major transitions that comprise the lowest-energy absorption band for tpy-HImzPh$_3$NMe$_2$ and tpy-ImzPh$_3$NMe$_2$.

To address the emission spectral behaviors, we optimized the geometries of the compounds in their lowest singlet (S1) excited states. The computed emission peaks at 595 and 622 nm that are observed for tpy-HImzPh$_3$NMe$_2$ and tpy-ImzPh$_3$NMe$_2$ respectively, agree reasonably well with their corresponding experimental values (575 and 596 nm). Moreover, the red-shift of emission band upon deprotonation of the NH motif of tpy-HImzPh$_3$NMe$_2$ is also reproduced by computation.

6.4. Logic Behavior of the Receptor. In the previous section, we have observed that the deprotonation of NH motif in tpy-ImzPh$_3$NMe$_2$ occurs under the influence of the strongly basic anions such as F^- and CN^-. Interestingly, the refurbishment of the original form of the receptor is made possible upon the action of acid and this deprotonation-protonation process is reversible.

It would be interest to note that addition of either Fe^{2+} or CN^- quenched the fluorescence of the receptor. Addition of Fe^{2+} leads to the formation of [Fe(tpy-HImzPh$_3$NMe$_2$)$_2$]$^{2+}$ complex which is non-emissive because of the presence of low-lying triplet and/or quintet ligand field state ($^{3/5}$LF). In presence of F^- and/or CN^-, incipient hydrogen bonding between the imidazole NH proton and the said anions, followed by anion-induced proton transfer takes place from the receptor backbone. The observed emission quenching in presence of F^- and CN^-, is probably because of photo-induced electron transfer from the deprotonated imidazolate moiety to the excited fluorophore. Interestingly, sequential addition of Fe^{2+} followed by CN^- recovers the fluorescence of the receptor. As already mentioned, addition of Fe^{2+} induces the formation of [Fe(tpy-HImzPh$_3$NMe$_2$)$_2$]$^{2+}$ complex and thereby almost complete quenching of fluorescence takes place. Now, incremental addition of either F^- or CN^- gives rise to gradual increase in emission intensity till saturation up to ~12 equiv of F^- or CN^-. This observation suggests that addition of the said anions lead to sequester Fe^{II} from the complex backbone and produces a more stable ion-pair or complex anion of the type $[FeX_6]^{4-}$ (X= F^- or CN^-) and in presence of excess anions complete de-coordination takes places leading to the restoration of the initial state of the receptor. Consequently, the emission profile of the initial free form of the receptor is restored. Hence, by using the spectral outputs arising out of reversible deprotonation-protonation and complexation-decomplexation characteristics of the receptor, the functions of multiple logic gates could be mimicked.

6.4.1. Not Transfer (NOT) and Transfer (YES) Effect of CN^-. We have fabricated a combinational logic system of NOT and YES gate using the action of CN^- on Fe^{2+} complex. For this purpose, we have chosen the absorption and emission intensity at 576 and 575 nm, respectively as the outputs. Figure 6.21a and b clearly shows that in presence of CN^-, the absorbance at 576 nm quenched below the threshold barrier and emission intensity at 575 nm overcomes the threshold barrier, indicating the "OFF" and "ON" states, respectively (Figure 6.21c).

We can also see the action of not transfer (NOT) and transfer (YES) gates in analog circuits (Figure 6.21e). In "NOT" gate, the presence of CN^- bypass the current from the output lamp source but for "YES" gate CN^- allows the passage of current through the circuit (Figure 6.21e).

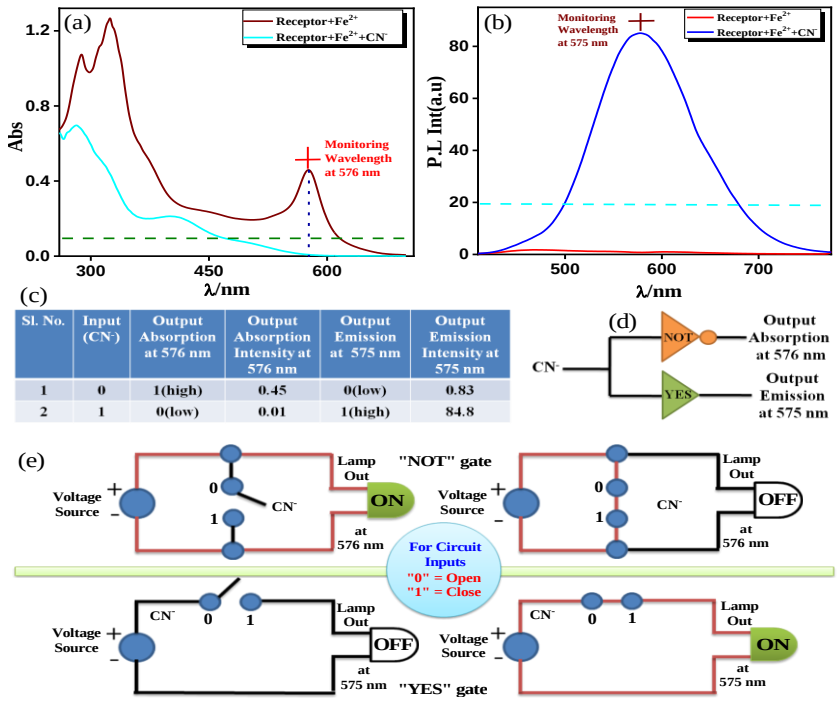

Sl. No.	Input (CN^-)	Output Absorption at 576 nm	Output Absorption Intensity at 576 nm	Output Emission at 575 nm	Output Emission Intensity at 575 nm
1	0	1(high)	0.45	0(low)	0.83
2	1	0(low)	0.01	1(high)	84.8

Figure 6.21. Absorption and emission spectral response of the Fe^{2+}-complex upon the action of and CN^- (a and b, respectively). (c) Truth table of NOT and YES gate. (d) Schematic presentation of these gates. (e) Analog circuit diagram.

6.4.2. Fuzzy Logic (FL). Lotfi Zadeh pioneered the FL concept based on classical set theory. FL has advantage over BL as it can address the innumerable intermediate states in-between the two extremes. FL is introduced in the present system to monitor the

influence of Fe^{2+} (input 1) and CN^- (input 2) on the emission spectral change of the receptor (Figure 6.22a). To investigate the impact of the inputs on the emission signal, a triangular membership functions (*trimf*) (low, medium, high) is taken into consideration (Figure 6.22b, c and d). It is evident that emission intensity (at 575 nm) decreases on addition of Fe^{2+}, while restoration of the initial state is made possible upon addition of CN^-. All probable combination of variables {Fe^{2+} (input 1) and CN^- (input 2)} generates 15 rules. A 3-D sketch of the emission response is also portrayed in Figure 6.22e.

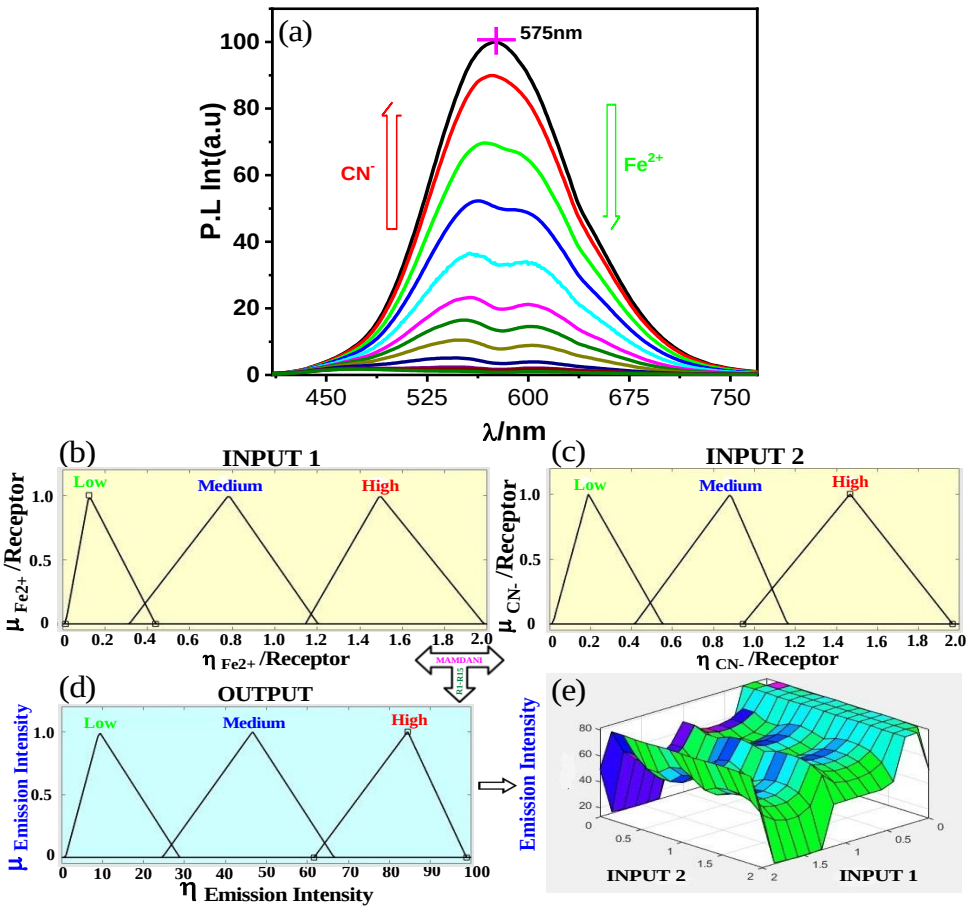

Figure 6.22. (a) Emission spectral response of the receptor upon the action of Fe^{2+} and CN^-. Graphic presentation of FL model as a function of Fe^{2+} and CN^-. (b) Fuzzy variables are divided in three *trimf* (b) Fe^{2+}: (1) low (trimf μ_{low},[0.01447 0.1255 0.438]); (2) medium (trimf μ_{medium}, [0.3148 0.7828 1.203]) (3) high (trimf μ_{high}, [0.9439 1.466 1.966]). (c) CN^-: (1) low (trimf μ_{low}, [0.01572 0.1893 0.5513]); (2) medium (trimf μ_{medium}, [0.416 0.882 1.161]); (3) high (trimf μ_{high}, [1.14 1.49 1.98]). (d) Emission intensity at 575 nm (Output): (1) low (trimf μ_{low}, [0.975 9.2 28.86]); (2) medium (trimf μ_{medium}, [24.6 46.62 66.5]); (3) high (trimf μ_{high}, [61.6 84.46 98.8]). (e) A 3-D sketch of the emission response.

6.4.3. Artificial Neural Network (ANN). The network execution details of ANN are narrated Chapter 4. The ANN-network is initiated with incorporation of a series of input data, while target data actually corresponds to the desired output. 40 different combination of inputs (input 1=Fe^{2+} and input 2=CN^-) and their respective outputs are taken. The best validation performance of the present network is 0.70444 at epoch 65 (Figure 6.23a).

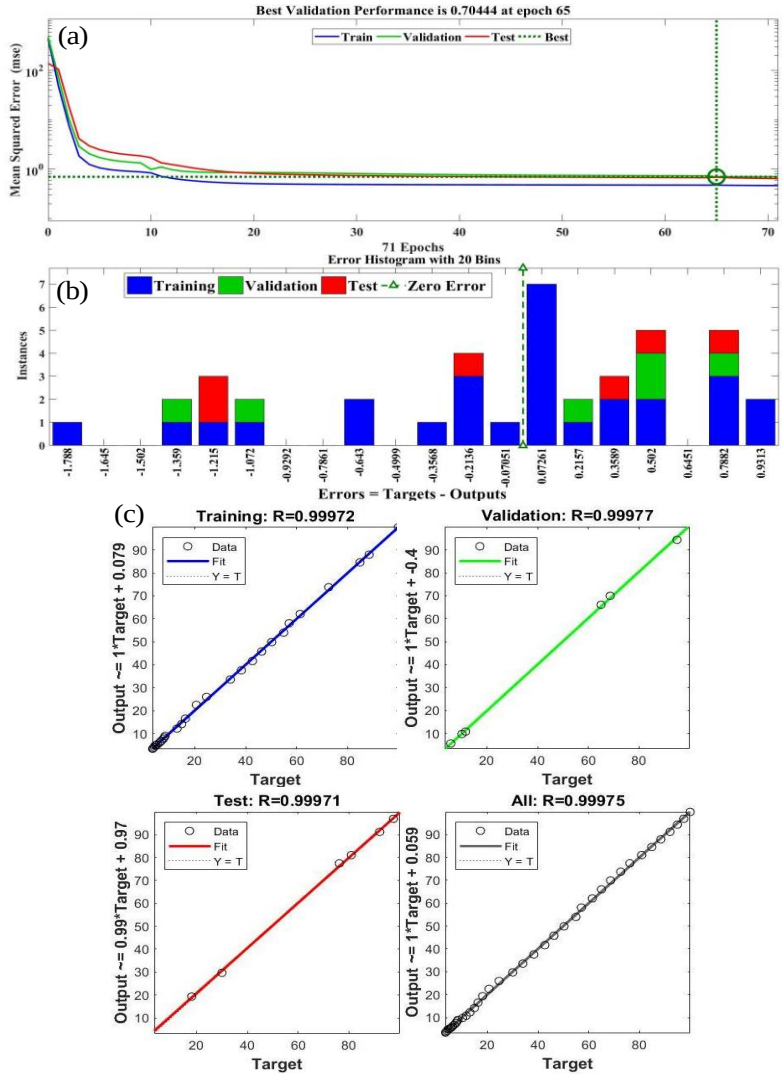

Figure 6.23. (a) Data validation and (b) error bar diagram. (c) Tallied data of ANN model with linear regression.

The bar-diagram in Figure 6.23b represents the deviation among the target and predicted values after training with a zero-error point located between the bin center 0.07051 and 0.07261. The value of regression analysis (R) close to unity implies good

correlation among the outputs and targets (Figure 6.23c). The training process of the system was done up to 71 epochs.

6.4.4. Adaptive Neuro-Fuzzy Inference System (ANFIS). ANFIS is a fusion of FL and ANN model which could overcome the disadvantage of each model and often yields excellent results. [54-59] We used the ANFIS model here to predict the alteration of emission signal upon variation of relative amounts of F^- and H^+ which involves fuzzification, knowledge base, ANN, and defuzzification layers. 70% of total data is used as training data set and the rest is employed for testing. Figure 6.24 shows that the learning process continues until it reaches 30 epochs together with reduction in the error. Because of 2 inputs and 3 membership functions each, the network will yield 3^2= 9 rules. The output emission response upon feasible consolidation of F^- and H^+ comprising of 9 rules on the basis of Sugeno's method is presented in Figure 6.25a. The emission output signal as a function Fe^{2+} and CN^- is also presented in a 3D plot (Figure 6.25c). Root means square error (RMSE) value of 0.5432 implies that the model is running precisely.

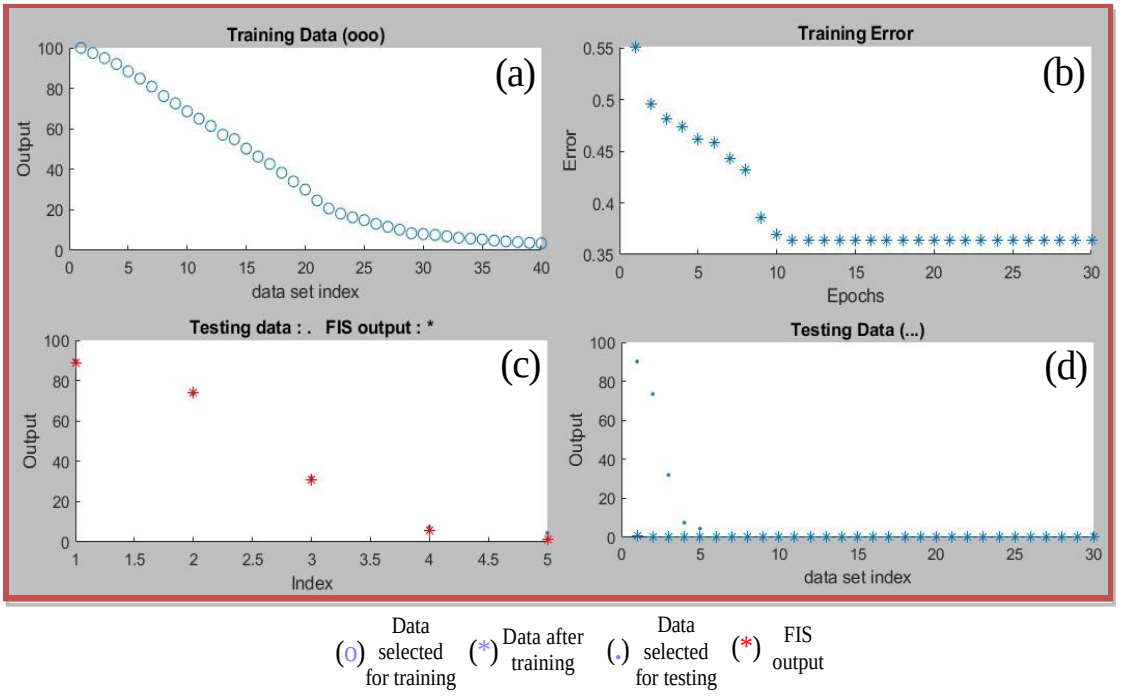

Figure 6.24. (a) Data set to train ANFIS network. (b) RMSE minimization up to 30 epochs. (c) Data for checking the accuracy of network output. (d) Grouping of testing data and FIS output.

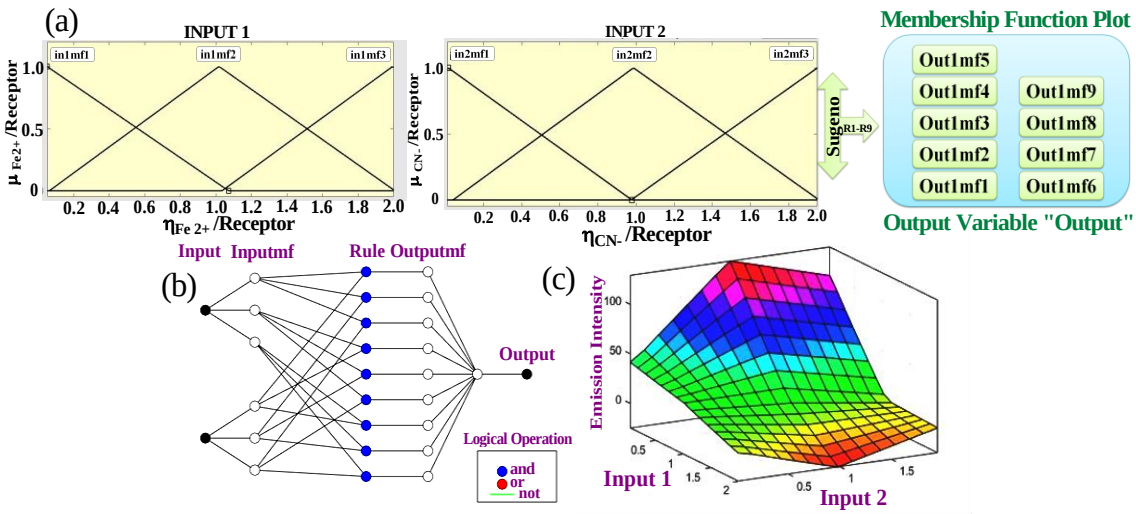

Figure 6.25. (a) ANFIS scheme based on Sugeno's method maintaining 9 rules. (b) Generated ANFIS structures for output. (c) 3D sketch of variation of emission response upon the cumulative influence of Fe^{2+} and CN.

6.4.5. Regression with Decision Tree (DTR). This is a sort of supervised ML technique that could be utilized to envisage a particular observation (dependent variables) relying on a specified attribute (independent variables) which supports the observation via "if-else" algorithm. A schematic display of a DT along with the depiction of each part is provided in Figure 6.26. Decision tree classifier (DTC) usually operates through

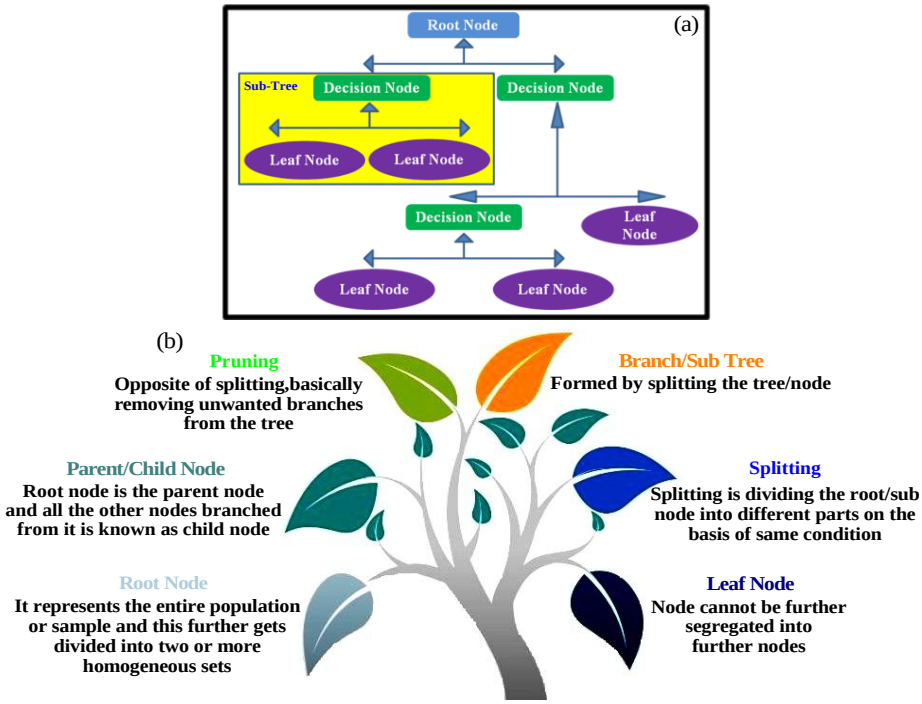

Figure 6.26. Schematic presentation of a decision tree (a) together with the description of each part (b).

quantifiable definite variables, viz. Yes (1) or No (0), while DTR functions through quantifiable continuous variables along with precision. In this case, we are paying attention to anticipate the emission intensities (dependent variables) as a function of varying concentration of both Fe^{2+} and CN^- (independent variable) (Figure 6.27). We implemented the DTR technique as we are interested to estimate the absolute

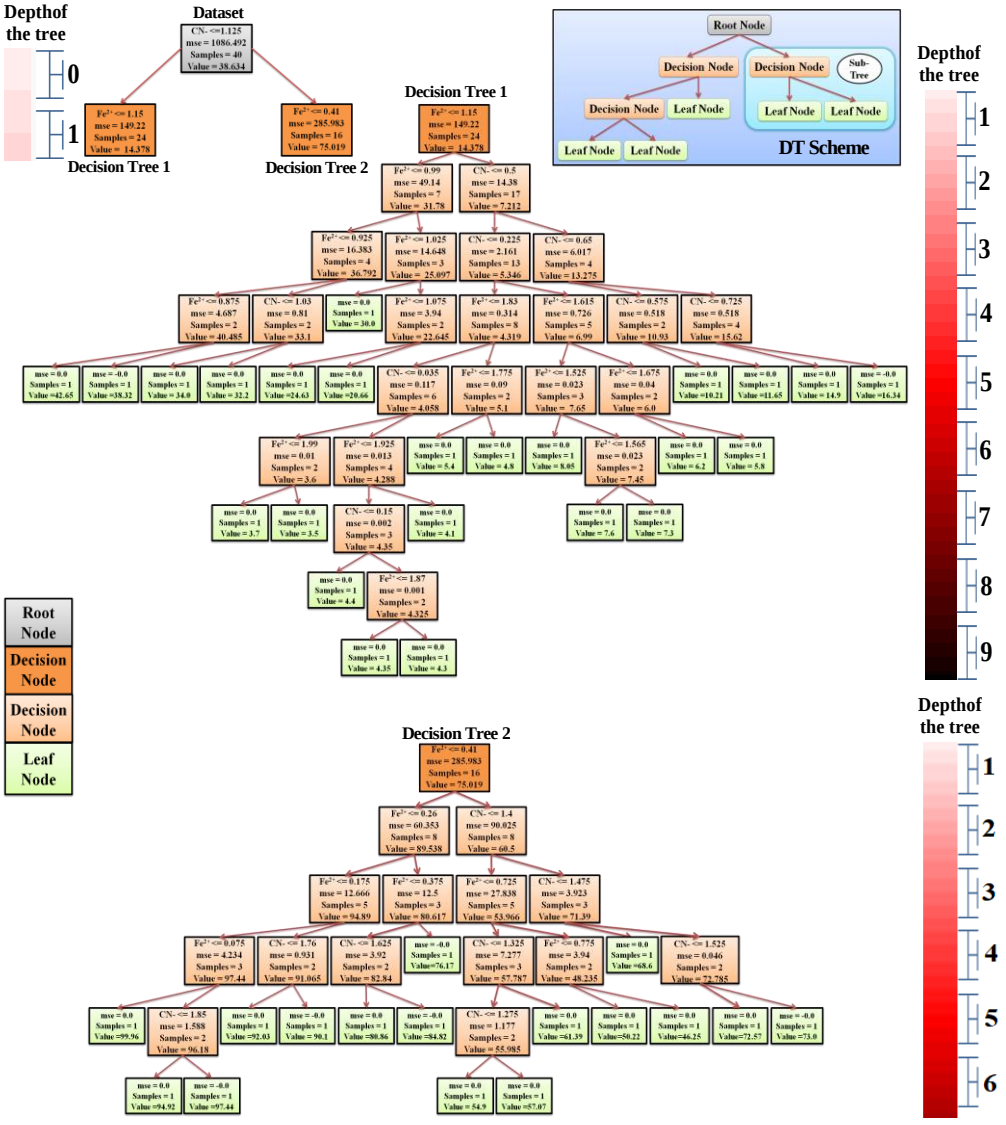

Figure 6.27. Schematic presentation of the decision tree.

emission intensities. We devised an in-house DTR programme through the use of Python language as it provides a broad choice of libraries and ML that might be used for processing of our data. Furthermore, the majority of the Python's popular libraries is easily available source and free of cost. The used libraries here are Pandas for treatment

and processing of the data set, Matplotlib for plotting and Scikit-Learn for computation. At the start, we employed a number of experimental data sets for training and testing. Subsequently, we fit the training data set in the DTR to devise a model that in turn could be used to forecast the observations by unknown features (testing data). Lastly, we will optimize the accuracy of the model relying on the R-square value or score. To get highest accuracy (without over fitting), we also fit our training data with the DTR model. The results of the DTR are then utilized to devise a DT (Figure 6.27). The achievement as well as statistical performance indicators of the model is presented in Figure 6.28 and Table 6.7, respectively. Comparison of experimental results with all the four model outputs is provided in Table 6.8 and Figure 6.29.

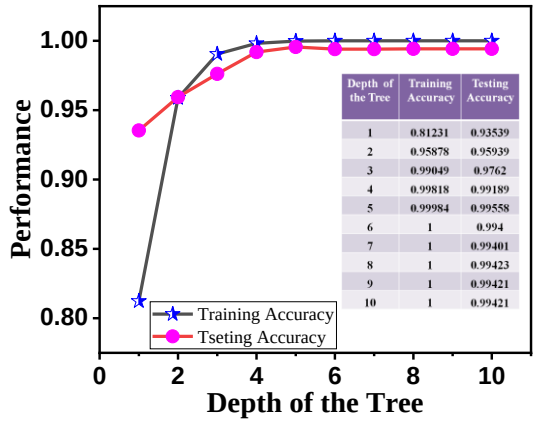

Figure 6.28. Performance of the decision tree up to depth 10.

Table 6.7. Statistical Performance Indicators of Supervised Learning Based Decision Tree Regression Model.

Decision Tree Regression	
R^2	0.9957
RMSE	0.9959
Training Accuracy (TrA)	1
Testing Accuracy (TeA)	0.9942
Error	TrA – TeA = 0.0058

Table 6.8. Comparison of Model Outputs and Experimental Data Derived from 5 Different Input Combinations.

Combinations of Inputs	Fe^{2+} (Equiv.)	CN^- (Equiv.)	Experimental Output	Fuzzy Assisted Output	ANN Assisted Output	ANFIS Assisted Output	DT Regression Assisted Output
1	0.22	1.78	90.2	70.1	85.4	90.0	90.1
2	0.42	1.58	73.2	50.3	78.1	73.2	73.0
3	0.98	1.02	32.0	25.2	28.2	31.3	34.0
4	1.58	0.42	7.5	10.8	8.2	7.2	7.3
5	1.88	0.22	4.5	2.0	3.5	4.3	4.3

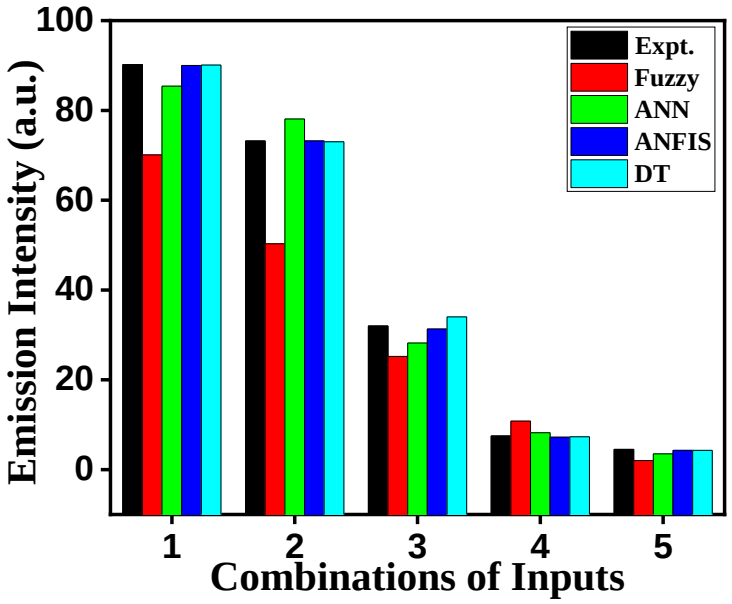

Figure 6.29. Histograms showing the comparison of the experimental outputs and the outcomes of ANN, ANFIS and DT models.

6.5. Conclusions

With respect to our continued curiosity for exploring the opportunity to mimic computational activity at the molecular level as well as to implement machine learning tools in chemical systems, we designed herein a terpyridyl-imidazole based receptor (tpy-$HImzPh_3NMe_2$) which on treatment with selective anions and cations promotes considerable alteration of its photophysical properties. The terpyridine moiety is used for

cation binding site, while the imidazole motif as the anion binding site. Covalent coupling of electron-donating dimethylamino groups in the phenyl-imidazole unit with terpyridyl electron acceptor unit yields ligand to ligand charge transfer (LLCT) probe whose optical spectral properties is very much responsive with selected anions, cations, acid as well as solvents of varying polarity. In reality, the receptor acts as multi-channel optical sensor for F^- and CN^- among the anions as well as for Fe^{2+} among the other bivalent 3d metals. Selectivity of the receptor towards anions dramatically improved on going from organic to predominantly aqueous media where the receptor acts as selective sensor for CN^-. In conjunction with experiment, DFT and TD-DFT calculations are also executed to acquire insight about the electronic structure of the probe as well as for appropriate assignment of the experimental spectral bands. The spectral outputs upon the action of the ionic inputs are used to demonstrate Boolean logic operations (Not Transfer and Transfer). In order to address the innumerable number of intermediate states among the two extremes, FL is also applied to establish an infinite-valued logic system by taking into account its emission spectral output upon the influence of ionic inputs. Execution of exhaustive ion-sensing behavior of the receptor within a wide range is very tedious, protracted as well as pricey. To overcome the difficulty, several ML and artificial intelligence (AI) tools such as ANNs, ANFIS and regression based Decision Tree have been applied to anticipate the complete ion-sensing conduct of the receptor. Comparison was also made among the models' outputs and the experimental values. The statistical performance indicators (such as MSE, RMSE, training and testing accuracy) strongly suggest that the forecasted values of the ion-sensing data by decision tree regression model are the best. Hence, the adopted ML based methodologies can act as authoritative tools for appropriate modeling for ion sensing behaviors of the present receptor.

6.6. References

1. Sessler, J. L.; Gale, P. A.; Cho, W. S. Anion Receptor Chemistry, Royal Society of Chemistry, Cambridge, U.K., **2006**.
2. Sessler, J. L.; Davis, J. M. Sapphyrins: Versatile Anion Binding Agents. *Acc. Chem. Res*., **2001**, *34*, 989-997.
3. Miyaji, H.; Sessler, J. L. Off-the-Shelf Colorimetric Anion Sensors. *Angew. Chem. Int. Ed.*, **2001**, *40*, 1.
4. Bhaumik, C.; Das, S.; Maity, D.; Baitalik, S. A Terpyridyl-Imidazole (tpy-HImzPh3) Based Bifunctional Receptor for Multichannel Detection of Fe^{2+} and F^- Ions. *Dalton Trans*., **2011**, *40*, 11795-11808.
5. Beer, P. D. Electrochemical and Optical Sensing of Anions by Transition Metal Based Receptors. *Coord. Chem. Rev*., **2000**, *205*, 131-155.
6. Beer, P. D.; Gale, P. A. Anion Recognition and Sensing: The State of the Art and Future Perspectives. *Angew. Chem. Int. Ed*., **2001**,*40*, 486-516.
7. Kuhn, H.; Docker, A.; Beer, P. D. Anion Recognition with Sb (III) and Bi (III) Triaryl-Based Pnictogen Bonding Receptors. *Chem. Eur. J.*, **2022**, *28***,** e202201838.
8. Docker, A.; Shang, X. D.; Yuan, Kuhn, H. Z. Zhang, J.J. Davis, P.D. Beer, M.J. Langton, Halogen Bonding Tetraphenylethene Anion Receptors: Anion Induced Emissive Aggregates and Photoswitchable Recognition. *Angew. Chem., Int. Ed. Engl.*, 2021, *60* , 19442-19450.
9. Sun, S.-S.; Lees, A. J. Transition Metal Based Supramolecular Systems: Synthesis, Photophysics, Photochemistry and Their Potential Applications as Luminescent Anion Chemosensors. *Coord. Chem. Rev*., **2002**, *230* , 171-192.
10. Suksai, C.; Tuntulani, T. Chromogenic Anion Sensors. *Chem. Soc. Rev*., **2003**, *32*, 192-201.
11. Amendola, V.; Gomez, E. D.; Fabbrizzi, L.; Licchelli, M. What Anions Do to N−H-Containing Receptors. *Acc. Chem. Res*., **2006**, *39*, 343-353.

12. Pe´rez, J.; Riera, L. Stable Metal-Organic Complexes As Anion Hosts. *Chem. Soc. Rev*., **2008**, *37*, 2658-2667.

13. Caltagirone, C.; Gale, P. A. Anion Receptor Chemistry: Highlights from 2007. *Chem. Soc. Rev*., **2009**, *38*, 520-563.

14. Gale, P. A.; Garcia-Garrido, S. E.; Garric, J. Anion Receptors Based on Organic Frameworks: Highlights from 2005 and 2006. *Chem. Soc. Rev*., **2008**, *37*, 151-190.

15. de silva, A. P.; Gunaratne, H. Q. N.; McCoy, C. P. A Molecular Photoionic AND Gate Based on Fluorescent Signaling. *Nature*., **1993**, *364*, 42−44.

16. de Silva, A. P.; McClenaghan, N. D. Molecular-Scale Logic Gates. *Chem.-Eur. J*., **2004**, *10*, 574−586.

17. de Silva, A. P. Molecular Logic Gate Arrays. *Chem.-Asian J*., **2011**, *6*, 750−766.

18. Conrad, M. Molecular Computin. *Adv. Comput*., **1990**, *31*, 235–324.

19. Szaciłowski, K. Molecular Logic Gates Based on Pentacyanofer Rate Complexes: from Simple Gates to Three-Dimensional Logic Systems. *Chem.-Eur. J*., **2004**, *10*, 2520−2528.

20. Adamatzky, A.; Costello, B. D. L. Experimental Logical Gates in a Reaction-Diffusion Medium: the XOR Gate and Beyond. *Phys. Rev. E: Stat., Nonlinear, Soft Matter Phys*., **2002**, *66*, 046112.

21. Adamatzky, A.; Jones, J.; Mayne, R.; Tsuda, S.; Whiting, J.; Logical Gates and Circuits Implemented in Slime Mould. *Advances in Physarum Machines, Springer*., **2016**, 37−74.

22. Mondal, D.; Bar, M.; Maity, D.; Baitalik, S. Anthraimidazoledione-Terpyridine-Based Optical Chemosensor for Anions and Cations That Works as Molecular Half-Subtractor, Key-pad Lock, and Memory Device. *J. Phys. Chem.*, C **2015**, *119*, 25429–25441.

23. Mardanya, S.; Mondal, D.; Karmakar, S.; Baitalik, S. Smart Ruthenium and Osmium Complexes Mimic the Complicated Functions of Traffic Signal and Memory Device. *Sens. Actuators*., B **2017**, *239*, 635–641.

24. Deb, S.; Sahoo, A.; Ahmed, T.; Baitalik, S. Stimuli-Responsive Molecular Switches and Logic Devices Based on Ru(II)−Terpyridyl−Imidazole Coordination Motif. *J. Phys. Chem*., B **2021**, *125*, 8919−8931.

25. Goldsworthy, V.; LaForce, G.; Abels, S.; Khisamutdinov, E. F. Fluorogenic RNA Aptamers: A Nano-platform for Fabrication of Simple and Combinatorial Logic Gates. *Nanomaterials*., **2018**, *8*, 984.

26. Szaciłowski, K.; Wojciech, M.; Grażyna, S. Light-driven OR and XOR Programmable Chemical Logic Gates. *J. Am. Chem. Soc*., **2006**, *128*, 4550–4551.

27. Ling, J.; Daly, B.; V. Silverson, A. D.; de Silva, A. P. Taking Baby Steps in Molecular Logic-based Computation. *Chem. Commun*., **2015**, *51*, 8403−8409.

28. Schmittel, M.; Mal, P.; de los Rios, A. Multiport Logic Operations Triggered by Protonation-a Trisphenanthroline as a 3-input AND-NOR-OR Circuit. *Chem. Commun*., **2010**, *46*, 2031−2033.

29. Adamatzky, Tegelaar, A.; M.; H. Wosten, A. B.; Powell, A. L.; Beasley, A. E.; Mayne, R. On Boolean Gates in Fungal Colony. *Biosystems*., **2020**, *193−194*, 104138.

30. Gale, E.; de Lacy Costello, B.; Adamatzky, A. Boolean Logic Gates from a Single Memristor via Low-level Sequential Logic. *Int. Conf. Unconventional Comput. Nat. Comput*., **2013**, 79–89.

31. Liu, J.; He, X.; Zhang, J.; He, T.; Huang, L.; Shen, J.; Li, D.; Qiu, H.; Yin, S. A BODIPY Derivative for Colorimetric and Fluorometric Sensing of Fluoride Ion and its Logic Gates Behavior. *Sens. Actuators B Chem*., **2015**, *208*, 538-545.

32. He, T.; Tang, D.; Lin, C.; Shen, X.; Lu, C.; Xu, L.; Gu, Z.; Xu, Z.; Qiu, H.; Zhang, Q.; Yin, S. Conjugated Polymers Containing BODIPY and Fluorene Units for Sensitive Detection of CN^- Ions: Site-selective Synthesis, Photo-Physical and Electrochemical Properties. *Polymers*., **2017**, *9*, 512.

33. Manna, U.; Das, G.; Hossain, M. A. Insights Into the Binding Aspects of Fluoride with Neutral Synthetic Receptors. *Coord. Chem*., Rev. **2022**, *455*, 214357.

34. Zhou, Y.; Zhang, J. F.; Yoon, J. Fluorescence and Colorimetric Chemosensors for Fluoride-ion Detection. *Chem. Rev*., **2014**, *114*, 5511-5571.

35. Zhou, X.; Kim, J.; Liu, Z.; Jo, S.; Pak, Y. L.; Swamy, K. M. K.; Yoon, J. Selective Fluorescent and Colorimetric Recognition of Cyanide via Altering Hydrogen Bonding Interaction in Aqueous Solution and Its Application in Bioimaging. *Dyes Pigm*., **2016**, *128*, 256-262.

36. Zhang, Y.; Gong, S.; Song, J.; Li, M.; Qin, A.; Gao, Y.; Wang, Z.; Wang, S. A Robust Camphor-based Colorimetric and Fluormetric Dual-modal Probe with a Large Stokes Shift for Real-time Monitoring of Endogenous Labile $Fe2^{+}$ In vivo and In vitro. *Dyes Pigm*., **2021**, *194*, 109590.

37. Gentili, P. L. Boolean and Fuzzy Logic Gates Based on the Interaction of Flindersine with Bovine Serum Albumin and Tryptophan. *J. Phys. Chem*., A **2008**, *112*, 11992−11997.

38. Gentili, P. L. The Fundamental Fuzzy Logic Operators and Some Complex Boolean Logic Circuits Implemented by the Chromogenism of a Spirooxazine. *Phys. Chem. Chem. Phys*., **2011**, *13*, 20335−20344.

39. Gentili, P. L. Boolean and Fuzzy Logic Implemented at the Molecular Level. *Chem. Phys*., **2007**, *336*, 64–73.

40. Gentili, P. L.; Giubila, M. S.; Germani, R.; Romani, A.; Nicoziani, A.; Spalletti, A.; Heron, B. M. Optical Communication Among Oscillatory Reactions and Photo-excitable Systems: UV and Visible Radiation Can Synchronize Artificial Neuron Models. *Angew. Chem. Int. Ed*., **2017**, *56*, 7535–7540.

41. Gentili, P. L.; Giubila, M. S.; Heron, B. M. Processing Binary and Fuzzy Logic by Chaotic Time Series Generated by a Hydrodynamic Photochemical Oscillator. *ChemPhysChem*., **2017**, *18*, 1831−1841.

42. Mamdani, E. H. Application of Fuzzy Logic to Approximate Reasoning Using Linguistic Synthesis. *IEEE Trans. Comput*., **1977**, *26*, 1182–1191.

43. Zadeh, L. A. Fuzzy Sets, Fuzzy Logic, and Fuzzy Systems: Selected Papers, World Scientific 1996, 394−432.

44. Karmakar, S.; Nandi, M.; Mukherjee, S.; Baitalik, S. Polypyridyl-imidazole Based Smart Ru(II) Complex Mimicking Advanced Boolean and Fuzzy Logic Functions. *Inorg. Chim. Acta*., **2017**, *454*, 76−88.

45. Mukherjee, S.; Sahoo, A.; Deb, S.; Baitalik, S. Light and Cation Driven Optical Switch Based on a Stilbene-Appended Terpyridine System for the Design of Molecular-Scale Logic Devices. *J. Phys. Chem. A*., **2021**, *125*, 8261−8273.

46. Paul, A.; Sahoo, A.; Bhattacharya, S.; Baitalik, S. Anion and Temperature Responsive Molecular Switches Based on Trimetallic Complexes of Ru(II) and Os(II) that Demonstrate Advanced Boolean and Fuzzy Logic Functions. *Inorg. Chem*., **2022**, *61*, 3186-3201.

47. Pal, P.; Sahoo, A.; Paul, A.; Baitalik, S. Anion and Light Responsive Molecular Switches Based on Stilbene-Appended Ru(II) Terpyridyl-Imidazole Complexes that Mimic Sdvanced Boolean and Fuzzy Logic Operations. *Eur. J. Inorg. Chem*., **2022**, e202200219, 1-10.

48. Mills, K.; Ryczko, K.; Luchak, I.; Domurad, A.; Beeler, C.; Tamblyn, I. Extensive Deep Neural Networks for Transferring Small Scale Learning to Large Scale Systems. *Chem. Sci*., **2019**, *10*, 4129–4140.

49. Curtis, C.; McKenna, M.; Pontes, H.; Toghani, D.; Choe, A.; Nance, E. Predicting *in situ* Nanoparticle Behavior Using Multiple Particle Tracking and Artificial Neural Networks. *Nanoscale*., **2019**, *11*, 22515–22530.

50. Giri Nandagopal, M. S.; Selvaraju, N. Prediction of Liquid-Liquid Flow Patterns in a Y-Junction Circular Microchannel Using Advanced Neural Network Techniques. *Ind. Eng. Chem. Res*., **2016**, *55*, 11346−11362.

51. Sahoo, A.; Ahmed, T.; Deb, S.; Baitalik, S. Neuro-Fuzzification Architecture for Modeling of Electrochemical Ion-Sensing Data of Imidazole-Dicarboxylate-Based Ru (II)–Bipyridine Complex. *Inorg. Chem*., **2022**, *61*, 10242–10254.

52. Sahoo, A.; Baitalik, S. Fuzzy Logic, Artificial Neural Network, and Adaptive Neuro-Fuzzy Inference Methodology for Soft Computation and Modeling of Ion Sensing Data of a Terpyridyl-Imidazole Based Bifunctional Receptor. *Front. Chem*., **2022**, *10*, 864363.

53. Ghorai, A.; Sahoo, A.; Baitalik, S.; Banerjee, S. Multifunctional Sulfonated Polytriazoles: Proton-Exchange Membrane Properties, Molecular Logic Gates, and Modeling of Stimuli-Responsive Behaviors. *ACS Appl. Polym. Mater*., **2022**, *4*, 5583−5595.

54. Mensah, R. A., Xiao, J.; Das, O.; Jiang, L.; Xu, Q.; Alhassan, M. O. Application of Adaptive Neuro-Fuzzy Inference System in Flammability Parameter Prediction. *Polymer*., **2020**, *12*, 122.

55. Lv, H.; Chen, X. Intelligent Control of Nanoparticle Synthesis Through Machine Learning. *Nanoscale*., **2022**, *14*, 6688–6708.

56. Huang, M.; Ma, Y.; Wan, J.; Zhang, H.; Wang, Y. Modeling a Paper-Making Wastewater Treatment Process by Means of an Adaptive Network-Based Fuzzy Inference System and Principal Component Analysis. *Ind. Eng. Chem. Res*., **2012**, *51*, 6166–6174.

57. Babanezhad, M.; Behroyan, I.; Nakhjiri, A. T.; Marjani, A.; Shirazian, S. Computational Modeling of Transport in Porous Media Using an Adaptive Network-Based Fuzzy Inference System. *ACS Omega*., **2020**, *5*, 30826–30835.

58. Razzak, S. A.; Rahman, S. M.; Hossain, M. M.; Zhu, J. Artificial Neural Network and Neuro-Fuzzy Methodology for Phase Distribution Modeling of a Liquid-Solid Circulating Fluidized Bed Riser. *Ind. Eng. Chem. Res*., **2012**, *51*, 12497-12508.

59. Bingöl, D.; Inal, M.; Çetintaş, S. Evaluation of Copper Biosorption Onto Date Palm (Phoenix Dactylifera L.) Seeds with MLR and ANFIS Models. *Ind. Eng. Chem. Res*., **2013**, *52*, 4429–4435.

60. Goswami, S.; Pramanick, R.; Patra, A.; Rath, S. P.; Foltin, M.; Ariando, A.; Thompson, D.; Venkatesan, T.; Goswami, S.; Williams, R. S. Decision Trees Within a Molecular Memristor. *Nature*., **2021**, *597*, 51–56.

61. Shiratori, K.; Bishop, L. D.; Ostovar, B.; Baiyasi, R.; Cai, Y. Y.; Rossky, P. J.; Landes, C.; Link, F. S. Machine-Learned Decision Trees for Predicting Gold Nanorod Sizes from Spectra. *J. Phys. Chem. C*. **2021**, *125*, 19353–19361.

62. LeCun, Y.; Bengio, Y.; Hinton, G. Deep Learning. *Nature*. **2015**, *521*, 436– 444.

63. Pedretti, G.; Graves, C. E.; Serebryakov, S.; Mao, R.; Sheng, X.; Foltin, M.; Li, C.; Strachan, J. P. Tree-Based Machine Learning Performed In-Memory with Memristive Analog CAM. *Nat. Commun*. **2021**, *12*, 1–10.

64. Geurts, P.; Irrthum, A.; Wehenkel, L. Supervised Learning with Decision Tree-Based Methods in Computational and Systems Biology. *Mol. BioSyst*. **2009**, *5*, 1593–1605.

65. Swaney, D. L.; McAlister, G. C.; Coon, J. J. Decision Tree-Driven Tandem Mass Spectrometry for Shotgun Proteomics. *Nat. Methods*. **2008**, *5*, 959–964.

66. Loh, W. Y. Classification and Regression Trees. *Wiley Interdiscip. Rev. Data Min. Knowl. Discov*. **2011**, *1*, 14–23.

67. Altman, N.; Krzywinski, M. Ensemble Methods: Bagging and Random Forests. *Nat. Methods*. **2017**, *14*, 933–934.

68. Choi, M. Y.; Ma, C. Making a Big Impact with Small Datasets using Machine-Learning Approaches. *Lancet Rheumatol*. **2020**, *2*, e451–e452.

69. Pott, K. T.; Usifer, D. A.; Abruna, H. D. 4-Vinyl-, 6-Vinyl-, and 4'-Vinyl-2,2':6',2''- Terpyridinyl Ligands: Their Synthesis and the Electrochemistry of their Transition-Metal Coordination Complexes . *J. Am. Chem. Soc*. **1987**, *109*, 3961-3967.

70. SAINT (version 6.02), SADABS (version 2.03); Bruker AXS Inc.: Madison, WI, **2002**.

71. Sheldrick, G. M. ***SHELXT*** - Integrated Space-Group and Crystal-Structure Determination. *Acta Cryst. A*. **2015**, *71*, 3-8.

72. Dolomanov, O. V.; Bourhis, L. J.; Gildea, R. J.; Howard, J. A. K.; Puschmann, H. J. A Complete Structure Solution, Refinement and Analysis Program. *Appl. Crystallogr*. **2009**, *42*, 339-341.

73. Spek, A. L. Single-Crystal Structure Validation with the Program PLATON. *J. Appl. Cryst*. **2003**, *36*, 7-13.

74. Bradenburg, K. Diamond, version 3.1 e, Crystal Impact GbR: Bonn, Germany, **2005**.

75. Frisch, M. J.; Trucks, G. W.; Schlegel, H. B.; Scuseria, G. E.; Robb, M. A.; Cheeseman, J. R.; Scalmani, G.; Barone, V.; Mennucci, B.; Petersson, G. A. et al. Gaussian 09, revision A.02; Gaussian Inc.: Wallingford, CT, **2009**.

76. Becke, A. D. Density Functional Thermochemistry. III. The Role of Exact Exchange. *J. Chem. Phys*. **1993**, *98*, 5648-5652.

77. Lee, C. T.; Yang, W. T.; Parr, R. G. Development of the Colle-Salvetti Correlation-Energy Formula into a Functional of the Electron Density. *Phys. Rev. B*. **1988**, *37*, 785-789.

78. Casida, M. E.; Jamorski, C.; Casida, K. C.; Salahub, D. R. Molecular Excitation Energy to High-Lying Bound State from Time-Dependent Density Functional Response Theory: Charecterization and Correction of the Time Dependent Local Density Approximation Ionization Threshold. *J. Chem. Phys*. **1998**, *108*, 4439-4449.

79. Stratmann, R. E.; Scuseria, G. E.; Frisch, M. J. An Efficient Implementation of Time-Dependent Density-Functional Theory for the Calculation of Excitation Energies of Large Molecules. *J. Chem. Phys*. **1998**, *109*, 8218-8224.

80. Caricato, M.; Mennucci, B.; Tomasi, J.; Ingrosso, F.; Cammi, R.; Corni, S.; Scalmani, G. Formation and Relaxation of Excited States in Solution: A New Time Dependent Polarizable Continuum Model Based on Time Dependent Density Functional Theory. *J. Chem. Phys*. **2006**, *124*, 124520-124530.

81. Mennucci, B.; Cappelli, C.; Guido, C. A.; Cammi, R.; Tomasi, J. Structures and Properties of Electronically Excited Chromophores in Solution from the Polarizable Continuum Model Coupled to the Time-Dependent Density Functional Theory. *J. Phys. Chem. A*. **2009**, *113*, 3009.

82. Dennington, R. II.; Keith, T.; Millam, J. Gauss View 3; Semichem, Inc.: Shawnee Mission, KS, **2007**.

83. O Boyle, N. M.; Tenderholt, A. L.; Langner, K. M. cclib: A Library for Package Independent Computational Chemistry Algorithms. *J. Comput. Chem*. **2008**, *29*, 839.

84. Marcus, Y. J. Thermodynamics of Solvation of Ions. *J. Chem. Soc. Faraday Trans*. **1991**, *87*, 2995-2999.

****

7.1. Introduction

The usage of machine learning (ML) and diverse artificial intelligence (AI) tools[1-8] have been growing enormously in chemistry, biology and materials sciences. Contemporary research interest is focused mainly on the design of smart materials together with the analysis of their physicochemical data (such as sensing, bio-sensing and imaging) for the diagnostic purposes. Little progress has been made in other sub areas of AI, e.g. fuzzy[9-19], ANNs, ANFIS, robotics, evolutionary computation and natural language processing and planning.[20-27] Creation of dependable and exhaustive database can extend the ML to a wider domain of application. Lot of efforts is now been given to prosper the AI with vague and imprecise inputs. The function in Boolean logic (BL)[28-39] relies on stretching of the output signal in-between the two extreme "0" or "1". But majority of the real systems composed of many intermediate states. The fuzzy logic (FL) is believed to be a probable alternative of BL in identifying the intermediate states. The motivation in choosing FLS relies on the motivation that thought and decision making process in human is extremely complicated to be precisely defined and believed to function as an automatic fine-controlling administer for innumerable number of intervening steps with varied degree of truths. FLS consists of non-linear scaling of the input vectors to the scalar outputs. The number of molecular systems implementing the FLS is relatively sparse in the literature.

In this work, we have utilized our previously reported terpyridyl-imidazole system (tpy-HImzPh$_3$)[40] wherein a terpyridine moiety capable of coordinating with a number of bivalent 3d metals is covalently coupled with a triphenyl-imidazole motif capable of interacting with selected anions (Chart 7.1).[41-44] By using its absorption and emission spectral responses as a function of specific set of cations and anions, multiple Boolean logic (BL) functions such as combinatorial logic of AND, OR and NOT gates[45-48] as well as molecular level keypad lock are demonstrated.[45-59] Herein, we also executed fuzzy logic for creating an infinite-valued logic scheme by using the emission spectral output upon the action of specific cations (H^+ and/or Fe^{2+}) and anion (F^-).

ANNs are biologically motivated systems comprising of extensively connected processing elements arranged in layers and bind together with weighted interrelations. Usually, the ANN is framed by numerical learning algorithm and could be “trained” to approximate effectively any nonlinear function to a required degree of accuracy. To this

end, the ANN is believed to be as a class of universal approximator. We have designed two ANN models based on reversible deprotonation-protonation induced by anions and acid as well as recomplexation-decomplexation behavior of the receptor in presence of M^{2+} and F^- ions. Due to lack in learning capability of fuzzy model and paucity of transparency of ANN model, we also implemented the neuro-fuzzy system which represents a type of hybrid intelligent system amalgamating the principle features of ANN and fuzzy logic. The objective is to get rid of the difficulty associated with implementing fuzzy logic through numerical knowledge or contrarily in implementing ANN via linguistic information. Importantly, we also compared the outcomes of Fuzzy, ANN and ANFIS methods with the experimental outputs for better modeling of the deprotonation-protonation and as well as complexation-decomplexation behavior of the receptor.

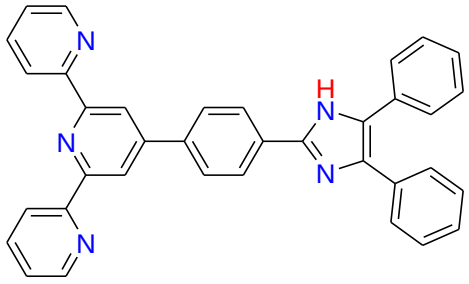

Tpy-HImzPh3

Chart 7.1. Chemical structure of the terpyridyl-imidazole based receptor.

7.2. Experimental Section

7.2.1. Materials. Reagent grade chemicals obtained from commercial sources were used as received. Solvents were purified and dried according to standard methods.[60] Benzil and tetrabutylammonium (TBA) salt of the anions were purchased from Sigma–Aldrich. 4'- (p–methylphenyl)-2,2':6',2"-terpyridine (**tpy**–**PhCH$_3$**), 4'–(*p*–dibromomethylphenyl)–2,2':6',2"–terpyridine(**tpy**–**PhCHBr$_2$**), 4'–formyl–2,2':6',2"–terpyridine (**tpy**–**PhCHO**), were synthesized according to the literature procedures.[61-65]

7.2.2. Preparation of the ligand. 4′-[4-(4,5-Diphenyl-1H-imidazol-2-yl)-phenyl]-[2,2′:6′,2″] terpyridine (tpy-HImzPh$_3$). The synthesis of the compound was undertaken by following a method previously described.[66] A mixture of 4′-(*p*-formylphenyl)-2,2':6',2"-terpyridine (tpy-PhCHO) (1.00 g, 2.97 mmol), benzil (630 mg,

3.00 mmol), and ammonium acetate (2.3 g, 30 mmol) in acetic acid (30 mL) was heated at reflux for 2h. The resulting orange-red solution was cooled to room temperature and poured into crushed ice (250 mL) with vigorous stirring. A grey colored precipitate thus obtained was filtered off. It was then slurried with water (*ca.* 200 mL) and slowly treated with 25% aqueous ammonia to pH ≈ 8 when the color changed to light pink. The solid was collected by filtration and washed several times with water. The residue was purified by silica gel column chromatography in chloroform and recrystallized from chloroform-methanol (1:1) to give the desired compound as light green crystalline solid (1.41 g, 2.68 mmol, yield 87%). ^{1}H NMR (DMSO, 300 MHz): δ = 12.90 (s, 1H, NH(imidazole)), 8.78 (m, 4H (2H3′+2H6)), 8.68 (d, 2H, *J* = 7.9 Hz, H3), 8.30 (d, 2H, *J* = 8.0 Hz, H8), 8.09-8.00 (m, 4H (2H4+2H7)), 7.58-7.20 (m, 12H (10H (phenyl) + 2H5)). ESI-MS: *m*/*z* 527.63 ($[L+H]^+$). Anal. Calcd for $C_{36}H_{25}N_5$: C, 81.95; H, 4.78; N, 13.27. Found: C, 81.87; H, 4.81; N, 13.25.

7.2.3. Synthesis of $[Fe(tpy\text{-}HImzPh_3)_2](ClO_4)_2$. To a stirred chloroform-methanol (1:1) solution (30 mL) of the ligand (0.11 g, 0.21 mmol) was added solid $Fe(ClO_4)_2\cdot 6H_2O$ (0.36 g, 0.1 mmol). The colorless solution changed immediately to violet, and during stirring at room temperature for ~1h microcrystalline compound deposited. The compound was filtered, washed with water, and dried in a vacuum. On recrystallization from acetonitrile-methanol (1:1) violet crystalline compound were obtained: yield 0.10 g (76%). ^{1}H NMR (DMSO, 300 MHz): δ = 13.02 (s, 2H, NH(imidazole)), 9.73 (s, 4H, H3′), 9.08 (d, 4H, *J* = 8.0 Hz, H3), 8.70 (d, 4H, *J* = 8.4 Hz, H8), 8.50 (d, 4H, *J* = 8.3 Hz, H7), 8.04 (t, 4H, *J* = 7.6 Hz, H4), 7.63-7.29 (m, 24H (20 phenyl-H + 4H6)), 7.20 (t, 4H, *J* = 6.4 Hz, H5). Anal. Calcd for $C_{72}H_{50}N_{10}Cl_2O_8Fe$: C, 66.00; H, 3.84; N, 10.69. Found: C, 65.95; H, 3.81; N, 10.71. ESI-MS (positive, CH_3CN) *m/Z* = 554.75 (100%) $[Fe(tpy\text{-}HImzPh_3)_2]^{2+}$; 1209.12 (5%) $[Fe(tpy\text{-}HImzPh_3)_2(ClO_4)]^+$.

Caution! Perchlorate salts of different metal and of the Fe(II) complex used in this study are potentially explosive and therefore should be handled in small quantities with care.

7.2.4. Physical Measurements. The details of different equipments used and experimental process to measure absorption and luminescence spectral behaviors have already been discussed in chapter 2.

7.3. Results and Discussion

7.3.1. Synthesis and Characterization. A mixture of benzil and 4′-(*p*-formylphenyl)-2,2':6',2"-terpyridine (tpy-PhCHO) in 1:1 molar ratio was subjected to undergo condensation in acetic acid in presence of excess of ammonium acetate for the synthesis of the ligand, tpy-HImzPh$_3$. When a methanol-chloroform solution of the ligand (2 equivalent) was treated with Fe(ClO$_4$)$_2$ (1 equivalent) the solution became intensely violet and the complex was isolated from the solution as dark violet crystalline solid. Both the ligand and its Fe(II) complex have been characterized by their elemental (C, H and N) analyses, ESI-MS, UV-Vis, ^{1}H NMR spectroscopic measurements and the results are given in the Experimental Section. The ESI-MS of Fe(II) complex in CH$_3$CN shows (Figure 7.1) two abundant peaks at *m*/*z* 554.75 and 1209.12, respectively. The isotopic patterns of the original peak at *m*/*z* 554.75 separated by 0.5 Da fit very well to the isotope distribution pattern calculated for [Fe(tpy-HImzPh$_3$)$_2$]$^{2+}$ (100 %). The peak at *m*/*z* 1209.12 is assigned to [Fe(tpy-HImzPh$_3$)$_2$(ClO$_4$)]$^+$ (5 %).

7.3.2. ^{1}H NMR spectra. The ^{1}H NMR spectra of both the receptor and [Fe(tpy-HImzPh$_3$)$_2$](ClO$_4$)$_2$ complex recorded in DMSO−d_6 (Figure 7.2) show the occurrence of a number of resonances in the aromatic region. The COSY spectra have been particularly useful to locate spin couplings of these protons. The numbering scheme used to assign the observed resonances is given in Figure 7.2. The distinct signal, which is most

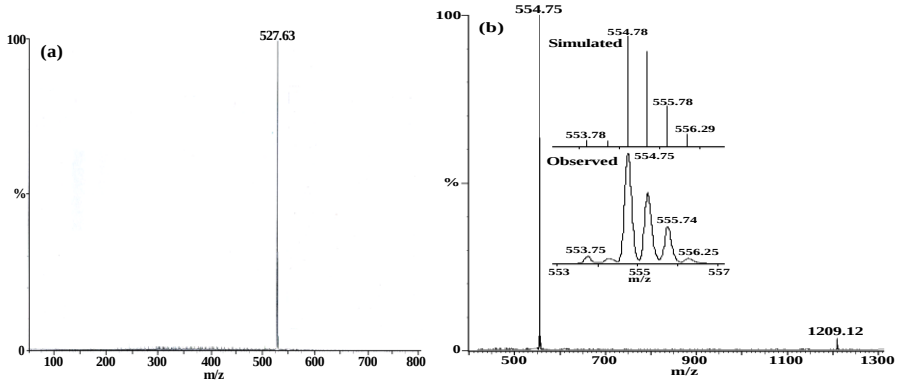

Figure 7.1. ESI–MS for (a) tpy-HImzPh$_3$ (*m*/*z* = 527.63) in dimethylformamide and (b) complex cation [Fe(tpy-HImzPh$_3$)$_2$]$^{2+}$ (*m*/*z* = 554.75) and [Fe(tpy-HImzPh$_3$)$_2$(ClO$_4$)]$^+$ (*m*/*z* = 1209.12) in acetonitrile showing the observed and simulated isotopic distribution patterns.

downfield-shifted, is observed as a singlet at 12.90 ppm for the ligand and 13.02 ppm for its Fe(II) complex are due to the imidazole NH proton. The protons of two phenyl rings attached to the imidazole moiety are characterized by a bunch of signals in the region 7.20-7.58 ppm, assigned on the basis of coupling constants and chemical shifts. The terpyridine protons H3-H6, on the other hand, lie in the range of 7.20-8.78 ppm. Figure 7.2(a) shows that addition of F^- leads to complete removal of the N–H signal and small up-field shifts of H8 and phenyl ring protons, although the chemical shifts for the tpy protons are far less affected. Clearly, F^- ion acts as the proton abstractor. The up-field shift of C–H8 and protons of two phenyl ring in the ligand is due to augmentation of electron density at these sites due to delocalization of the negative charge of the imidazole ring brought about by N–H deprotonation.

The ^{1}H NMR spectrum of $[Fe(tpy\text{-}HImzPh_3)_2]^{2+}$ is consistent with a symmetrical complex as shown by X-ray crystal structure in the solid state. Figure 7.2(b) illustrates the effect of coordination of Fe^{2+} center to the ligand on the chemical shifts values of its different protons. As can be seen that the chemical shifts of H3, H7 and H8 protons shifted to down-field region while the phenyl protons and H4 of terpyridine moiety are almost unaffected by coordination. Proton H6 of tpy moiety is affected the most and shifts to significantly up-field region because this proton lying above the shielding region of a pyridine ring of other tpy ligand.

7.3.3. Overview of the Anion and Cation Sensing Behavior of the Receptor. The method of synthesis, thorough characterization, and anion- as well as cation sensing properties of $tpy\text{-}HImzPh_3$ was previously reported by our group.[40] A brief overview of the ion-sensing behavior of the receptor is again summarized here for the benefit of the readers. $Tpy\text{-}HImzPh_3$ shows two intense bands, the lowest energy one at 340 nm is due to imadazole→tpy intra-ligand charge transfer (ILCT) transition, while the higher energy band at 285 nm is due to π–π* transition in DMF-MeCN (1:9, v/v) solution. The receptor also exhibits a strong emission band at 485 nm having quantum yield (Φ) of 0.095 and lifetime (τ) of 2.55 ns The anion and cation sensing behaviour of $tpy\text{-}HImzPh_3$ was studied in DMF-MeCN (1:9, v/v) solution through absorption and emission spectroscopic techniques. The receptor functions as selective sensor for F^- and Fe^{2+} among the studied anions and cations, respectively. The spectral change upon incremental addition of F^-

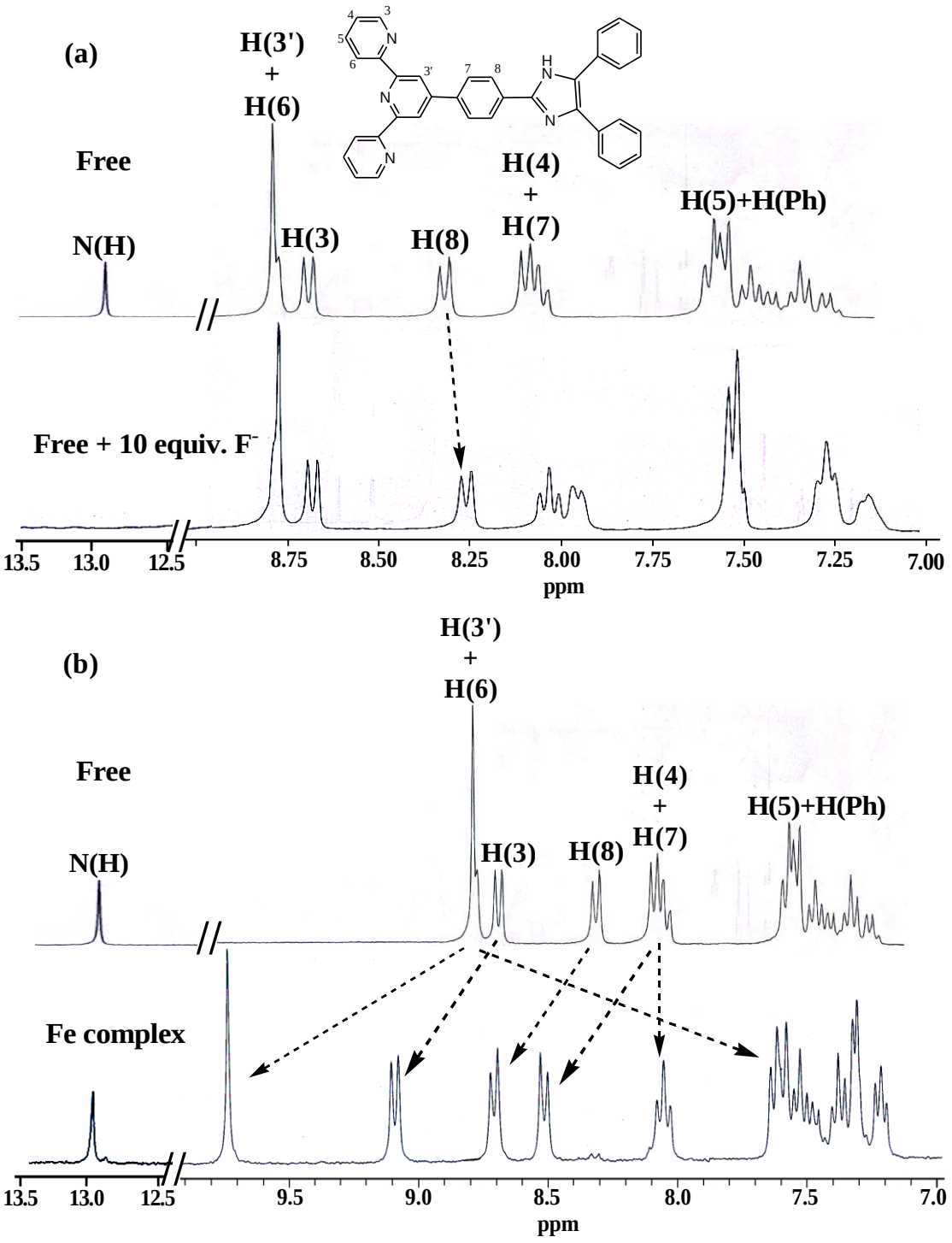

Figure 7.2. ^{1}H spectra of the receptor in absence and in presence of (a) 10 equiv. F^- and (b) 0.5 equiv. of $Fe(ClO_4)_2$ in DMSO-d_6.

and Fe^{2+} are displayed in Figure 7.3. The absorption peak at 341 nm gets diminished systematically accompanied with increase of new band at 420 nm together with evolution of bright yellow color upon gradual addition of F^-. The bathochromic shift is probably because of F^--induced deprotonation of the NH motif which enhances the electron density at the imidazolate moiety and facilitates the electron transfer process. Addition of Fe^{2+}, on the other hand, leads to generation and gradual intensification of the peak at 575 nm with evolution of a violet color and saturation occurs with 0.5 equiv. Fe^{2+}. The violet color is due to Fe(d)→tpy (π^*) MLCT transition in the resulting $[Fe(tpy\text{-}HImzPh_3)_2]^{2+}$ complex. Complete quenching of emission of the receptor is observed in presence of both Fe^{2+} and F^- ions. It is to be noted that upon excitation at 575 nm, the Fe(II) complex does not show any emission band due to presence of low-lying triplet/quintet metal-centred ($^{3/5}$MC) excited states.

It is of interest to note that complexation of tpy-$HImzPh_3$ by Fe^{2+} and its decomplexation by F^- is reversible and can be repeated many times. Similarly, deprotonation of the receptor by F^- and reverting back into its initial protonated form by acid is also reversible and can be recycled many times (Figure 7.3). The reversible deprotonation-protonation and complexation-decomplexation behavior of the receptor has been employed for the construction of different types of logic devices. In the next section, we will demonstrate that the receptor is able to mimic various logic operations by using its spectral responses through sequential use of ionic inputs.

7.3.4. Combinatorial Logic System. It is a type of digital logic which is implemented by Boolean circuits. In this section, we utilize the spectral response of the tpy-$HImzPh_3$ upon the action of Fe^{2+} as input 1 and the rest of the studied bivalent cations can be treated as input 2. Among the studied cations, only Fe^{2+} is capable to induce a strong absorption band at 575 nm which is well above the threshold energy level and gives rise to the "ON" state (1) (Figure 7.4). Based on the absorption spectral behavior of tpy-$HImzPh_3$ upon the influence of different cations and monitoring the signal at 575 nm, the function of a combinatorial logic system can be mimicked.

Two other combinatorial logic functions can also be mimicked by utilizing the spectral outputs in presence of different anions. Among the studied anions, only OH^- (input 1) or F^- (input 3) leads to the evolution of the absorption maximum at 420 nm

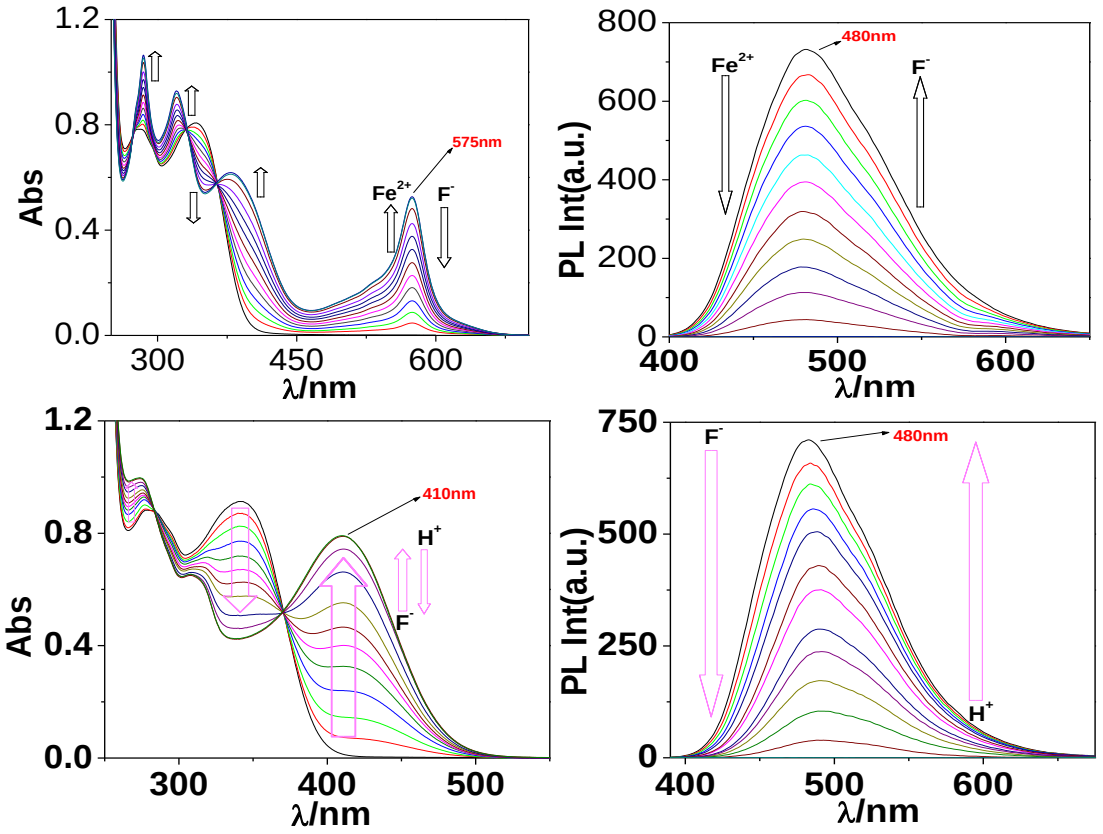

Figure 7.3. UV-vis absorption and emission spectrum of tpy-HImzPh$_3$ upon incremental addition of Fe^{2+} followed by F^- (a and b, respectively), while figure c and d represent the absorption and emission of tpy-HImzPh$_3$ upon incremental addition of F^- followed by H^+ in DMF-MeCN, 1:9, v/v).

above the threshold level and thus corresponds to the ON-state (Figure 7.5a), while the remaining anions (input 2) correspond to the OFF-state. By contrast, OH^- (input 1) or F^- (input 3) induce complete quenching of emission displaying the OFF-state, while the remaining anions that are unable to quench the emission intensity corresponds to the ON-state (Figure 7.6). The output arising from the different possible combinations of inputs are provided in the truth table of Figure 7.5b and Figure 7.6b.

7.3.5. Keypad Lock: The absorbance at 580 nm is used as the output signal upon the influence of Fe^{2+} (input 1) and F^- (input 2) for this purpose. In Figure 7.7a, the input Fe^{2+} is earmarked as "**I**", whereas F^- is allocated as "**N**", while "**B**' and "**K**" correspond to the "ON-state" and "OFF-state", respectively. There is no absorption above the threshold energy level at 580 nm in absence of both inputs implying the "OFF-state". Addition of

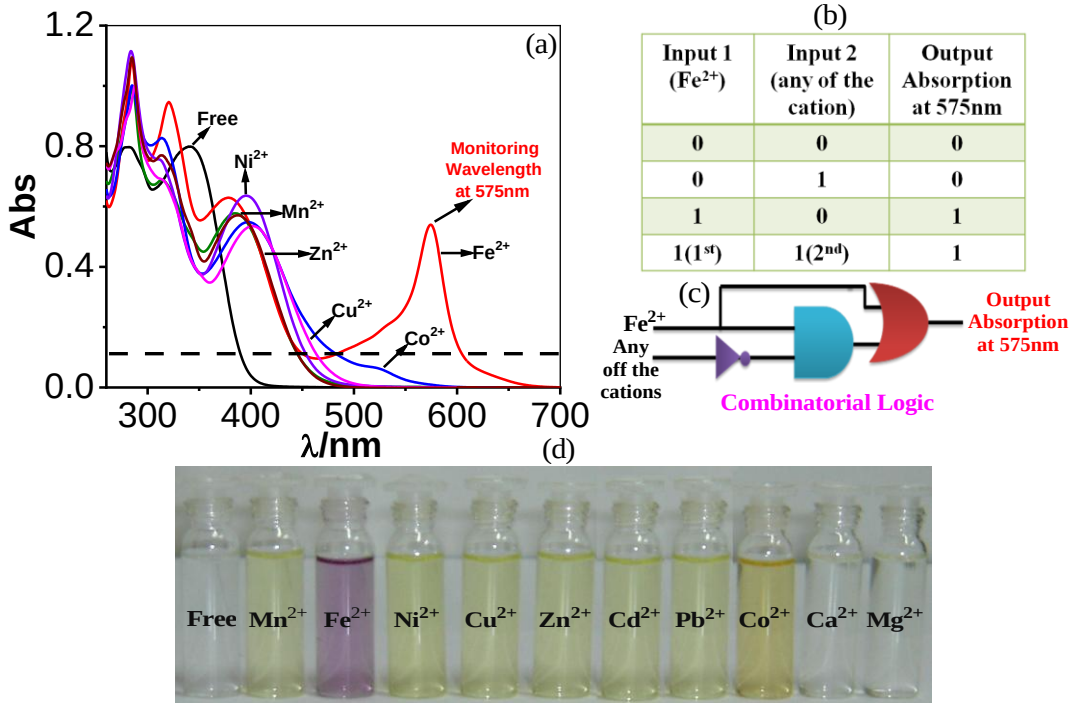

Figure 7.4. (a) UV-vis absorption spectrum of tpy-HImzPh$_3$ in presence of different cations. (b) Truth table of combinatorial logic system. (c) Schematic diagram of the combinatorial logic system. (d) Visual color changes in presence of various cations.

"**N**" followed by "**I**" induces enhancement of absorption above the threshold level leads to the "ON-state" and creates a secret password "**NIB**". Reversing the sequence of addition ("**I**" followed by "**N**") induces remarkable decrease of emission below the threshold indicating the "OFF-state" and leads to the creation of the password "**INK**" which cannot unlock the keypad lock. Thus, only the authorized person can unlock and it is a very novel approach to protect information at the molecular level and much better over common number-based PIN (Figure 7.7).

7.3.6. Fuzzy Logic Operations. In Boolean systems, we use crisp values that define a strict boundary, either true (1) or false (0). They are unable to define any intermediate values. In the real world, very often we encounter a situation where we cannot confidently determine whether the state is true (1) or false (0). The fuzzy logic, first proposed by Lotfi Zadeh in 1965, provides an easy alternative to this end and provides some sort of flexibility in reasoning. Due to the unclear and vagueness of most of the chemical reactions, the computation based on fuzzy logic is assumed to be

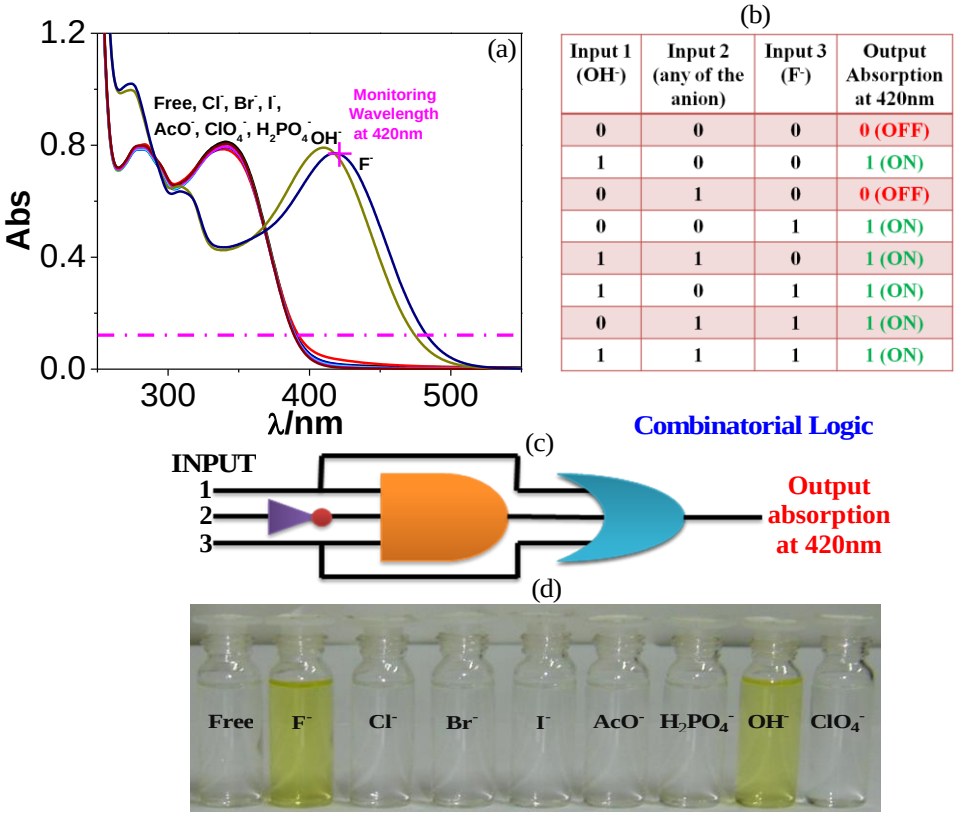

Input 1 (OH^-)	Input 2 (any of the anion)	Input 3 (F^-)	Output Absorption at 420nm
0	0	0	0 (OFF)
1	0	0	1 (ON)
0	1	0	0 (OFF)
0	0	1	1 (ON)
1	1	0	1 (ON)
1	0	1	1 (ON)
0	1	1	1 (ON)
1	1	1	1 (ON)

Figure 7.5. (a) UV-vis absorption spectrum of tpy-HImzPh$_3$ in presence of different anions. (b) Truth table of combinatorial logic system. (c) Schematic diagram of the combinatorial logic system. (d) Visual color changes in presence of different anions.

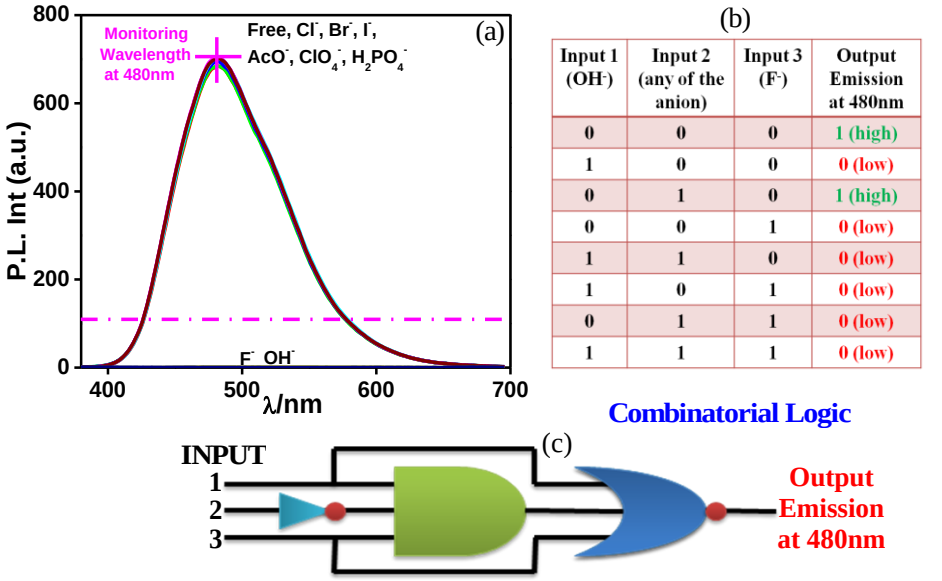

Input 1 (OH^-)	Input 2 (any of the anion)	Input 3 (F^-)	Output Emission at 480nm
0	0	0	1 (high)
1	0	0	0 (low)
0	1	0	1 (high)
0	0	1	0 (low)
1	1	0	0 (low)
1	0	1	0 (low)
0	1	1	0 (low)
1	1	1	0 (low)

Figure 7.6. (a) Photoluminescence spectrum of tpy-HImzPh$_3$ in presence of different anions. (b) Truth table of combinatorial logic system. (c) Schematic diagram of the combinatorial logic system.

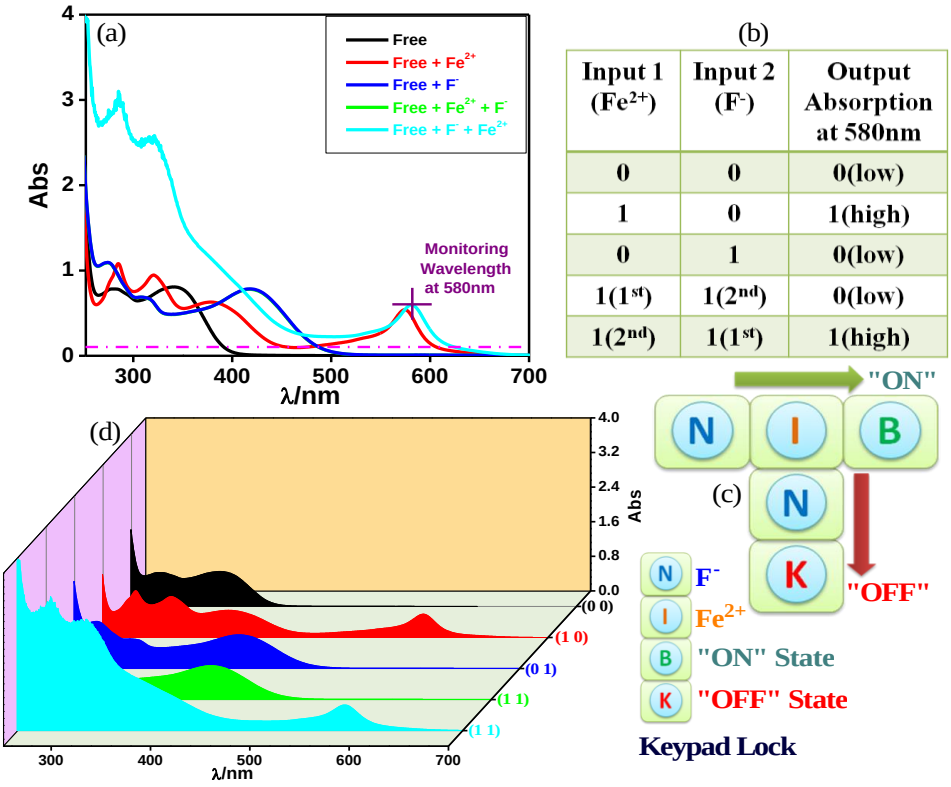

Figure 7.7. (a) UV-vis absorption spectrum of tpy-HImzPh$_3$ upon interaction with F^- and Fe^{2+}. Truth table and schematic display of the security keypad lock (b and c, respectively). (d) 3D display of the variation of absorbance in presence of the inputs.

probable substitute to tackle the indecisive information in the analogue domain of the binary logic scheme.

As shown in Figure 7.8, the spectral change of tpy-HImzPh$_3$ varies to a great extent upon the action of F^- (input 1) and H^+ (input 2). In lieu of its indefinite character as well as large degree of change, the variables for the present system can be disclosed in terms of five lingual parameters of the triangular molecular functions (*trimf*), viz. very low, low, medium, high, and very high. The influence of varying amount of H^+ and F^- on the emission intensity of tpy-HImzPh$_3$ could be presented in the form of fuzzy sets (Figure 7.8). The IF-portion conforms to the antecedent, while the THEN-portion correlates to the consequence. The quenching of emission occurs in presence of F^-, while regeneration of emission takes place upon the action H^+. To this end, fuzzy logic is applied to tpy-HImzPh$_3$ upon monitoring the emission intensity with changing concentrations of H^+ and F^- inputs. The feasible consolidation of F^- and H^+ generates 38

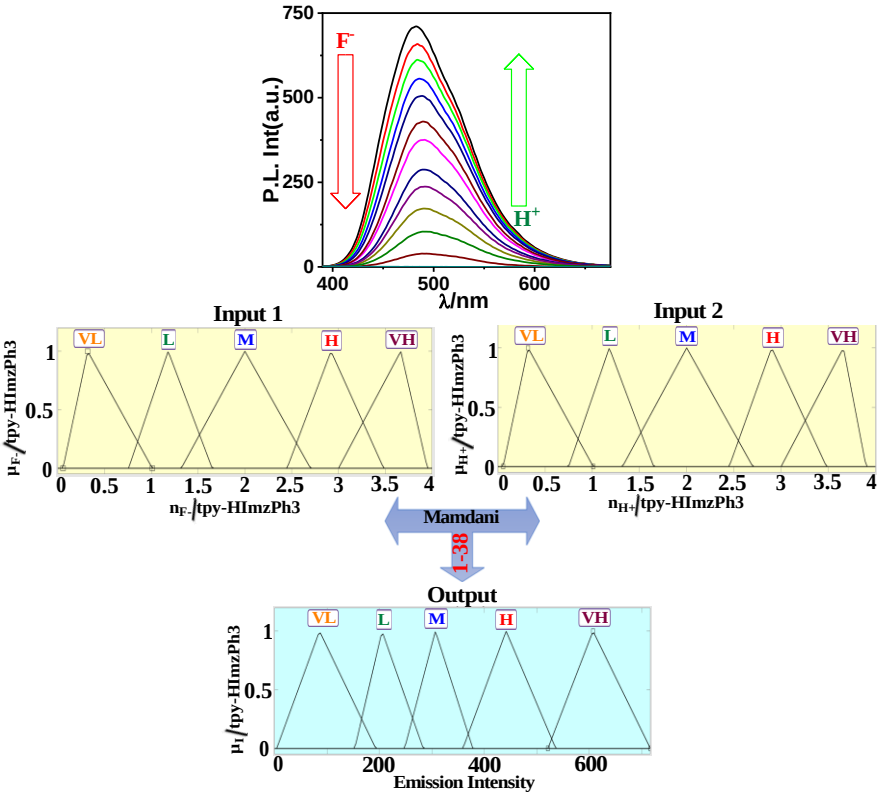

Figure 7.8. Schematic display of fuzzy logic scheme based on fuzzy inference rules upon monitoring the emission intensity as a function of F^- and H^+. Fuzzy variables are decomposed in five fuzzy sets. F^-: (1) very low (trimf $\mu_{verylow}$, [0.056 0.32 1.01]); (2) low (trimf μ_{low}, [0.757 1.18 1.65]); (3) medium (trimf μ_{medium}, [1.32 2 2.72]) (4) high (trimf μ_{high}, [2.45 2.92 3.482]) (5) very high (trimf $\mu_{veryhigh}$, [3 3.665 3.95). H^+: (1) (1) very low (trimf $\mu_{verylow}$, [0.056 0.32 1.01]); (2) low (trimf μ_{low}, [0.757 1.18 1.65]); (3) medium (trimf μ_{medium}, [1.32 2 2.72]) (4) high (trimf μ_{high}, [2.45 2.92 3.482]) (5) very high (trimf $\mu_{veryhigh}$, [3 3.665 3.95). Emission intensity (Output): (1) very low (trimf $\mu_{verylow}$, [4.28 85.8 193]); (2) low (trimf μ_{low}, [153 205 283.5]); (3) medium (trimf μ_{medium}, [248 306.7 378]); (4) high (trimf μ_{high}, [359 441.4 536]); (5) very high (trimf $\mu_{veryhigh}$, [521 607 716.3]).

rules. Furthermore, the variation of emission intensity upon combined actions of H^+ and F^- is portrayed in a 3D plot (Figure 7.9).

7.3.7. Artificial Neural Network (ANN). Fuzzy logic has good knowledge representation ability but weak learning capability. To this end, we tried to formulate the ANN mathematical algorithm and modeling method that correlates the input and output dependence of the receptor. ANN is a powerful aid for modeling nonlinear functions which represents the real world systems. ANN is constructed via compilation of artificial

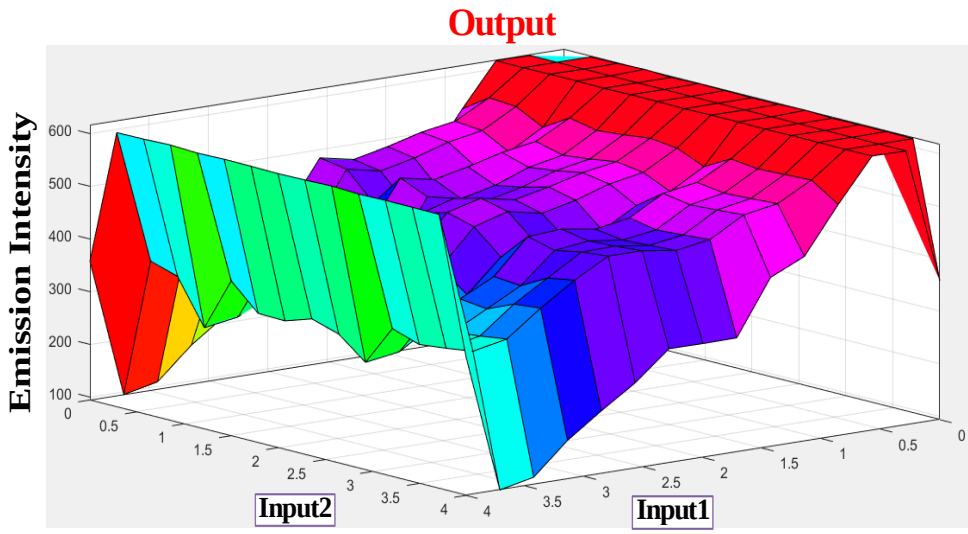

Figure 7.9. 3D display of the dependence of emission intensity of tpy-HImzPh$_3$ at 485 nm upon the action of F^- and H^+.

neurons which mirror the connectedness of neurons in human brain to carry out a task with enhanced performance via learning, training and continuous improvement. We used Levenberg-Marquardt algorithm for training purpose. Input data present the network and target data define the desired network output. We have taken the emission outputs upon the action of 25 different combinations of two inputs (input 1=F^- and input 2=H^+). Thus, the 25×2 matrix represents the static input data of 25 samples involving 2 inputs, while 25×1 matrix represents the static output data of one element. Now, the 25 samples are divided into 3 sets of data. 70% of the data are conferred for the training and the network is corrected according to its error. 15% data are employed to compute the network generalization and to halt training, when generalization stops improving, data validation takes place. The remaining 15% data provide an independent measure of the network performance during and after the training, called testing data (Figure 7.10).

It clearly shows that the model's best validation performance is 4335.47 at epoch 2. The enhancement of green colored line after epoch 2 suggests that the increment of the mean squared error (mse) and training is halted. The regression values (R) measure the correlation between the outputs and targets. The R values close to 1 imply that there is a close relationship between output and targets and the model is performing very well (Figure 7.11). The bins are the number of vertical bars on the graph (Figure 7.12). The Y-

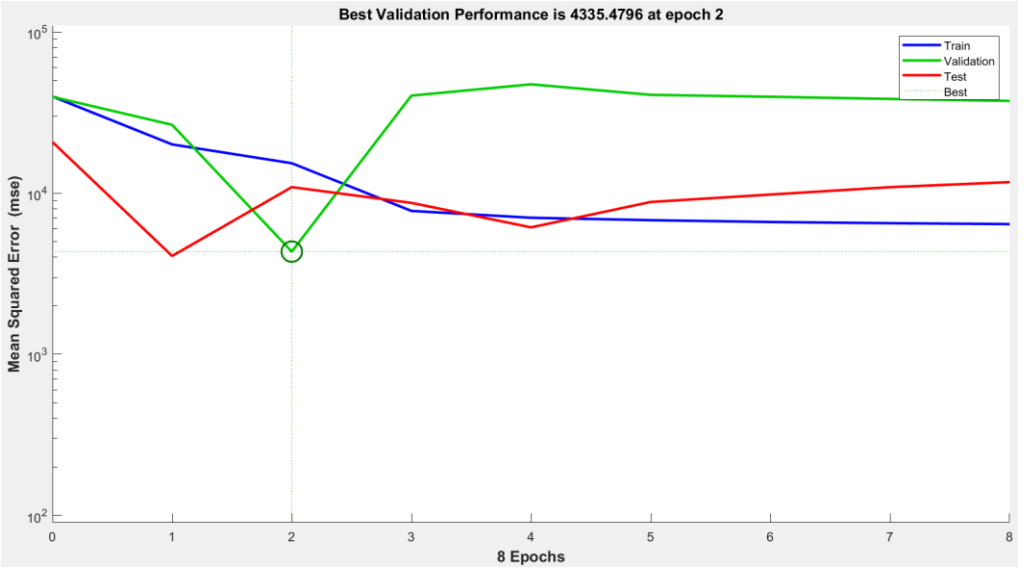

Figure 7.10. The performance of the designed ANN model.

axis designates the number of samples in the database which exit in a particular bin, e.g. at the middle of the plot, the bin corresponding to the error of -7.425 to 13.42 and the height of that bin for training data set lies below but close to 2 and validation data set varies between 2 and 3. In the present case, the zero error point is situated under the bin with centre at -7.425. The total error from neural network ranges from -278.5 (leftmost bin) to 117.7 (rightmost bin). The error histogram represents the histogram of the errors between target values and predicted values after training a feed-forward neural network. As the error values suggest how predicted values are deviating from the target values, hence this could be negative. This error range is spitted up into 20 smaller bins, so each bin has a width of (117.7-(-278.5))/20 = 19.81 (Figure 7.12). There are three layers, viz. an input-, hidden- and an output layer. Each of the hidden layers performs non linear transformation of the inputs entered into the network. Inputs are loaded into the input layer, and each node gives rise to an output value through an activation function. The outputs of the input layer again act as the inputs to the next hidden layer (Figure 1.13). On putting the different values of inputs in the rule viewer of fuzzy logic and the command section of ANN model in matlab R2018a, we obtain the following values of outputs as presented in Table 7.1 which clearly indicates that the difference between experimental and fuzzy logic output is greater than the difference between experimental and ANN model output. This is because of the neural network's inability to explain decision (lack of transparency) and fuzzy logic's weakness of learning.

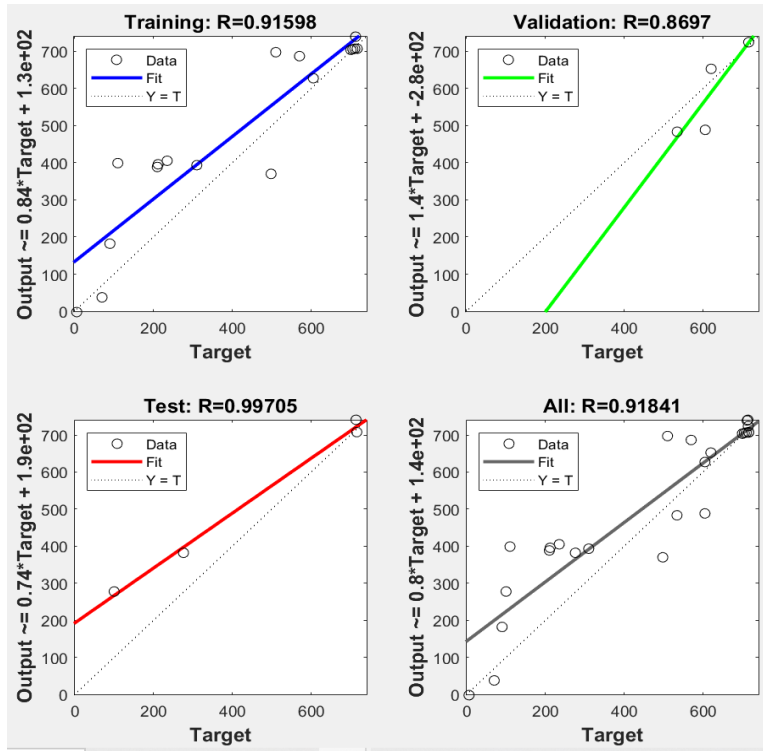

Figure 7.11. Comparison between linear regression and ANN model results plotted versus the observed values for training, validation and testing.

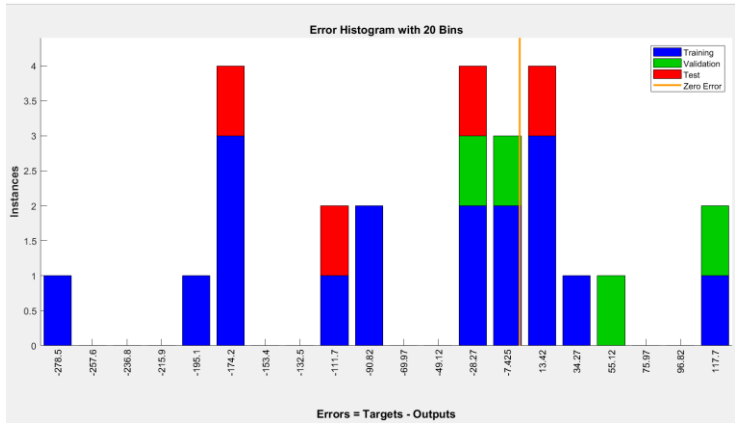

Figure 7.12. Error histogram in ANN model training process.

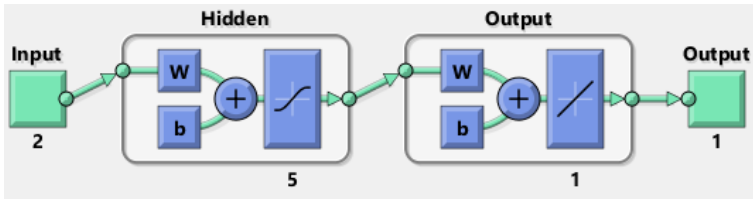

Figure 7.13. Artificial neural network model consisting of 2 inputs, 5 hidden layers and 1 output.

Table 7.1. Experimental, Fuzzy and ANN Model Data in Presence of Different Combinations of Inputs.

Input 1 (F^-)	Input 2 (H^+)	Experimental output Data	Data output based on Fuzzy logic	Data output based on ANN model
1	1	620	580	652
4	4	212	400	395
4	0	6	35	1
1	3	700	680	703
1	2	510	390	697

7.3.8. Adaptive Neuro-Fuzzy Inference System (ANFIS). It is the combination of fuzzy and neural network to overcome the drawback of individual ones Robustness, solidity and high generalization capability of ANFIS model provides room for applications that involve crisp inputs and outputs. To develop the system, we have used 70% data for the training purpose and the rest 30% data for testing. Figure 7.14b shows that the training error is reduced every time up to 50 epochs indicating that the system is learning in every single step. Due to presence of two inputs and 5 membership functions each, the system will generate 5^2= 25 rules. The feasible consolidation of F^- and H^+ generates 25 rules on the basis of Sugeno's method (Figure 7.15). On running the generated ANFIS on matlab-R2018a and upon commanding the

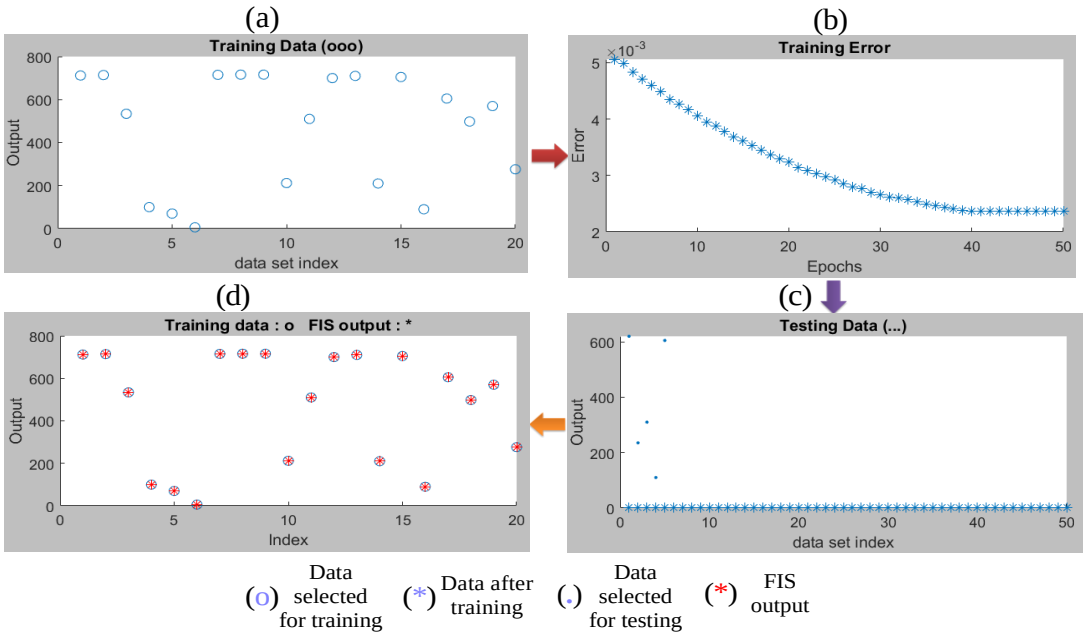

Figure 7.14. (a) Selected training data to design the ANFIS model. (b) Training error minimization up to 50 epochs. (c) Combination of training and testing data. (d) Compilation of testing data and FIS output.

system with different value of inputs, the obtained outputs are summarized in Table 7.2. Furthermore, the variation of emission intensity upon combined operation of F^- and H^+ is portrayed in a 3D plot (Figure 7.16). The performance of the ANFIS models in the present study is statically measured by root mean squared error (RMSE). The testing RMSE value for this model is 0.0023 suggesting that the model is working properly. We can see that the ANFIS generated output values are more close to the experimental outputs. So it is more accurate optimization system than fuzzy and neural network. On the basis of 25 rules, we have constructed the ANFIS structure (Figure 7.17). The comparison as well as the deviation of the experimental data to those of Fuzzy, ANN and ANFIS outputs is presented in Figure 7.18.

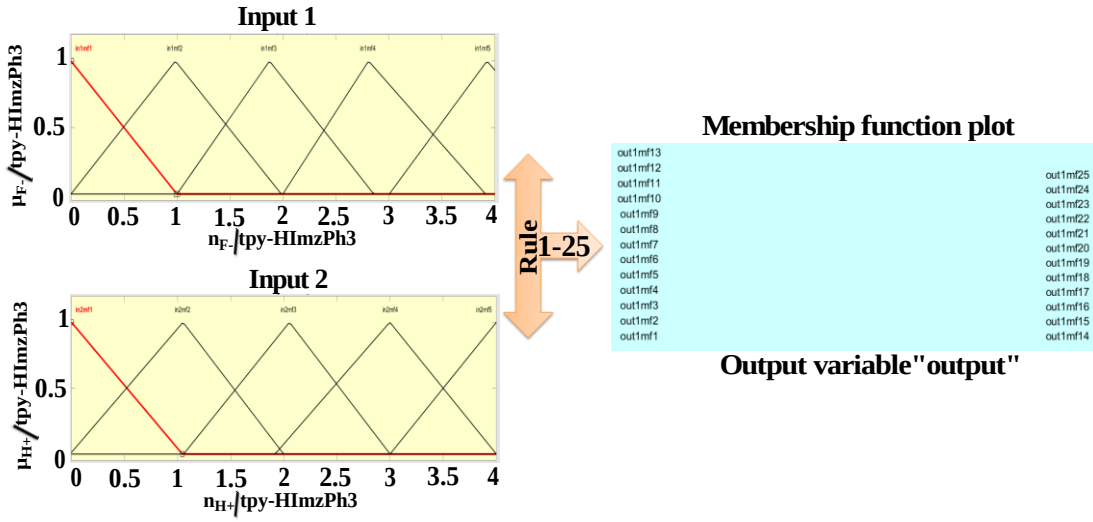

Figure 7.15. Schematic presentation of ANFIS based on Sugeno's method maintaining 25 rules.

Table 7.2. Experimental and ANFIS generated outputs.

Input 1 (H^+)	Input 2 (F^-)	Experimental output Data	Data output based on ANFIS model
1	1	620	618
4	4	212	211
4	0	6	8
1	3	700	700
1	2	510	530

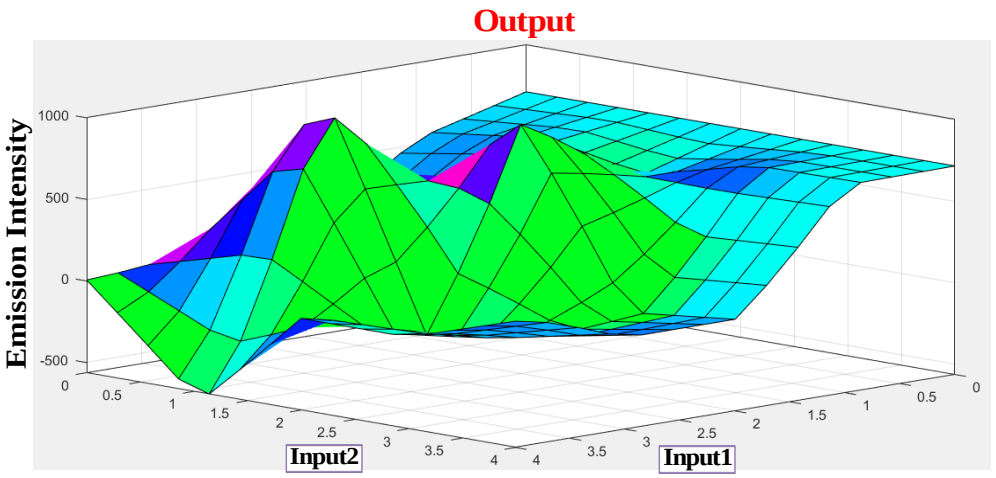

Figure 7.16. Three-dimensional representation (based on Sugeno's method) of the dependence of emission intensity of tpy-HImzPh$_3$ at 485 upon simultaneous action of two inputs (F^- and H^+).

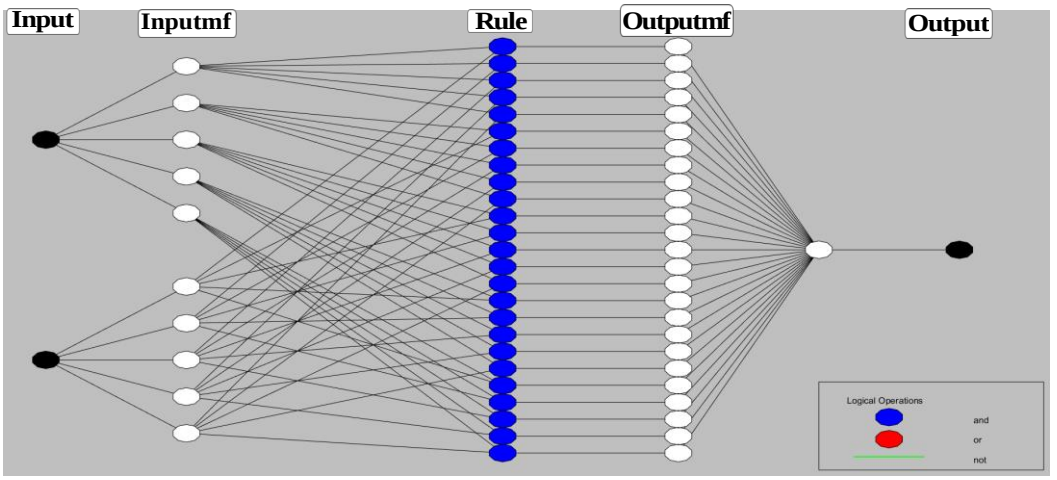

Figure 7.17. Generated ANFIS structure based on 25 rules.

Addition of Fe^{2+} causes enhancement of absorbance at 575 nm of tpy-HImzPh$_3$ (due to complexation), while F^- causes the depletion of absorbance (because of decomplexation). We implement fuzzy logic to the receptor upon changing the concentrations of Fe^{2+} and F^- ions and by monitoring the absorption spectral response. We have taken three triangular membership functions (*trimf*) for each inputs and output. The feasible consolidation of Fe^{2+} and F^- generates 15 rules (Figure 7.19). Furthermore, the variation of absorption intensity upon combined operation of Fe^{2+} and F^- is portrayed in a 3D plot (Figure 7.20).

7.3.9. Artificial Neural Network (ANN). We also used here the Levenberg-Marquardt algorithm for training purpose. The input data present the network and target data define the desired network output. Input 16×2 matrix represents static data of 16 samples of 2 inputs and output 16×1 matrix represents static data of 16 samples of 1 element. 16 samples are divided into 3 sets of data. 70% of data (12 samples) are feeded to the network during training and the network is optimized according to its error, 15% (2 samples) data are used to measure network generalization and to halt training, while remaining 15% (2 samples) data have no effect on training but give an independent measure of network performance during and after training.

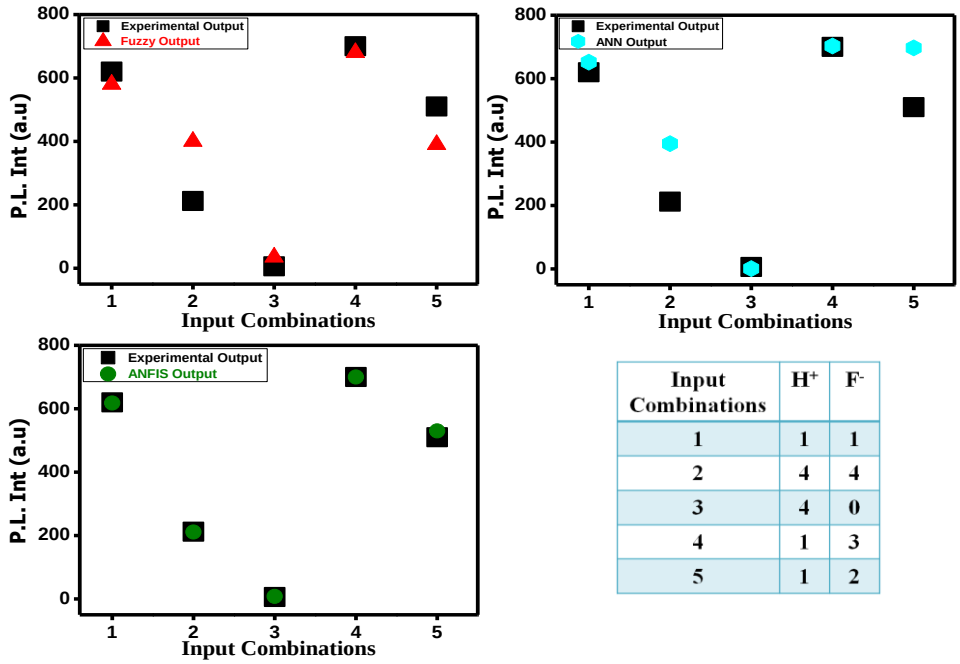

Input Combinations	H^+	F^-
1	1	1
2	4	4
3	4	0
4	1	3
5	1	2

Figure 7.18. Comparison between experimental emission output data and Fuzzy, ANN and ANFIS output data.

The model's best validation performance is 0.0005813 at epoch 14. The enhancement of green coloured spectra after epoch 14 suggests the increment of mean squared error (mse) and training is halted. Regression (R) values measured the co-relation between outputs and targets. The R values close to 1 imply that there is a close relationship between output and targets and the model is performing very well. The Y-axis designates the number of samples from the database which lies in a particular bin, e.g. at the middle of the plot, the bin corresponding to the error of -0.00186 to 0.00214 and the height of

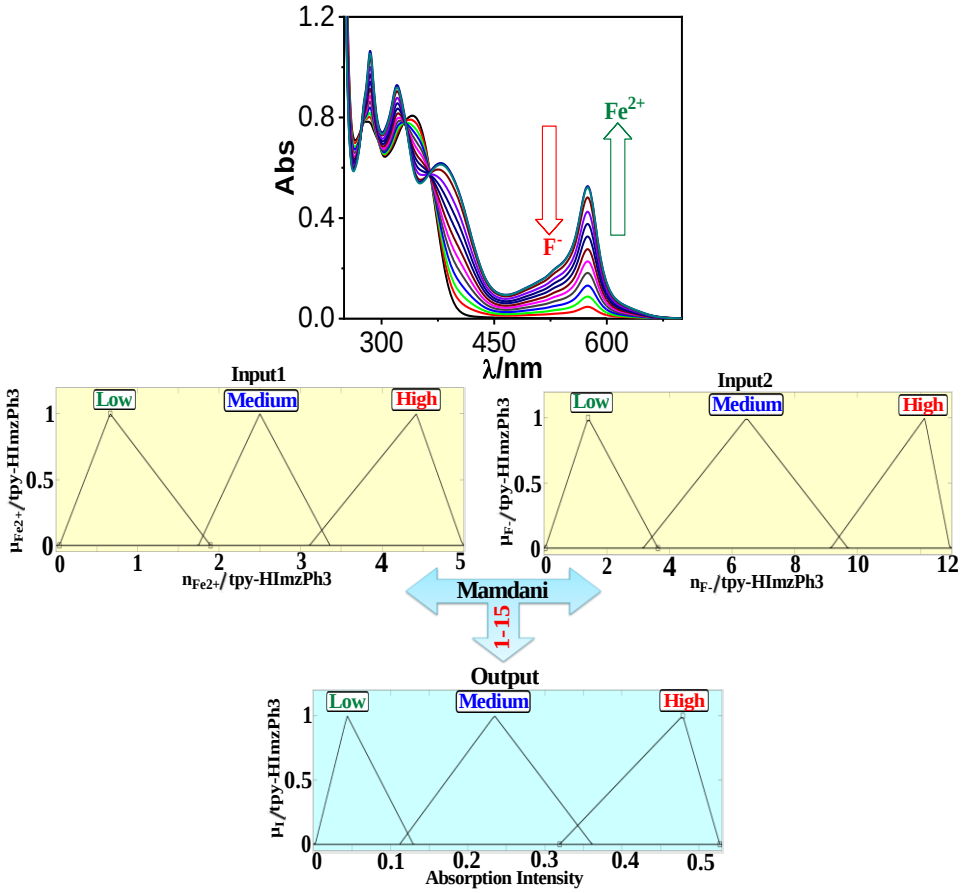

Figure 7.19. Schematic display of fuzzy logic based on fuzzy inference rules by monitoring absorbance at 575 nm upon the action Fe^{2+} and F^- as inputs. Fuzzy variables are decomposed in three fuzzy sets. Fe^{2+}: (1) low (trimf μ_{low}, [0.042 0.665 1.89]); (2) medium (trimf μ_{medium}, [1.747 2.51 3.36]); (3) high (trimf μ_{high}, [3.109 4.419 4.989]). F^-: (1) low (trimf μ_{low}, [0.0426 1.41 3.633]); (2) medium (trimf μ_{medium}, [3.16 6.46 9.69]); (3) high (trimf μ_{high}, [9.146 12.14 13.01]). Absorption intensity (Output): (1) low (trimf μ_{low}, [0.00253 0.0439 0.1297]); (2) medium (trimf μ_{medium}, [0.112 0.235 0.361]); (3) high (trimf μ_{high}, [0.319 0.479 0.527]).

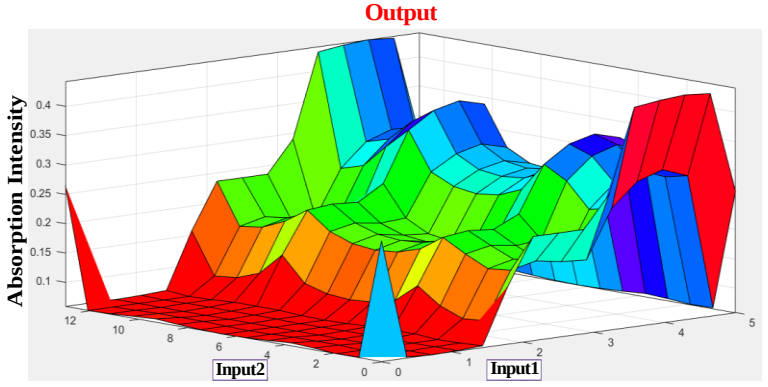

Figure 7.20. Three-dimensional representation of the dependence of absorption intensity of tpy-$HImzPh_3$ at 575nm as a function of simultaneous injection of two chemical inputs (Fe^{2+} and F^-).

that bin for training data set lies below but close to 5 and validation data set varies between 5 and 6. In the present case, the zero error point is situated under the bin with centre at -0.00186. The total error from neural network ranges from -0.03387 (leftmost bin) to 0.04215 (rightmost bin). This error range is divided into 20 smaller bins, so each bin has a width of (0.04215-(-0.03387))/20 = 0.0038. On putting the different values of inputs in the rule viewer of fuzzy logic and the command section of ANN model in matlab R2018a we got the following values of outputs (Table 7.3).

7.3.10. Adaptive Neuro-Fuzzy Inference System (ANFIS). To develop the system we have used 70% data for training purpose and the rest 30% data for testing. The training error is reduced every time up to 50 epochs which indicates that the system is learning in every single step. Due to presence of two inputs and 3 membership functions each, the system will generate 3^2= 9 rules. The plausible compilation of Fe^{2+} and F^- generates 9 rules on the basis of Sugeno's method. On running the generated ANFIS on matlab-R2018a and command the system with different value of inputs we got the following outputs (Table 7.4). The variation of absorption intensity upon combined operation of Fe^{2+} and F^- is shown in a 3D plot (Figure 7.21).

Table 7.3. Experimental, Fuzzy and ANN Model Data in Presence of Different Combinations of Inputs.

Input 1 (Fe^{2+})	Input 2 (F^-)	Experimental output Data	Data output based on Fuzzy logic	Data output based on ANN model
2	6	0.22	0.153	0.207
1	5	0.24	0.059	0.196
5	9	0.15	0.064	0.186
5	0	0.53	0.265	0.496
3	7	0.19	0.161	0.196

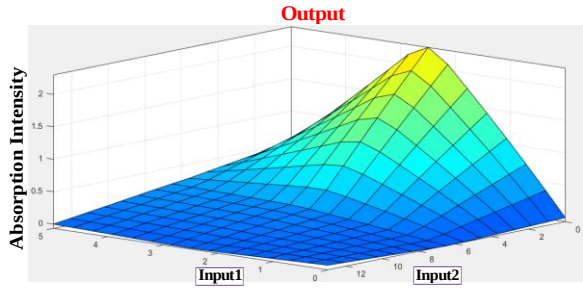

Figure 7.21. Three-dimensional representation (based on Sugeno method) of the dependence of absorption intensity of tpy-$HImzPh_3$ at 575nm as a function of simultaneous injection of two chemical inputs (Fe^{2+} and F^-).

Table 7.4. Experimental and ANFIS Generated Outputs.

Input 1 (H^+)	Input 2 (F^-)	Experimental output Data	Data output based on ANFIS model
2	6	0.22	0.211
1	5	0.24	0.241
5	9	0.15	0.155
5	0	0.53	0.531
3	7	0.19	0.192

The testing root mean square error (RMSE) value for this model is 0.0036. This suggests that the model is working properly. We can see that the ANFIS generated output values are more close to the experimental outputs. So it is more accurate system then fuzzy and neural network. On the basis of 9 rules we have constructed the ANFIS structure (Figure 7.22).

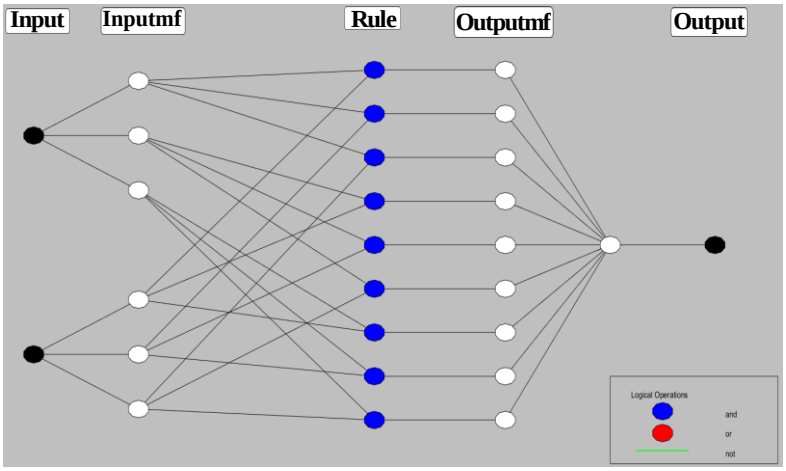

Figure 7.22. Generated ANFIS structure based on 9 rules.

7.4. Conclusions

With regard to our recent interest to process information at the molecular level, we employed in this work a terpyridyl-imidazole based receptor (tpy-HImzPh_3) which upon interaction with specific cations and anions gives rise to significant modulation of absorption and emission spectral properties. By using the absorption and emission spectral outputs towards specific anions and cations, we are able to demonstrate combinatorial Boolean logic functions of AND, OR and NOT gates as well as the keypad lock. Additionally, the fuzzy logic is employed to fabricate an infinite-valued setup to

identify the indefinite values in between true (1) and false (0) states. ANN- and ANFIS-based modeling approaches were also employed by using different combinations of inputs and output data. The results show that Fuzzy, ANN and ANFIS are capable of predicting the experimental data quite accurately. The statistical performance indicators (such as MSE, RMSE) indicate that the predicted values of the sensing data (absorption and emission spectral outputs) by ANFIS models are comparable to the experimental data. Therefore, the adopted computational intelligence-based approach can be considered as a potential ion sensing data model for tpy-HImzPh_3.

7.5. References

1. Artrith, N.; Butler, K. T.; Coudert, F. X.; Han, S.; Isayev, O.; Jain, A.; Walsh, A. Best Practices in Machine Learning for Chemistry. *Nat. Chem.*, **2021**, *13*, 505-508.
2. Gentili, P. L. A Strategy to Face Complexity: The Development of Chemical Artificial Intelligence. In Advances in Artificial Life, Evolutionary Computation, and Systems Chemistry. Rossi, F.; Piotto, S.; Concilio, S.; *Eds.; Springer: Cham, Switzerland; New York, NY, USA.*, **2017**, *708*, 151-160.
3. Mater, A. C.; Coote, M. L. Deep Learning in Chemistry. *J. Chem. Inf. Model.*, **2019**, *59*, 2545-2559.
4. Pflüger, P. M.; Glorius, F. Molecular Machine Learning: The Future of Synthetic Chemistry?. *Angew. Chem., Int. Ed. Engl.*, **2020**, *59*, 18860-18865.
5. Szaciłowski, K. Digital Information Processing in Molecular Systems. *Chem. Rev.*, **2008**, *108*, 3481-3548.
6. Zadeh, L. A. Toward Human Level Machine Intelligence-is it Achievable? The Need for a Paradigm Shift. *IEEE Comput. Intell. Mag.* **2008**, *3*, 11-22.
7. Zadeh, L.A. Outline of a New Approach to the Analysis of Complex Systems and Decision Processes. *IEEE Trans. Syst. Man Cyb.* **1973**, *3*, 28-44.
8. He, L.; Bai, L.; Dionysiou, D. D.; Wei, Z.; Spinney, R.; Chu, C.; Xiao, R. Applications of Computational Chemistry, Artificial Intelligence, and Machine Learning in Aquatic Chemistry Research. *J. Chem. Eng.*, **2021**, *426*, 131810.
9. Gentili, P. L. Boolean and Fuzzy Logic Implemented at the Molecular Level. *Chem. Phys.*, **2007**, *336*, 64-73.
10. Gentili, P. L. Boolean and Fuzzy Logic Gates Based on the Interaction of Flindersine with Bovine Serum Albumin and Tryptophan. *J. Phys. Chem. A.*, **2008**, *112*, 11992-11997.
11. Gentili, P. L. The Fundamental Fuzzy Logic Operators and Some Complex Boolean Logic Circuits Implemented by the Chromogenism of a Spirooxazinew. *Phys. Chem. Chem. Phys.*, **2011**, *13*, 20335-20344.
12. Gentili, P. L. The Fuzziness of the Molecular World and Its Perspectives. *Molecules.*, **2018**, *23*, 2074.

13. Gentili, P.L. The Fundamental Fuzzy Logic Operators and Some Complex Boolean Logic Circuits Implemented by the Chromogenism of a Spirooxazine. *Phys. Chem. Chem. Phys.*, **2011**, *13*, 20335-20344.
14. Gentili, P.L. The Human Sensory System as a Collection of Specialized Fuzzifiers: A Conceptual Framework to Inspire New Artificial Intelligent Systems Computing with Words. *J. Intell. Fuzzy Syst*., **2014**, *27*, 2137-2151.
15. Gentili, P. L.; Giubila, M. S.; Heron, B. M. Processing Binary and Fuzzy Logic by Chaotic Time Series Generated by a Hydrodynamic photochemical oscillator. *ChemPhysChem*., **2017**, *18*, 1831-1841.
16. Gentili, P. L.; Giubila, M. S.; Germani, R.; Romani, A.; Nicoziani, A.; Spalletti, A.; Heron, B. M. Optical Communication Among Oscillatory Reactions and Photo-Excitable Systems: Uv and Visible Radiation can Synchronize Artificial Neuron Models. *Angew. Chem. Int. Ed.*, **2017**, *56*, 7535-7540.
17. Gentili, P. L.; Rightler, A. L.; Heron, B. M.; Gabbutt, C. D. Extending Human Perception of Electromagnetic Radiation to the UV Region Through Biologically Inspired Photochromic Fuzzy Logic (BIPFUL) Systems. *Chem. Commun.*, **2016**, *52*, 1474-1477.
18. Schumann, A.; Adamatzky, A. The Double-Slit Experiment with Physarum Polycephalum and P-Adic Valued Probabilities and Fuzziness. *Int. J. General Syst*., **2015**, *44*, 392-408.
19. Zadeh, L. A. Fuzzy Sets. In Fuzzy Sets, Fuzzy Logic, and Fuzzy Systems: Selected Papers by Lotfi A Zadeh. **1996**, 394-432.
20. Babanezhad, M.; Behroyan, I.; Nakhjiri, A. T.; Marjani, A.; Shirazian, S. Computational Modeling of Transport in Porous Media Using an Adaptive Network-Based Fuzzy Inference System. *ACS omega*., **2020**, *5*, 30826-30835.
21. Babanezhad, M.; Nakhjiri, A. T.; Shirazian, S. Changes in the Number of Membership Functions for Predicting the Gas Volume Fraction in Two-Phase Flow Using Grid Partition Clustering of the ANFIS Method. *ACS omega*., **2020**, *5*, 16284-16291.

22. Babanezhad, M.; Rezakazemi, M.; Marjani, A.; Shirazian, S. Predicting Air Superficial Velocity of Two-Phase Reactors Using ANFIS and CFD. *ACS omega*., **2020**, *6*, 239-252.
23. Bingöl, D.; Inal, M.; Çetintaş, S. Evaluation of Copper Biosorption Onto Date Palm (Phoenix Dactylifera L.) Seeds with MLR and ANFIS Models. *Ind. Eng. Chem. Res*., **2013**, *52*, 4429-4435.
24. Giri Nandagopal, M. S.; Selvaraju, N. Prediction of Liquid–Liquid Flow Patterns in a Y-Junction Circular Microchannel Using Advanced Neural Network Techniques. *Ind. Eng. Chem. Res*., **2016**, *55*,11346-11362.
25. Huang, M.; Ma, Y.; Wan, J.; Zhang, H.; Wang, Y. Modeling a Paper-Making Wastewater Treatment Process by Means of an Adaptive Network-Based Fuzzy Inference System and Principal Component Analysis. *Ind. Eng. Chem. Res*., **2012**, *51*, 6166-6174.
26. İnal, M. Predicting the Conversion Ratio for the Leaching of Celestite in Sodium Carbonate Solution Using an Adaptive Neuro-Fuzzy Inference System. *Ind. Eng. Chem. Res*., **2014**, *53*, 4975-4980.
27. Razzak, S. A.; Rahman, S. M.; Hossain, M. M.; Zhu, J. Artificial Neural Network and Neuro-Fuzzy Methodology for Phase Distribution Modeling of a Liquid–Solid Circulating Fluidized Bed Riser. *Ind. Eng. Chem. Res*., **2012**, *51*, 12497-12508.
28. Adamatzky, A.; Costello, B. D. L. Experimental Logical Gates in a Reaction-Diffusion Medium: The XOR Gate and Beyond. *Phys. Rev. E*., **2002**, *66*, 046112.
29. Adamatzky, A.; Jones, J.; Mayne, R.; Tsuda, S.; Whiting, J. Logical Gates and Circuits Implemented in Slime Mould. *Advances in Physarum Machines.*, **2016**, 37-74.
30. Adamatzky, A.; Tegelaar, M.; Wosten, H. A.; Powell, A. L.; Beasley, A. E.; Mayne, R. On Boolean Gates in Fungal Colony. *Biosystems*., **2020**, *193*, 104138.
31. De Silva, A. P.; McClenaghan, N. D. Molecular-Scale Logic Gates. *Chem. Eur. J*., **2004**, *10*, 574-586.

32. De Silva, A. P.; Fox, D. P.; Huxley, A. J. M.; Moody, T. S. Combining Luminescence, Coordination and Electron Transfer for Signalling Purposes. *Coord. Chem. Rev*., **2000**, *205*, 41-57.
33. De silva, A. P.; Gunaratne, H. Q. N.; McCoy, C. P. A Molecular Photoionic AND Gate Based on Fluorescent Signaling. *Nature*., **1993**, *364*, 42-44.
34. De Silva. A. P. Molecular Logic Gate Arrays. *Chem. Asian J.*, **2011**, *6*, 750-766.
35. Gale, E.; De Lacy Costello, B.; Adamatzky, A. Boolean Logic Gates from a Single Memristor via Low-Level Sequential Logic. *International Conference on Unconventional Computing and Natural Computation.*, **2013**, 79-89.
36. Karmakar, S.; Mardanya, S.; Pal, P.; Baitalik, S. Design of Multichannel Osmium-Based Metalloreceptor for Anions and Cations by Taking Profit from Metal-Ligand Interaction and Construction of Molecular Keypad Lock and Memory Device. *Inorg. Chem*., **2015**, *54*, 11813-11825.
37. Ling, J.; Daly, B.; Silverson,V. A. D.; De Silva, A. P. Taking Baby Steps in Molecular Logic-Based Computation. *Chem. Commun.* **2015**, *51*, 8403-8409.
38. Szaciłowski, K. Molecular Logic Gates Based on Pentacyanoferrate Complexes: From Simple Gates to Three-Dimensional Logic Systems. *Chem. Eur. J*., **2004**, *10*, 2520-2528.
39. Szaciłowski, K.; Wojciech, M.; Grażyna, S. Light-Driven OR and XOR Programmable Chemical Logic Gates. *J. Am. Chem. Soc.*, **2006**, *128*, 4550-4551.
40. Bhaumik, C.; Das, S.; Maity, D.; Baitalik, S.; A Terpyridyl-Imidazole (tpy-HImzPh3) Based Bifunctional Receptor for Multichannel Detection of Fe^{2+} and F^- ions. *Dalton Trans*., **2011**, *40*, 11795-11808.
41. Karmakar, S.; Maity, D.; Mardanya, S.; Baitalik, S. Demonstration of Multiple Logic Operations in a Heteroditopic Pyrene-Phenyimidazole-Terpyridine Conjugate Based on Optical Responses by Selective Anions and Cations: An Experimental and Theoretical Investigation. *J. Phys. Chem. A*., **2014**, *118*, 9397-9410.

42. Karmakar, S.; Mardanya, S.; Das, S.; Baitalik, S. Efficient Deep-Blue Emittier and Molecular-Scale Memory Device Based on Dipyridyl-Phenylimidazole-Terpyridine Assembly. *J. Phys. Chem. C.*, **2015**, *119*, 6793-6805.
43. Mondal, D.; Pal, P.; Baitalik, S. Anthraquinone-Biimidazole Based Ruthenium (II) Complexes as Selective Multichannel Anion Sensors and Multi-Readout Molecular Logic Gates and Memory Devices: Combined Experimental and DFT/TD-DFT Study. *Sens. Actuators B.*, **2017**, *242*, 746-759.
44. Mukherjee, S.; Sahoo, A.; Deb, S.; Baitalik, S. Light and Cation-Driven Optical Switch Based on a Stilbene-Appended Terpyridine System for the Design of Molecular-Scale Logic Devices. *J. Phys. Chem. Lett.*, **2021**, *125*, 8261-8273.
45. Goldsworthy, V.; LaForce, G.; Abels, S.; Khisamutdinov, E. F. Fluorogenic RNA Aptamers: A Nano-Platform for Fabrication of Simple and Combinatorial Logic Gates. *Nanomaterials*. **2018**, *8*, 984.
46. Magri, D. C.; Spiteri, J. C. Proof of Principle of a Three-Input AND-INHIBIT-OR Combinatorial Logic Gate Array. *Org. Biomol. Chem.*, **2017**, *15*, 6706-6709.
47. Omana, M.; Papasso, G.; Rossi, D.; Metra, C. (). A Model for Transient Fault Propagation in Combinatorial Logic. *In 9th IEEE On-Line Testing Symposium.*, **2003**, 111-115.
48. Zhang, Y.; Liu, W.; Zhang, W.; Yu, S.; Yue, X.; Zhu, W.; Wang, J. DNA-Mediated Gold Nanoparticle Signal Transducers for Combinatorial Logic Operations and Heavy Metal Ions Sensing. *Biosens. Bioelectron.*, **2015**, *72*, 218-224.
49. Carvalho, C. P.; Domınguez, Z.; Da Silva, J. P.; Pischel, U. A Supramolecular Keypad Lock. *Chem. Commun.*, **2015**, *51*, 2698-2701.
50. Chen, J.; Zhou, S.; Wen, J. Concatenated Logic Circuits Based on a Three-way DNA Junction: A Keypad-Lock Security System with Visible Readout and an Automatic Reset Function. *Angew. Chem. Int. Ed.*, **2015**, *54*, 446-450.
51. Andrasson, J.; Straight, S.; Moore, T.; Moore, A.; Gust, D. An All-Photonic Molecular Keypad Lock. *Chem. Eur. J.*, **2009**, *15*, 3936-3939.

52. Bhalla, V.; Kumar, M. Fluoride Triggered Fluorescence "Turn On" Sensor for Zn^{2+} Ions Based on Pentaquinone Scaffold that Works as a Molecular Keypad Lock. *Org. Lett.*, **2012**, *14*, 2802-2805.
53. Kumar, S.; Luxami V.; Saini, R.; Kaur, D. Superimposed Molecular Keypad Lock and Half-Subtractor Implications in a Single Fluorophore. *Chem. Commun*., **2009**, *21*, 3044-3046.
54. Jiang, X. J.; Ng, D. K. P. Sequential Logic Operations with a Molecular Keypad Lock with Four Inputs and Dual Fluorescence Outputs. *Angew. Chem*., **2014**, *126*, 10649 -10652.
55. Margulies, D.; Felder, C. E.; Melman, G.; Shanzer, A. A Molecular Keypad Lock: A Photochemical Device Capable of Authorizing Password Entries. *J. Am. Chem. Soc*., **2007**, *129*, 347-354.
56. Mondal, D.; Bar, M.; Maity, D.; Baitalik, S Anthraimidazoledione-Terpyridine-Based Optical Chemosensor for Anions and Cations that Works as Molecular Half Subtractor, Key-Pad Lock, and Memory Device. *J. Phys. Chem. C.*, **2015**, *119*, 25429−25441.
57. Strack, G.; Ornatska, M.; Pita, M.; Katz, E. Biocomputing Security System: Concatenated Enzyme-Based Logic Gates Operating as a Biomolecular Keypad lock. *J. Am. Chem*., **2008**, *130*, 4234-4235.
58. Sugeno, M.; Yasukhiro, T. A Fuzzy-Logic-Based Approach to Qualitative Modeling. *IEEE Trans. Fuzzy Syst*., **1993**, *1*, 7-3.
59. Zou, Qi.; Li, X.; Zhang, J.; Zhou, J.; Sun, B.; Tian, H. Unsymmetrical Diarylethenes as Molecular Keypad Locks with Tunable Photochromism and Flurescence via Cu^{2+} and CN^- Coordinations. *Chem. Commun*., **2012**, *48*, 2095-2097.
60. Perrin, D. D.; Armarego, W. L.; Perrin, D. R. *Purification of Laboratory Chemicals*., 2nd ed.; Pergamon: Oxford, U.K., **1980**.

61. Bhaumik, C.; Das, S.; Saha, D.; Dutta, S.; Baitalik, S. Synthesis, Characterization, Photophysical, and Anion-Binding Studies of Luminescent Heteroleptic Bis-Tridentate Ruthenium (II) Complexes Based On 2, 6-Bis (Benzimidazole-2-yl) Pyridine and 4′-Substituted 2, 2′: 6′, 2″ Terpyridine Derivatives. *Inorg. Chem.*, **2010**, *49*, 5049.
62. Pott, K. T.; Usifer, D. A.; Abruna, H. D. 4-Vinyl-, 6-Vinyl-, and 4'-Vinyl-2, 2': 6', 2"-Terpyridinyl Ligands: Their Synthesis and the Electrochemistry of Their Transition-Metal Coordination Complexes. *J. Am. Chem. Soc.*, **1987,** *109*, 3961.
63. Case, F. H.; Kaspen, T. J. The Preparation of Some Substituted 2, 6-Bis-(2-Pyridyl)-Pyridines. *J. Am. Chem. Soc.*, **1956**, *78*, 5842.
64. Spahni, W.; Calzaferri, G. Synthese Von Para-Substituierten Phenyl-Terpyridin Liganden. *Helv. Chim. Acta.*, **1984**, *67*, 450.
65. Constable, E. C.; Ward, M. D.; Corr, S. A Convenient, High Yield Synthesis of 2, 2′: 6′, 2 ″-Terpyridine and Its Iron (II) Complex. *Inorg. Chim. Acta.*, **1988**, *141*, 201.
66. Miyamoto, Y.; Kikuchi, A.; Iwahori, F.; Abe, J. Synthesis and Photochemical Properties of a Photochromic Iron (II) Complex of Hexaarylbiimidazole. *J. Phys. Chem. A.*, **2005**, *109*, 10183.

****

List of Publications

1. **Sahoo, A.**; Bar, M.; Biswas, R.; Abedin, T.; Baitalik, S*. "Modulation of Ground and Excited State Properties of Ruthenium Complexes through Sequential Incorporation of Metal in Polypyridyl-Imidazole Bridging Ligand: Experimental and DFT/TD-DFT Study". ***Dalton Trans***. **2023**, *52*, 15896-15906.

2. **Sahoo, A.**; Bar, M.; Bhattacharya, S.; Baitalik, S*. "Exploring the Impact of Membership Functions on the Performance of Artificial Intelligence-based Neuro-Fuzzification System (ANFIS) for Comprehensive Analysis of Anion-Responsive Behaviors in Polypyridyl-Imidazole-Based Ru(II) Receptors". (Communicated).

3. **Sahoo, A.**; Ahmed, T.; Deb, S.; Baitalik, S*. "Neuro-Fuzzification Architecture for Modeling of Electrochemical Ion-Sensing Data of Imidazole-Dicarboxylate-Based Ru (II)–Bipyridine Complex". ***Inorg. Chem***. **2022**, *61*, 10242-10254.

4. **Sahoo, A.**; Bhattacharya, S.; Jana, S.; Baitalik, S*. "Neural Network and Decision Tree-Based Machine Learning Tools to Analyse the Anion-Responsive Behaviours of Emissive Ru (II)–Terpyridine Complexes". ***Dalton Trans***. **2023**, *52*, 97-108.

5. **Sahoo, A.**; Deb, S.; Das, S.; Baitalik, S*. "Multi-Channel Anion and Cation Sensing Conduct of a Terpyridyl-Imidazole Receptor: Experimental Demonstration and Implication of Artificial Intelligence Tools for Analysis and Data Prediction". ***Dyes Pigm.*** **2023**, 111425.

6. **Sahoo, A.**; Baitalik, S*. "Fuzzy Logic, Artificial Neural Network, and Adaptive Neuro-Fuzzy Inference Methodology for Soft Computation and Modeling of Ion Sensing Data of a Terpyridyl-Imidazole Based Bifunctional Receptor". ***Front. Chem***. **2022**, *10*, 864363.

7. Deb, S.; **Sahoo, A.**; Pal, P.; Baitalik, S*. "Exploitation of the Second Coordination Sphere to Promote Significant Increase of Room-Temperature Luminescence Lifetime and Anion Sensing in Ruthenium-Terpyridine Complexes". ***Inorg. Chem.*** **2021,** *60*, 6836-6851.

8. Deb, S.; **Sahoo, A.**; Mondal, P.; Baitalik, S*. "Analysis and Prediction of Anion- and Temperature Responsive Behaviours of Luminescent Ru(II)-Terpyridine Complexes by Using Boolean, Fuzzy Logic, Artificial Neural Network and Adapted Neuro Fuzzy Inference Models". ***Dalton Trans***. **2022**, *51*, 15601-15613.

9. Paul, A.; **Sahoo, A.**; Bhattacharya, S.; Baitalik, S*. "Anion and Temperature Responsive Molecular Switches Based on Trimetallic Complexes of Ru (II) and Os (II) that Demonstrate Advanced Boolean and Fuzzy Logic Functions". ***Inorg. Chem.*** **2022**, *61*, 3186-3201.

10. Bhattacharya, S.; **Sahoo, A.**; Baitalik, S. "Human Brain-Inspired Chemical Artificial Intelligence Tools for the Analysis and Prediction of the Anion-Sensing Characteristics of an Imidazole-Based Luminescent Os (ii)-Bipyridine Complex". ***Dalton Trans.*** **2023**, *52*, 6749-6762.

11. Pal, P.; Ganguly, T.; **Sahoo, A.**; Baitalik, S*. "Emission Switching in the Near-Infrared by Reversible Trans–Cis Photoisomerization of Styrylbenzene-Conjugated Osmium Terpyridine Complexes". ***Inorg. Chem.*** **2021**, *60*, 4869-4882.

12. Mukerjee, S.; **Sahoo, A.**; Deb, S.; Baitalik, S*. "Light and Cation-Driven Optical Switch based on a Stilbene-Appended Terpyridine System for the Design of Molecular-Scale Logic Devices". ***J. Phys. Chem. A.*** **2021**, *125*, 8261-8273.

13. Deb, S.; **Sahoo, A.**; Ahmed, T.; Baitalik, S*. "Stimuli-Responsive Molecular Switches and Logic Devices Based on Ru (II)-Terpyridyl-Imidazole Coordination Motif"'. ***J. Phys. Chem. B.*** **2021**, *125*, 8919-8931.

14. Ghorai, A.; **Sahoo, A.**; Baitalik, S*.; Banerjee, S*. "Multifunctional Sulfonated Polytriazoles: Proton-Exchange Membrane Properties, Molecular Logic Gates, and Modeling of Stimuli-Responsive Behaviors". ***ACS Appl. Polym. Mater.*** **2022**, *4*, 5583-5595.

15. Deb, S.; **Sahoo, A.**; Baitalik, S*. "Harnessing Deep Neural Networks to Analyze Multi-Channel Anion Sensing Characteristics of Ru(II)-Pyrazolyl-Bis(Benzimidazole) complex". ***Eur. J. Inorg. Chem.*** **2023**, e202300009.

16. Deb, S.; **Sahoo, A.**; Karmakar, S.; Baitalik, S*. "Multi-Channel Anion Sensing Behaviour of a Ru(II)-Bipyridine Complex Based on Benzothiazolyl Pyrazole Ligand: Experimental and Implication of Machine Learning Tools for Data Prediction". ***Inorg. Chim. Acta.*** **2023**, *550*, 121451.

17. Pal, P.; **Sahoo, A.**; Paul, A.; Baitalik, S*. "Anion and Light Responsive Molecular Switches Based on Stilbene-Appended Ru (II) Terpyridyl-Imidazole Complexes That Mimic Advanced Boolean and Fuzzy Logic Operations". ***Eur. J. Inorg. Chem.*** **2022**, e202200219.

18. Mukherjee, S.; Pal, P.; **Sahoo, A.**; Baitalik, S*. "Low-Cost Photo-Switches Based on Stilbene-Appended Zn (II)–Terpyridine Complexes". ***Photochem. Photobiol. Sci.*** **2021**, *20*, 1125-1145.

19. Mukherjee, S.; Pal, P.; **Sahoo, A.**; Baitalik, S*. "Photo-Switchable Iron-Terpyridine Complexes Functionalized with Styrylbenzene Unit". ***J. Photochem. Photobiol. A.*** **2021**, *407*, 113059.

20. Das, S.; **Sahoo, A.**; Baitalik, S*. "Advancing Molecular-Scale Logic Devices through Multi-Stage Switching in a Luminescent Bimetallic Ru(II)-Terpyridine Complex". (Equally contributed with 1st author) (Communicated).

21. Bhattacharya, S.; **Sahoo, A.**; Baitalik, S*. "Fabrication of molecular-scale logic devices and implication of artificial neural networks for analysis of anion-responsive behaviors of luminescent ruthenium-terpyridine complex". (Equally contributed with 1st author) (Communicated).

Publications 1-6 are included in the thesis

*****